# Passivation of Vapour Deposited Metal Halide Perovskites for High Performance Photovoltaic Devices


Siyu Yan

Pembroke College

University of Oxford

A thesis submitted for the degree of

*Doctor of Philosophy*

Trinity 2025

谨以此文献给我亲爱的父母

# Abstract

Metal-halide perovskites have exhibited excellent optoelectronic properties and are widely used as the photoactive layers in photovoltaics. While predominantly a research innovation which showed significant promise on a lab-scale, as of 2024, perovskite solar cells are moving towards large-scale commercialisation. While vapour phase deposition processes dominate the established thin-film manufacturing, perovskite solar cells are still predominantly developed using solution-based methods. To enable scalable fabrication and industry adoption, it is imperative to advance the understanding of metal-halide perovskite thin-films fabricated by the vapour deposition technique. This thesis advances the understanding of vapour-deposited perovskite thin films and establishes several key strategies to reduce bulk and interfacial defect densities, thereby enhancing the performance and stability of vapour-deposited devices.

A major advance presented in this work is the elucidation of how organic impurities in commercial formamidinium iodide precursors influence film formation in both solution- and vapour-deposited systems. It is demonstrated that, while such impurities can beneficially passivate defects in solution-processed films, they induce altered sublimation behaviour in vapour deposition, leading to off-stoichiometric compositions and the formation of non-photoactive polytype phases. These findings establish impurity control as a critical requirement for achieving phase-pure, high-quality perovskite layers by vapour deposition.

A second key contribution is the introduction of a templating strategy that decouples perovskite nucleation from the underlying charge-transport substrate. This approach enables consistent film morphology, crystallographic orientation, and optoelectronic quality across diverse substrates. By providing a means to tune initial perovskite stoichiometry and suppress unwanted interfacial reactions, this templating method offers a scalable route toward reproducible, high-performance vapour-deposited perovskite devices.

Furthermore, this thesis demonstrates the use of aromatic ammonium halides as vapour-deposited passivation agents and reveals that their structural and functional properties depend strongly on the deposition method and post-deposition treatment. The work establishes that measurement atmosphere and thermal annealing can drive surface reconstruction and modulate passivation efficiency, thereby highlighting new levers for interface engineering in vapour-deposited perovskites.

Collectively, this research provides a comprehensive understanding of impurity effects, interfacial templating, and molecular passivation in vapour-deposited perovskite solar cells. These insights pave the way toward scalable, stable, and high-efficiency perovskite photovoltaics compatible with industrial thin-film manufacturing.

# Acknowledgements

I would like to thank everyone who has supported and encouraged me throughout my DPhil journey. This work would not have been possible without the gracious and invaluable contributions of each of you!

I am deeply grateful to my supervisors, Professor Nakita K. Noel and Professor Michael B. Johnston, for your unwavering guidance throughout my degree. Thank you for your unconditional support, insightful guidance and for granting me the freedom to investigate a wide range of research projects. I would also like to thank Professor Laura M. Herz, for the inspiring scientific discussions and for promoting collaborative science.

A huge thank you to all my friends and colleagues of the Novel Energy Materials and Advanced Characterisation research group, the Terahertz Photonics research group, the Semiconductors research group and the Physics department for the insightful conversations–both scientific and beyond–with: Jay B. Patel, Marcello Righetto, Silvia G. Motti, James M. Ball, Chelsea Xia, Mathias Uller Rothmann, Kun Peng, Kilian B. Lohmann, Aleksander M. Ulatowski, Karim A. Elmestekawy, Vincent J-Y Lim, Jae Eun Lee, Snigdha Lal, Ford Wagner, Fengning Yang, Ruohan Zhao, Saqlain Choudhary, Alexandra A. Sheader, Sinclair R. Ratnasingham, Joshua R. S. Lilly, Jiaxing Du, Tom Siday, Jakob Möbs, Gurpreet Kaur, Sarah Scripps, Petr Akinshin, Thomas Haward, Emily A. Hudson, Bembe Cameron Mackintosh, Alan Bowman, Jasmin Buerger, Terng Junn Keat, Yi Zhu, Adam Wood, Bryan Herrington. Special thanks to Jay B. Patel for your mentorship and all the fascinating scientific conversations. More than that, thank you for showing me the true meaning of teamwork and the pure joy of research it can bring. I am also especially grateful to Marcello Righetto, Karim A. Elmestekawy, Vincent J-Y Lim, Jae Eun Lee, Snigdha Lal, Ford Wagner, Fengning Yang, Ruohan Zhao, Saqlain Choudhary. Sharing this journey with you turned the laborious lab days and the most challenging moments of my DPhil from lemons into lemonade. I truly cannot imagine how I could make it without your warm and steadfast encouragement and companionship. You are friends for life!

To my family: thank you for your constant and unshakable support as always. I would not be who I am or where I am today without my parents. I love you forever, with all my heart! I am deeply thankful to all my friends, near and far. Thank you for showing me the richness and diversity of life and for helping me stay open-minded about the world that I have not known yet!

# Contents

# List of Publications

**Yan, S.** , Patel, J. B., Lee, J. E., Elmestekawy, K. A., Ratnasingham, S. R., Yuan, Q., Herz, L. M., Noel, N. K., Johnston, M. B., "*A Templating Approach to Controlling the Growth of Coevaporated Halide Perovskites*" , *ACS Energy Letters*, **2023**, *8*(10), 4008–4015.

Lilly, J. R. S., Lim, V. J.-Y., Patel, J. B., **Yan, S.**, Lee, J. E., Johnston, M. B., Herz, L. M., "*Impact of Halide Alloying on the Phase Segregation of Mixed-Halide Perovskites*" , **2025**, manuscript under review.

Scripps, S. J., **Yan, S.**, Yuan, Q., Herz, L. M., Noel, N. K., Johnston, M. B., "*Contamination of Metal Halide Perovskite Films After the Evaporation of an Organic Passivating Agent*" , **2025**, manuscript under preparation.

Lee, J. E., Righetto, M., Putland, B. W. J., **Yan, S.**, Lilly, J. R. S., Lal, S., Jin, H., Noel, N. K., Johnston, M. B., Snaith, H. J., Herz, L. M., "*Impact of Charge Transport Layers on the Structural and Optoelectronic Properties of Co-evaporated* $Cu_2AgBiI_6$" , *ACS Applied Materials & Interfaces*, **2025**, *17*(28), 40363–40374.

Pham, H. T., **Yan, S.**, Xu, Z., Johnston, M., Etheridge, J., "*Direct Observation of Grain Boundaries and Chemical Composition of* $Cs_xFA_{1-x}Pb(I_yCl_{1-y})_3$ *Photoactive Perovskites*" , *13th Asia Pacific Microscopy Congress 2025 (APMC13)*, **2025**, ScienceOpen, 302.

Du, J., Righetto, M., Kober-Czerny, M., **Yan, S.**, Elmestekawy, K. A., Snaith, H. J., Johnston, M. B., Herz, L. M., "*Inter-Layer Diffusion of Excitations in 2D Perovskites Revealed by Photoluminescence Reabsorption*" , *Advanced Functional Materials*, **2025**, Wiley, 2421817.

Lim, V. J.-Y., Righetto, M., **Yan, S.**, Patel, J. B., Siday, T., Putland, B., McCall, K. M., Sirtl, M. T., Kominko, Y., Peng, J., "*Contrasting Ultra-Low Frequency Raman and Infrared Modes in Emerging Metal Halides for Photovoltaics*" , *ACS Energy Letters*, **2024**, *9*(8), 4127–4135.

Lee, J. E., Motti, S. G., Oliver, R. D. J., **Yan, S.**, Snaith, H. J., Johnston, M. B., Herz, L. M., "*Unraveling Loss Mechanisms Arising from Energy-Level Misalignment between Metal Halide Perovskites and Hole Transport Layers*" , *Advanced Functional Materials*, **2024**, *34*(30), 2401052.

Ulatowski, A. M., Elmestekawy, K. A., Patel, J. B., Noel, N. K., **Yan, S.**, Kraus, H., Huggard, P. G., Johnston, M. B., Herz, L. M., "*Contrasting Charge-Carrier Dynamics across Key Metal-Halide Perovskite Compositions through In Situ Simultaneous Probes*" , *Advanced Functional Materials*, **2023**, *33*(51), 2305283.

Yuan, Q., Lohmann, K. B., Oliver, R. D. J., Ramadan, A. J., **Yan, S.**, Ball, J. M., Christoforo, M. G., Noel, N. K., Snaith, H. J., Herz, L. M., "*Thermally Stable Perovskite Solar Cells by All-Vacuum Deposition*" , *ACS Applied Materials & Interfaces*, **2022**, *15*(1), 772–781.

# Abbreviations and Nomenclature

| | |
|---|---|
| AM 1.5 | Air Mass 1.5 |
| ATR-FTIR | Attenuated Total Reflectance-Fourier Transform Infrared Spectroscopy |
| CB | Conduction Band |
| CTL | Charge Transport Layer |
| EQE | External Quantum Efficiency |
| ETL | Electron Transport Layer |
| FA | Formamidinium $CH(NH_2)_2^+$ |
| FF | Fill Factor |
| FTO | Fluorine-Doped Tin Oxide |
| FWHM | Full Width at Half Maximum |
| GIWAXS | Grazing-Incident Wide-Angle X-Ray Scattering |
| HTL | Hole Transport Layer |
| $J_{sc}$ | Short-Circuit Current Density |
| MA | Methylammonium $CH_3NH_3^+$ |
| MHP | Metal Halide Perovskite |
| MS | Mass Spectrometry |
| NIR | Near Infrared |
| NMR | Nuclear Magnetic Resonance |
| OPTP | Optical Pump THz Probe |
| PCE | Power Conversion Efficiency |
| PL | Photoluminescence |
| PSC | Perovskite Solar Cell |
| PV | Photovoltaics |
| QCM | Quartz Crystal Microbalance |
| RGA | Residual Gas Analysis |
| SEM | Scanning Electron Microscopy |
| SPO | Stabilized Power Output |
| TCSPC | Time-Correlated Single Photon Counting |
| THz | Terahertz |
| UV | Ultra Violet |

| | |
|---|---|
| VB | Valence Band |
| $V_{oc}$ | Open-Circuit Voltage |
| XRD | X-Ray Diffraction |
| 3D | Three-Dimensional |
| 2D | Two-Dimensional |
| 1D | One-Dimensional |
| $\alpha$ | Absorption Coefficient |
| $D_n$ | Diffusion Coefficient for Electrons |
| $D_p$ | Diffusion Coefficient for Holes |
| $E_F$ | Fermi Level |
| $E_g$ | Bandgap |
| $\hbar$ | Reduced Planck Constant |
| $k_B$ | Boltzmann's Constant |
| k | Wavevector |
| $\varepsilon_n$ | Total Energy of the Electron in the Orbital |
| $\psi_n(x)$ | Wavefunction of the Electron |
| U | Potential Energy |
| $f(\varepsilon)$ | Fermi-Dirac Distribution |
| $\mu_n$ | Electron Mobility |
| $\mu_p$ | Hole Mobility |
| $\phi$ | Electrostatic Potential |
| n | Electron Density |
| p | Hole Density |
| $\eta$ | Power Conversion Efficiency |

# List of Figures

# 1

# Introduction

## Contents



## 1.1 Motivation

The escalating climate crisis has made the reduction of annual greenhouse gas emissions a global priority. The energy sector has remained the largest global contributor to greenhouse gas emissions, accounting for approximately 26% of global emissions in 2023. To achieve the goal of net-zero emissions and power a green future, the transition from fossil fuels to renewable energy sources such as solar photovoltaic, wind energy, hydropower, geothermal, concentrated solar power, and marine energy is critical. The United Nations Environment Programme (UNEP) Emission Gap Report 2024 points out that, technically, limiting global warming to 1.5°C remains at least technically possible by increasing the deployment of solar photovoltaic technologies and wind energy to contribute 27% of the total emission

reduction potential (the maximum possible reduction in greenhouse gas emissions through different mitigation strategies and technologies) in 2030 and 38% in 2035.[1]

The implementation of renewable energy was initially stymied by concerns about costs and the challenges of integration. However, the global electricity system has undergone a profound transformation from 2010 to 2023. Up to now, solar energy has increasingly become the default source of least-cost new power generation. The International Renewable Energy Agency (IRENA) Renewable Cost Database demonstrates the global levelized cost of electricity (LCOE) of renewable energies compared with that of fossil fuel (Figure 1.1). Notably, solar power has seen the most rapid cost reductions, with a decrease of 90% between 2010 and 2023.[2]

The year 2024 marked a significant milestone for solar power. Global solar installations reached nearly 600 gigawatts (GW), representing a 33% increase over the previous year (Figure 1.2). Solar energy accounted for 81% of all new renewable energy capacity added worldwide, solidifying its role as one of the major drivers of the global energy transition. For the first time, photovoltaic energy production accounted for >10% of the world' s electricity consumption.[3] This remarkable progress has been powered by rapid technological advancements that have substantially reduced costs, and historically low prices driven by global manufacturing overcapacities.

Silicon photovoltaics are the mainstream technologies in the solar power market, accounting for over 95% of all installations.[3] However, photovoltaic devices based on halide perovskites, a relatively new solar absorber material, have significant

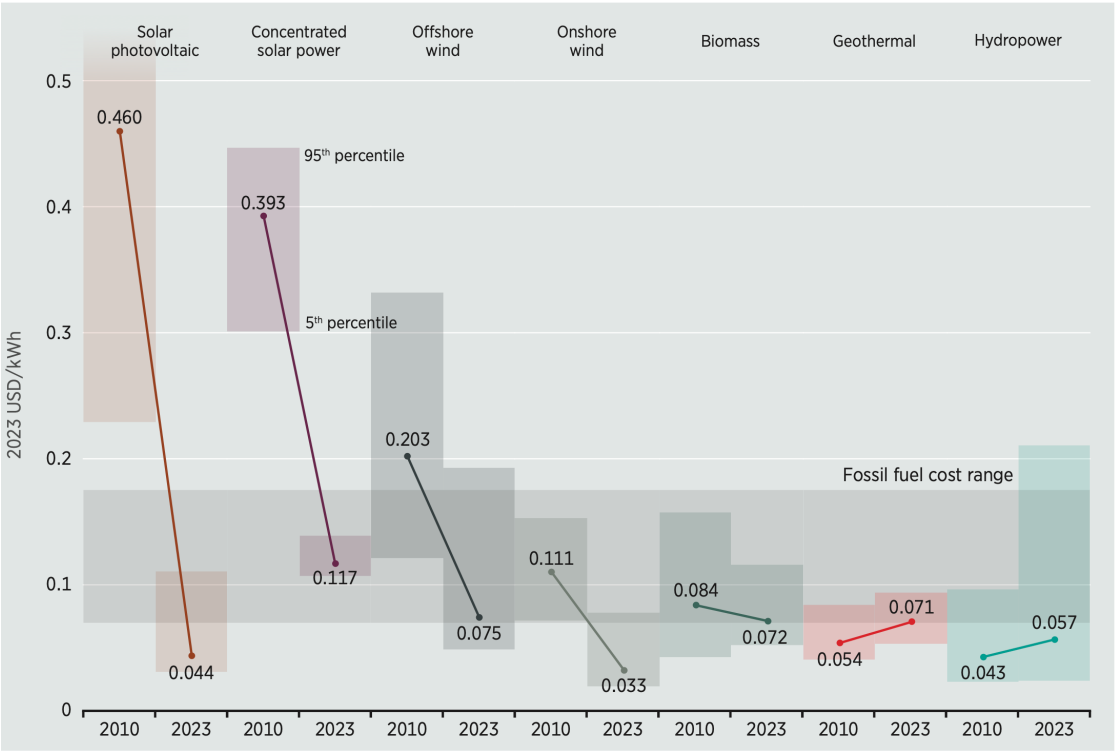


**Figure 1.1:** Global levelized cost of electricity (LCOE) from newly-commissioned, utility-scale renewable power technologies, 2010 and 2030. The thick lines are the global weighted average LCOE value derived from the individual plant commissioned in each year. The grey band represents the fossil fuel-fired power generation cost in 2023, while the bands for each technology and year represent the $5^{th}$ and $95^{th}$ percentile bands for renewable projects. Reproduced with permission from IRENA© 2024[2]

promise to infiltrate this market; drawing attention from both the scientific community as well as industry.[4–8] Since Miyasaka and colleagues first reported the perovskite solar cell in 2009,[9] the power conversion efficiency has leapt to 26.95% for single-junction solar cells, making it comparable to the efficiency of crystalline Si photovoltaics.[10] The remarkable improvements of perovskite photovoltaics in such a short period result from the excellent optoelectronic material properties and rapid improvements in fabrication approaches.[11–15] Additionally, the low-cost fabrication and tunable bandgap provide opportunities for commercialisation, particularly through integration with silicon solar cells to create multi-junction cells. By more efficiently converting solar power into electricity, perovskite photovoltaics allow

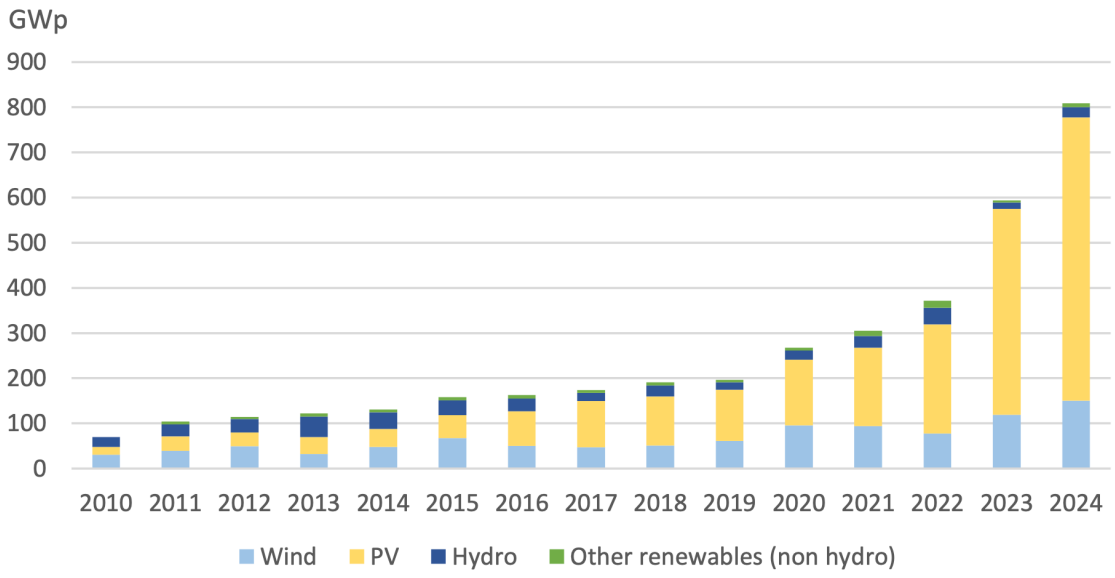


**Figure 1.2:** Evolution of annual renewable energy installations. Sourced from International Energy Agency Photovoltaic Power Systems Programme Snapshot of Global PV Markets 2025. Reproduced with permission from IEA PVPS© 2025[3]

silicon photovoltaics to go beyond their current performance limits.[16–18]

As of now, while perovskite photovoltaics are on the edge of commercialisation, the scalability from research lab to industrial scale and long-term operational stability are two fundamental challenges that must be addressed.[19] While perovskites can be easily processed by the solution method, the solvents used for precursor inks bring health and safety issues to large-scale fabrication. Besides looking for green solvents, the vapour deposition technique is another alternative which allows for conformal deposition, controllable layer thickness, and high compatibility with multijunction devices.[20] Therefore, focusing research on the development of vapour-based perovskite solar cells will be essential for facilitating the transition to large-scale production required for photovoltaic applications.

## 1.2 Research Objectives

This thesis presents a systematic investigation into the factors limiting the power conversion efficiency of vapour-deposited perovskite solar cells and develops potential strategies to address these challenges.

Chapter 2.4.5 gives a brief introduction to the fundamental concepts of semiconductor materials from a band theory perspective. I then proceed to discuss the device physics of photovoltaics and the corresponding methodologies used to characterise the devices. Finally, I present a broad overview of halide perovskites, the primary material investigated in this thesis, by introducing the key concepts and recent advances in material and device engineering.

Chapter 3.5 outlines the key principles and experimental details of the techniques used throughout the thesis, including the fabrication and characterisation of perovskite thin films and devices, together with the nuclear magnetic resonance spectroscopy and mass spectroscopy techniques employed to determine molecular structure and investigate precursor composition. The section on thin-film characterisation techniques details the approaches used to probe the structural, morphological and optoelectronic properties of perovskite thin-films.

Chapter 4.4 describes the first experimental research work in this thesis. It deals with the investigation of the types of organic impurities in commercially available formamidinium iodide (FAI) and probes their impact on perovskite films and devices. This chapter demonstrates that while the inclusion of some impurities can improve the quality of films and devices produced through spin-coating, in vapour-

deposition the presence of these impurities changes the sublimation behaviour of FAI, resulting in a significant deviation from the target stoichiometry and leading to the formation of non-photoactive phases. The existence of these non-photoactive phases impairs device performance; therefore, it is essential to remove these impurities from precursor materials used for vapour deposition.

Given the importance of eliminating undesirable non-perovskite phases discussed in Chapter 4.4, it is essential to develop a high-quality bottom charge transport layer/co-evaporated perovskite interface, as this plays a vital role in the nucleation and growth of the entire perovskite film. Chapter 5.4 offers a promising strategy for decoupling the nucleation and growth of co-evaporated perovskite films from the influence of substrate materials. By employing a templating layer, co-evaporated perovskite films display identical morphology, structure, and optoelectronic properties, irrespective of the choice of substrate. This precise control of the interface facilitates fine-tuning the stoichiometry of the initial perovskite deposited onto the substrate, thus enhancing photovoltaic performance.

Another plausible route to enhance the performance and stability of vapour-deposited perovskite solar cells is to passivate surface defects. Chapter 6.4 explores the impact of various vapour-deposited passivation agents on co-evaporated perovskite films. Structural and optoelectronic investigations highlight the critical influence of measurement atmospheres and annealing treatments on the passivation effects. Notably, the improvement of optoelectronic properties at the perovskite/hole transport layer interface when applying annealed vapour-deposited passivation agents does not directly translate to an enhancement of device performance in either p-i-n or n-i-p architectures, indicating a more complex mechanism

at play in a full device. A comparison with spin-coated passivation layers further reveals that the structural properties and passivation effects of the passivation layer depend on the deposition methods.

# 2

# Theory and Background

## Contents



This chapter introduces fundamental concepts that are relevant to the rest of this thesis. Semiconductor band structure will be explained, followed by a description of photovoltaic device physics. Finally, recent advances in process engineering to improve the structural and optoelectronic quality of metal halide perovskite films

are summarised in the context of thin film growth deposition techniques.

## 2.1 Semiconductor Materials

In general, there are different classification schemes for solids based on crystal structure and electronic properties. One important and intuitive classification of solids is based on the geometrical symmetry of their crystal structures, which is not directly related to their electronic properties. Another classification scheme is based on the configuration of the valence electrons in wave vector space. This determines the most important distinction between metals and insulators, which depends on whether there are partially filled bands or overlapping bands at the Fermi level. Figure 2.1 shows the electron occupancy of allowed energy bands for an insulator, a metal, and a semiconductor. A material is generally classified as an insulator if there is a relatively large energy gap (bandgap), $E_{\mathrm{g}}$, between the top of the highest filled band (the valence band) and the bottom of the lowest empty band (the conduction band). In contrast, a material is considered a semiconductor if the bandgap is relatively small, allowing electrons to be promoted into the conduction band by thermal excitation at a certain temperature, or by impurity doping.[21]

A solid with an energy gap will be nonconducting at absolute temperature $T = 0$ K. However, when the temperature is not absolute zero there is a probability that some electrons will be thermally excited across the energy gap. The resulting conductivity depends strongly on the magnitude of the bandgap, since the number of electrons thermally promoted to the conduction band at temperature $T$ follows an exponential dependence on the bandgap energy. For an intrinsic semiconductor,

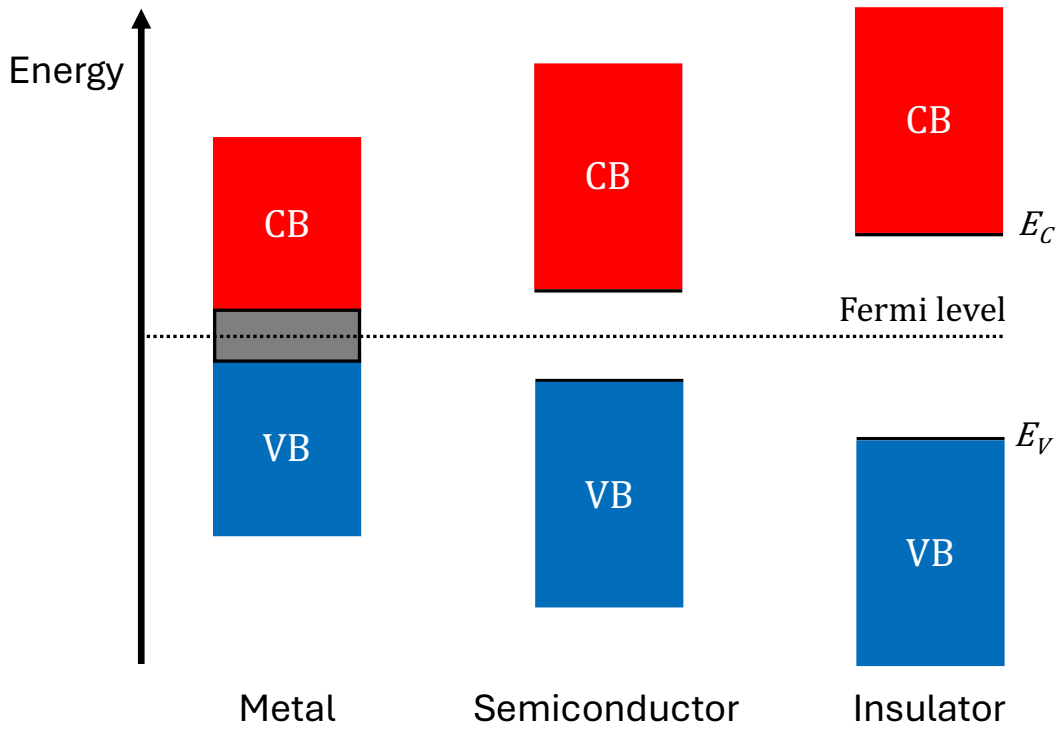


**Figure 2.1:** Schematic electron occupancy of allowed energy bands for a metal, a semiconductor and an insulator. The vertical extent of the boxes indicates the allowed energy regions; $E_C$ and $E_V$ are the minimum energy level within the conduction band and the maximum energy level within the valence band, respectively.

in which the Fermi level lies in the center of the bandgap, this fraction is roughly on the order of $e^{-E_g/(2k_BT)}$ (Boltzmann factor). Therefore, at room temperature ($k_BT$ ≈0.025 eV, the fraction is $e^{-58} \approx 10^{-26}$) for a material with the $E_g$ value of 3 eV, in which thermal excitation of electrons across the bandgap almost will not occur. If, however, $E_g$ is 0.25 eV, the fraction is $e^{-5} \approx 10^{-2}$, in which appreciable conduction will happen. Therefore, the $E_g$ of semiconductors is usually in the range of 0.5-3 eV. Typical resistivities of semiconductors at room temperature are between $10^{-3}$ to $10^{9}$ $\Omega \cdot$ cm.

Since the number of thermally-excited electrons across the bandgap is proportional to $1/T$, the electrical conductivity of a semiconductor rapidly increases

with increasing temperature. Conversely, in a metal, the conductivity decreases with increasing temperature. This results in a negative coefficient of resistance in semiconductors. Aside from this, semiconductors also show unique large Seebeck coefficient, the photoconductivity, and rectifying effects. To comprehensively understand characteristic properties in semiconductors, we need to introduce the band theoretical explanations.

### 2.1.1 Band Structure

The band structure of a material refers to the relationship between energy and the electron wavevector. To understand the energy states of electrons in the solid, let us consider the energy states from the simplest scenario first. In the Free Electron Model without considering the interactions between electrons and ions, the wavefunction $\psi_n(x)$ of the electron is a solution of the time-independent Schrödinger equation $\hat{H}\psi = \varepsilon\psi$; with the neglect of potential energy, we have[22]

$$\hat{H}\psi_n = -\frac{\hbar^2}{2m}\frac{d^2\psi_n}{dx^2} + 0 = \varepsilon_n\psi_n \tag{2.1}$$

where $\varepsilon_n$ is the total energy of the electron in the $n^{th}$ orbital. For the equation in the middle, the left term is the kinetic energy, and the right term is the potential energy $U(x)$ ($U(x) = 0$ in this case). If we apply $\frac{d^2\psi_n}{dx^2} = -k^2\psi_n$, the energy $\varepsilon_{\mathbf{k}}$ of the orbital with the wavevector $\mathbf{k}$ is[23]

$$\varepsilon_{\mathbf{k}} = \frac{\hbar^2\mathbf{k}^2}{2m} \tag{2.2}$$

The wavefunction of the free electron is

$$\psi_{\mathbf{k}}(\mathbf{r}) = e^{i\mathbf{k}\cdot\mathbf{r}} \tag{2.3}$$

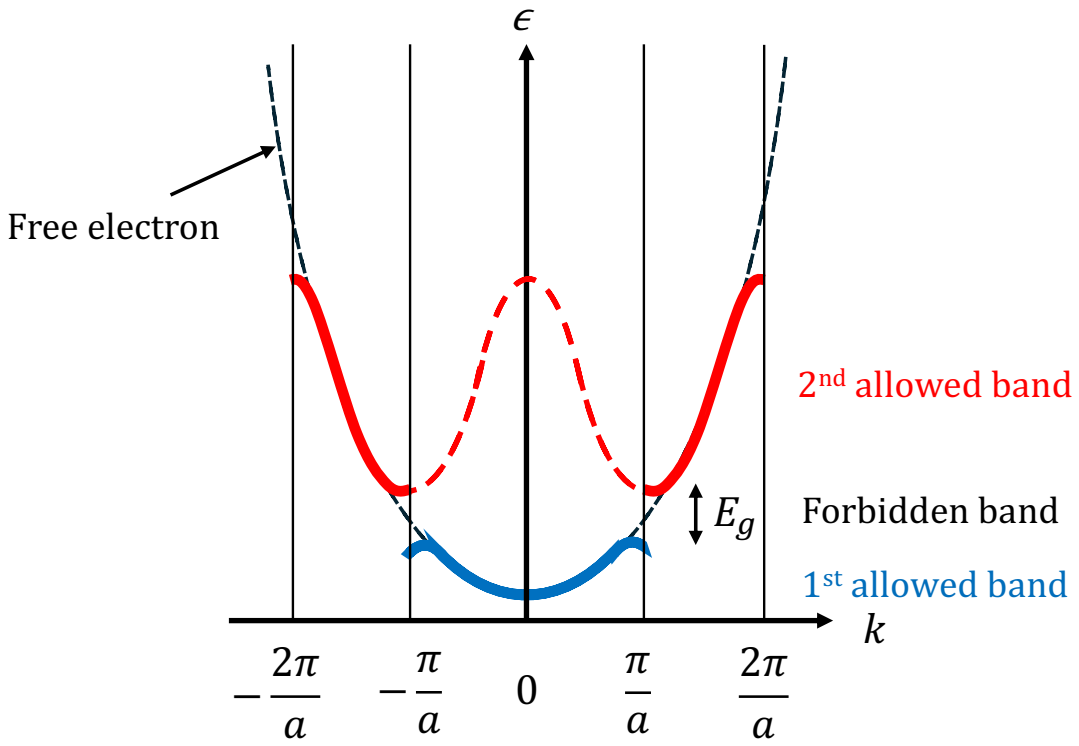


**Figure 2.2:** Plot of energy $\varepsilon$ versus wavevector $k$. The black dashed line represents the dispersion relation of the free electron model. The (red and blue) solid lines correspond to the dispersion relation of the nearly free electron model (NFE). The weak NFE potential perturbation forms the energy gap at the zone boundaries. The energy difference between the 1st allowed band and 2nd allowed band is the energy gap $E_g$. The red dashed line in the 1st Brillouin zone is the equivalent dispersion in the reduced zone scheme.

Figure 2.2 shows the energy $\varepsilon_{\mathbf{k}}$ is parabolic in $\mathbf{k}$ for entirely free electrons.

When the electron waves propagate in solids, the band electrons are perturbed by the periodic potential from the periodicity of the lattice. In this case, Bloch's theorem provides the solution of the time-independent Schrödinger equation with the potential energy $U(\mathbf{r})$, where $U(\mathbf{r}+\mathbf{R}) = U(\mathbf{r})$ for all vectors $\mathbf{R}$ in the Bravais lattice. In Bloch's theorem, the eigenstates $\psi$ of the one-electron Hamiltonian are the products of a plane wave times a function $u(\mathbf{r})$ with the periodicity of the lattice:

$$\psi_{n\mathbf{k}}(\mathbf{r}) = e^{i\mathbf{k}\cdot\mathbf{r}} u_{n\mathbf{k}}(\mathbf{r}) \tag{2.4}$$

where

$$u_{n\mathbf{k}}(\mathbf{r}+\mathbf{R}) = u_{n\mathbf{k}}(\mathbf{r}) \tag{2.5}$$

From Equations 2.4 and 2.5 we can derive that

$$\psi_{n\mathbf{k}}(\mathbf{r}+\mathbf{R}) = e^{i\mathbf{k}\cdot\mathbf{R}}\psi_{n\mathbf{k}}(\mathbf{r}) \tag{2.6}$$

Now we introduce the Born-von Karman boundary condition for the periodic system

$$\psi(\mathbf{r}+\mathbf{R}) = \psi(\mathbf{r}) \tag{2.7}$$

Applying Bloch's theorem to this boundary condition (Equation 2.7), it requires that

$$e^{i\mathbf{k}\cdot\mathbf{R}} = 1 \tag{2.8}$$

Since $\mathbf{R}$ is the Bravais lattice vector, for simplicity, in 1D must have

$$k = \frac{2n\pi}{L} = \frac{2n\pi}{Na} \quad n = \pm 1, \pm 2, \pm 3 \ldots \pm \frac{N}{2} \tag{2.9}$$

where $L$ is the length of the crystal, and $a$ is the lattice constant. This means that $k$ has discrete allowed values. The first reflections and the first energy gap occur at $k = \pm\pi/a$. The region in $\mathbf{k}$ between $-\pi/a$ and $\pi/a$ is the first Brillouin zone of this lattice. For two traveling waves

$$e^{\pm i\pi x/a} = \cos(\pi x/a) \pm i\sin(\pi x/a) \tag{2.10}$$

These traveling waves interact with each and form the standing waves

$$\psi(+) = e^{i\pi x/a} + e^{-i\pi x/a} = 2\cos(\pi x/a) \propto \cos(\pi x/a) \tag{2.11}$$

$$\psi(-) = e^{i\pi x/a} - e^{-i\pi x/a} = 2i\sin(\pi x/a) \propto \sin(\pi x/a) \tag{2.12}$$

where $(+)$ and $(-)$ represent whether the standing waves change sign when replacing $x$ with $-x$. The two standing waves pile up electrons in different regions,

and therefore they have different potential energy values in the field of the lattice, which yields the energy gap. In order to get the energy $\varepsilon$, we start by considering when $\mathbf{k}$ is exactly on a zone boundary. If $\mathbf{G}$ is the reciprocal lattice vector, then $\mathbf{k}' = \mathbf{k} + \mathbf{G}$ is also on a zone boundary. In this case, $\varepsilon_0(\mathbf{k}) = \varepsilon_0(\mathbf{k} + \mathbf{G})$, and the characteristic equation simplifies to

$$(\varepsilon_0(\mathbf{k}) - \varepsilon)^2 = |U_{\mathbf{G}}|^2 \tag{2.13}$$

and now

$$\varepsilon_{\pm} = \varepsilon_0(\mathbf{k}) \pm |U_{\mathbf{G}}| \tag{2.14}$$

Thus, at the zone boundary, the energy gap opens up and energies split by $\pm|U_{\mathbf{G}}|$ (Figure 2.2). In this case, the band structure has small gaps open at the zone boundary and quadratic dispersion near the band gap, instead of the parabolic spectrum in the free electron model.

For a crystalline solid, its electrical characteristics can be extracted from its band structure. As previously mentioned, determining whether the material is a metal, insulator or semiconductor is based on the number of electrons in each band and the size of the energy gap. When an electron is excited into the conduction band, there is an absence of an electron in the valence band, known as a hole. The electron usually moves from the valence band maximum (VBM) to the conduction band minimum (CBM). If the CBM is located at the same point in $k$-space as the VBM, then the transition can directly happen when the energy of the incident radiation exceeds the band gap, known as a direct transition. If the CBM and VBM occur at different points in $k$-space, then a phonon must also participate in the process to conserve the crystal momentum, and this is known as

an indirect transition. Such transition processes in semiconductor materials can be straightforwardly distinguished by optical measurements.

One of the most important characteristics of semiconductors is that their concentration of intrinsic carriers is a function of temperature and bandgap. In an intrinsic semiconductor, carrier concentration is related to the number of electrons excited to the conduction band at temperature $T$. The determination of carrier concentration involves both the probability that any particular state is occupied and the number of states in each band. The probability of a state at energy $\varepsilon$ being occupied is given by the Fermi-Dirac distribution[24,25]

$$f(\varepsilon) = \frac{1}{exp[(\varepsilon - \mu)/k_B T] + 1} \tag{2.15}$$

where $\mu$ is the electrochemical potential, also known as the Fermi level in semiconductor physics. The Fermi-Dirac distribution gives the probability of an orbital at energy $\varepsilon$ being occupied by electrons at thermodynamic equilibrium. The Fermi level can be considered to be a hypothetical energy level of an electron which would have a 50% probability of being occupied at any given time. Figure 2.3 shows the Fermi-Dirac distribution function and band diagram on the same energy scale for an intrinsic semiconductor. To determine the number of electrons in the CB and the number of holes in the VB, we must also know the density of states (DOS) —the number of available energy states in a system at a given energy level. The DOS is defined as the number of states per unit energy per unit volume and is a function of energy ($\varepsilon$). It can be calculated from the quantised solutions of the Schrödinger equation. It is important to note that the DOS varies based on the dimensionality of the system, leading to differences when moving from bulk to low-dimensional systems.

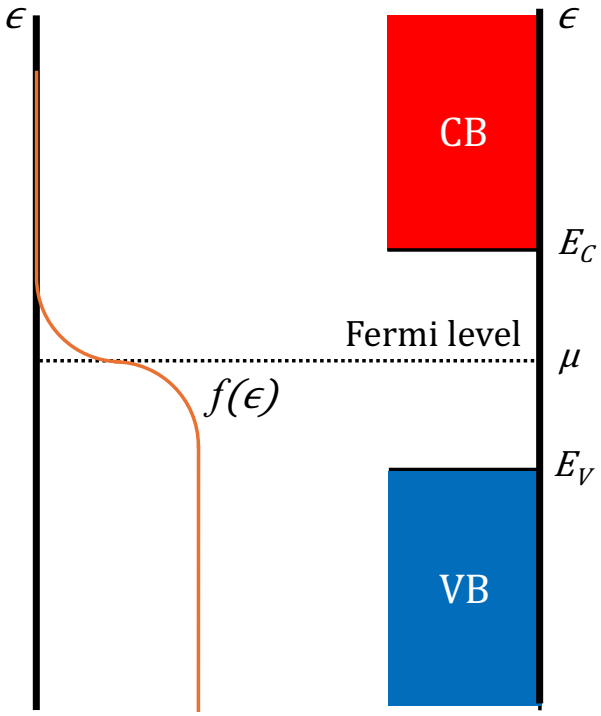


**Figure 2.3:** The Fermi-Dirac distribution and corresponding band structure on the same energy scale for an intrinsic semiconductor. $f(\varepsilon) = \frac{1}{2}$ when $\varepsilon = \mu$.

Different from intrinsic semiconductors, in which the electrical properties are essentially determined by the electronic band scheme of the material, when containing certain impurities and imperfections, the electrical properties of a semiconductor can be drastically modified and even dominated by the impurities. The deliberate addition of impurities to a semiconductor is called doping. The concentration of electrons and holes in doped semiconductors is no longer the same as that of intrinsic semiconductors. Therefore, when doping with electron donors (n-type doping) or electron acceptors (p-type doping), the Fermi level will shift upwards towards the CB or downwards towards the VB.

## 2.2 Principles of Photovoltaics

So far, this chapter has considered semiconductors at equilibrium. To more comprehensively understand the operation of a solar cell, this section will start by discussing what happens to the semiconductor when it is exposed to an external stimulus, such as light. It then introduces charge separation by the asymmetric junction which is key for photovoltaic energy conversion, and the importance of effective charge transport.[26,27]

### 2.2.1 Optical Absorption

Charge carrier generation is an electronic excitation event which increases the number of free carriers available to carry charge. While different types of absorption transitions can happen as a result of the electronic band structure of a typical semiconductor, for the solar cell, the most important form of charge carrier generation is inter-band optical absorption. During the inter-band optical absorption process, the absorbed photon will cause the promotion of an electron from the VB to the CB, creating free electron-hole pairs. Since the total energy and the total momentum of the electron-photon pair need to be conserved during this process, direct transitions only happen in direct gap semiconductors. In this case, the absorption of photons with energy $\hbar\omega_{\text{photon}} < E_g$ is forbidden. For photons with higher energy ($\hbar\omega_{\text{photon}} > E_g$), the excess energy is lost through thermalisation. Near the bandgap, the absorption coefficient depends on the joint density of states (JDOS)–the number of states that are available for a photon with certain energy to interact with–in the VB and CB. Therefore, we can directly

extract the $E_g$ value by using the Elliott fitting model, which will be discussed in Chapter 3.5. Given that the total light absorption depends on the absorption coefficient ($\alpha$), which is an intrinsic property of the semiconductor, and the optical length, increasing the thickness of the absorbing layer is usually the practical strategy to increase absorption.

The standard spectrum for solar cell calibration is air mass 1.5, also known as AM1.5.[28,29] The air mass is the path length which light takes through the atmosphere, normalised to the shortest possible path length where the sun is directly overhead. For AM1.5, it signifies the path length of sunlight through the atmosphere when the sun is at a 48.2° angle with an irradiance of 1000 W/m$^2$ which is a typical condition for many locations on Earth. In the ideal situation, the power conversion efficiency (PCE) of the solar cell should be a function just of $E_g$ and the incident spectrum. If the incident spectrum is fixed, then PCE only depends on the bandgap. Since the final PCE is the product of photovoltage and photocurrent (only incident photons of energy $E > E_g$ can be absorbed), there is an optimum band gap at which PCE has a maximum value. In 1961, Shockley and Queisser analysed the theoretical maximum efficiency under the AM1.5 solar spectrum, commonly referred to as the detailed balance limit.[30] Figure 2.4 shows the efficiency as a function of $E_g$ for the standard AM1.5 solar spectrum. For a single-junction solar cell, the peak efficiency of 33.7% can be achieved with a band gap of 1.34 eV.

Another important change to semiconductors during photogeneration is the deviation from equilibrium states due to external disturbances. By exposure to light or an applied electric bias, the population of electrons and holes increases

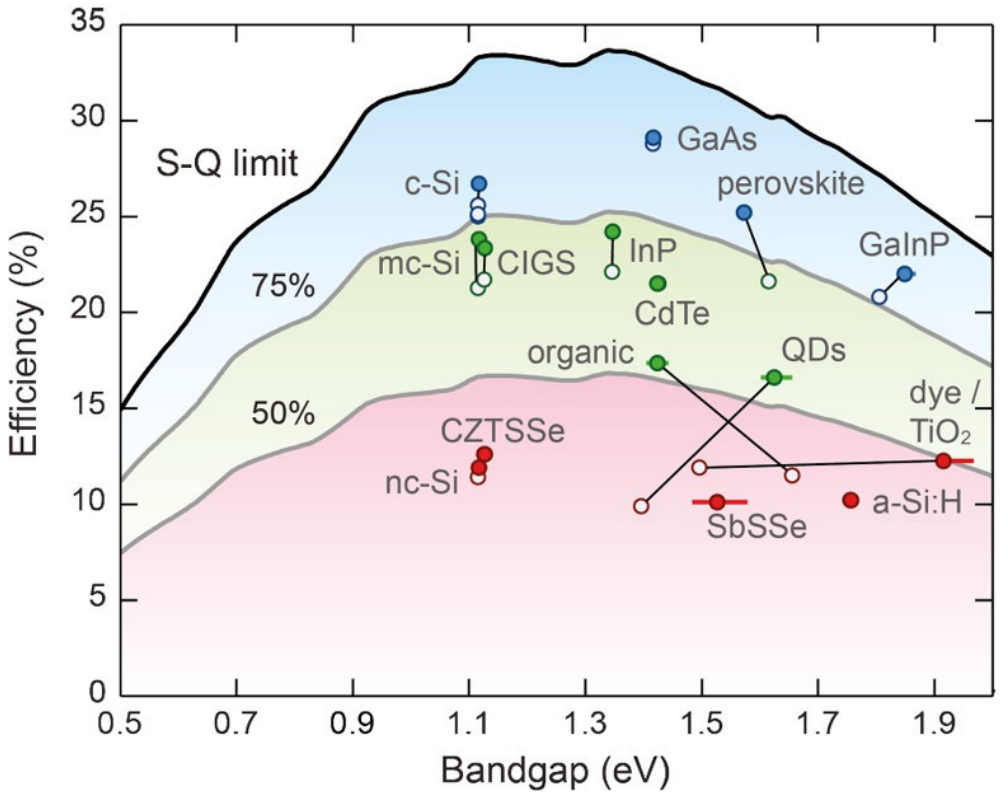


**Figure 2.4:** Record efficiency of solar cells of different materials against their bandgap at AM1.5 illumination conditions. The top solid line is the SQ limit. Reproduced with permission from Polman, A. et al., *Science*, 2016, 352(6283)© 2016 AAAS[31]

above their equilibrium values, which can no longer be described by the Fermi-Dirac distribution.

In this case, electrons in conduction bands and valence bands have different distribution functions $f_c(\mathbf{k}, \mathbf{r})$ and $f_v(\mathbf{k}, \mathbf{r})$, which are both position- and $\mathbf{k}$-state dependent. Therefore, the key simplification for semiconductors under nonequilibrium conditions–provided the disturbance is neither too large nor too rapid–is that the population of electrons and holes each can achieve a quasi-thermal equilibrium,

$$f_c(\mathbf{k}, \mathbf{r}) \approx f_0(E, E_{Fn}, T_n) \tag{2.16}$$

$$f_v(\mathbf{k}, \mathbf{r}) \approx f_0(E, E_{Fp}, T_p) \tag{2.17}$$

The new apparent Fermi levels for electrons and holes are the electron and hole quasi-Fermi levels, $E_{Fn}$ and $E_{Fp}$. The electron and hole densities in a semiconductor under quasi-thermal equilibrium can be written as

$$n = n_i e^{(E_{Fn}-E_i)/k_B T_n} \tag{2.18}$$

$$p = n_i e^{(E_i-E_{Fp})/k_B T_p} \tag{2.19}$$

where $T_n$ and $T_p$ are the effective temperatures of electrons and holes, which may be different from the ambient temperature $T$. These electrons and holes quickly lose their excess energy as heat by interacting with the lattice, and only the bandgap energy is harvested as electrical power, we assume $T_n = T_p = T$. Given that $E_{Fn} \neq E_{Fp} \neq E_F$, the difference in quasi-Fermi levels is also known as quasi-Fermi level splitting,

$$\Delta\mu = E_{Fn} - E_{Fp} \tag{2.20}$$

The electron hole product is now written as

$$np = n_i^2 e^{\Delta\mu/k_B T} \tag{2.21}$$

### 2.2.2 Charge Separation

To generate power using the photovoltaic effect, the generated electrons and holes need to be extracted and collected, which requires a mechanism for charge separation. Essentially, an asymmetric junction, typically a semiconductor $p$-$n$ junction, is needed to drive the electrons and holes away from the point of generation. Based on the Boltzmann transport equation and relaxation time approximation, the electron and hole current densities can be derived,

$$J_n(\mathbf{r}) = \mu_n n \nabla_{\mathbf{r}} E_{Fn} \tag{2.22}$$

$$J_p(\mathbf{r}) = \mu_p p \nabla_{\mathbf{r}} E_{Fp} \tag{2.23}$$

The total current at a point is $J = J_n + J_p$. Therefore, to convert light into electricity, light needs to produce a gradient in at least one of the quasi-Fermi levels. To understand this, the drift-diffusion equation is introduced. Drift is the current driven by an electric field inside the semiconductor. Diffusion is the current driven by a concentration gradient of electrons and holes in the semiconductor. The drift current density equations are given by

$$J_{ndrift} = \mu_n n E = -\mu_n n \nabla \phi \tag{2.24}$$

$$J_{pdrift} = \mu_p p E = -\mu_p p \nabla \phi \tag{2.25}$$

where $\mu_n$ and $\mu_p$ are electron and hole mobilities, $E$ is the electric field, and $\phi$ is the electrostatic potential.

Diffusion current in semiconductors typically arises from carrier concentration gradients. The electron and hole diffusion current density equations are given by,

$$J_{ndif} = q D_n \nabla n \tag{2.26}$$

$$J_{pdif} = -q D_p \nabla p \tag{2.27}$$

where $D_n$ and $D_p$ are the diffusion coefficient for electrons and holes. The simplified total current density in one dimensional can be written as,

$$J_{nT} = -q\mu_n n \frac{d\phi}{dx} + q D_n \frac{dn}{dx} \tag{2.28}$$

$$J_{pT} = -q\mu_p p \frac{d\phi}{dx} - q D_p \frac{dp}{dx} \tag{2.29}$$

Now assume that we have two separate semiconductor blocks (Figure 2.5). Block A is $n$-type material, and Block B is $p$-type material. When they contact

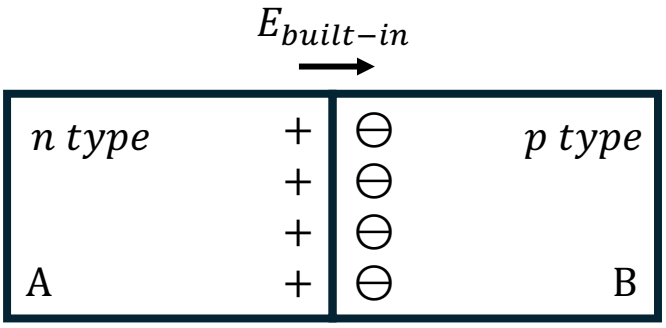


**Figure 2.5:** Block A and Block B are n-type and p-type semiconductors, respectively. The diagram shows the built-in electric field that arises, pointing from Block A to Block B, when the two blocks are in contact.

each other, the mobile electrons from Block A will diffuse to Block B since the concentration of electrons in Block A is higher than in Block B. As a result, positively charged ions are left behind in Block A near the interface, while Block B becomes negatively charged near the interface. This creates an electric field that points from Block A to Block B, known as the built-in electric field. This built-in potential generates a drift current to counteract the diffusion flow. Consequently, without an applied voltage, there is no net current across the junction. Since this region has no mobile charge carriers, it is also called the depletion region.

When Block A and Block B are isolated from each other, their Fermi levels are independent. When they are brought into electronic contact, the Fermi levels must line up. Figure 2.6 illustrates the band profiles of Block A ($n$-type) and Block B ($p$-type) semiconductors, both in isolation and after they form a $p$–$n$ junction in equilibrium. The built-in electric field at the junction drives photogenerated electrons towards the $n$ side (Block A) and holes towards the $p$ side (Block B). The built-in bias, $V_{bi}$, in equilibrium, is the difference in work functions of the two materials (in this case, $V_{bi} = \frac{1}{q}(\phi_A - \phi_B)$).

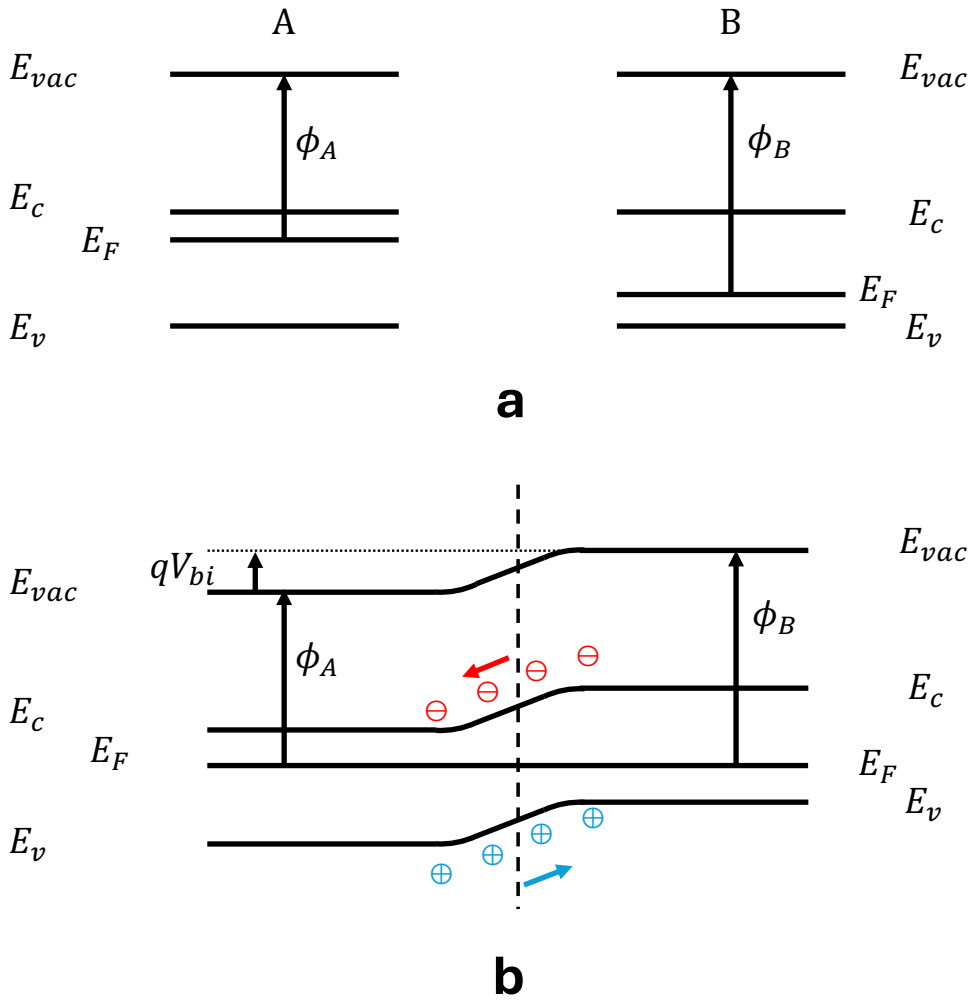


**Figure 2.6:** (a) Band profiles of Block A ($n$-type) and Block B ($p$-type) semiconductors in isolation. (b) Band profile of the $p$–$n$ junction in equilibrium.

### 2.2.3 Charge Collection

To complete the charge collection process, the separated carriers need to move to the external circuits. As mentioned above, this is an asymmetric structure that drives the electrons/holes away from the point of generation. Therefore, the $p$–$n$ junction also forms a diode, which allows electric current to flow in one direction but not in the other. The equation for the ideal diode is

$$J_{dark} \approx J_0[e^{qV/k_BT} - 1] \tag{2.30}$$

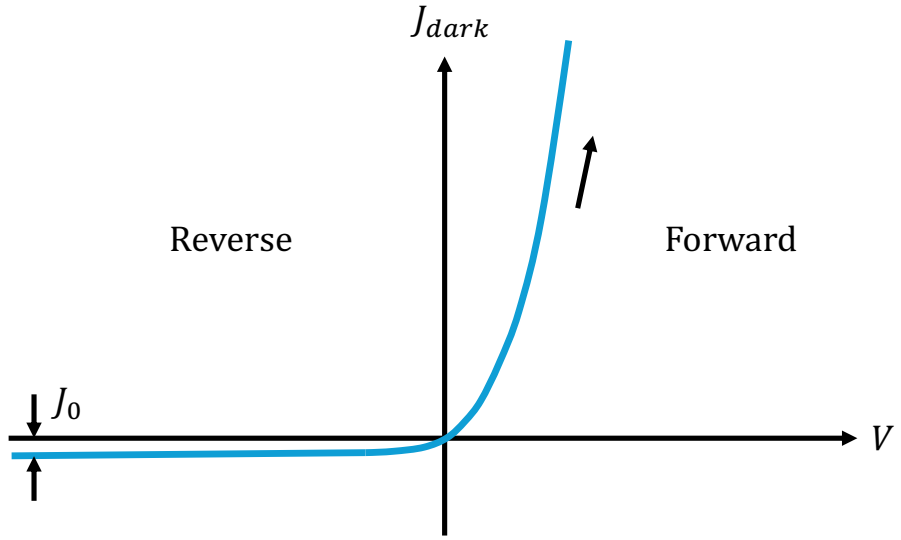


**Figure 2.7:** Plot of current density-voltage characteristic under dark conditions in the ideal p-n junction diode.

where $J_0$ is a constant, $V$ is the applied voltage (a positive number when the positive terminal is connected to the $p$ side). In this case, if an external voltage is applied to the $p$–$n$ junction, it exhibits rectification properties (Figure 2.7). Specifically, when the forward voltage bias is applied (positive), substantial current can flow through the diode. In contrast, in reverse bias, the current is greatly suppressed, allowing only a small leakage current $J_0$ to pass through.

In forward bias, the applied positive external voltage generates an electric field in the opposite direction to the built-in electric field, thereby reducing the drift current. The diffusion current now is greater than the drift current and a net current will flow. In this case, $J_{\text{dark}} \approx J_0 \left(e^{qV/k_BT}\right)$. In reverse bias, the external electric field is in the same direction as the built-in electric field. However, the charge carriers in the enhanced electric field are minority carriers; the drift current slightly increases, which is many orders of magnitude smaller than the forward bias current, $J_{\text{dark}} \approx -J_0$.

## 2.3 Characterisation of Photovoltaic Devices

### 2.3.1 Photocurrent-Voltage

In a classical photovoltaic cell, under illumination, the photogenerated electrons and holes accumulate on the n side and p side, shifting the Fermi levels as if a positive bias is applied. When there is no load, the photocurrent generated by the solar cell under illumination is the short-circuit current density, $J_{sc}$.

$$J_{sc} = q \int_0^\infty QE(E) b_s(E)\, dE \tag{2.31}$$

where $QE(E)$ is the probability that an incident photon of energy $E$ will deliver one electron to the external circuit, and $b_s(E)$ is the incident spectral photon flux density. Given that the quantum efficiency $QE(E)$ is the product of the collection and absorption efficiencies, we assume perfect charge separation and collection processes, in which the photocurrent is only a function of the band gap and the incident spectrum, $J_{sc} = q \int_{E_g}^\infty b_s(E)\, dE$.

Therefore, based on the superposition approximation, the overall current density–voltage characteristics ($J$–$V$ curve) of the photovoltaic cell can be approximated as the sum of the $J_{sc}$ and the dark current density $J_{dark}$ (Equation 2.30).

$$J = J_{sc} - J_0[e^{qV/k_BT} - 1] \tag{2.32}$$

When the terminals are isolated, the maximum potential difference is the open-circuit voltage, $V_{oc}$. In this case, the dark current and short-circuit photocurrent exactly cancel out. From the ideal diode in Equation 2.32, we can derive

$$V_{oc} = \frac{k_BT}{q} \ln(\frac{J_{sc}}{J_0} + 1) \tag{2.33}$$

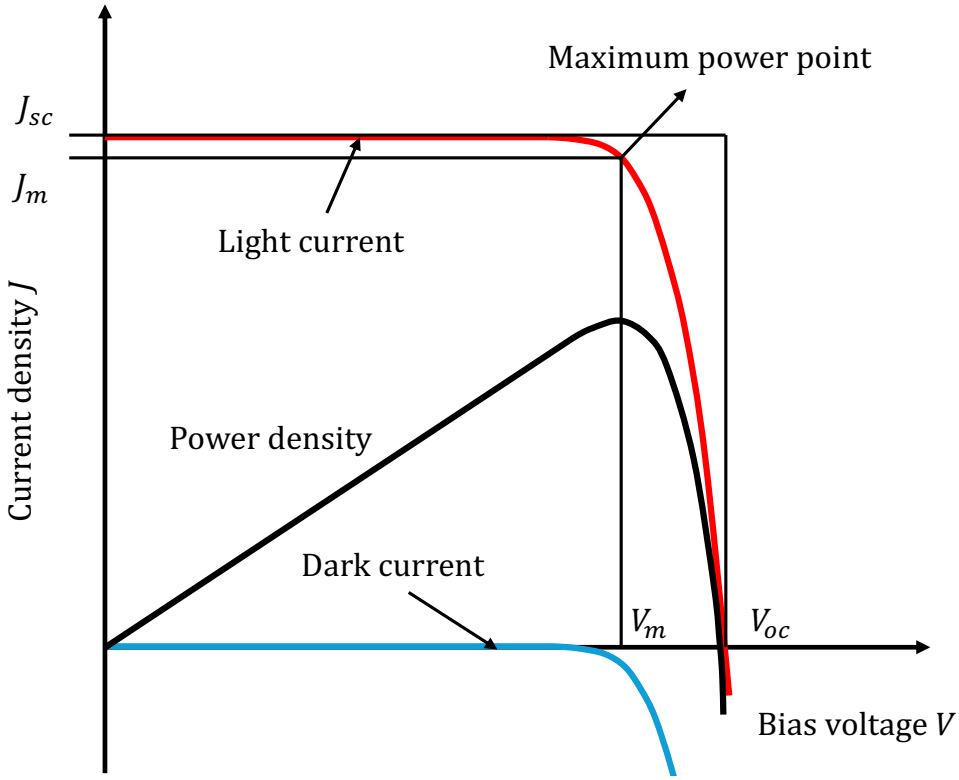


**Figure 2.8:** The current density-voltage characteristics ($J$–$V$ curve) of an ideal solar cell under illumination. Power density reaches its maximum value at the bias voltage $V_m$ and current density $J_m$, which is given by the area of the inner rectangle. The sign convention is that the short-circuit photocurrent is positive.

The operating regime of the solar cell to deliver power is from 0V to $V_{oc}$. The maximum power conversion efficiency of solar cells occurs at the maximum power point, with the voltage $V_m$ and current density $J_m$. The fill factor ($FF$) is defined as $FF = \frac{J_m V_m}{J_{sc} V_{oc}}$ to describe the 'squareness' of the $J-V$ curve (Figure 2.8). The efficiency $\eta$ can be written as

$$\eta = \frac{J_m V_m}{P_s} = \frac{J_{sc} V_{oc} FF}{P_s} \tag{2.34}$$

where $P_s$ is the incident light power density.

### 2.3.2 Series and Shunt Resistance

Practically, the 'ideal' diode behaviour (Equation 2.32) is seldom seen. Instead, some power is dissipated via the resistance of the contacts and/or through leakage currents around the side of the device. The influence of these parasitic resistances can be modelled as resistances in series ($R_s$, $\Omega$) and in parallel ($R_{sh}$, k$\Omega$) to the electrical circuit.

The series resistance ($R_s$) results from the resistance of the material to the current flow, which is a particular problem at high current densities. The shunt resistance ($R_{sh}$) comes from leakage of current through the cell, around the edge of the device and/or between contacts with different polarities, which is a problem in poorly rectifying devices. When taking parasitic resistances into consideration, the diode equation is

$$J = J_{sc} - J_0[e^{q(V+JAR_s)/k_BT} - 1] - \frac{V + JAR_s}{R_{sh}} \tag{2.35}$$

where $A$ is the active area of the cell.

### 2.3.3 Urbach Energy

In 1953, the Austrian-American physicist Franz Urbach found that the plot of the logarithm of the absorption edge versus photon energy approaches a straight line. The slope is near to $1/k_BT$ (Figure 2.9a).[32] These exponential absorption coefficient ($\alpha$) tails below the bands (sub-gap absorption) are so-called Urbach tails ($E_u$) following the expression

$$\alpha(E,T) \propto exp(\frac{E - E_{on}(T)}{E_u(T)}) \tag{2.36}$$

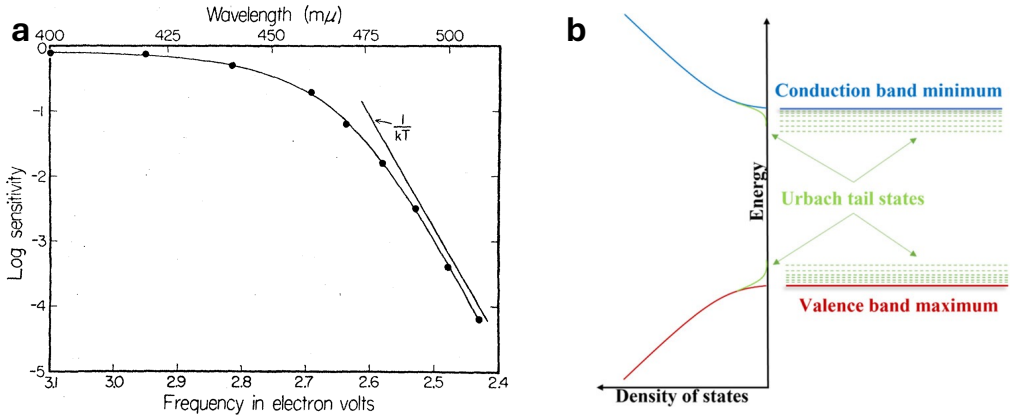


**Figure 2.9:** (a) Spectral sensitivity of an unfinished pure AgBr emulsion at 22°C. Reproduced with permission from F. Urbach, *Physical Review*, 92, 5, 1324, 1953© 1953 APS[32] (b) Schematic representation of Urbach tail states in a semiconductor system. Reproduced with permission from O. V. Rambadey, et. al. *ACS Omega*, 6, 47, p32231–32238, 2021© 2021 ACS[33]

where $E$ is the photon energy, and $E_{on}$ is the energy onset of the tail. The Urbach energy is a measure of the total energetic disorder of the system, which can modify the bonding scheme of the atoms/ions, giving rise to the onsite potential fluctuations. As a result, the states near the CB/VB could extend to the forbidden energy region (Figure 2.9b).[33]

A frequently employed method to determine $E_U$ is to extract the apparent Urbach energy from the external quantum efficiency (EQE) measurement. Via the modified Beer-Lambert law, the absorbance in the sub-gap can be regarded as proportionally related with the absorption coefficient ($\alpha$). Since the carrier collection efficiency is generally excitation energy independent, EQE $\propto A$ and $\propto \alpha$. By fitting a small range in the sub-gap range, the apparent Urbach energy ($E_u^{app}$) can be written as[34]

$$E_u^{app}(E) = [\frac{d\ln(EQE)}{dE}]^{-1} \tag{2.37}$$

## 2.4 Metal Halide Perovskite

This section outlines the brief history of metal halide perovskites (MHPs), introducing the most fundamental concepts related to the crystal structure, optoelectronic properties, and defect physics in MHPs. Then, recent advances in process engineering to improve the structural and optoelectronic quality of metal halide perovskite films are summarised in the context of thin film growth deposition techniques.

### 2.4.1 Introduction

In 1839, calcium titanate ($CaTiO_3$) was first discovered in the Ural mountains of Russia, named after Russian mineralogist Von Perovski. Subsequently, materials with the same crystal structure as $CaTiO_3$ were known as perovskite materials. Generally, perovskite materials are classified into several categories: oxide perovskites, chalcogenide perovskites and metal halide perovskites (MHPs).[9,35] While the ferroelectric and superconducting properties of oxide-based perovskites intrigued scientists very early on,[36] MHPs have only emerged as promising materials in the photovoltaic field over the past decade due to their high absorption coefficients, long charge carrier diffusion lengths, defect tolerance, and low exciton binding energies.[13,37] In 2009, the first perovskite solar cell (PSC) was reported by Miyasaka and colleagues, achieving a power conversion efficiency (PCE) of 3.8%.[9] They used methylammonium lead iodide ($MAPbI_3$) to replace the organic dyes on mesoporous $TiO_2$ in dye-sensitized solar cells. However, it was not until a PCE of over 10% was achieved in solid-state $MAPbI_3$ PSCs, that physicists and chemists became intensely interested in developing high-performance PSCs.[38] In 2013, Liu

et al. fabricated the first efficient planar heterojunction PSC with a champion PCE of 15.4% via the vapour co-deposition method.[39] This successful change of the device structure marked a significant advancement in the PSC field. To date, the planar heterojunction architecture is still the dominant device structure used in high-efficiency PSCs. Although the highest certified efficiency of single junction PSCs has reached 26.95% today, developing high-performance devices of large-area with long-term stability will be the major challenge to successfully commercialise PSCs.[40–42]

### 2.4.2 Crystal Structure

The general structural formula of MHPs is $ABX_3$, where A is usually a monovalent alkali metal or organic cation (such as cesium $Cs^+$, methylammonium $MA^+$, formamidinium $FA^+$), B is a metal ion (such as lead $Pb^{2+}$, tin $Sn^{2+}$), and X is a halide anion (such as iodide $I^-$, bromide $Br^-$, chloride $Cl^-$). Adjacent $BX_6$ octahedra are connected through corner-sharing to form the three-dimensional (3D) framework, with A-site cations positioned in the gaps formed by the octahedra (Figure 2.10). For $FAPbI_3$, the photoactive phase has a cubic structure. The ability of a combination of ions to crystallise into this structure is predicted by the octahedral factor ($\mu$) and Goldschmidt's tolerance factor ($t$),[43,44]

$$\mu = \frac{r_B}{r_X} \tag{2.38}$$

$$t = \frac{r_A + r_X}{\sqrt{2}(r_B + r_X)} \tag{2.39}$$

where $r_A$, $r_B$, and $r_X$ represent the ionic radius values of A, B, and X, respectively. The tolerance factor reflects how well the A cation fits into the 12-fold coordinated cuboctahedral site formed by $BX_6$ octahedra, and the octahedral factor reflects how

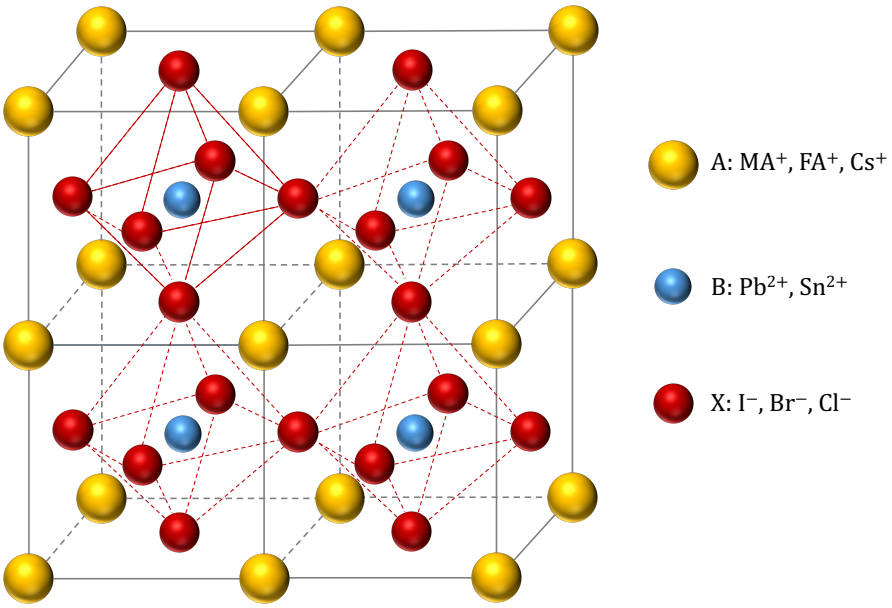


**Figure 2.10:** The $ABX_3$ structure of metal halide perovskites incorporates a large cation on the A-site, a metal cation on the B-site, and a halide anion on the X-site.

well the B cation fits into the center of an octahedron of anions. For the AX–$BX_2$ halide system, a (pseudo)cubic-phase $ABX_3$ perovskite is favoured when $0.442 < \mu < 0.895$ and $0.813 < t < 1.107$; otherwise, the tetragonal-phase (I4/mcm) or orthorhombic-phase ($Pna2_1$) are the preferred structures.

Although these metal halide perovskites perform well in the field of solar cells, their poor stability limits further commercialisation. The instability arises from the decomposition or transformation of perovskite compounds under the action of water, heat, ultraviolet radiation, or electric field. In the case of $FAPbI_3$ for example, the photoactive phase which is in the perovskite structure ($\alpha$ phase, space group P3m1) is only metastable at room temperature. Under ambient storage the films and crystals revert to their thermodynamically favourable phase which is a lower dimensional hexagonal phase, otherwise known as the $\delta$ phase (space group $P6_3mc$). One approach to solving this problem is the partial substitution of $FA^+$ cations with other smaller volume cations (such as $Cs^+$, $MA^+$, $Rb^+$), or by

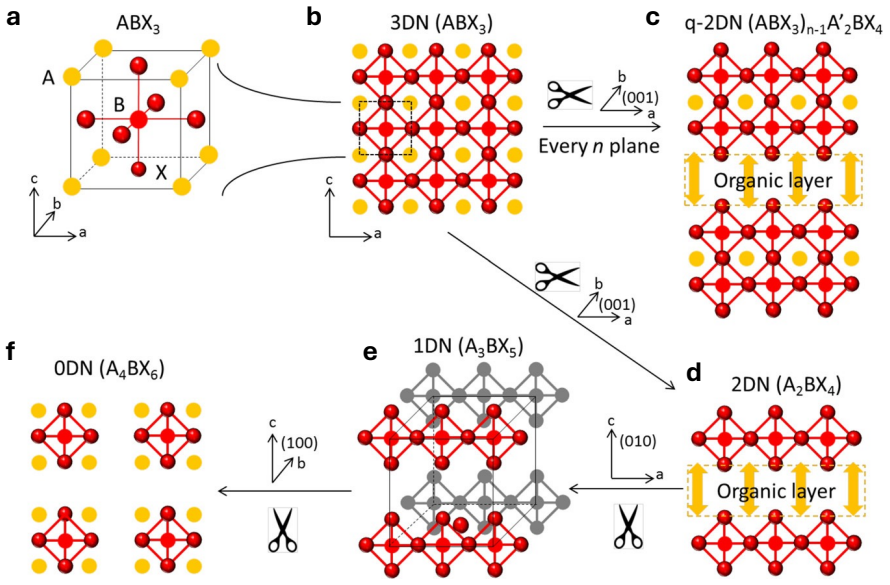


**Figure 2.11:** Schematic representations of crystal structures of perovskites from 3D $ABX_3$(a, b), quasi-2D $(ABX_3)_{n-1}A'_2BX_4$(c), 2D $A_2BX_4$(d), 1D $A_3BX_5$(e), and 0D $A_4BX_6$(f). Reproduced with permission from M I. Saidaminov et. al., *ACS Energy Letters*, 2, 4, 889–896, 2017© 2017 ACS[48]

incorporating smaller anions (such as $Br^-$, $Cl^-$) into the lattice.[45–47]

Additionally, replacing A-site cations with larger-volume cations can lead to new lower dimensional materials. Based on their octahedral dimensions, ranked from high to low, they can be divided into quasi-two-dimensional (quasi-2D), two-dimensional (2D), one-dimensional (1D), and zero-dimensional (0D) perovskites (Figure 2.11).[48] Compared to the original 3D structure, these low-dimensional derivatives exhibit enhanced thermodynamic stability, thereby mitigating degradation under environmental stressors such as humidity, temperature fluctuations, ultraviolet light, and oxygen exposure.

Structurally, the organic-inorganic hybrid $A_2BX_4$ perovskite can be formed by inserting larger A-site organic cations (along the [001] crystal plane) between the $[BX_6]^{4-}$ layers in the 3D perovskite. This structure, composed of ordered

intercalation of $[BX_6]^{4-}$ inorganic perovskite layers and organic cation layers, is referred to as a 2D perovskite. The A cation in the 3D compound is partially replaced by the bulky A′ cation, and the stacked $ABX_3$ perovskite layers are periodically separated to form a superlattice. The structure with the general formula $A_{n-1}A'_2B_nX_{3n+1}$ is defined as a quasi-2D perovskite. Compared with 2D perovskites, 1D perovskites are obtained by further separating the 2D perovskite along the [010] plane that connects $[BX_6]^{4-}$ units, giving the general formula $A_3BX_5$ or $ABX_3$. If the $[BX_6]^{4-}$ octahedra connected in the 3D perovskite are completely separated, i.e., the 1D perovskite is separated along the [100] plane, its 0D derivative can be obtained with the structural formula $A_4BX_6$ or $A_3B_2X_9$.

### 2.4.3 Optoelectronic Properties

The commonly used 3D MHPs, such as $MAPbI_3$, $FAPbI_3$, etc., have excellent optical and electronic properties for photovoltaic applications such as: high absorption coefficients ($10^4$-$10^5$ $cm^{-1}$), optimal optical band gaps (1.2-1.6 eV) and carrier diffusion lengths of 1 $\mu$m.[49] As a result, they serve as ideal light-harvesting semiconductor materials for efficient light collection and low-energy barrier photogenerated exciton separation.

The excellent optoelectronic properties of perovskites come from their unique band-edge energy state distribution. Generally, the lead-based halide perovskites are direct band gap semiconductors, having CBM and VBM aligned in the same $k$-point in reciprocal space. The strong interband transitions offer large absorption coefficients. The electronic bands in perovskites are formed through the overlap of $[BX_6]^{4-}$ orbitals. For $MAPbI_3$ in particular, Pb 6s-I 5p $\sigma$-antibonding orbitals

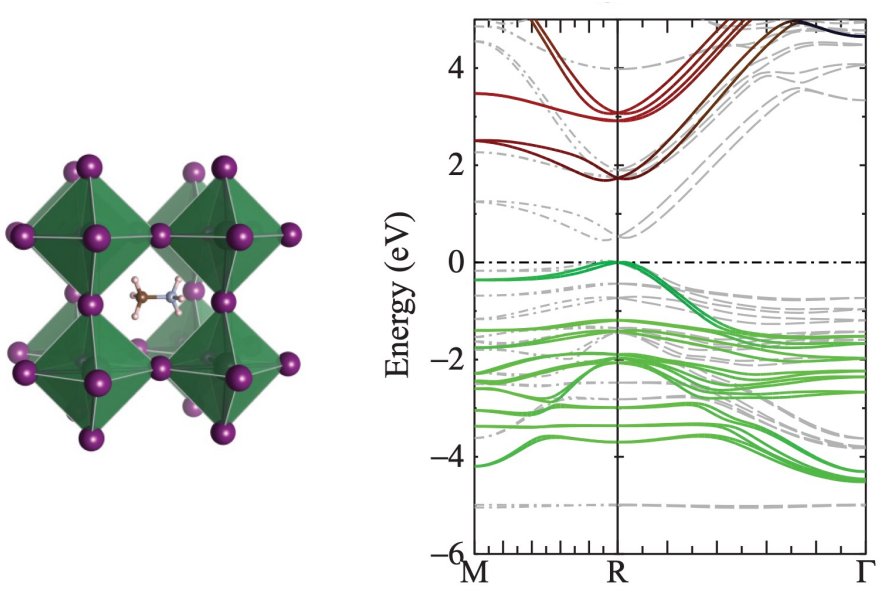


**Figure 2.12:** Quasiparticle self-consistent GW theory (*QSGW*) band structure of $MAPbI_3$. Reproduced with permission from F. Brivio et. al., *Physical Review B*, 89, 15, 155204, 2014© 2014 APS[50]

comprise the VBM, while Pb empty 6p orbitals mainly constitute the CBM. The heavy nature of Pb and I ions results in significant spin-orbit coupling, which can lower the band gap and cause a splitting of the conduction band states with the lower, split-off band forming the CBM. The antibonding states lie higher energy and shift more easily with different degrees of orbital overlap, which can offer perovskites the ease of bandgap tunability.[51]

Additionally, the antibonding orbitals form dispersive bands with steep slopes, leading to smaller effective masses and higher mobilities than organic semiconductors. Given that most defects formed in perovskites are shallow defects, they do not strongly localise charge carriers, which is often described as 'defect tolerance'.[52] The high mobility and long charge-carrier lifetime contribute to the long carrier diffusion length in perovskites.[53,54] Figure 2.12 shows that similar dispersion at the band edge of perovskites, resulting in electrons and holes with comparable effective

mass and mobility.[50] It is evident from this electronic structure that perovskites exhibit balanced charge-carrier transport.

### 2.4.4 Defect Physics

Metal halide perovskites have exhibited superior optoelectronic properties compared to traditional semiconductor materials, such as crystalline silicon (c-Si), polycrystalline silicon, and cadmium telluride (CdTe). However, compared with the well-controlled manufacturing of c-Si semiconductors, the crystal growth rate of MHPs is generally rapid and results in polycrystalline films, containing more structural defects than the high-quality single-crystal films that dominate traditional photovoltaics. These defects become the major non-radiative recombination centers in perovskite films and reduce device performance.[55] Compared with other photovoltaic performance parameters, the open-circuit voltage ($V_{oc}$) is highly dependent on the density of these defects,[56]. This is because $V_{oc}$ is sensitive to the quasi-Fermi levels splitting of electrons and holes in the perovskite films. The difference between the material bandgap and the $V_{oc}$ measured is defined as the $V_{oc}$ deficit. Additionally, the migration of certain shallow defects can cause ion migration and accumulation at the interface, resulting in photocurrent hysteresis, unfavourable band bending and even phase segregation.[57,58] This will increase the intrinsic instability of perovskite films, weakening the thermal and photostability of PSCs. Hence, the passivation of perovskite films can be introduced as an efficient approach to improve device performance and stability.

#### 2.4.4.1 Defects in Metal Halide Perovskites

Figure 2.13 illustrates the possible defect types in crystalline semiconductors.[59] For perovskites, native point defects are the most extensively studied defects (Figure 2.13a-d). Generally, a specific type of defect is thermodynamically favourable if its formation energy in a semiconductor is negative. A conventional approach involves theoretically calculating the formation energies of defects in a particular material. However, in reality, the formation energy is closely related to atomic environements around the defects and the charge states of defects, causing the defect structures vary substantially based on growth conditions and the presence of competing secondary phases.

To simplify the situation, we will mainly discuss the defect types in $FAPbI_3$, as this composition serves as the basic structure for all studies conducted in this thesis. The point defects in the neutral charge-state in $FAPbI_3$ include interstitials ($FA_i$, $Pb_i$, $I_i$), vacancies ($V_{FA}$, $V_{Pb}$, $V_I$) and antisites ($FA_{Pb}$, $Pb_{FA}$, $FA_I$, $Pb_I$, $I_{FA}$, $I_{Pb}$). Liu et al. found that different from $MAPbI_3$, in which MA-related defects $MA_I$ and $I_{MA}$ had high formation energies, FA-related intrinsic defects had low formation energies in $FAPbI_3$. Antisites $FA_I$ and $I_{FA}$ can create deep levels in the bandgap, acting as non-radiative recombination centers. To avoid the formation of $FA_I$ defects, materials should be grown in an I-rich environment.[60]

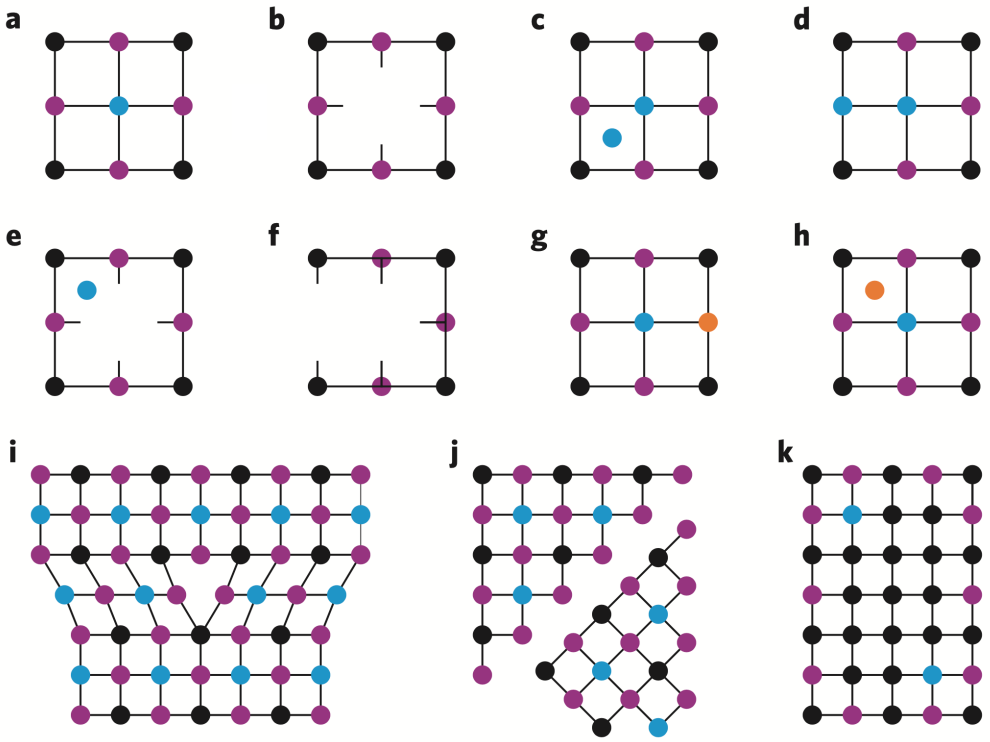


**Figure 2.13:** Defect chemistry in metal halide perovskites (blue, black, and purple dots represent the A-, B-, and X-site cations/anions, respectively). (a) perfect lattice; (b) vacancy; (c) interstitial; (d) anti-site substitution; (e) Frenkel defect; (f) Schottky defect; (g) substitutional impurity (orange dot represents the impurity); (h) interstitial impurity; (i) edge dislocation (line defect propogation); (j) grain boundary; (k) precipitate. Reproduced with permission from J. M. Ball et. al., *Nature Energy*, 1, 11, 2016© 2016 Springer Nature[59]

#### 2.4.4.2 Effects of Defects on the Optoelectronic Processes in Semiconductors

When evaluating whether a specific mechanism is a relevant carrier recombination process, we need to consider the charge-carrier density and the statistics of carrier interactions with defect states in the bandgap. In general, non-radiative defect-mediated charge-carrier recombination is particularly important to solar cell performance under open-circuit conditions. Given that the quasi-Fermi level splitting is determined by the charge-carrier density, non-radiative defect-mediated charge-carrier recombination will reduce the quasi-Fermi level splitting by decreasing the

steady-state charge-carrier density.

To maximise the collection efficiency, the absorber layer in a solar cell must be thick enough for effective absorption; meanwhile, be thin enough for the efficient charge transport. When the photogenerated charge-carrier density is higher than the trap density, the trap states are likely to be fully populated and therefore have negligible influence on the charge transport. However, when the photogenerated charge-carrier density is lower than the trap density, the trap states possibly change the charge transport mechanism based on the type of defects present.

Additionally, unintentional defects in the bulk or at the interfaces can influence the electric field distribution within an operating solar cell. The shallow defects with corresponding electronic states can ionise at room temperature acting as donor/acceptor states doping the semiconductor. The deep defects will form sub-bandgap states and substantially limit the quasi-Fermi level splitting.

### 2.4.5 Crystallisation Kinetics

Considering the polycrystalline nature of perovskite thin films used in photovoltaics, the quality of the film essentially limits the device performance and stability. To fabricate high-quality films, it is crucial to understand how these materials crystallise. This section will summarise what is currently understood with regards to the crystallisation kinetics of vapour-deposited perovskites.

Figure 2.14 shows five fundamental processes which occur during vapour deposition, including ① evaporation, ② transport, ③ absorption/desorption, ④ diffusion,

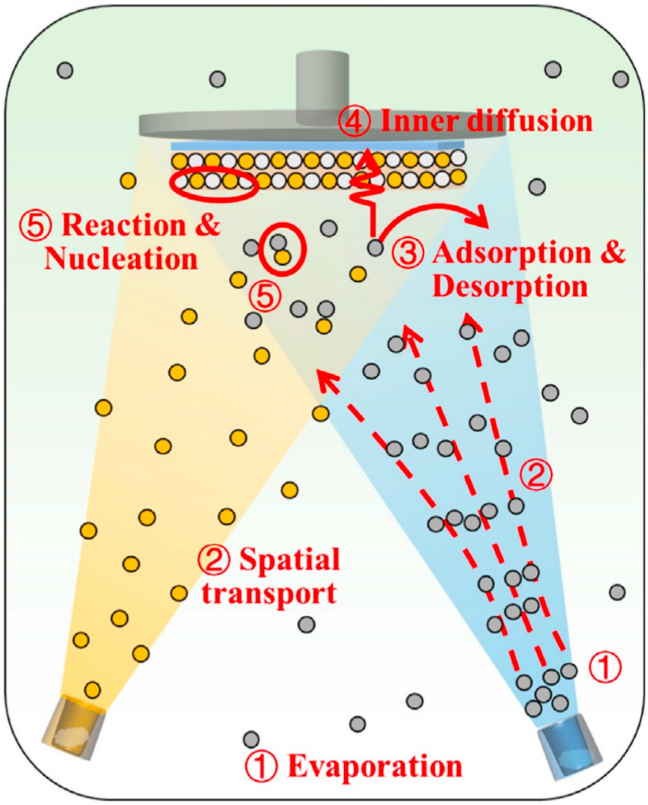


**Figure 2.14:** Fundamental processes in vapour deposition. Reproduced with permission from D. Lin et. al., *Materials Today Advances*, 16, 100277, 2022© 2022 Elsevier Ltd.[61]

and ⑤ molecular reaction and nucleation.[61]

Based on the types of precursor materials used in perovskites and the way they evaporate, they can be divided into two types of sources, the inorganic sources (i.e., $PbI_2$, CsI) which usually have directional evaporation behaviours, and the organic sources (i.e., MAI, FAI) which are volatile and dispersive. The non-directional evaporation of organic molecules which arises from their high vapour pressure is likely to disturb the evaporation of other sources and reduce the mean free path of the vapour.[62,63]

The ideal spatial transport process is free molecular flow, in which the average distance that the molecule travels before colliding with another molecule is larger

than the working distance of the evaporation system. The average distance that the molecule travels before colliding with another molecule is known as the mean free path ($\lambda$),[64] defined as

$$\lambda = \frac{k_B T}{\sqrt{2}\pi d^2 P} \tag{2.40}$$

where $d$ is the molecular diameter, and $P$ is the pressure. Given that the distance between source and substrate in the evaporation system is usually much shorter than $\lambda$ under high vacuum ($10^{-6}$ mbar), it is reasonable to assume that molecules in gas phase transport as the ideal free molecular flow.

After the molecules adsorb onto the surface of the substrate, they can diffuse on the surface until they encounter other molecules or reevaporate from the substrate. Generally, we assume that the diffusion rate is much slower than the rate of adsorption and desorption of atoms/molecules. Therefore, at the beginning of the evaporation, the initial adsorbed atom density on the surface is determined by the equilibrium of adsorption and desorption.

When the adsorbed atom density on the surface increases, each atom has a higher possibility to bond with each other. The movement of particles starts, driven by the gradient of particles, also known as diffusion. The diffusion process can occur in plane contributing to the growth of isolated clusters. It can also happen out of plane to diffuse into the underlying layer. The ability of an adsorbed atom to diffuse us defined as the diffusion length of adsorbed atoms, $\lambda_s = \sqrt{D_s \tau_v}$ ($D_s$ is the diffusion coefficient, $\tau_v$ is the residence time of an adsorbed atom before evaporating from the surface).

Depending on the difference in surface energy and lattice mismatch with the substrate, the nucleation reaction and film growth processes can follow one of the three modes: Frank-Van der Merwe (layer-by-layer growth), Stranski-Krastanov (layer plus island growth) and Volmer-Weber (island growth) modes.[65–68] In the Volmer-Weber mode, the atoms or molecules nucleate directly on the substrate surface and grow into islands. Subsequently, the islands coalesce and form a continuous film. In this case, the bonding between adsorbed atoms is stronger than the bonding between the atoms and the substrate. Held et al. confirmed the three-stage growth of co-evaporated $FAMAPbI_3$ following the Volmer-Weber mode by using in-situ photoluminescence and X-ray scattering.[69] They showed that at the beginning of the deposition, small islands nucleated and gradually increased in size. As the individual crystallines grew, they coalesced and formed continuous layers. Finally, the continuous perovskite layer grew vertically. However, the actual processes of nucleation and film growth can differ depending on the vapour deposition technique used. For instance, in sequential vapour deposition, the reactions between precursors and film growth tend to be limited by diffusion.[70–72] Therefore, it is important to keep in mind that small changes to a specific process condition can lead to substantial differences in the film formation, subsequently altering the optoelectronic properties and device performance.

# 3

# Experimental Methods

## Contents



This chapter presents the methods for fabrication and characterisation of both metal halide perovskite films and devices utilised for the following investigations discussed in this thesis.

# 3.1 Fabrication

## 3.1.1 Perovskite Thin-Film Fabrication

### 3.1.1.1 Spin-Coated Perovskite

In the experimental work described in this thesis, a one-step process with anti-solvent treatment was employed to fabricate spin-coated perovskite films.

For spin-coated perovskite films investigated in Chapter 4.4, $PbI_2$ (99.99% trace metals basis, Tokyo Chemical Inductry, TCI), $PbBr_2$, FAI, CsI (99.99% metal basis, Alfa Aesar) were weighed stoichiometrically in a $N_2$-filled glovebox to the target composition of $FA_{0.83}Cs_{0.17}Pb(I_{0.8}Br_{0.2})_3$. FAI purchased from Greatcell Solar (supplier A) with different batch numbers (batch 1: 485105; batch 2: 508004), was used as as-received FAI. Recrystallised FAI was obtained by the recrystallisation of as-received FAI. High-purity FAI was purchased from Dyenamo (supplier B), batch number N6Q1X. The precursor salts were dissolved in a mixture (4:1 ratio by volume) of dimethylformamide (DMF) and dimethylsulfoxide (DMSO) to obtain a perovskite concentration of 1.3 M. The precursor solution was stirred overnight in the glovebox at room temperature before use. During spin coating, perovskite precursor solution (175 µL) was dispensed dynamically onto a substrate spinning at 1000 rpm. The substrate was accelerated to 5000 rpm over 5 seconds and remained at this speed for 35 seconds. 5 seconds before the end of the process, anisole (335 µL) was applied to the spinning substrate as an anti-solvent quench. The films were then annealed at 100°C for 60 min in a $N_2$-filled glovebox. After cooling down to room temperature, the films were ready to use.

For the recrystallised FAI precursor investigated in Chapter 4.4, Greatcell FAI powder was dissolved in ethanol heated at 75°C to obtain a supersaturated solution. Once fully dissolved, the solution was cooled down naturally for around one hour, then placed in a refrigerator at 5°C for overnight recrystallization. The obtained large white flakes were washed with diethyl ether three times and dried in the vacuum oven at 40°C for two days. After cooling down to room temperature, the recrystallized FAI was stored in the glovebox.

#### 3.1.1.2 Vapour-Deposited Perovskite

In the experimental work described in this thesis, two types of vapor deposition methods were used to fabricate metal halide perovskite films, including sequential deposition and co-evaporation. The co-evaporation method is the predominant technique used to fabricate thin films of $FAPbI_3$ in Chapter 4.4 and $FA_{0.9}Cs_{0.1}PbI_{3-x}Cl_x$ in Chapter 5.4 and Chapter 6.4 as absorber layers in planar heterojunction photovoltaic devices. The sequential deposition method is reported to fabricate the templating layer to modulate the growth of co-evaporated perovskite films in Chapter 5.4.

The thermal evaporation chamber used for the investigations in this thesis contains five thermal sources for low-temperature thermal evaporation. For each source, a tungsten filament wraps cylindrically around the aluminum oxide ($Al_2O_3$) crucible. The metal cylinder caps the crucible and filament to keep the crucible temperature during the heating process. Generally, the precursors are sublimated under high vacuum ($10^{-6}$ to $10^{-5}$ mbar) to deposit the film on the targeted substrate. To obtain the vapour-deposited film with uniform composition, each source

has independent quartz crystal microbalances (QCMs) to monitor the deposition rate of precursors. When an AC voltage is applied, the QCM oscillates at its resonant frequency due to the piezoelectric effect of quartz, which depends on the mass and mechanical properties of the crystal. The accumulation of precursor material on the surface can increase the total mass of the crystal, leading to a decrease in the resonance frequency. Therefore, measuring the change of oscillation frequency allows for finely determining the amount of materials deposited on the QCM. To more accurately reflect the deposition rate on the substrate, two QCMs (one without a shutter and one with a shutter) are located close to the position of the substrate. The QCM with shutter allows for deposition on the substrate only after reaching the stabilised deposition rate. The one with the shutter is reported to investigate the templating layer in Chapter 5.4, since it can more accurately reflect the initial growth dynamics of the perovskite layer by simultaneously opening the QCM shutter and the substrate shutter. For every deposition, the temperature of the inner chamber wall was kept constant at 17 °C, while the temperature of the substrate was held constant at 20 °C. Figure 3.1 shows a schematic diagram of the thermal evaporation chamber.

For the $FAPbI_3$ layers in Chapter 4.4, $PbI_2$ (ultra-dry 99.999% metal basis, Alfa Aesar) and FAI were co-evaporated in two separate crucibles. For FAI (>99.99%, Greatcell Solar), the pressure can go up to 1-2 $\times$ $10^{-5}$ mbar during the subsequent co-evaporation process. For FAI (99.999% trace elements basis, DN-P10-5N, Dyenamo AB), the pressure can go up to 5-6 $\times$ $10^{-5}$ mbar during the subsequent co-evaporation process. The actual deposition rate of $PbI_2$ was kept constant at 0.20 Å/s using the QCM close to the $PbI_2$ source, which is named as "$PbI_2$ source rate". The actual deposition rate of FAI was kept constant at 0.19 Å/s by

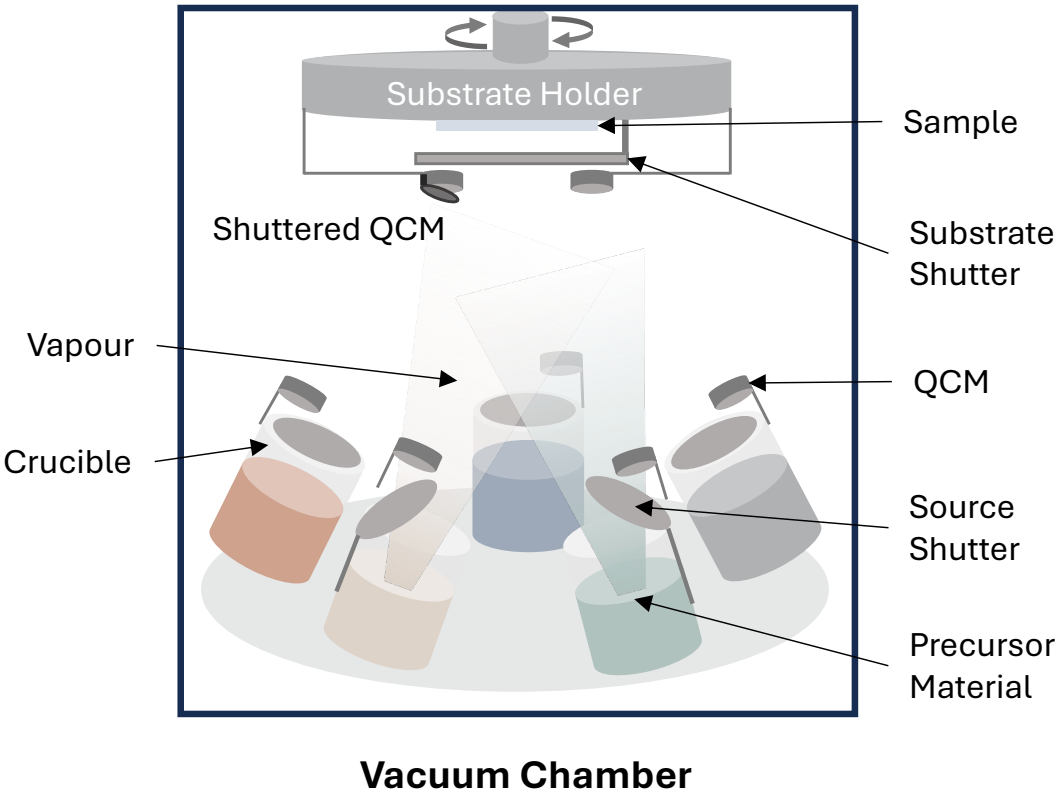


**Figure 3.1:** A schematic diagram of the thermal evaporation chamber used to fabricate the vapour-deposited perovskite films in this thesis. The rate is individually controlled by the gold-plated quartz crystal microbalance (QCM) close to the source or substrate position. The precursor materials are heated by the resistive heater.

controlling the overall reading of the QCM close to the substrate position, which is named as "substrate rate". The typical thickness of $FAPbI_3$ used in this study is 550 nm. After deposition, the samples were annealed at 150 °C for 5 min and 135 °C for 25 min in a $N_2$-filled glovebox.

For the templating layer in Chapter 5.4, the ultrathin perovskite films were deposited by the two-step thermal evaporation technique. In the first step, $PbI_2$ (ultra-dry 99.999% metal basis, Alfa Aesar), CsI (99.99% metal basis, Alfa Aesar), and $PbCl_2$ (99.998% metal basis, Alfa Aesar) were co-evaporated to deposit 9 nm films with the molar ratio of CsI: $PbI_2$: $PbCl_2$ = 0.1: 0.8: 0.39. In the second step, 9nm FAI (99.999% trace elements basis, DN-P10-5N, Dyenamo AB) was evaporated

on top of the inorganic films. The deposition rates of inorganic precursors were controlled by their source rates. The deposition rate of FAI was controlled by the substrate rate. The typical thickness of the templating layer is 15 nm. After deposition, the samples were annealed at 135 °C for 2 min in a $N_2$-filled glovebox.

For the absorption layer in Chapter 5.4 and Chapter 6.4, the perovskite films with the composition of $FA_{0.9}Cs_{0.1}PbI_{3-x}Cl_x$ were fabricated using the four-source, co-evaporation of FAI (99.999% trace elements basis, DN-P10-5N, Dyenamo AB), CsI (99.99% metal basis, Alfa Aesar), $PbI_2$ (ultra-dry 99.999% metal basis, Alfa Aesar) and $PbCl_2$ (99.998% metal basis, Alfa Aesar) under high vacuum. The deposition rates of inorganic precursors were controlled by their source rates. The deposition rate of FAI was controlled by the overall substrate rate. The typical thickness of $FA_{0.9}Cs_{0.1}PbI_{3-x}Cl_x$ used in this study is 630 nm. After deposition, the samples were annealed at 150 °C for 5 min and 135 °C for 25 min in a $N_2$-filled glovebox.

## 3.1.2 Device Fabrication

Unless stated otherwise, all other materials and solvents were purchased from Sigma-Aldrich and used without further purification.

### 3.1.2.1 Substrate Cleaning

Indium-doped tin oxide (ITO) coated glass (Biotain, 30 mm × 30 mm × 1.1 mm, 10-15 Ω/sq) was used as the substrate. The substrates were cleaned in a series of ultrasonic baths using industrial detergent Decon90 (1% vol in deionized

water), deionized water, acetone, and isopropyl alcohol (each step for 5 min). After ultrasonic cleaning, the substrates were dried with nitrogen gas, and were then placed in the UV ozone for 15 min.

#### 3.1.2.2 Deposition of Charge Transport Layers

**Hole Transport Layers**

Poly[bis(4-phenyl)(2,4,6-trimethylphenyl)amine (PTAA, purchased from Xi' an Polymer Light Technology) was dissolved in toluene with a concentration of 2 mg/mL. 100 µL solution was dynamically deposited onto a substrate at a speed of 6000 rpm for 30 s. After spin-coating, the substrate was annealed at 100 °C for 10 min. After cooling down to room temperature, the substrate was ready to use.

[4-(3,6-Dimethyl-9H-carbazol-9-yl)butyl]phosphonic acid (Me-4PACz, >99.0%, TCI) was dissolved in ethanol with a concentration of 0.33 mg/mL. 350 µL solution was statically deposited onto a substrate After 10 s to help the solution spread, the substrate was spinning at 3000 rpm for 30 s. After spin-coating, the substrate was annealed at 100 °C for 10 min. After cooling down to room temperature, $Al_2O_3$ nanoparticles (1:150 vol% in 2-propanol) were spin-coated dynamically on top at 2000 rpm for 20 s as a wetting agent. The film was annealed at 100 °C for 1 min. After cooling down to room temperature, the substrate was ready to use.

2,2′,7,7′- Tetrakis(N,N -di-p-methylphenylamino)-9,9′-spirobifluorene (spiroTTB) was vacuum-deposited in the thermal evaporator chamber to 5 nm at 0.1 Å/s. The rate was controlled using a gold-plated QCM. The as-prepared substrate was ready to use.

2,2′,7,7′-Tetrakis[N,N-di(4-methoxyphenyl)amino]-9,9′-spirobifluorene (spiro-OMeTAD, Lumtec) was dissolved in chlorobenzene at a concentration of 85 mg/mL, with added lithium bis(trifluoromethanesulfonyl)imide (Li-TFSI) dissolved in 1-butanol at a concentration of 520 mg/mL, and tert-butylpiridine (tBP). For 1 mL of the spiro-OMeTAD solution, 20 µL of the Li-TFSI solution and 33 µL of tBP were added. 100 µL of the solution was statically spin-coated at 2000 rpm for 45 s. Before depositing the final electrode, the films were kept in a desiccator for 12-18 hours to allow for the oxidation of the spiro-OMeTAD.

**Electron Transport Layers**

Fullerene (C60, 99.9%, Acros Organics) was vacuum-deposited in the thermal evaporator chamber to 25 nm at 0.1 Å/s. BCP was vacuum deposited in the thermal evaporator chamber to 5 nm at 0.1 Å/s. The as-prepared substrate was ready to use.

200 L $SnO_2$ colloidal solution (diluted to 2.5 weight%) was deposited by static spin-coating at 3000 rpm for 30 s (1000 rpm ramp), followed by annealing at 150 °C for 30 min in ambient air.

#### 3.1.2.3 Deposition of Metal Contacts

100 nm silver (Ag) or 80 nm gold (Au) contacts were thermally evaporated with shadow masks under high vacuum ($< 3 \times 10^{-6}$ torr) using a thermal evaporator (Nano 36, Kurt J. Lesker) placed in ambient environment.

## 3.2 Thin-Film Characterisation

### 3.2.1 Absorption Spectroscopy

Photogeneration is by far the most important generation process in photovoltaic devices, by which the generation of mobile electrons and holes through the absorption of light in the semiconductor. Since photogeneration is the promotion of an electron from a valence band (VB) to a conduction band (CB) energy level, the energy dependence of absorption coefficient ($\alpha$) must be strongly related to the density of VB and CB states, and hence to the band structure of the materials. For a typical direct bandgap ($E_{\mathrm{g}}$) semiconductor, when exposed to photons of energy greater than $E_{\mathrm{g}}$, it strongly absorbs these photons while exciting electrons from the valence band to the conduction band. For a material with uniform $\alpha$, the attenuation of the light intensity $I$(x) reduces to the simple Beer-Lambert law, where $I(0)$ is the incident intensity of radiation, and $x$ is the thickness of a film

$$I(x) = I(0)10^{-\alpha x} \tag{3.1}$$

Since absorptance $A_{\mathrm{p}}$ can be calculated using the formula

$$A_p = 1 - R - T \tag{3.2}$$

where $R$ and $T$ are the reflection and transmission, respectively, the absorbance or optical density, $A$ of the film can be written as

$$A = -log_{10}(\frac{I}{I_0}) = -log_{10}(\frac{T}{1-R}) \tag{3.3}$$

The absorption spectra were measured using a Bruker Vertex 80v Fourier transform infrared (FTIR) spectrometer with a reflection-transmission setup. Visible

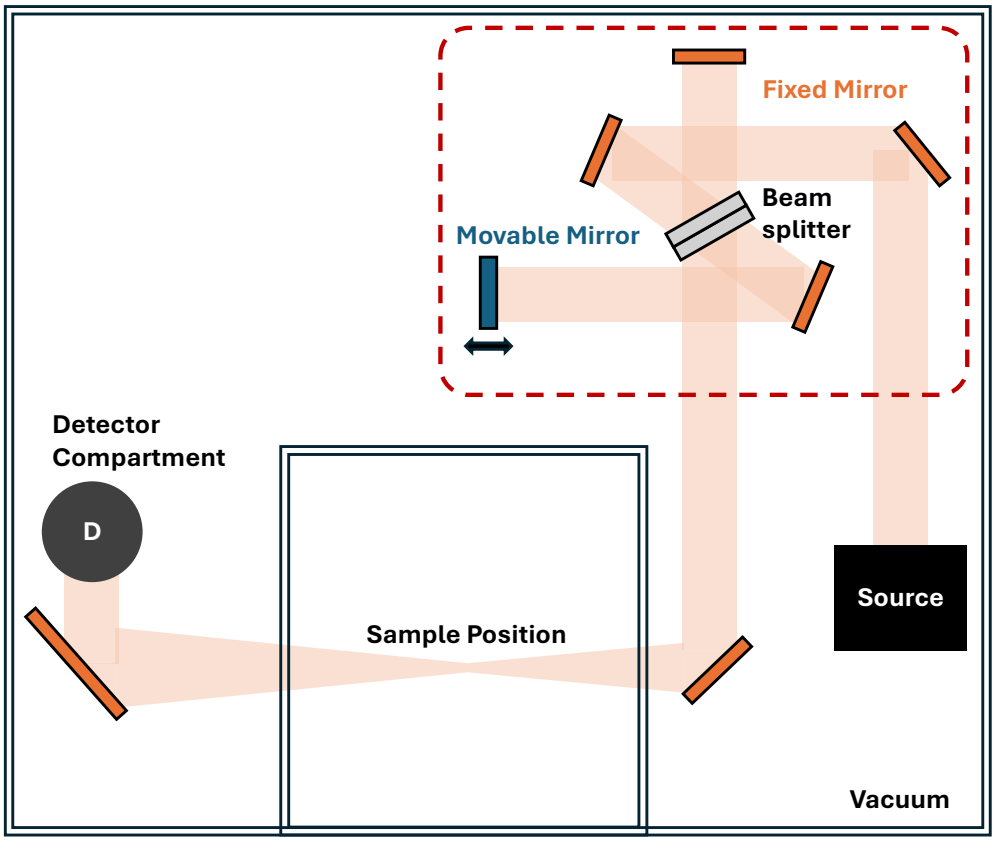


**Figure 3.2:** The Fourier transform infrared spectroscopy setup used in this thesis. The part highlighted by the red box shows the mirror arrangement in a Michelson interferometer.

measurements were taken using a tungsten halogen lamp source and a silicon diode detector. Figure 3.2 shows the FTIR setup used in this thesis. The essential part of optical hardware in an FTIR spectrometer is the interferometer, which consists of a fixed mirror, a movable mirror, and a beamsplitter. The quantity measured by the detector is the intensity of the combined beams as a function of the movable mirror displacement, the so-called interferogram. After Fourier transformation, the interferogram can be converted into a spectrum as a function of wavenumber.

### Bandgap Extraction Method

In Chapter 5.4, bandgaps extracted from Elliott model fitting were performed

by Jae Eun Lee. Compared with the widely used Tauc method, Elliott model is a more reliable metric to estimate the bandgap values by considering the presence of excitonic effects.

The absorption coefficient spectra were fitted by the Elliott model to obtain the optical bandgap ($E_{\mathrm{g}}$), exciton binding energy ($E_{\mathrm{b}}$) and electronic sub-bandgap disorder ($\gamma$). The Elliott model represents the total absorption coefficient ($\alpha(E)$) as a linear combination of the absorption coefficient from bound excitons ($\alpha_{\mathrm{EX}}(E)$) and electron-hole continuum states ($\alpha_{\mathrm{C}}(E)$) for a direct semiconductor as shown below[73,74]

$$\alpha(E) = \alpha_{EX}(E) + \alpha_{C}(E) \tag{3.4}$$

The contribution from $\alpha_{\mathrm{EX}}(E)$ is expressed as

$$\alpha_{EX}(E) = \frac{b_0}{E} \sum_{n=1}^{\infty} \frac{4\pi E_b^{3/2}}{n^3} \delta(E - [E_g - \frac{E_b}{n^2}]) \tag{3.5}$$

where $b_0$ is a constant of proportionality that includes the electric dipole transition matrix element between the valence and conduction band, $|\langle \Psi_c \mid P \mid \Psi_v \rangle|^2$ and $n$ is a positive integer quantum number. Equation 3.5 describes lines series at energies -$E_{\mathrm{b}}/n^2$ below $E_{\mathrm{g}}$ and their magnitudes are proportional to -$1/n^3$. The contribution from $\alpha_{\mathrm{C}}(E)$ is expressed as

$$\alpha_C(E) = \frac{b_0}{E} \left[ \frac{2\pi \sqrt{\frac{E_b}{E-E_g}}}{1 - \exp\left(-2\pi \sqrt{\frac{E_b}{E-E_g}}\right)} \right] c_0^{-1} \, JDoS(E) \tag{3.6}$$

where the joint density of states $JDoS$ is given by

$$JDoS(E) = \begin{cases} c_0 \sqrt{E - E_g}, & \text{for } E > E_g \\ 0, & \text{otherwise} \end{cases} \tag{3.7}$$

and the joint density of states constant $c_0$ is given by

$$c_0 = \frac{1}{(2\pi)^2} \left( \frac{2\mu}{\hbar^2} \right)^{3/2} \times 2 \tag{3.8}$$

where $\mu$ is the reduced effective mass of the electron-hole system, which is assumed to be $0.15m_e$.[75] The term in the square brackets in Equation 3.6 in the Coulombic enhancement factor, which represents the probability of an electron and a hole existing in the same space. The second term $c_0^{-1}\,JDoS(E)$ represents the absorption coefficient of free electrons and holes in the absence of Coulombic attraction, $\alpha_{\mathrm{Free}}(E)$.

The linear combination of the contributions from the excitonic and continuum states as shown in Equation 3.4 is then convolved with a broadening function, which is written as

$$g(E) = \frac{1}{\cosh\left(\frac{E-E_x}{\gamma_{Abs}}\right)} \tag{3.9}$$

where $\gamma_{\mathrm{Abs}}$ is the absorption edge broadening parameter.[76]

**Attenuated Total Reflectance-Fourier Transform Infrared Spectroscopy Measurements**

The Attenuated Total Reflectance-Fourier Transform Infrared Spectroscopy (ATR-FTIR) is a technique utilized to identify chemical structures. An infrared (IR) light beam passes through the ATR crystal. Due to the high refractive index of the ATR crystal (typical materials include diamond, germanium and zinc selenide), the IR light reflects once/multiple times at the interface in contact with the sample. Given the wave-like property of the light, the reflection forms the evanescent wave slightly penetrating into the sample. The internal reflected IR light carries the absorption information of the sample and is collected by the detector.[77–79]

In Chapter 6.4, the ATR-FTIR measurements for the powder and evaporated

films were conducted using a single reflection diamond ATR accessory (Bruker Platinum ATR Spectrometer) mounted on a Bruker Vertex 80v Fourier Transform Interferometer. The measurement was performed at room temperature under vacuum in the range between 400-4500 $cm^{-1}$. Pressure was applied for both powder and thin-film samples to ensure contact between the sample and the ATR crystal.

### 3.2.2 Photoluminescence Spectroscopy

#### Steady-State Photoluminescence

Photoluminescence (PL) is based on measuring the emission of photons from a semiconductor that have been created by radiative recombination. Radiative recombination requires one electron and one hole to participate in the recombination process. Due to the microscopic reversibility, radiative recombination is the inverse process of absorption. Therefore, the emission spectrum is strongly influenced by the shape of the absorption near the band edge and is more related to the intrinsic properties of materials.

In this thesis, the PL measurements were taken by illuminating the samples using a 398 nm diode laser (PicoHarp, LDH-D-C-405M) (Chapter 4.4), a 470 nm diode laser (PicoQuant, LDH-D-C-470M) (Chapter 5.4), a 398 nm diode laser (PicoHarp, LDH-D-C-405M) or a 670 nm diode laser (PicoQuant, LDH-D-C-670M) (Chapter 6.4) on a continuous wave. The PL emitted by the samples was coupled into a grating spectrometer (Princeton Instruments, SP-2558) and then directed onto a silicon iCCD (PI-MAX4, Princeton Instruments). The samples were measured under $N_2$ (Chapters 4.4 and 6.4), vacuum (Chapters 5.4 and 6.4), or air

(Chapter 6.4) atmosphere.

### Time-Resolved Photoluminescence

In this thesis, the time-resolved PL measurements were taken by using time-correlated single photon counting (TCSPC), which measures the exact arrival time of single photons after an excitation pulse. A 398 nm picosecond pulsed diode laser (PicoHarp, LDH-D-C-405M) operated at 2.5 MHz (Chapter 4.4), a 470 nm picosecond pulsed diode laser (PicoHarp, LDH-D-C-470M) operated at 1MHz (Chapter 5.4), a 398 nm picosecond pulsed diode laser (PicoHarp, LDH-D-C-405M) or a 640 nm picosecond pulsed diode laser (PicoQuant, LDH-D-C-670M) operated at 2.5 MHz (Chapter 6.4) was used to measure the samples in $N_2$ (Chapters 4.4 and 6.4), vacuum (Chapters 5.4 and 6.4), or air (Chapter 6.4) atmosphere. The PL emitted by the samples was collected by a photon-counting detector (PDM series from MPD) and the timing was controlled using a PicoHarp300 event timer.

### Trap-Assisted Recombination Fitting

The PL decays were fitted using a stretched exponential that can be expressed in the form of,[80]

$$I(t) = I_0 e^{-\left(\frac{t}{\tau_c}\right)^{\beta}} \tag{3.10}$$

where $I(t)$ is the time dependent PL intensity, $I_0$ is the initial PL intensity, $t$ is the time, $\tau_c$ is the characteristic lifetime, and $\beta$ is the distribution parameter. Based on the characteristic lifetime and distribution parameter, the average lifetime $\tau_{avg}$ can be calculated as

$$\tau_{avg} = \frac{\tau_c}{\beta}\Gamma\left(\frac{1}{\beta}\right) \tag{3.11}$$

$$\Gamma\left(\frac{1}{\beta}\right) = \int_0^\infty x^{\frac{1-\beta}{\beta}} e^{-x}\, dx \tag{3.12}$$

For the monomolecular charge-carrier recombination, which likely originates from trap-assisted recombination, the recombination rate $k_1$ can be calculated by the following equation,[81]

$$k_1 = \frac{1}{2\tau_{\text{avg}}} \tag{3.13}$$

### 3.2.3 X-Ray Diffraction

X-ray diffraction (XRD) is a routine technique to assess the crystalline structure of solids. The principle of XRD is the result of elastic scattering from atoms in the materials. The incident X-ray beam diffracts in precise directions at a scattering angle ($\theta$) undergoing constructive interference. Figure 3.3a shows the well-known Bragg's law: $n\lambda = 2d\sin\theta$.[82] Here $n$ is the order of the diffraction and the direction of the orientated scattering planes. In reciprocal space, an incident beam with momentum $\vec{k}_i$, is scattered from the crystal with momentum $\vec{k}_f$. The corresponding scattering vector $\vec{q}$ orthogonal to the lattice plane (Figure 3.3b) can be given by

$$\vec{q} = \vec{k}_f - \vec{k}_i \tag{3.14}$$

where $q = \left(\frac{4\pi}{\lambda}\right)\sin\theta$. Since the Bragg condition is satisfied when the diffracted waves from adjacent lattice planes interfere constructively, the Equation 3.14 can be simplified to

$$q = q_B = \frac{2\pi}{d_{hkl}} \tag{3.15}$$

In this thesis, XRD measurements were conducted using a Panalytical X-pert powder diffractometer. The Cu-K$\alpha$ X-ray source ($\lambda$=1.54 ) was set to 40 kV voltage

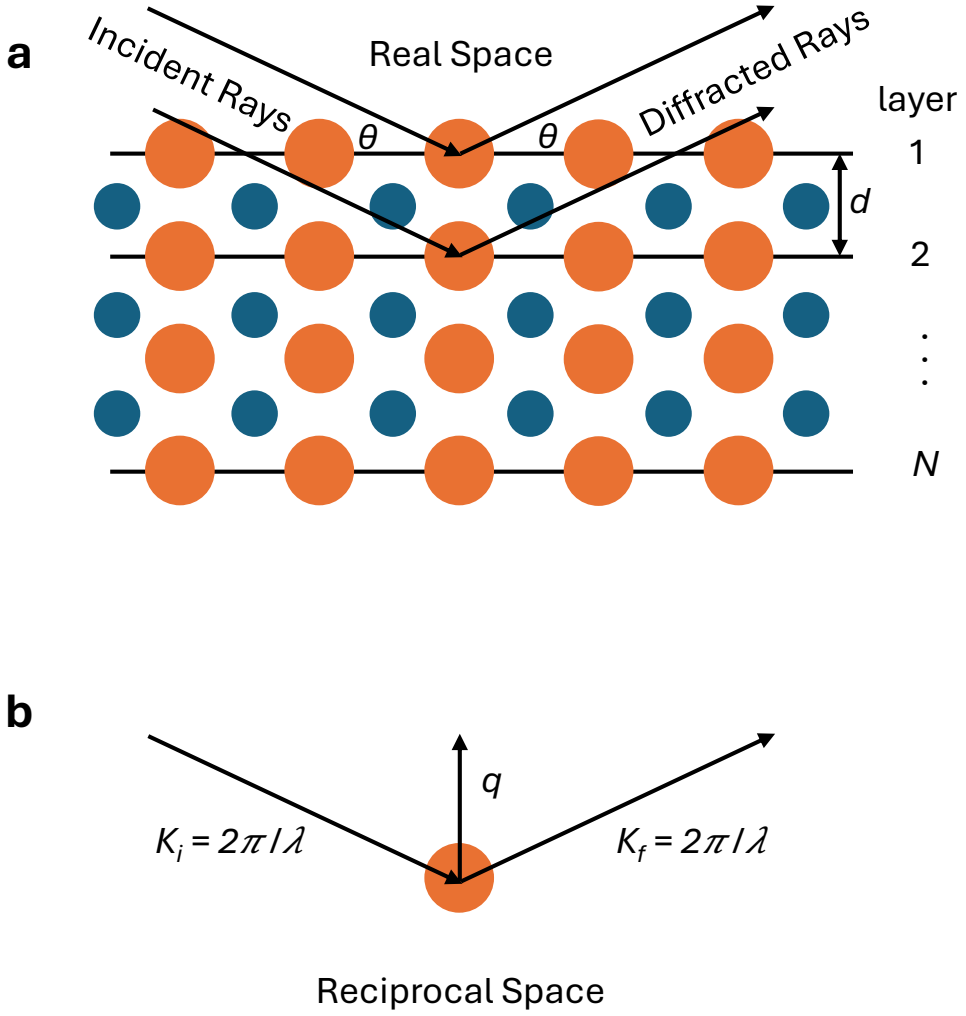


**Figure 3.3:** (a) Illustration of Bragg diffraction from X-rays scattering off atoms (orange circles) positioned along a lattice plane (black line) separated by distance $d$. B) Scattering wavevector $q$ resulting from the wavevector change of the incident and diffracted waves.

and 40 mA current. The XRD patterns were corrected by shifting the $2\theta$-axis based on the ITO substrate reference peak at $2\theta$=30.3° or z-cut quartz substrate reference peak at $2\theta$=16.4°.[74,83] HighScore Plus software was used to implement the refinement to extract lattice parameters.

### 3.2.4 Grazing-Incident Wide-Angle X-Ray Scattering

Grazing-incident wide-angle X-ray scattering (GIWAXS) is a valuable technique to probe and understand the structure-property relationships that fundamentally limit the optoelectronic performance for a wide variety of compositions and structural motifs (i.e., from single-crystal, polycrystalline systems, quantum dots to layered superlattices). Different from XRD using Bragg-Brentano reflection geometry, GIWAXS collects the X-ray scattering from the sample using a grazing incidence geometry. Therefore, instead of penetrating deep into the bulk of the material, GIWAXS has a higher surface sensitivity and provides both in-plane and out-of-plane structural information.[84]

Since metal halide perovskites commonly contain relatively heavy Pb atoms, metallic lead is known as an effective X-ray shielding/stopping material and exhibits strong X-ray fluorescence when excited far above the absorption edge of it. During the GIWAXS measurements, the emitted X-ray resulting from the X-ray photo-electric absorption will elevate the background intensity and can be troublesome. For these reasons, GIWAXS experiments conducted on Pb-based perovskites are typically performed just below the L absorption edges (Figure 3.4), at X-ray beam energies between 10-12.9 keV.

The GIWAXS measurements in Chapter 5.4 were performed by Karim A. Elmestekawy. In this thesis, the GIWAXS measurements were taken by using a Rigaku Smart-lab X-ray diffractometer using the Cu-K$\alpha$ X-ray source ($\lambda$=1.54 , corresponding photon energy of 8.04 keV) with the voltage and current set to 40 kV and 40 mA, respectively, and a HyPix-3000 2D X-ray detector. All the GIWAXS detector

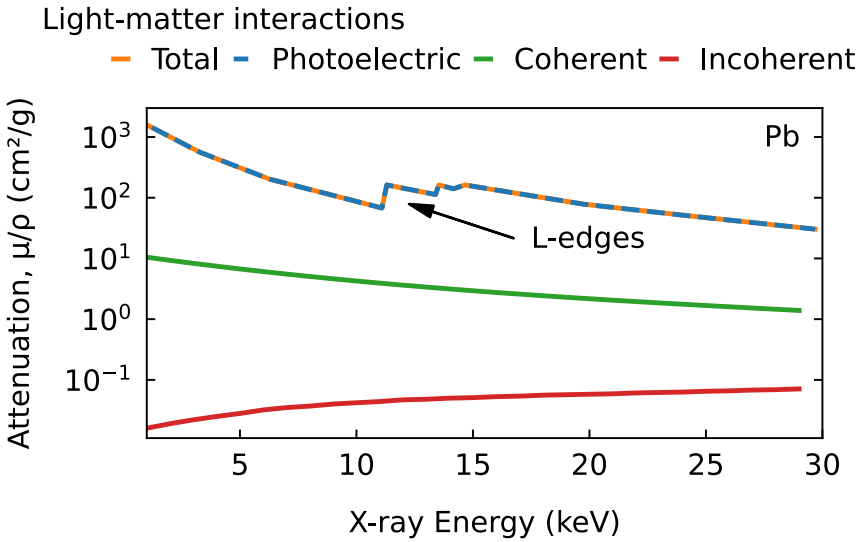


**Figure 3.4:** Energy-dependent X-ray attenuation mechanisms in lead (Pb), highlighting L-edge absorption and contributions from photoelectric (blue line), coherent (green line), and incoherent (red line) scattering. Coherent scattering, also known as Rayleigh scattering, is an elastic process where X-rays scatter without energy loss. Incoherent scattering, also called Compton scattering, is an inelastic process where X-rays lose energy during interaction with loosely bound or free electrons. Data extracted from J. A. Steele et al., *Advanced Energy Materials*, 13(27), 2300760 (2023)© 2023 Wiley-VCH GmbH[84]

images were reshaped and converted to wavevector space based on the relationship between the scattering vector and the diffraction signal from the detector.

### Ewald Sphere and Missing Wedge

Since there should be no energy loss during the elastic scattering, when the crystal planes satisfy the Bragg condition for diffraction at a given incident X-ray wavelength, the magnitude of incident and diffracted wavevectors should remain the same. If a sphere with the radius of $2\pi/\lambda$ is centered at the tip of incident beam $\vec{k_i}$, all reciprocal lattice points that satisfy the condition for constructive interference should lie on the surface of this sphere, which is also called Ewald sphere. When the Ewald sphere intersects with the reciprocal lattice, it produces a curved surface that is projected onto the flat 2D detector. Given that the scattered photons are

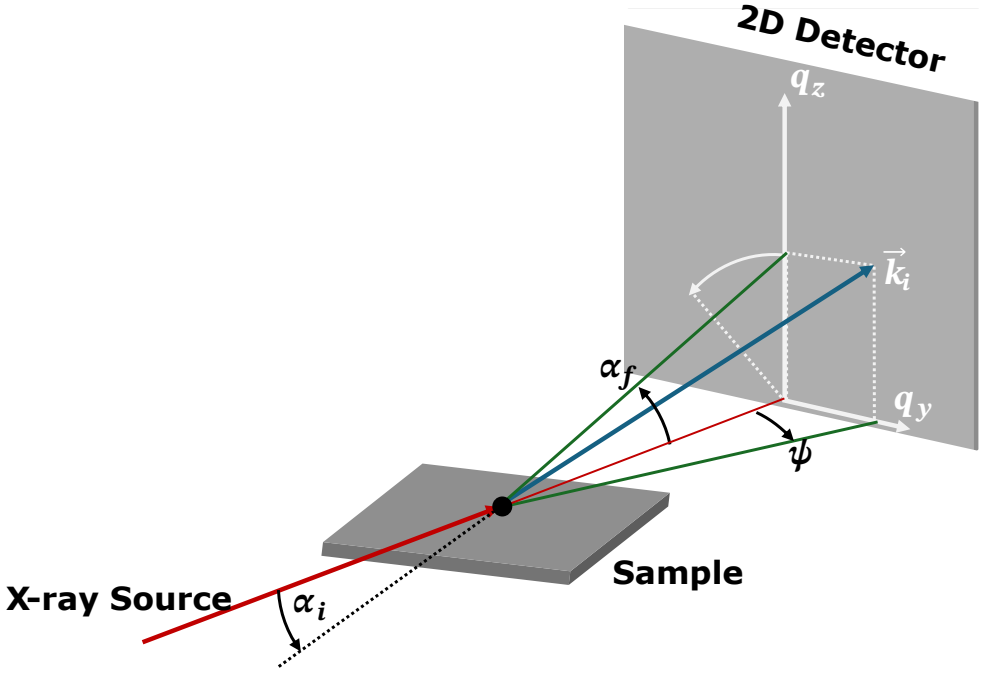


**Figure 3.5:** Grazing-incident wide-angle X-ray scattering geometry.

recorded using a pixelated area detector to directly convert X-ray photons into electric signals and map the 2D image, image correction is necessary to reconstruct the 2D reciprocal space by factoring in the curvature of the Ewald sphere.

The coordinate system used in GIWAXS is placed at the point of diffraction on the top of the sample surface, with $x$- and $y$-axes parallel to the sample surface and $z$-axis in the normal direction (Figure 3.5). The scattering wavevector $\vec{q}$ can be given by

$$\vec{q} = \begin{pmatrix} q_x \\ q_y \\ q_z \end{pmatrix} = \begin{pmatrix} \cos\alpha_f \cos\psi - \cos\alpha_i \\ \cos\alpha_f \sin\psi \\ \sin\alpha_i + \sin\alpha_f \end{pmatrix} \tag{3.16}$$

where $\alpha_i$, $\alpha_f$ and $\psi$ are incident angle, in-plane exit angle, and out-of-plane angle, respectively. The in-plane scattering wavevector in the GIWAXS geometry can be described by

$$q_r = \sqrt{q_x^2 + q_y^2} \neq 0 \tag{3.17}$$

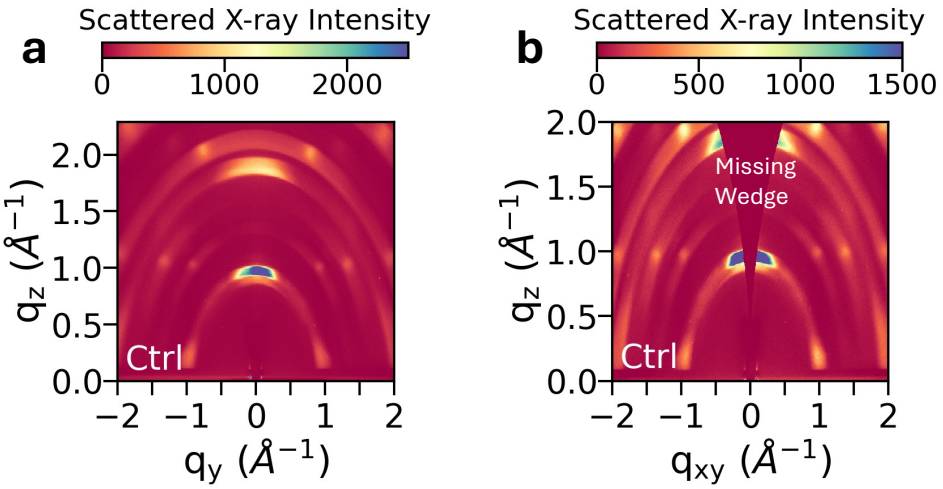


**Figure 3.6:** GIWAXS images of the co-evaporated $FA_{0.9}Cs_{0.1}PbI_{3-x}Cl_x$ perovskite film. (a)GIWAXS image without correction. (b) GIWAXS image after transformation with respect to $q_r$ and $q_z$.

Here $q_r \neq 0$ means that there is always a contribution in $\vec{q}_x$ along the incident beam direction. This leads to the blindspot in the reciprocal space and the formation of the missing wedge-shaped area in the final corrected GIWAXS image.[85,86] Figure 3.6 shows the GIWAXS image before and after the image correction.

### Radial Integration of 1D Scattering Profiles

Given that GIWAXS can provide both in-plane and out-of-plane structural orientation information, the integrated 1D scattering profile generated by the whole azimuthal range can provide more complete structural information for the oriented polycrystalline films than the XRD measurements using a Bragg-Brentano geometry. Meanwhile, changing the angle of the grazing incidence beam $\alpha_i$ can tune the penetration depth of the X-ray beam.[87] It is important to mention that the penetration depth does not correspond to the scattering information depth, considering the attenuation of scattered X-rays in order to transverse and exit back through the film surface.[88] However, when GIWAXS measurements are conducted

below or just above the critical angle, the scattering signals range from the top-surface to the subsurface and bulk of the film, allowing for extracting information as a function of the depth by varying $\alpha_i$. In Chapter 6.4, the depth-dependent GIWAXS measurements were conducted to investigate the passivation effect of spin-coated FPEAI and evaporated FPEAI on co-evaporated $FA_{0.9}Cs_{0.1}PbI_{3-x}Cl_x$ perovskite film.

### 3.2.5 Terahertz Time-Domain Spectroscopy

Terahertz time-domain spectroscopy measurements and data fitting of the perovskite films were performed by Jae Eun Lee. In Chapter 5.4, the optical-pump teraherz-probe (OPTP) technique was used to investigate the photophysical characteristics of directly co-evaporated and templated perovskite films. An amplified laser system (Spectra Physics, Mai Tai-Ascend-Spitfire Pro Ti/sapphire regenerative amplifier) with a central wavelength 800 nm, 35 fs pulse duration and 5 kHz repetition rate was split into THz beam, pump beam and gate beam. The THz radiation was generated by a spintronic emitter based on the inverse spin hall effect. The electro-optic sampling with a 1 mm-thick ZnTe (110) crystal, a Wollaston prism and a pair of balanced photodiodes were used to detect the pulse. The THz pulse was measured in transmission geometry. The pump beam was generated at 400 nm by a $\beta$-barium-borate (BBO) crystal. The samples were photoexcited as various fluences ranging from 2.38 to 38.75 $J/cm^2$ under vacuum ($<10^{-2}$ mbar).

#### Mobility Fitting

The effective charge-carrier mobility was extracted from the OPTP data using

the method illustrated previously by Wehrenfennig et al.[89] The sheet photoconductivity ΔS of a thin film between two media of refractive indices $n_{\mathrm{A}}$ and $n_{\mathrm{B}}$ with its thickness much smaller than the THz wavelength can be expressed as

$$\Delta S = -\varepsilon_0 c(n_A + n_B)\left(\frac{\Delta T}{T}\right) \tag{3.18}$$

where $\varepsilon_0$ is the vacuum permittivity, $c$ is the speed of light and $\Delta T/T$ is the ratio of photo-induced change in the THz electric field to the transmitted THz electric field in the dark. In this study, $n_{\mathrm{A}}$ is the refractive index of a z-cut quartz, which is 2.13 and $n_{\mathrm{B}}$ is the refractive index of vacuum which is 1.

Deriving the charge-carrier mobility $\mu$ from ΔS requires the knowledge of the number of photo-excited charge-carriers N, which can be calculated as

$$N = \varphi\frac{E\lambda}{hc}\left(1 - R_{\mathrm{pump}} - T_{\mathrm{pump}}\right) \tag{3.19}$$

where $\varphi$ is the photon-to-charge branching ratio, E is the energy obtained in an optical excitation pulse with wavelength $\lambda$, $h$ is the Planck' s constant, $R_{\mathrm{pump}}$ and $T_{\mathrm{pump}}$ are the reflected and transmitted fractions of the pump beam. Then, $\mu$ can be calculated with

$$\mu = \frac{\Delta S A_{\mathrm{eff}}}{Ne} \tag{3.20}$$

where $A_{\mathrm{eff}}$ is the effective area of the overlap of optical pump and THz probe pulse considering the Gaussian beam profiles and e is the elementary charge. By using the above equations, the effective mobility $\tilde{\mu} = \varphi\mu$ is expressed as

$$\varphi\mu = -\varepsilon_0 c(n_A + n_B)\left(\frac{A_{\mathrm{eff}}\, hc}{E\lambda e(1 - R_{\mathrm{pump}} - T_{\mathrm{pump}})}\right)\left(\frac{\Delta T}{T}\right) \tag{3.21}$$

Here, $\varphi$ is set to 1 given that the exciton binding energies are low and free charge-carriers are mostly generated right after excitation.[90] The charge-carrier mobility

obtained here is the sum of electron and hole mobilities and they cannot be separated.

To obtain $\varphi\mu$, $\Delta T/T$ at time zero against E was plotted and a linear function was fitted based on Equation 3.21 up to the point where nonlinear processes were not observed. Then, $\varphi\mu$ was obtained from the gradient.

**THz Photoconductivity Transients Fitting**

The recombination dynamics in a perovskite semiconductor may be governed by first, second and third order processes as shown in the following rate equation

$$\frac{dn(t)}{dt} = -k_1 n(t) - k_2 n(t)^2 - k_3 n(t)^3 \tag{3.22}$$

where $k_1$ is the first order non-radiative trap-assisted recombination, $k_2$ is the second order radiative recombination rate constant and $k_3$ is the third order Auger recombination rate constant. $k_1$ is taken from the TCSPC measurements. $k_3$ is set as $10^{-29}$ $cm^6 s^{-1}$ as obtained from literature because the effect of $k_3$ becomes significant only when $n > 10^{18}$ $cm^{-3}$.[91]

Equation 3.22 is first solved in terms of the experimentally observed quantity $x(t) = \Delta T/T$, which is the photoinduced change in THz transmission. $n(t)$ is proportional to $x(t)$ with the following relationship

$$n(t)^i = \varphi^{i-1} C^{i-1} x(t)^i \tag{3.23}$$

where $i$ is the recombination order, $\varphi$ is the photon-to-charge branching ratio, $C = \tilde{n}_0/x(0)$ is the proportionality factor between the absorbed photon density $x(0)$ and the initial photon density $\tilde{n}_0$ as shown below

$$\tilde{n}_0 = \frac{N}{A_{\text{eff}} d} \tag{3.24}$$

where $d$ is the thickness of each sample. By substituting Equation 3.23 into Equation 3.22, Equation 3.22 is rewritten as

$$\frac{dx(t)}{dt} = -k_{\text{nonrad}}\, x(t) - C\varphi R_{\text{rad}}\, x(t)^2 - C^2\varphi^2 R_{\text{Auger}}\, x(t)^3 \tag{3.25}$$

The numerical solutions to this ordinary differential equation (ODE) are fitted globally to the decays using the least squares method across all fluences in order to extract $\varphi k_2$. Given that $0 \leq \varphi \leq 1$, the values presented for $k_2$ in the main text are underestimated compared to the true intrinsic values.

In order to account for an initially spatially varying charge-carrier density (due to absorption following the Beer-Lambert law), the fitting algorithm takes into account an exponentially decaying charge-carrier profile created by the pump beam. This is done by dividing the sample into 30 equally thick slices and computing the decay function for each of these individually.

### 3.2.6 Scanning Electron Microscopy

Scanning electron microscopy (SEM) is a technique that produces images of a sample by scanning the surface with a focused beam of electrons. The electrons interact with the atoms in the sample, and therefore provide the surface topography or composition information. SEM has two basic and commonly used signals, secondary electron (SE) and back-scattered electron (BSE). Hence, SE mainly reflects the morphology-based contrast, whereas BSE represents composition-based as well as some morphology-based contrast. SEs have very low energies which will limit their mean free path in solid matter. Consequently, SEs can only escape from the top few nanometers of the sample surface. The signal from SEs tends to be

highly localized at the point of the primary electron beam, making it possible to collect the image with a relatively higher resolution than BSEs.[92,93]

In Chapter 5.4, scanning electron microscopy (SEM) images were taken by a Hitachi S-4300 microscope using the secondary electron detection mode, with 3 kV accelerating voltage and 10 A emission current. The thicknesses of the perovskite films were calculated by the mean thickness of 3 measurements across the cross-section SEM.

## 3.3 Device Measurement

### 3.3.1 Current Density-Voltage Characterisation

The current density-voltage ($J$-$V$) characteristics for solar cells were measured in air using a Keithley 2400 source meter under approximately 100 mW/cm$^2$ of AM1.5G irradiation generated by an ABET Sun 2000 Class A simulator. Before the device measurement, the intensity of the solar simulator was automatically measured by a KG5-filtered silicon reference cell (certified by Fraunhofer ISE) to calibrate the accurate power conversion efficiency (PCE). The illuminated active area was 0.25 cm$^2$ defined by black anodized metal masks. The $J$-$V$ curves were taken from 1.2 V to -0.2 V and followed by the forward scan (from -0.2 V to 1.2 V), at a scan rate of 0.013 V/s in each direction.

### 3.3.2 Fourier Transform Photocurrent Spectroscopy

In Chapters 4.4 and 5.4, photocurrent was measured through a custom-built Fourier transform photocurrent spectrometer based on a Bruker Vertex 80v Fourier Transform Interferometer. Devices were illuminated with a tungsten halogen light source. The solar cells were masked with a metal aperture, with a defined active area of 0.25 $cm^2$. A current amplifier, Stanford Research 570, was used to detect low currents. All the photocurrent measurements were conducted under vacuum.

#### External Quantum Efficiency

The external quantum efficiency (EQE) represents how effectively a solar cell converts photons into electrical current by taking the ratio of charge carriers collected by a solar cell to the number of incident photons on the device. In this thesis, the EQE of devices was measured using a Fourier transform photocurrent spectrometer based on a Bruker Vertex 80v Fourier Transform Interferometer. The active area of devices (0.25 $cm^2$) was illuminated by a tungsten halogen lamp. The accurate EQE value was calibrated by a Newport-calibrated reference silicon solar cell of a known EQE. The short-circuit current density from the EQE measurement was determined by the overlap integral of the AM1.5 photon flux with the EQE.

#### Urbach Energy

The Urbach energy measurements in this thesis were performed by Jay B. Patel. The Urbach energy ($E_u$) measurements were taken on the EQE setup, using a near-infrared source and a 780 nm low-pass filter, such that the band edge could be taken

at a high sensitivity. $E_u$ was obtained by using the single exponential to fit the data from the tail of the band edge region.

### 3.3.3 Stability Test

In this thesis, all perovskite solar cells used for the stability tests were unencapsulated and aged using an Atlas SUNTEST XLS+ (1,700 W air-cooled Xenon lamp) light-soaking chamber under simulated full-spectrum AM1.5 sunlight with 76 $mW \cdot cm^{-2}$ irradiance. All aging tests were conducted in open-circuit conditions, and to perform *J-V* characterisation the samples were taken out from the chamber and tested at different time intervals, following the measurement protocol as described above. No ultraviolet filter was applied during the aging process. The aging chamber for storing the samples was air-cooled with the temperature controlled at 70±5°C. The temperature for the aging chambers was measured by a black standard temperature control unit. During the aging period the relative humidity in the laboratory was monitored in the range of 50±5%.

## 3.4 Nuclear Magnetic Resonance Spectroscopy

Nuclear magnetic resonance (NMR) is a nucleus-specific spectroscopy to identify molecular structures, by providing information about individual compounds and functional groups. This technique is based on the reorientation of atomic nuclei with non-zero nuclear spins in an external magnetic field. The absorption of electromagnetic radiation in the radio frequency region occurs with reorientation. Through the Fourier transformation of the time-domain electric currents signals,

the frequency-domain spectrum with the signal of each different nucleus can be obtained. The different frequencies are called chemical shifts. Meanwhile, neighbouring nuclear spins can interact with each other through the bonding electrons, also known as J-coupling. The influence of J-coupling is visualised by the splitting of the signal, called multiplets. In proton NMR, the formula to predict the number of multiplets is known as the n+1 rule, where n is the number of neighbouring protons. The integration of a given peak is proportional to the number of protons giving rise to the peak. In general, the NMR measurements can identify the molecular structure by chemical shift and multiplets. The most common types of NMR include proton and carbon-13 NMR spectroscopy.[94].

In Chapter 4.4, a two-channel Bruker Avance III HD Nanobay 400 MHz instrument running TOPSPIN 3 equipped with a 5 mm z-gradient broadband/fluorine observation probe is used to measure proton NMR ($^1$H NMR) spectroscopy. The signal from deuterated DMF or deuterated DMSO solvent is used for reference.

## 3.5 Mass Spectrometry

Mass spectrometry is a powerful analytical technique used to identify unknown compounds within a sample. The whole process includes the generation of multiple ions from the sample, the separation of ions according to their specific mass-to-charge ratio ($m/z$), and the detection of the relative abundance of each ion type. A mass spectrometer usually consists of an ion source (to produce gaseous ions), analyser (to resolve the ions into their characteristic mass components based on their $m/z$), and a detector system (to detect the ions and record the abundance).[95]

To monitor the composition of the gas remaining in the chamber during evaporation in Chapter 4.4, I employed a residual gas analysis system using a Hiden Analytical quadrupole mass spectrometer. The spectrometer was fitted with a filament (ion source), a quadrupole mass filter (analyser) and dual Faraday/Single Channel Electron Multiplier (SCEM) detectors. Operation of the mass spectrometer at pressures exceeding specified values ($1\times10^{-4}$ Torr for Faraday and $5\times10^{-6}$ Torr for SEM) may damage both filaments and the detectors. Given that the chamber pressure during the evaporation was in the range of $5\times10^{-6}$-$2\times10^{-5}$ mbar, all mass spectra were collected by the Faraday detector.

# 4

# The Impact of Impurities in Formamidinium Iodide on Solution- and Vapour-Processed Metal Halide Perovskite

## Contents



Siyu Yan fabricated the samples, designed and conducted the experiments, and analysed the data. Nakita K. Noel and Siyu Yan conducted the recrystallisation experiments. Siyu Yan, Saqlain Choudhary and Emily A. Hudson performed the device fabrication.

## 4.1 Broad Context

While metal halide perovskites have shown remarkable power conversion efficiencies in photovoltaic applications, their limited long-term stability remains a significant barrier to commercialisation. Previous studies have demonstrated that trace impurities present in perovskite precursor materials can influence the crystallisation dynamics of perovskite thin films and hence, affect crystal structure, morphology and optoelectronic properties. However, the nature of the impurities in formamidinium iodide (FAI) and their effects on film quality and device performance are still underexplored.

In this chapter, I carry out an analysis of the impurities present in commonly used commercial FAI sources, and probe their impact on the composition, structure, and optoelectronic quality of the resulting perovskite thin films and devices. I find that while some impurities in these precursors can improve the optoelectronic properties of solution-processed perovskite thin films, in vapour-processed films, their presence alters the sublimation behaviour of FAI, favouring irreversible degradation pathways which lead to the formation of sym-triazine. This results in films which deviate significantly from the target stoichiometry, and do not fully convert into the desired photoactive phase, eventually causing poor material stability. The results highlight the importance of understanding and controlling impurity concentrations in perovskite precursor materials as a route to enhancing both process reproducibility and the performance of perovskite solar cells.

## 4.2 Introduction

At present, next-generation solar cells based on metal halide perovskite (MHP) semiconductors have already achieved promising certified power conversion efficiencies (PCEs) of 26.95% in single-junction devices, and 34.85% in Si/perovskite tandem devices.[10] While the rapid increase in the efficiency of these devices is partly due to the excellent intrinsic optoelectronic properties of perovskites,[49,54,96] significant performance gains have been made as a result of improving the structural and optoelectronic quality of perovskite thin films. These improvements have largely been made through advances in process engineering, compositional alloying, solvent and additive engineering in precursor inks, and various interface passivation techniques.[15,83,97–99] Notably, it has been observed that precisely controlling crystallisation kinetics is crucial to achieving efficient and stable perovskite solar cells (PSCs).[42,100,101]

One underexplored area of research is the impact of trace precursor impurities on the optoelectronic properties and long-term stability of perovskite films. In the vast majority of published literature, perovskite precursor materials ($PbI_2$, FAI etc) are usually used as-received without further purification. However, recent reports suggest that there are impurities present in these precursors which can modulate the crystallisation process during perovskite film formation, and can have competing effects based on the nature and concentration of the impurities.[102–107] For example, Kerner et al. characterised five commercially available lead iodide ($PbI_2$) materials and found that one $PbI_2$ source contained a higher concentration of a lead acetate trihydrate ($Pb[OAc]_2 \cdot 3H_2O$) impurity which had a negative effect on perovskite device performance, while another $PbI_2$ source contained potassium iodide (KI)

which resulted in higher quality films and improved device performance.[108] Given that precursor materials can contain a variety of different impurities which may have both beneficial and/or detrimental effects on devices, it stands to reason that a thorough understanding–and subsequent fine control–of which impurities precursors contain can be beneficial to perovskite film quality, device performance, long-term stability, and even batch-to-batch reproducibility.

Another point which should be considered here is that the presence of impurities in perovskite precursors may have different effects based on whether the perovskite films are fabricated using solution-based or vapour-based deposition techniques. Borchert et al. have previously investigated the impact of organic precursor impurities on the quality of methylammonium lead triiodide ($MAPbI_3$) films deposited through thermal vapour deposition.[109] It was found that while the presence of phosphorus-based impurities had a negligible impact on device performance, it did significantly affect the consistency of the evaporation rate. Conversely, research probing the impact of these phosphorus-based impurities in spin-coated perovskite solar cells showed an improvement in device performance as a result of changing the crystallisation dynamics of the perovskite thin film.[110,111] This suggests that precursor impurities may play very different roles in dry deposition processes than they do in solvent-mediated ones.

Currently, a significant portion of research into perovskite solar cells is focused on formamidinium-based perovskites due, in part, to their superior thermal and chemical stability, as compared to their MA-based counterparts.[112–115] In comparison to MAI, another advantage of FAI is that it yields a more controllable, and significantly more consistent, deposition rate.[90,116] However, during the thermal

evaporation of FAI, Kroll et al. detected a variety of degradation products using mass spectrometry. Of particular note here was the detection of sym-triazine (a product of the irreversible decomposition of FAI) at a lower temperature (50°C to 120°C) than the sublimation temperature of FAI (above 125°C).[117]

This raises questions as to if (and how) impurities present in FAI can on one hand, affect not only its sublimation temperature, but the composition and stability of vapour-deposited perovskite films, and on the other, what (if any) is the impact of these impurities on solution-processed films and devices. Herein, I seek to address two questions: i) what are the initial impurities in FAI and how do they impact film formation and thin-film properties in halide perovskites?; and ii) do they have unique effects depending on whether films are solution-processed or vapour-processed? The impurities in as-received FAI is first identified via nuclear magnetic resonance (NMR) measurements. Through a simple recrystallisation procedure, the as-received FAI is purified with the goal of removing the impurities. By comparing perovskite films fabricated with the as-received and recrystallised FAI, I probe the direct impact of these impurities, and show that their presence impacts the optoelectronic properties of both solution- and vapour-processed perovskite films, hence affecting device performance. Curiously, the results show that certain impurities in the FAI can have beneficial effects on the optoelectronic properties of the perovskite thin film. However, that is only the case for the solution-processed films. In the case of vapour-processed films, these impurities have detrimental effects. The identified underlying mechanism is the impurity-induced changes to the sublimation behaviour of FAI which leads to increased formation of sym-triazine. This change in sublimation behaviour results in perovskite films which likely deviate significantly from the target stoichiometry leading to the inclusion of unwanted

polytype phases. The existence of these non-photoactive polytype phases impairs device performance, and can be correlated with reduced material stability. These results highlight the importance of understanding the role of precursor impurities in modulating the crystallisation of perovskite thin films.

## 4.3 Results and Discussion

### 4.3.1 Impurity Analysis in Formamidinium Iodide

To understand the impact of FAI impurities on perovskite films and devices, I first screen for and identify potential impurities and determine whether they can be removed through simple purification techniques such as recrystallisation. To probe this, Figures 4.1a and 4.1b present the results of proton nuclear magnetic resonance ($^1$H NMR) experiments conducted on as-received and recrystallised FAI obtained from a commonly used supplier. In Figure 4.1a, both the as-received and recrystallised FAI show the characteristic peaks [CH group at 8.32 ppm (singlet) and amine groups at 9.26 ppm (singlet)] of $FA^+$. However, distinct spectral differences are observed in the range of 1 4.5 ppm (Figure 4.1b). The as-received FAI shows signals associated with ethyl acetate [$\delta$ 1.19 ppm (triplet), $\delta$ 2.01 ppm (singlet), $\delta$ 4.05 ppm (quartet)], ethanol [$\delta$ 1.10 ppm (triplet), $\delta$ 3.40 ppm (quartet)], and isopropanol [$\delta$ 1.08 ppm (doublet), $\delta$ 3.88 ppm (septet)]. These impurities are likely to be residual solvents from the synthesis and/or purification of FAI. After recrystallisation, these peaks are no longer present in the $^1$H NMR spectrum. Instead, new signals emerge in this range, corresponding to diethyl ether [$\delta$ 1.10 ppm (triplet), $\delta$ 3.54 ppm (quartet)], the solvent which is used to wash the recrystallised

product. To exclude the possibility that the presence of these impurities in the as-received FAI is simply a batch anomaly, I obtain and test samples from another batch number from supplier A, along with a sample from supplier B (Figures 4.1c and 4.1d). $^{1}$H NMR results confirm that both batches of as-received FAI (from supplier A) contain the same types of impurities, which can be effectively removed through a simple recrystallisation process.

### 4.3.2 Influence of FAI Impurities on Solution-Processed Perovskite Films and Devices

Having established the nature of the organic impurities in FAI from supplier A, I proceed to investigate the impact of these impurities on the structural and optoelectronic properties of solution-processed perovskite thin films and devices. For convenience, perovskite films fabricated using as-received and recrystallised FAI are abbreviated as 'ctrl' and 'rextal' films, respectively. The absorption coefficient and X-ray diffraction (XRD) patterns show negligible difference (Figures 4.2a and 4.2b) for solution-processed ctrl and rextal films, which indicates that removing the impurities in FAI does not change the structure of solution-processed perovskite films. However, there is a significant quenching of the photoluminescence (PL) accompanied by a reduction of the charge carrier lifetime in rextal films (Figures 4.2c and 4.2d). This indicates an increase in non-radiative recombination of charge carriers as a result of the removal of the organic impurities in FAI. Hence, it appears that in solution-processing, these impurities yield films with fewer electronic defects, either through modulating ink chemistry, or altering crystallisation kinetics.

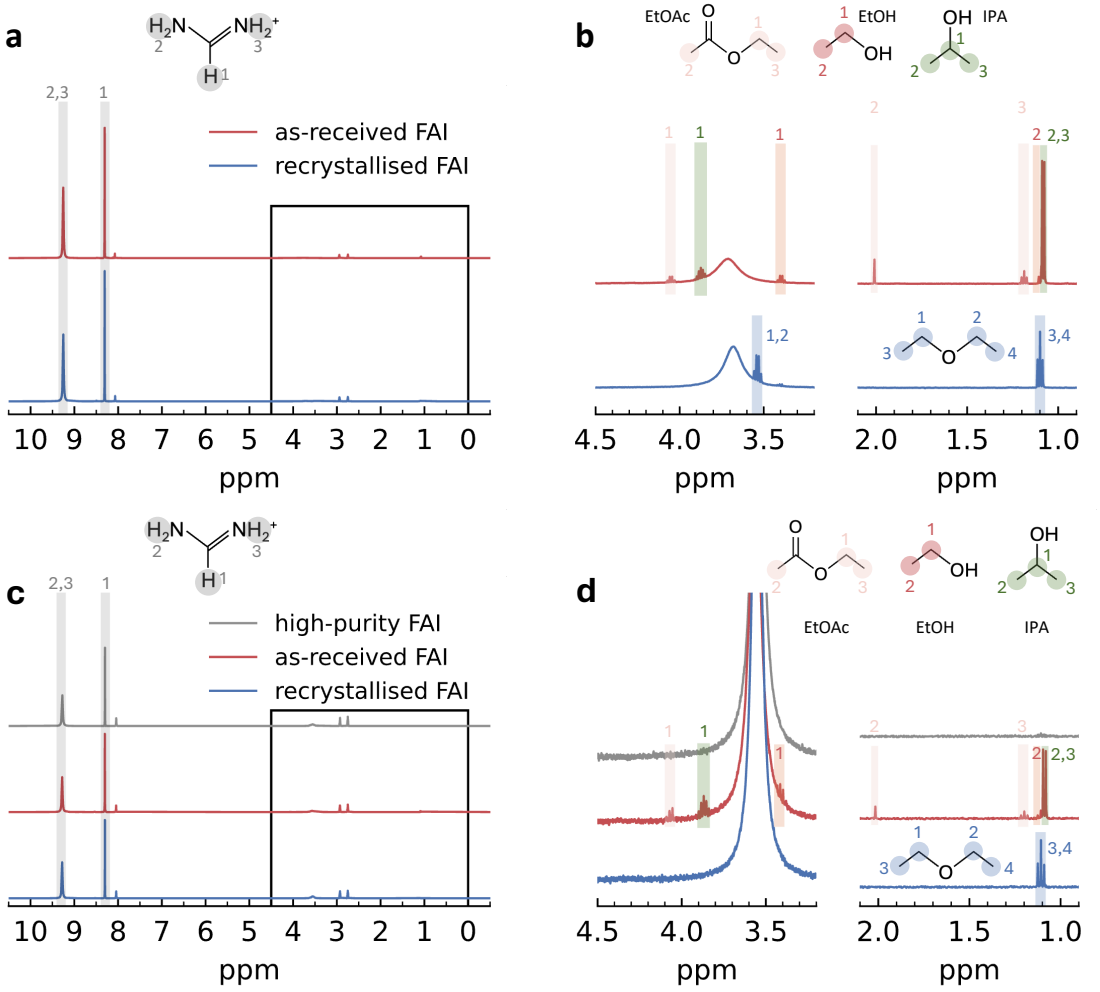


**Figure 4.1:** Solution $^{1}$H NMR spectra of as-received and recrystallised FAI in DMSO-$d_6$. (a) $^{1}$H NMR spectra of as-received and recrystallised FAI. In both cases, the main peaks can be attributed to the protons of the methine[CH (1)] and amine groups [$NH_2$ (2, 3)] groups of formamidinium. (b) Low ppm region of $^{1}$H NMR spectra of as-received and recrystallised FAI. As-received FAI presents signals from ethyl acetate, ethanol and isopropanol, whereas recrystallised FAI only shows a signal from diethyl ether. (c) NMR spectroscopy of high-purity FAI, as-received FAI and recrystallised FAI in the whole range. As-received FAI and recrystallised FAI measured here are from different recrystallisation rounds compared with the results shown in Figures 4.1a and b). (d) Impurity analysis from the zoomed-in NMR spectroscopy of (c).

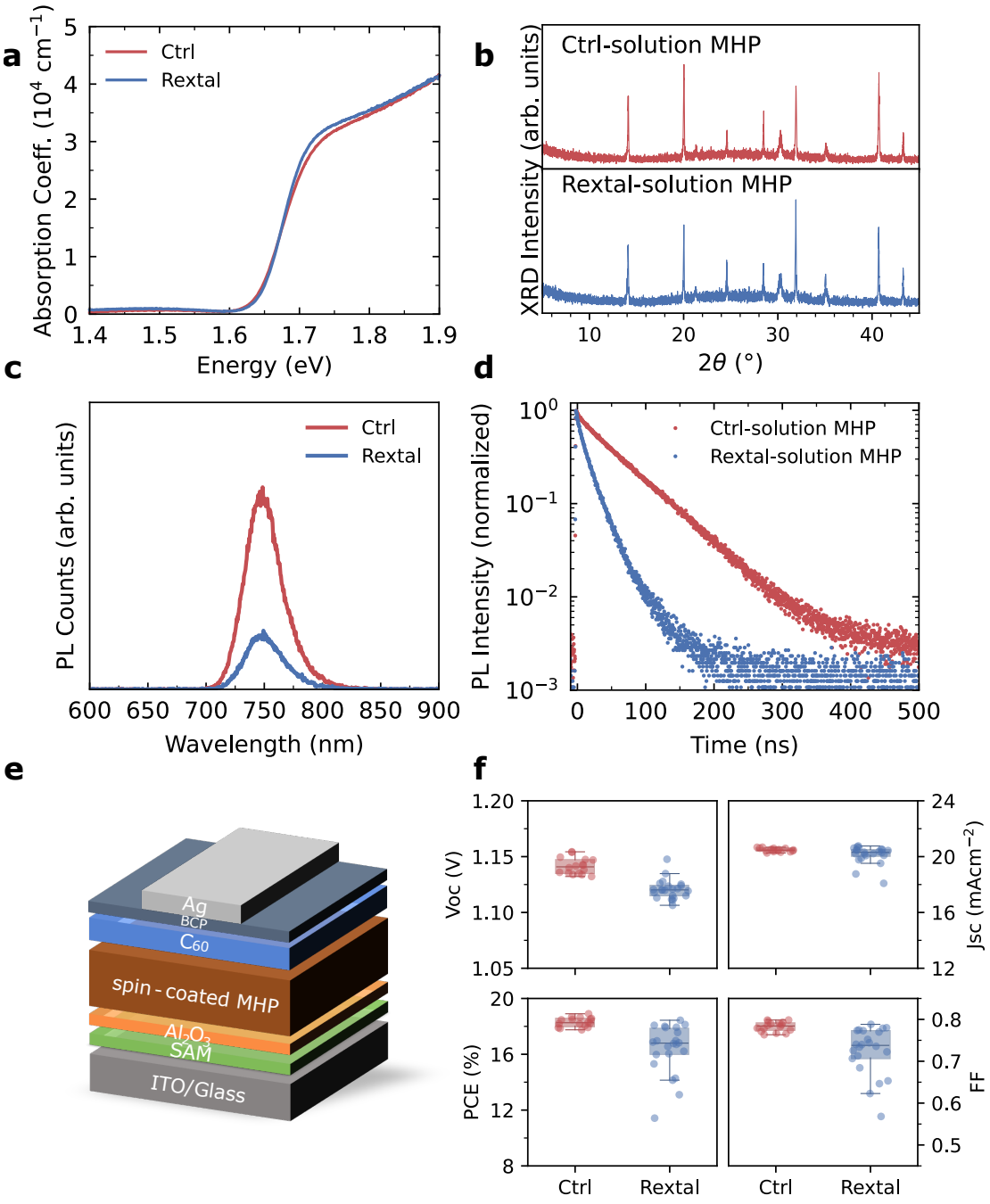


**Figure 4.2:** Characterisation of solution-processed $FA_{0.83}Cs_{0.17}Pb(I_{0.8}Br_{0.2})_3$ perovskite films and devices, made using as-received FAI (labelled as ctrl in the figure) and recrystallised FAI (labelled as rextal in the figure). (a) Absorption coefficient and (b) X-ray diffraction patterns of solution-processed perovskite films.(c) Steady-state PL spectra of solution-processed perovskite films. (d) PL dynamics of solution-processed perovskite films, excited by 398nm laser, at fluence of 45.4 nJ/cm$^2$. (e) Schematic of device architecture. (f) Performance parameters of perovskite devices fabricated with as-received and recrystallised FAI. In the box plots, the central line inside each box represents the median value of the dataset. The box edges (lower and upper sides) indicate the first quartile (Q1) and third quartile (Q3), corresponding to the $25^{th}$ and $75^{th}$ percentiles, respectively. The whisker extends from the box to the smallest and largest data points within 1.5 times the interquartile range (IQR) from Q1 and Q3. Data points lying outside of this range are plotted individually as outliers. Device fabrication performed by Emily A. Hudson and Siyu Yan.

| Device | $J_{sc}$ ($mA\,cm^{-2}$) | $V_{oc}$ (V) | PCE (%) | $FF$ | SPO (%) |
|---|---|---|---|---|---|
| Ctrl-champion | 20.80 | 1.13 | 18.93 | 0.82 | 18.50 |
| Ctrl-avg | 20.48±0.13 | 1.14±0.01 | 18.29±0.34 | 0.78±0.01 | 17.97±0.39 |
| Rextal-champion | 20.62 | 1.13 | 18.44 | 0.79 | 18.15 |
| Rextal-avg | 20.13±0.64 | 1.12±0.01 | 16.37±1.78 | 0.72±0.06 | 15.98±1.82 |

**Table 4.1:** Champion and average device performance parameters for solution-processed $FA_{0.83}Cs_{0.17}Pb(I_{0.8}Br_{0.2})_3$ perovskite solar cells fabricated with as-received (ctrl) and recrystallised (rextal) FAI measured under 1 sun simulated AM1.5G solar illumination. The values given in this table represent scans from open-circuit to short-circuit conditions. The statistical results are taken from a total 16 devices across 2 different batches.

To investigate whether this improvement in optoelectronic properties will translate into enhanced solar cell performance, these films are incorporated into photovoltaic devices (Figures 4.2e and 4.2f). Here, devices fabricated using rextal films show a drop across all performance parameters, resulting in a reduction of the average PCE from 18.3% to 16.4% accompanied by a much broader distribution in performance (Table 4.1). The large reduction in the average PCE for devices fabricated with rextal films is primarily due to a substantial decrease in the open-circuit voltage ($V_{oc}$) and fill factor ($FF$) (Figure 4.2f). To verify that the observed decrease in device performance is indeed due to the removal of impurities from as-received FAI (supplier A), I first make devices with high-purity FAI available from supplier B as a means of excluding the possible influence of diethyl ether in recrystallised FAI. Devices fabricated using recrystallised FAI (supplier A) and high-purity FAI (supplier B) achieve comparable efficiencies (see Figure 4.3). This confirms the negligible influence of diethyl ether in recrystallised FAI on the device performance. Meanwhile, they are both outperformed by devices made using as-received FAI (supplier A). This supports the hypothesis that the organic impurities present in FAI from supplier A improve the performance of perovskite films and devices.

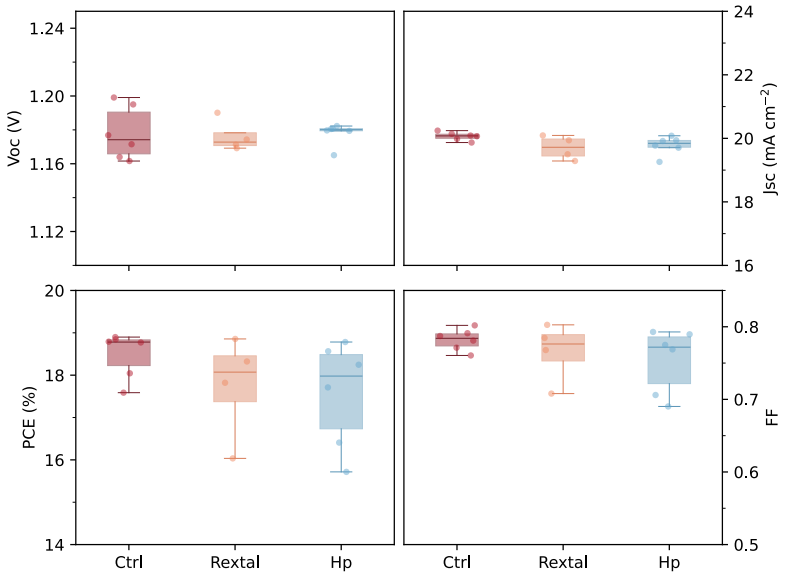


**Figure 4.3:** Statistical distribution of photovoltaic performance parameters of solution-processed $FA_{0.83}Cs_{0.17}Pb(I_{0.8}Br_{0.2})_3$ perovskite devices made by as-received FAI (ctrl), recrystallised FAI (rextal) and high-purity FAI (hp). In the box plots, the central line inside each box represents the median value of the dataset. The box edges (lower and upper sides) indicate the first quartile (Q1) and third quartile (Q3), corresponding to the $25^{th}$ and $75^{th}$ percentiles, respectively. The whisker extends from the box to the smallest and largest data points within 1.5 times the interquartile range (IQR) from Q1 and Q3. Data points lying outside of this range are plotted individually as outliers. Device fabrication performed by Saqlain Choudhary.

Given that ethyl acetate and alcohols (isopropanol and ethanol) are two main impurities identified in as-received FAI (supplier A), to determine which impurity/impurities are responsible for the improved device performance, different amounts of ethyl acetate and isopropanol are added to the perovskite precursor ink made using recrystallised FAI. When 1 vol% ethyl acetate is added to the precursor ink, the device performance is enhanced as a result of increased $V_{oc}$ and $FF$ (Figure 4.4). Interestingly, the performance improvement that arises from the ethyl acetate, brings the PCE of devices fabricated with recrystallised FAI in line with that of those fabricated with as-received FAI. This finding is consistent with previous studies, which have reported that the use of ethyl acetate, either as an anti-solvent[118] or as an additive to the perovskite precursor ink[119] can improve

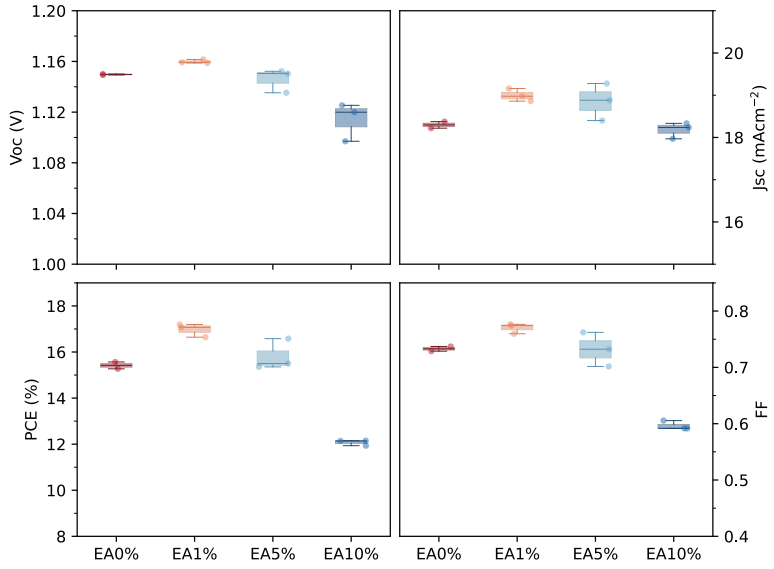


**Figure 4.4:** Statistical distribution of photovoltaic performance parameters of solution-processed $FA_{0.83}Cs_{0.17}Pb(I_{0.8}Br_{0.2})_3$ perovskite devices using recrystallised FAI with adding different amounts of ethyl acetate (EA0vol%, EA1vol%, EA5vol% and EA10vol%) to the perovskite precursor. In the box plots, the central line inside each box represents the median value of the dataset. The box edges (lower and upper sides) indicate the first quartile (Q1) and third quartile (Q3), corresponding to the $25^{th}$ and $75^{th}$ percentiles, respectively. The whisker extends from the box to the smallest and largest data points within 1.5 times the interquartile range (IQR) from Q1 and Q3. Data points lying outside of this range are plotted individually as outliers. Device fabrication performed by Saqlain Choudhary.

both thin-film quality through improving crystallisation and passivating defects. In contrast, the addition of isopropanol to the precursor ink does not significantly affect device performance (Figure 4.5). As such, it is very likely that the decrease in device performance is a result of the removal of ethyl acetate.

To further evaluate whether the organic impurities present in FAI influence the long-term stability of solution-processed perovskites, the aging tests are conducted on both ctrl and rextal films at 70±5°C under 1 sun illumination (Figure 4.6). Compared to ctrl films, solution-processed rextal films exhibit slightly but not significantly faster degradation over a 95h period. This suggests that impurities in FAI do not substantially influence the stability of solution-processed perovskite

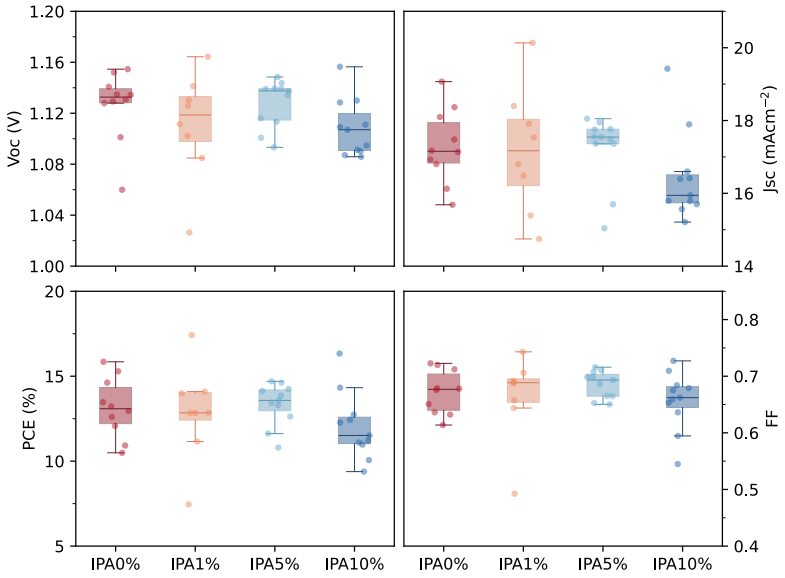


**Figure 4.5:** Statistical distribution of photovoltaic performance parameters of solution-processed $FA_{0.83}Cs_{0.17}Pb(I_{0.8}Br_{0.2})_3$ perovskite devices using recrystallised FAI with adding different amounts of isopropanol (IPA0vol%, IPA1vol%, IPA5vol% and IPA10vol%) to the perovskite precursor. In the box plots, the central line inside each box represents the median value of the dataset. The box edges (lower and upper sides) indicate the first quartile (Q1) and third quartile (Q3), corresponding to the $25^{th}$ and $75^{th}$ percentiles, respectively. The whisker extends from the box to the smallest and largest data points within 1.5 times the interquartile range (IQR) from Q1 and Q3. Data points lying outside of this range are plotted individually as outliers. Device fabrication performed by Saqlain Choudhary.

under thermal and light stress.

### 4.3.3 Influence of FAI Impurities on Vapour-Deposited Perovskite Films and Devices

It has been established that organic impurities in FAI, specifically trace amounts of ethyl acetate, have a positive impact on the optoelectronic properties of solution-processed perovskite thin films and devices. To test whether this holds true for vapour-deposition approaches I fabricate perovskite films and devices using thermal vapour deposition and present the results below. Interestingly, here, the absorption coefficient of rextal films (Figure 4.7a) is consistent with that of previously reported

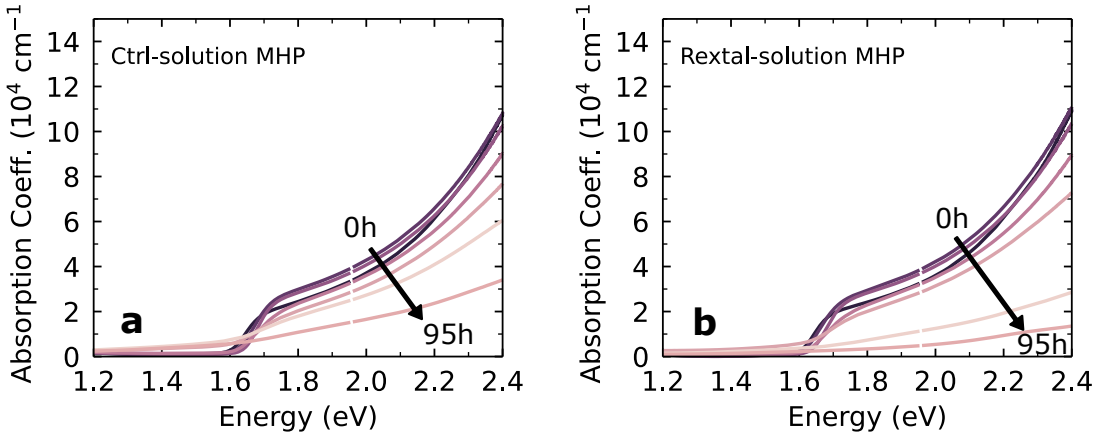


**Figure 4.6:** The absorption coefficient spectra of solution-processed $FA_{0.83}Cs_{0.17}Pb(I_{0.8}Br_{0.2})_3$ perovskite films made by as-received FAI (ctrl-solution MHP) (a) and recrystallised FAI (rextal-solution MHP) (b) aged at 70±5°C under 1 sun illumination in the ambient atmosphere from 0h to 95h. Film fabrication performed by Saqlain Choudhary

vapour-deposited films of the same composition;[116] however, it is significantly higher than that for films of nominally the same thickness, in the case of the ctrl, the precursors only partially react to form the desired photoactive ($\alpha$-) perovskite phase. The bandgap of both films is 1.56 eV as determined through an Elliott fit (Figure 4.8). Additionally, ctrl films exhibit lower PL intensity than rextal films (Figures 4.7b and 4.7c), suggesting that recrystallisation of the FAI results in the formation of perovskite films with fewer electronic defects, yielding reduced non-radiative recombination. However, in light of the lower absorption coefficient (Figure 4.7a), it is also possible that the as-received FAI results in the formation of less photoactive perovskite for the same total film thickness. Time-resolved PL measurements yield similar charge-carrier dynamics in ctrl and rextal films.

I then incorporate these films into p-i-n solar cells (Figure 4.7d). Devices made using rextal films (Figure 4.7e) show a boost of the average PCE from 6.16±2.77% to 15.63±0.92% , with reduced standard deviations (more details in Table 4.2). In this case, the performance enhancement is mainly due to an increase in the short-

| Device | $J_{sc}$ ($mA\,cm^{-2}$) | $V_{oc}$ (V) | PCE (%) | $FF$ | SPO (%) |
|---|---|---|---|---|---|
| Ctrl-champion | 17.05 | 1.04 | 11.71 | 0.66 | 11.37 |
| Ctrl-avg | 14.20±5.18 | 0.92±0.16 | 6.16±2.77 | 0.49±0.12 | 6.00±1.72 |
| Rextal-champion | 21.41 | 0.99 | 16.83 | 0.79 | 16.82 |
| Rextal-avg | 20.90±1.11 | 0.99±0.04 | 15.63±0.92 | 0.76±0.03 | 15.12±0.41 |

**Table 4.2:** Champion and average device performance parameters for vapour-processed $FAPbI_3$ perovskite solar cells fabricated with as-received (ctrl) and recrystallised (rextal) FAI measured under 1 sun simulated AM1.5G solar illumination. The values in this table represent data collected from open-circuit to short-circuit conditions across a total of 16 devices from 2 different batches for each group.

circuit current density ($J_{sc}$) and $FF$ (Figure 4.7f). This increase in photocurrent is consistent with the higher absorption coefficient.

Here, recrystallisation of the FAI results in opposite trends in solution- and vapour-processed perovskite films and devices. For solution-processing, these trace impurities improve film and device quality, while for vapour-processing, they cause a marked decrease in performance. Overall, this suggests that the same impurities play very different roles in the solution- processing of perovskite films than they do in vapour-processing.

### 4.3.4 Phase Impurity in Vapour-Deposited Perovskite Films

To probe the underlying cause of the performance enhancement in vapour-deposited perovskite devices fabricated using rextal films, a more detailed analysis of the optical and structural properties of these films is conducted. Herein, ctrl films exhibit more prominent above-bandgap oscillations in their absorption spectra (Figures 4.9a and 4.9b). Previous studies have shown that these above-bandgap oscillations in $FAPbI_3$, (which may be due to inclusions of secondary phases), can

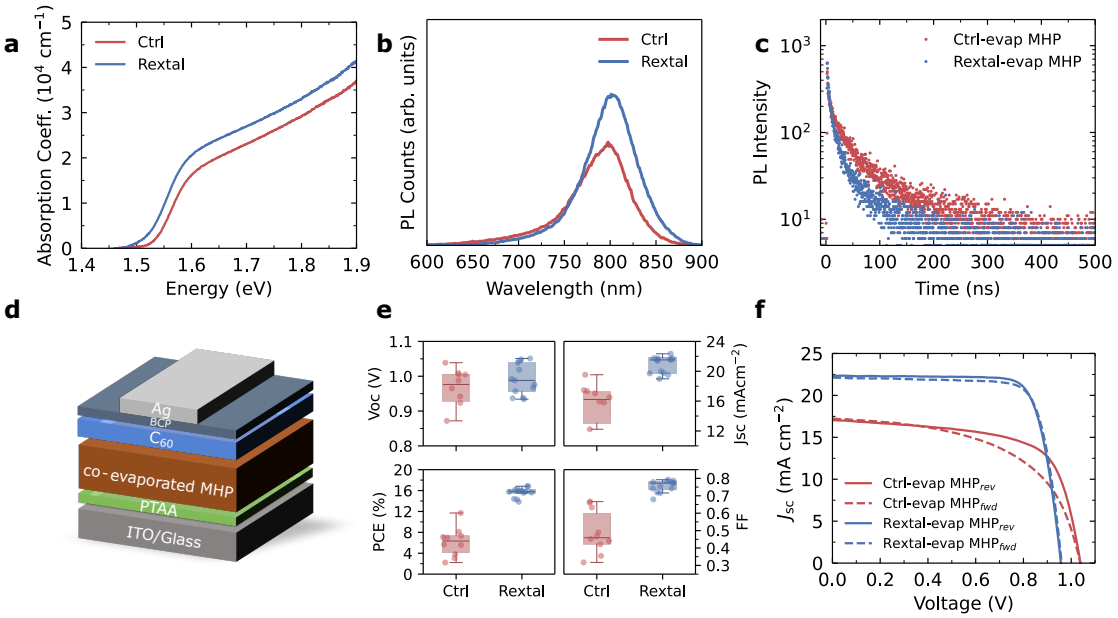


**Figure 4.7:** Characterisation of vapour-deposited $FAPbI_3$ perovskite films and devices, made using as-received FAI (labelled as ctrl in the figure) and recrystallised FAI (labelled as rextal in the figure). (a) Absorption coefficient and (b) steady-state PL spectra of vapour-deposited perovskite films fabricated with as-received and recrystallised FAI. (c) PL dynamics of vapour-processed perovskite films made using as-received FAI and recrystallised FAI, labelled as ctrl and rextal, separately, excited by 398nm laser, at fluence of 45.4 nJ/cm$^2$. (d) Schematic for the vapour-deposited device architecture. (e) Performance parameters of vapour-processed perovskite devices fabricated with as-received and recrystallised FAI. In the box plots, the central line inside each box represents the median value of the dataset. The box edges (lower and upper sides) indicate the first quartile (Q1) and third quartile (Q3), corresponding to the $25^{th}$ and $75^{th}$ percentiles, respectively. The whisker extends from the box to the smallest and largest data points within 1.5 times the interquartile range (IQR) from Q1 and Q3. Data points lying outside of this range are plotted individually as outliers. (f) Current density-voltage curve of best vapour-processed devices made by as-received and recrystallised FAI, labelled as ctrl and rextal, separately.

be directly correlated with reduced device performance.[120–122] Here, to investigate whether there is a correlation between the presence of non-perovskite phases and the above-bandgap oscillations observed in ctrl films, XRD measurement results are shown in Figures 4.9c and 4.9d. For ctrl films I observe, in the diffractogram, the presence of a lower dimensional, 4H polytype at 11.6°. The presence of these polytypes, not only negatively impacts the device performance but also material stability.[123] Indeed, when these thermally evaporated perovskite films are subjected

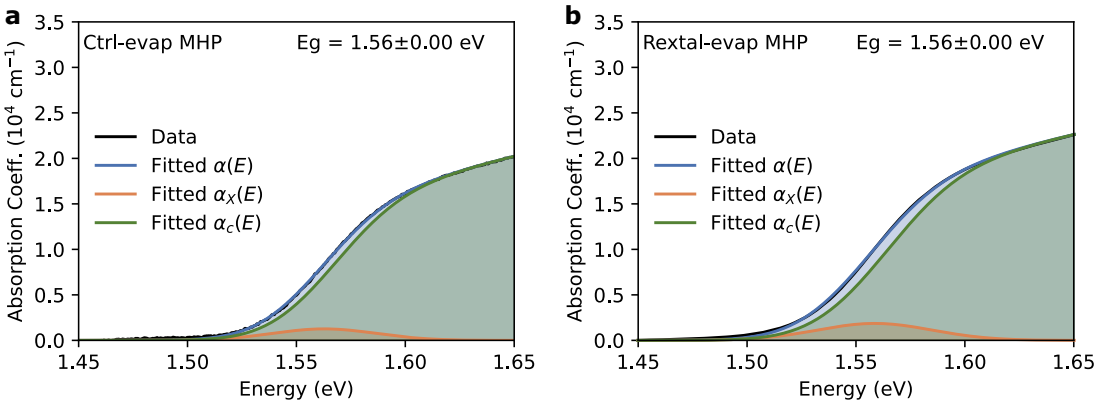


**Figure 4.8:** Elliott fitting results of the absorption coefficient values of vapour-deposited $FAPbI_3$ films fabricated using as-received and recrystallised FAI, labelled as ctrl and rextal, separately.

to elevated temperature and illumination (at 70±5°C under 0.765 sun without UV filter, in ambient air with a 50-60% relative humidity), ctrl films suffer far more severe degradation over a 96h period (Figures 4.9a and 4.9b). This is in agreement with literature reports that that the presence of lower dimensional polytypes has a detrimental effect on the thermal stability of FA-based perovskite films.[123,124]

### 4.3.5 Impurity-Related Degradation Process of FAI during the Vapour Deposition

Thus far, the results have shown that thermally evaporated perovskite films deposited with as-received and recrystallised FAI possess different optoelectronic and structural properties. However, it is still unclear how this arises from the presence of impurities in FAI. One could expect that given the volatile nature of these organic impurities, that they should readily evaporate under high vacuum conditions, and hence not be incorporated into vapour-deposited perovskite films. If nonetheless, the presence of volatile impurities can change the sublimation behaviour of FAI, or the rate at which it decomposes, it is conceivable that their presence can have a

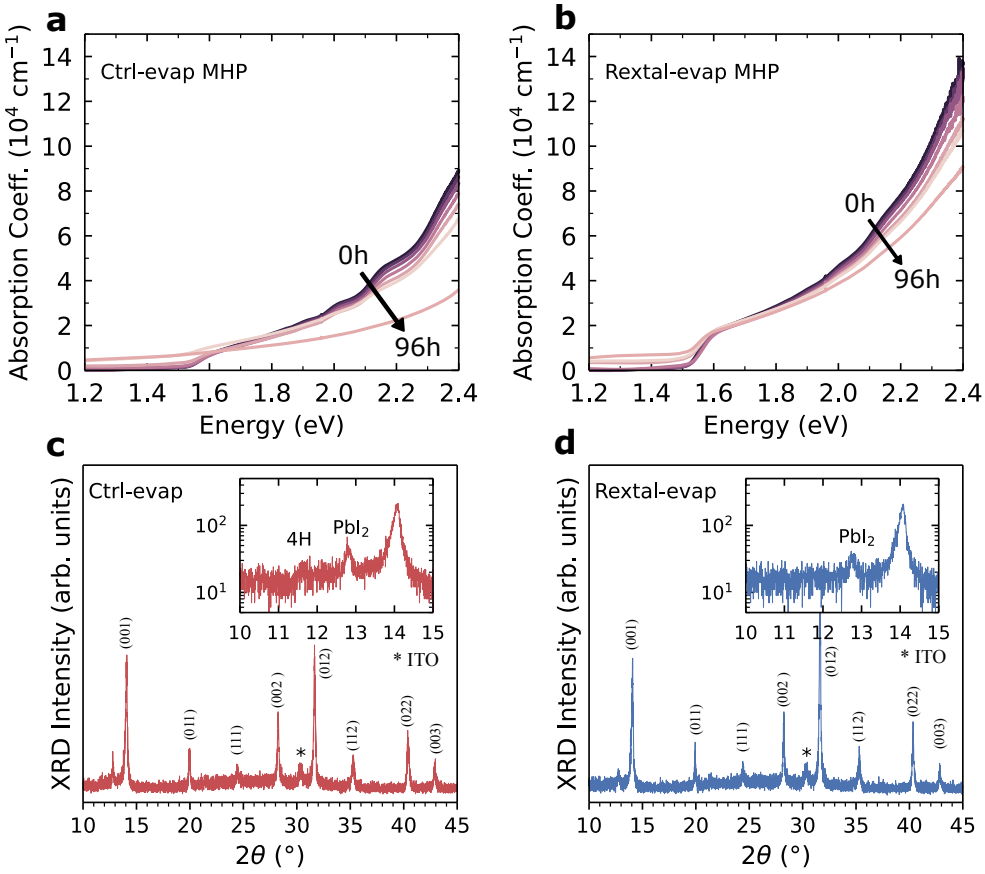


**Figure 4.9:** Stability and structural characterisation of vapour-processed $FAPbI_3$ perovskite films made using as-received FAI (labelled as ctrl in the figure) and recrystallised FAI (labelled as rextal in the figure). (a, b) The absorption coefficient spectra of vapour-processed $FAPbI_3$ perovskite films made by as-received FAI (ctrl-evap MHP) and recrystallised FAI (rextal-evap MHP) aged at 70±5°C under 1 sun illumination in the ambient atmosphere from 0h to 96h. (c, d) X-ray diffraction patterns of ctrl-evap MHP and rextal-evap MHP films. XRD signal from polytype (4H) is only identified in ctrl-evap MHP films (inset).

significant impact on the quality of the resulting perovskite films.

In vapour deposition, mass spectroscopy (MS) is an effective technique with which one can analyse the chamber atmosphere during the evaporation process. By tracking the distinguishable mass-to-charge ratio (m/z) of major molecules or fragments produced during the perovskite deposition, I can identify whether the impurities are evaporated along with the FAI, or if (and how) they alter the sublimation of the material. Previous studies have found that upon heating, FAI

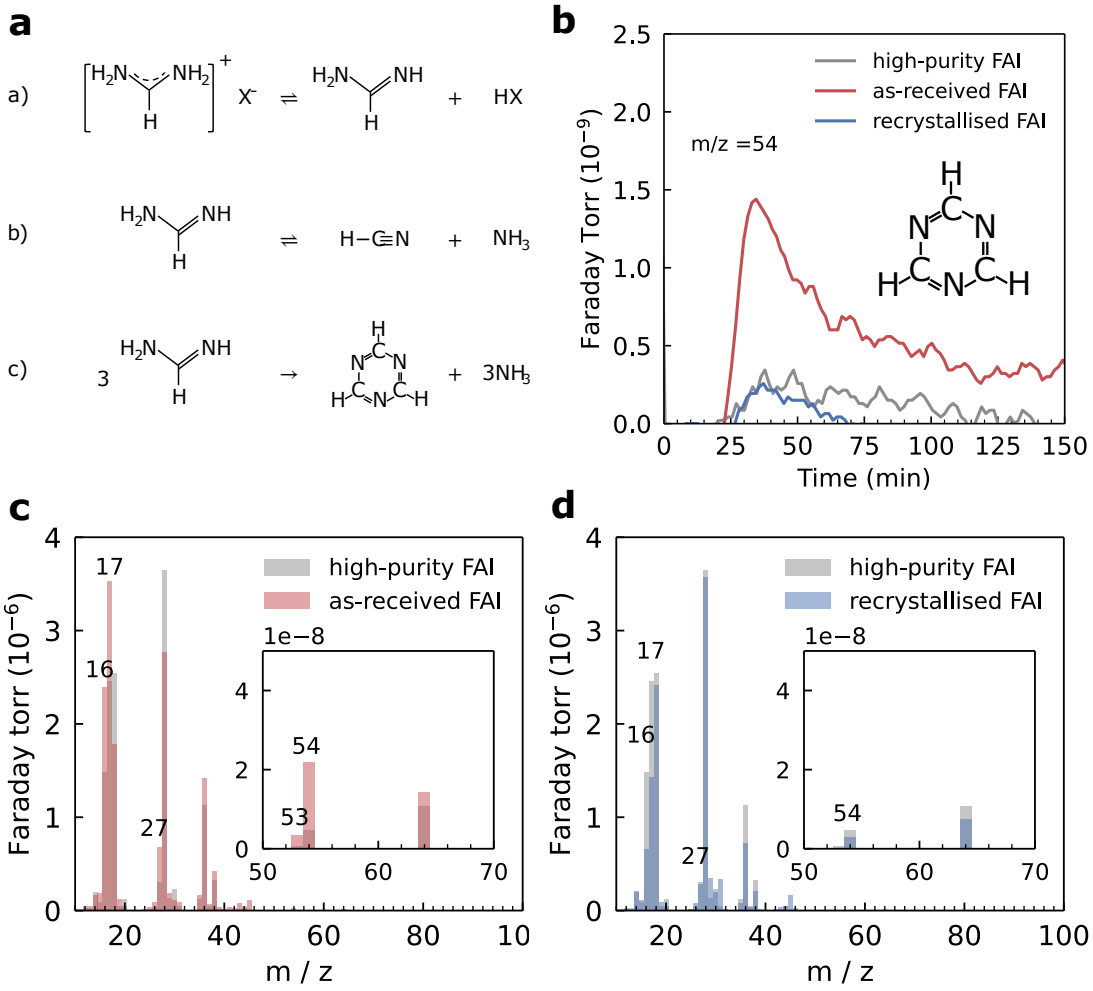


**Figure 4.10:** The impact of impurities on evaporation behaviours and corresponding degradation process in as-received FAI, recrystallised FAI and high-purity FAI. (a) Scheme of FAI degradation reations. (b) Mass spectra tracking of sym-triazine (the decomposition product of FAI, with the major m/z value of 54) during the vapour deposition. (c) Comparison of the cracking pattern of as-received FAI (red) and high-purity FAI (grey). (d) Comparison of the cracking pattern of recrystallised FAI (blue) and high-purity FAI (grey).

undergoes several chemical reactions (Figure 4.10a). Firstly, FAI ($CH(NH_2)_2I$) undergoes a reversible thermal decomposition forming formamidine ($HC(=NH)NH_2$) and hydroiodic acid (HI). Following this, there are two possible pathways for formamidine to further react. It can decompose into hydrogen cyanide (HCN) and ammonia ($NH_3$) (another reversible reaction), or it can react to form sym-triazine ($(HCN)_3$) and ammonia ($NH_3$).[117,125]

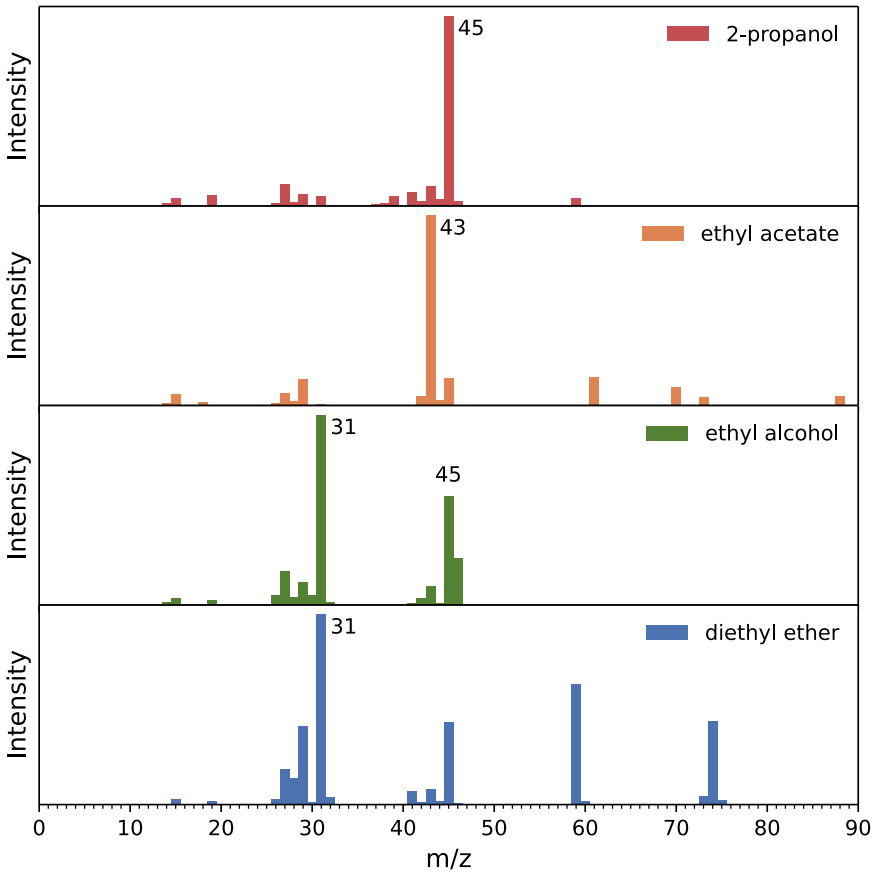


**Figure 4.11:** Reference mass spectroscopy patterns of impurities, including isopropanol, ethyl acetate, ethyl alcohol and diethyl ether. Sourced from AIST SDBS[126]

A recent study by Kuba et al. explored the possibility of directly synthesising FA-based perovskite using sym-triazine, ammonium source and HI (contradicting the irreversibility of sym-triazine formation).[117] Indeed, initial work by Grundmann et al. discussed the reversibility of the decomposition of formamidinium chloride to sym-triazine, but notes that the equilibrium of this reaction sits so far to the right, that the reverse reaction is 'far from being quantitative'.[127] As such, and with consideration of the high volatility of sym-triazine particularly under high-vacuum conditions, the decomposition of formamidine into sym-triazine and $NH_3$ is regarded as 'effectively irreversible'. Table 4.3 lists the m/z ratios of FAI and the fragments of its major thermal degradation products. Compared with

| m/z | Detected ion | Likely parent/fragment molecule |
|---|---|---|
| 14 | $N^+$ | nitrogen |
| 16 | $NH_2^+$ | $NH_3$ fragment |
| 17 | $NH_3^+$ | $NH_3$ parent peak |
| 18 | $H_2O^+$ | $H_2O$ parent peak |
| 27 | $HCN^+/CHN^+$ | HCN parent peak/FAI fragment |
| 28 | $N_2^+$ | nitrogen |
| 31 | $CH_2OH^+$ | major fragment of ethanol |
| 43 | $CH_3CO^+$ | major fragment of ethyl acetate |
| 45 | $CH_3CHOH^+$ | major fragment of isopropyl alcohol |
| 54 | $HCN(H)CN^+$ | major fragment of sym-triazine |

**Table 4.3:** List of m/z values of molecules detected in mass spectrometry measurements during the evaporation of FAI.

the standard MS of impurities (Figure 4.11), some of the peaks of common FAI degradation products overlap with the signals from the impurities. For example, all of the impurities identified (isopropanol, ethyl acetate, ethanol, diethyl ether) have the signal at m/z = 27, which is also assigned to a major fragment peak of HCN. Given that the impurities begin to evaporate at a lower temperature than that of the sublimation and degradation of FAI, misattributing these signals to HCN would incorrectly suggest that FAI starts to degrade before even subliming. Therefore, to reconstruct the accurate chemical picture of what occurs during evaporation, it is essential to identify unique signatures for the impurities, FAI, and the FAI degradation products.

Given that under atmospheric pressure the boiling points of the impurities are generally lower than the sublimation temperature of FAI (Table 4.4), during thermal evaporation one would expect that the signals from the more volatile impurities should dominate at lower temperatures (T $<$ 140°C); while at higher

| Materials | Boiling/sublimation temperatures at normal atmospheric pressure (1 atm) (°C) |
|---|---|
| Ethyl acetate (EtOAc) | 77.1 |
| Ethanol (EtOH) | 78.4 |
| Isopropanol (IPA) | 82.6 |
| Diethyl Ether | 46.7 |
| Formamidinium iodide (FAI) (sublimate/decompose) | ~220 |

**Table 4.4:** List of boiling/sublimation temperatures of materials at normal atmospheric pressure (1 atm). Sourced from NIST Standard Reference Database[128]

temperatures (150°C < T < 180°C) stronger signals signals from the FAI and its degradation products start appear. Preheating precursors is a commonly used purification strategy for thermal vapour deposition. In literature, this process generally only lasts 10 min at 100°C until the chamber pressure stops increasing. Here, the chamber pressure still increases after preheating as-received FAI at 100°C for 10 min. Therefore, I preheat as-received FAI at elevated temperature for longer time until the chamber pressure stops increasing and therefore set the preheating condition at 130°C for 30 min. For comparison, the preheated as-received FAI is cooled down to the room temperature and directly heated up again to the desired substrate rate 1.15 Å/s which is the standard rate of FAI for the $FAPbI_3$ co-evaporation. Figure 4.12 shows the resulting m/z vs. time contour plot. During the preheating, it shows stronger signals from ethyl acetate (m/z = 43), ethanol (m/z = 31, 45), and isopropanol (m/z = 45) than during the subsequent evaporation stage. This confirms that m/z signals at 31, 43, and 45 are primarily due to impurities (ethanol, ethyl acetate, isopropanol). When reheating the FAI to the temperature (T = 177°C), at which it reaches to the desired substrate rate of FAI for the $FAPbI_3$ co-evaporation, a new signal from m/z = 54 begins to appear. Unlike the ambiguous signal at m/z = 27, which may originate from either impurities or HCN, since none of the impurities have the signal at m/z = 54, it can only be attributed to

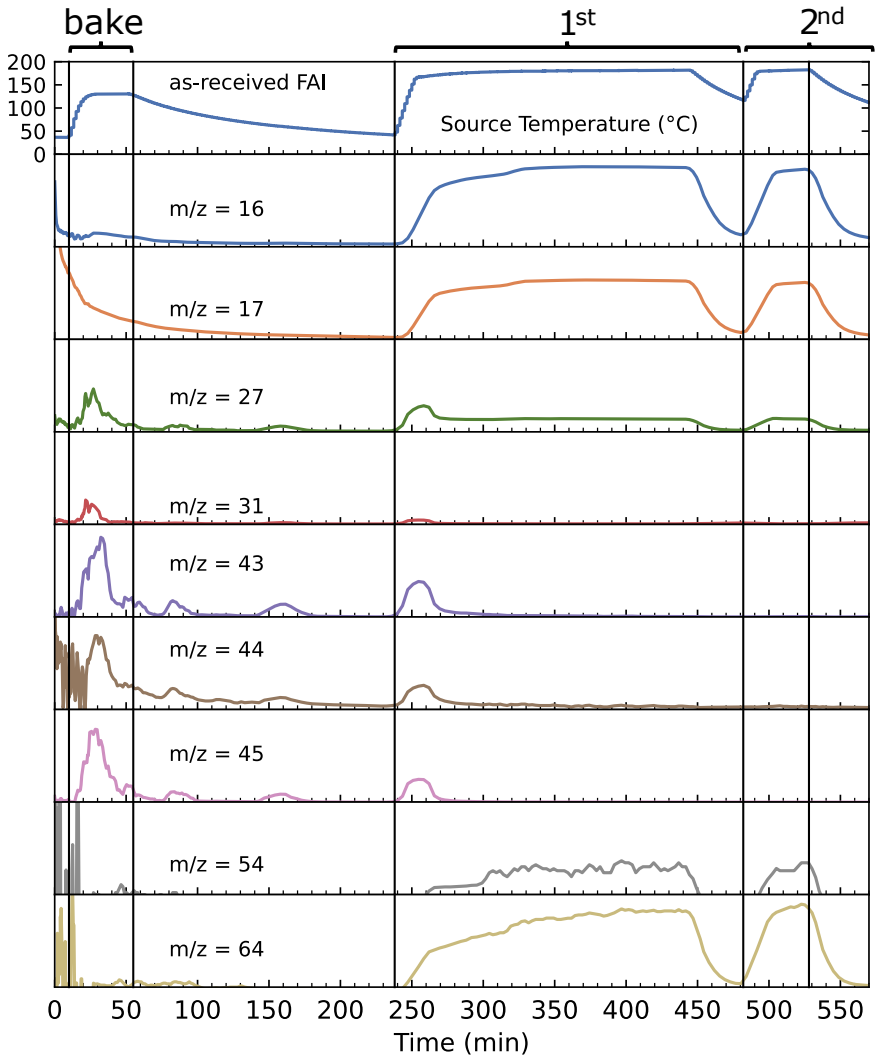


**Figure 4.12:** Mass spectra tracking of as-received FAI during low-temperature preheating (around 130°C, 30 min), the $1^{st}$ deposition (around 177°C, 180 min), and the $2^{nd}$ deposition (>180°C, 30 min) recorded with the Faraday detector of the residual gas analysis (RGA) system.

the major fragment of sym-triazine. While another degradation product, ammonia, has a distinct signal at m/z = 17, it is formed in both reversible and 'effectively irreversible' degradation pathways. Therefore, the MS signal at m/z = 54 indicates the point at which FAI begins to decompose into sym-triazine and ammonia.

Interestingly, when I reheat the FAI to its sublimation temperature (T = 177°C) after preheating the source at 130°C for 30 min, the MS impurity signals (m/z =

31, 43, 45) still quickly increase at the beginning of evaporation and only disappear after 30 min (Figure 4.12). This suggests that preheating at 130°C for 30 min is still not enough to completely remove the impurities (ethanol, ethyl acetate, isopropanol) from as-received FAI. Instead, to fully purify as-received FAI (no MS signals from impurities during the evaporation, Figure 4.12), the source needs to be preheated up to 177°C for 30 min.

Specific signatures for each of the impurities, FAI, and all its major degradation products have been established. The peak located at m/z = 54 (corresponding to sym-triazine) can be used to indicate the irreversible FAI degradation, and hence analyse differences in the sublimation behaviour of as-received and recrystallised FAI (high-purity FAI from supplier B is used as a standard reference).

Figure 4.10b shows the mass spectrograms of as-received and recrystallised FAI from supplier A, along with the spectrogram of high-purity FAI from supplier B. To compare different groups, in all cases, the same amount of FAI (approximately 1g) is added before the evaporation and the average substrate rate is controlled at 1.15 Å/s during the evaporation. As compared to recrystallised and high-purity FAI, in the case of the as-received FAI, I observe much stronger sym-triazine and ammonia signals in the early stages of evaporation (Figure 4.10). Additionally, as-received FAI shows a much weaker formamidine signal as compared to its higher purity counterparts (Figures 4.13, 4.14 and 4.15). This indicates that as-received FAI, which contains more impurities, experiences more severe 'effectively irreversible' degradation during the evaporation process compared to its high-purity counterparts (recrystallised and high-purity FAI). To assess whether the more severe degradation observed during the evaporation of as-received FAI

arises from decomposition of the FAI powder in the crucible, I analyse the residual high-purity FAI, recrystallised FAI, and as-received FAI powders after evaporation, (Figures 4.13, 4.14 and 4.15). Figure 4.16 confirms the absence of impurities or degradation products in all three residual precursors. These results indicate that the more severe degradation observed during evaporation of as-received FAI cannot be attributed to decomposition of the FAI powder in the crucible.

To determine whether the degradation products shown in MS also exist in the final films, the as-deposited perovskite films (prior to annealing) are characterised using NMR (Figure 4.17). For the films fabricated using as-received and recrystallised FAI, no presence of any impurities or FAI degradation products is detected, suggesting that these are not incorporated into the final films or their concentration is below the NMR detection threshold. Previous studies have suggested that the degradation products of FAI (hydrogen cyanide, sym-triazine, ammonia) are too volatile to adsorb on the substrates or produce any rate reading on the quartz crystal microbalance (QCM) during the thermal evaporation.[117] Therefore, the possible incorporation of trace sym-triazine in the ctrl films can be excluded. To figure out whether trace impurities are present in the ctrl films, the mass spectra signals during the evaporation process for as-received, recrystallised and high-purity FAI are compared (Figures 4.13, 4.14 and 4.15). Interestingly, for as-received FAI, the time point at which both the source and substrate rates begin to increase, coinciding with the initial rise in the main MS signals of EtOH (m/z = 31), EA (m/z = 43), and IPA (m/z = 45) (Figure 4.13). When the source and substrate rates reach their maximum values, the MS signals for EtOH (m/z = 31), EA (m/z = 43), and IPA (m/z = 45) are also at their peak intensity. These results demonstrate that the evaporation of impurities (EtOH, EA, and IPA) in as-received FAI produces

QCM rate readings at both the source and substrate levels. In contrast, with both recrystallised and high-purity FAI, the source and substrate rates only increase when FAI begins to evaporate (Figures 4.14 and 4.15). Consequently, the presence of trace organic impurities in as-received FAI leads to a misinterpretation of the deposition rates, as the deposition rate includes contributions from both FAI and the impurities. As a result, the composition of co-evaporated films deviates significantly from the target stoichiometry, preventing films from fully converting into the desired photoactive phase. This issue will persist until the complete removal of the impurities, which is likely to require multiple deposition runs.

## 4.4 Summary and Outlook

In conclusion, the study in this chapter has identified the chemical nature of impurities present in a commonly used commercial FAI source, and elucidated the varied effects of these impurities in both solution- and vapour-processing of metal halide perovskite thin films and devices. While ethyl acetate, as one of the impurities, can be beneficial for the quality of solution-processed perovskite films by modulating crystallisation dynamics and passivating defects, for vapour-processing, the impurities lead to decomposition of the precursor and off-stoichiometry in the final film. Off-stoichiometry is linked to the formation of non-photoactive phases, which negatively affect the optoelectronic properties of perovskite thin films. This results in both reduced film stability and decreased solar cell performance. These findings demonstrate that purification and removal of these impurities via recrystallisation is an effective mitigation strategy to achieve high-quality, reproducible and stable perovskite films and devices.

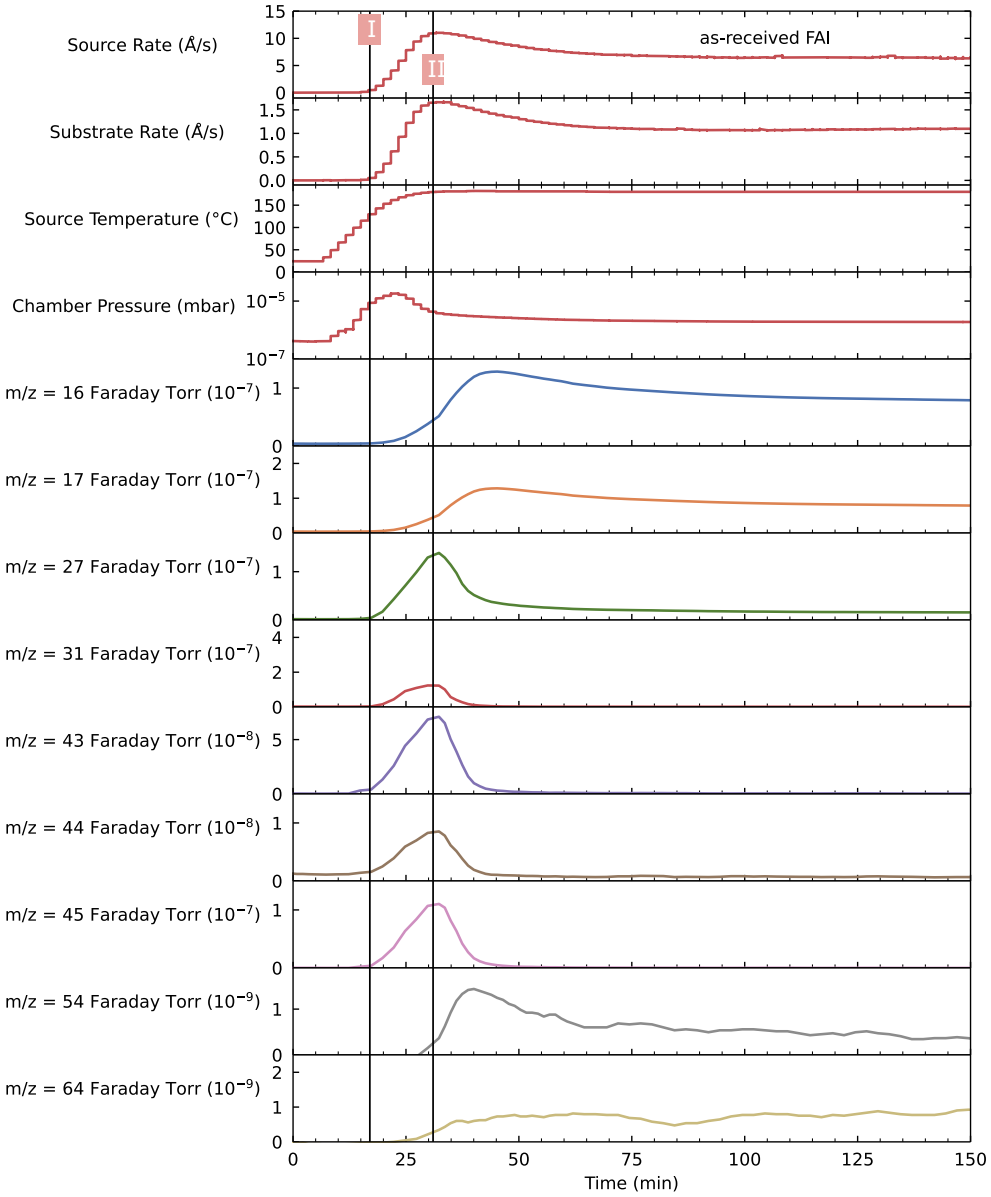


**Figure 4.13:** Evaporation parameters and mass spectra tracking of as-received FAI during the vapour deposition. Line I represents the time point at which both the source and substrate rates begin to increase, coinciding with the initial rise in the main MS signals of EtOH (m/z = 31), EA (m/z = 43), and IPA (m/z = 45). Line II labels the time point at which both the source and substrate rates reach their maximum values, aligning with the peak intensities of the MS signals for EtOH (m/z = 31), EA (m/z = 43), and IPA (m/z = 45). These results demonstrate that the evaporation of impurities (EtOH, EA, and IPA) in as-received FAI can affect the readings of the source and substrate sensors.

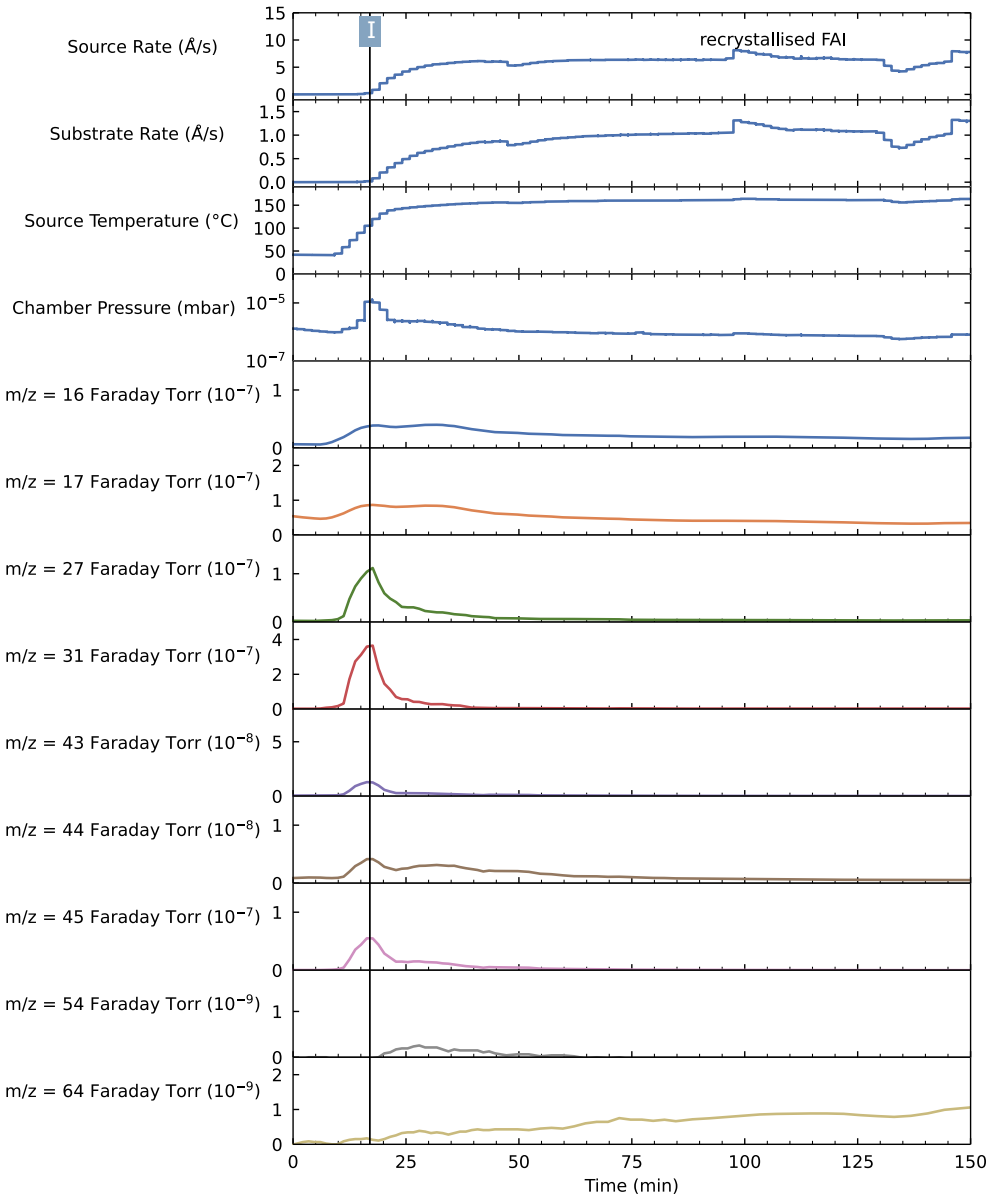


**Figure 4.14:** Evaporation parameters and mass spectra tracking of recrystallised FAI during the vapour deposition. Line I represents the time point at which both the source and substrate rates begin to increase, coinciding with the time point at which both the chamber pressure and the main MS signal of diethyl ether (m/z = 27, 31, 45) reach their maximum values. This suggests that the evaporation of diethyl ether does not contribute to the increase of the source rate and substrate rate. Instead, it leads to a rise in chamber pressure, which is consistent with the high vapour pressure of diethyl ether resulting from its low boiling point (Table 4.4).

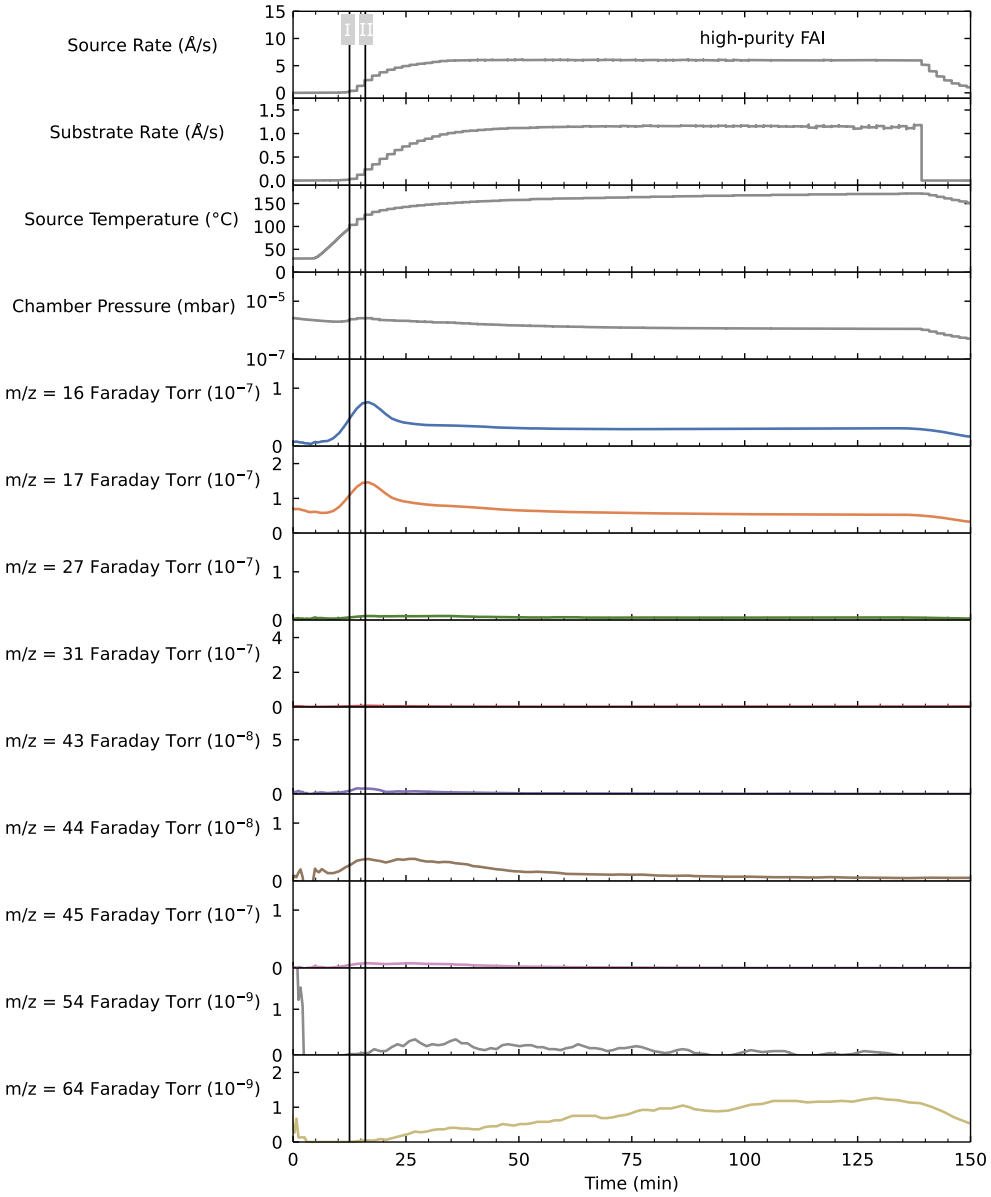


**Figure 4.15:** Evaporation parameters and mass spectra tracking of high-purity FAI during the vapour deposition. Line I represents the time point at which both the source and substrate rates begin to increase, coinciding with the initial rise in the main MS signals of FAI (m/z = 44). Line II labels the time point at which the chamber pressure reaches its maximum, aligning with the peak intensities of the MS signals for FAI (m/z = 44). These results suggest that for high-purity FAI, the evaporation of FAI primarily influences the sensor rates and the chamber pressure.

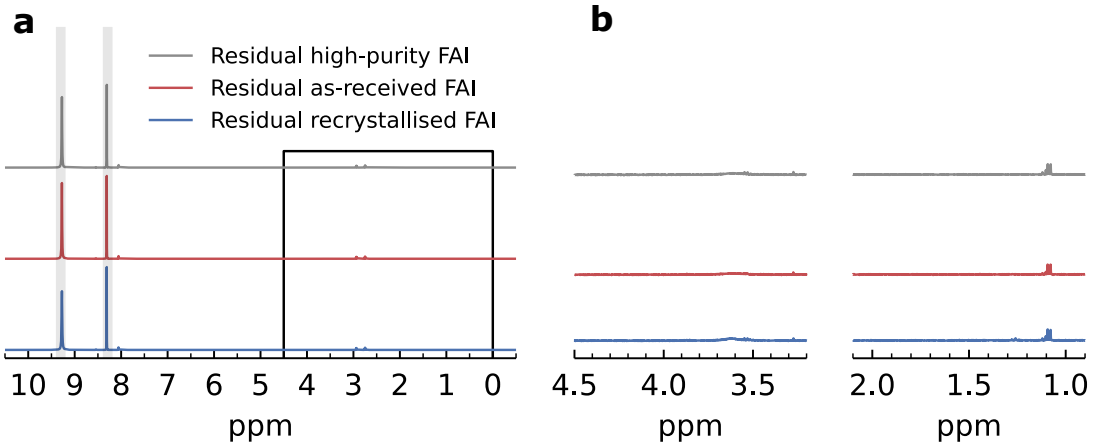


**Figure 4.16:** Liquid-state $^{1}$H NMR characterisation results of residual high-purity FAI, recrystallized FAI and as-received FAI powder after the evaporation (Figures 4.13-4.15), dissolved in DMSO-d6. In as-received FAI, signals from ethyl acetate, ethanol and isopropanol are not observed anymore.

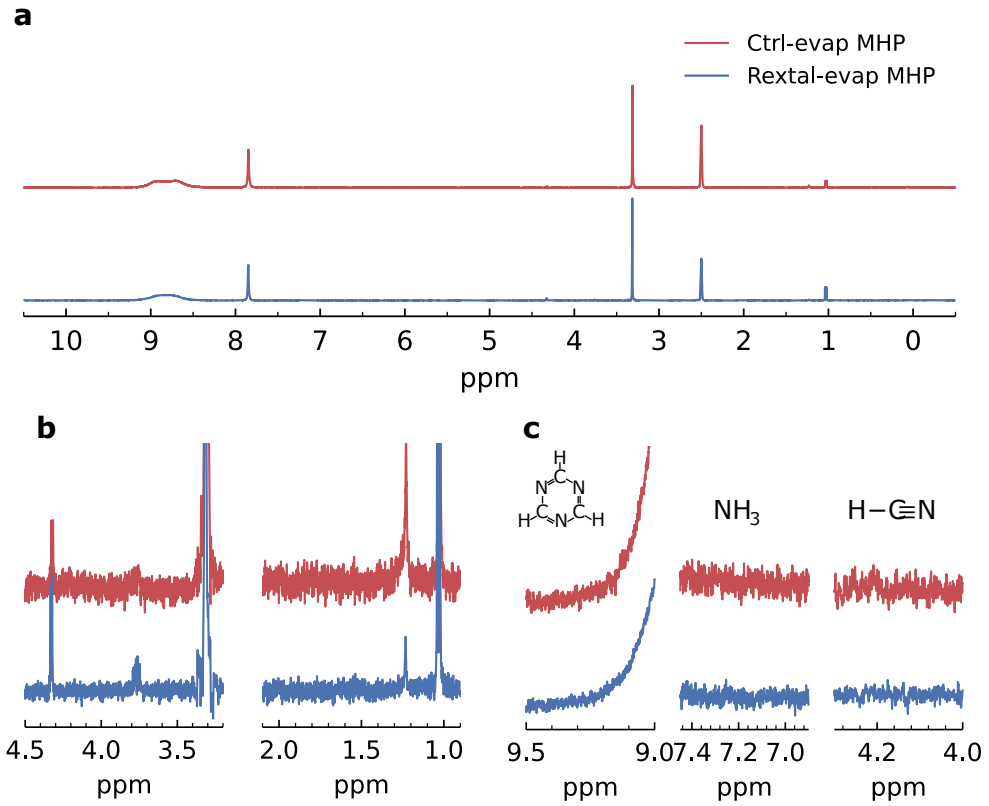


**Figure 4.17:** (a) Liquid-state $^{1}$H NMR characterization results of as-deposited vapour-deposited $FAPbI_3$ films fabricated using as-received (ctrl) and recrystallised (rextal) FAI redissolved in DMSO-d6. Signals from FAI impurities (b) or degradation products (c) are not observed in both cases.

# 5

# A Templating Approach to Controlling the Growth of Coevaporated Halide Perovskites

## Contents



The work presented in this chapter has been published in:


**Yan, S.**, Patel, J. B., Lee, J. E., Elmestekawy, K. A., Ratnasingham, S. R., Yuan, Q., Herz, L. M., Noel, N. K., Johnston, M. B., "*A Templating Approach to Controlling the Growth of Coevaporated Halide Perovskites*", *ACS Energy Letters*, **2023**, *8*(10), 4008–4015.[83]

Siyu Yan fabricated the samples, designed and conducted the experiments, and analysed the data. Jay B. Patel performed the Urbach energy measurements and assisted with the scanning electron microscopy measurements. Jae Eun Lee carried out the OPTP measurements and data analysis, and assisted with the optoelectronic measurements. Karim A. Elmestekawy performed the GIWAXS measurements. Nakita K. Noel and Michael B. Johnston supervised Siyu Yan, who prepared the first draft of the manuscript with input from all co-authors.

## 5.1 Broad Context

While fabrication of perovskite thin-films can be achieved through a variety of different techniques, thermal vapour deposition is particularly promising, allowing for high-throughput fabrication and large-scale production. However, the ability to control the nucleation and growth of these materials, particularly at the bottom charge-transport layer (CTL) /co-evaporated perovskite interface, is critical to unlocking the full potential of vapour-deposited perovskite PV. The cause of the significant impact of the bottom CTL/co-evaporated perovskite interface arises from the nature of the substrate exerting a substantial impact on the alteration of the entire perovskite film. Therefore, the selection of the CTL affects the morphology, crystal structure and optoelectronic properties of co-evaporated perovskite.

This places significant constraints on the pool of CTLs to seed better crystallization and film growth of co-evaporated perovskite. Moreover, such strong substrate dependency requires the individual optimisation of deposition parameters for each substrate, which substantially limits the economic feasibility of co-evaporation tech-

nique for large scale manufacturing. Hence, the ability to decouple the nucleation and growth of the co-evaporated perovskite films from the influence of substrate materials is of utmost importance. In this chapter, I design a templating layer as a means to reproducibly control the growth of co-evaporated perovskites on various CTLs. The templated perovskite films show not only improved device performance, but also offer more freedom in the selection of substrate materials.

## 5.2 Introduction

Metal halide perovskites (MHPs) have shown tremendous promise as absorber layers for the next-generation of photovoltaic (PV) devices, achieving certified power conversion efficiencies (PCEs) of up to 26.95% in single-junction devices and 36.85% in Si/perovskite tandem devices.[10] This impressive device performance stems from a combination of factors: the desirable optoelectronic properties of MHP materials, including high absorption coefficients, long charge-carrier diffusion lengths and balanced charge-carrier transport;[129–131] and concurrently, rapid improvements in fabrication approaches such as compositional engineering, tuning crystallisation kinetics, and interfacial engineering.[14,15,132,133] Another interesting optoelectronic property of lead HPs is their 'defect tolerance', which means that bulk defects are located close to the bands and do not form deep charge-carrier traps.[59,134] However, in a thin film, defect states often exist at the grain boundaries and interfaces where they can act as electronic traps, affecting charge-carrier transport in the films, hence hindering the performance of optoelectronic devices.[134–137] Given that surface defects are influenced by various factors such as

poor morphology and energy level misalignment, significant effort has been placed on these areas in order to improve optoelectronic device performance.[138–142]

To date, many of the key advances in MHP solar cell research have been made using solution-processed perovskite films. However, recent developments in dry vapour deposition methods have resulted in devices with >26% PCE in single-junction architectures.[39,90,143–147] Thermal vapour deposition allows for uniform, conformal coating of films and fine control of the thickness, affording significant opportunity to achieve high-throughput fabrication and large-scale production.[116,148,149] However, previous research has highlighted the paramount importance of having a high-quality charge transport layer (CTL)/perovskite interface in order to unlock the full potential of vapour-deposited perovskites.[63,150,151] Xu et al. have contended that a lead iodide ($PbI_2$) phase located near the bottom of the perovskite film, closest to the substrate, is unavoidably formed on all substrates during the initial deposition process-even under a methylammonium iodide (MAI)-rich environment - since the sticking coefficient (defined as the ratio of atoms adsorbed to all atoms incident upon the surface) of MAI is small compared to that of $PbI_2$.[152] However, as opposed to the sole formation of $PbI_2$, it is quite likely that a mixture of precursor materials/phases is present in this bottom region. Meanwhile, Patel et al. have uncovered that compared to phenyl-C61-butyric acid methyl ester (PCBM), co-evaporated devices using compact titanium dioxide (c-$TiO_2$) as the bottom electron transport layer (ETL) experience more severe hysteresis. This clearly indicates the extent to which the nature of the substrate impacts the quality of the perovskite at the bottom interface.[153] It is apparent that growing co-evaporated films on inorganic substrates is not trivial, and therefore, in most cases, perovskite films are co-evaporated onto organic layers on order to seed

better crystal growth.[63,90,116,144,146,150] This may be one of the factors hindering the further performance improvement of co-evaporated perovskite PV devices, considering that most high-performing single-junction devices utilize tin oxide ($SnO_2$) as the ETL (at the time of publication).[143] As previously mentioned, one possible explanation for this observation is that the initial stages of the perovskite growth may lead to the deposition of a layer of material which deviates from the target stoichiometry. Meanwhile, in-situ photoelectron spectroscopy studies have shown that the electronic properties of the initial 2-3 nm of the perovskite are strongly affected by the nature of the substrate, giving rise to band bending and additional defect states.[154] Subsequent investigations have revealed that the surface of the substrate material exerts a substantial impact beyond the bottom CTL/perovskite interface, leading to alterations in the morphology of the entire film.[155–157] Consequently, achieving uniform deposition of alkylammonium halides, and appropriate crystallisation of the perovskite material are a critical requirement when selecting an appropriate CTL. Unfortunately, for vapour-deposited perovskites, this places significant constraints on the pool of viable CTLs. However, it should be noted that even when suitable substrates that meet the criteria above are identified, optimising the evaporation parameters for deposition on various substrates remains a laborious task. Furthermore, this issue limits the economic feasibility of industrial applications, as the most attractive scale-up technique is to produce all device layers on the same vacuum fabrication lines.[158] Therefore, the ability to decouple the nucleation and growth of co-evaporated perovskite films from the influence of substrate materials is of utmost importance.

This work introduces an effective strategy to reproducibly control the growth of co-evaporated perovskites by using a templating layer. The results show that

independent of the substrate choice for perovskite growth, the co-evaporated perovskite films with the templating layer exhibit identical morphology, structure, and optoelectronic properties. A series of spectroscopic experiments present evidence that the optoelectronic properties of the perovskite remain unchanged after the insertion of this templating layer. When these templated perovskite films are incorporated into devices, improved device performance is observed as a result of reduced interfacial resistance, (as indicated through increased short-circuit current ($J_{sc}$) and fill factor ($FF$)). This improvement can be attributed to accurate interface control allowing for fine-tuning the stoichiometry of the initial perovskite deposited onto the substrate. Furthermore, the use of templating layers allows for the fabrication of high-performance devices on both organic and inorganic CTLs in the same batch, which shows the universality of using templating layers in different device architectures. Overall, this templating strategy offers co-evaporated perovskites more freedom in the selection of substrate materials and provides a way to exert fine control over the bottom interface in perovskite optoelectronic devices.

## 5.3 Results and Discussion

### 5.3.1 Selection of Templating Layers

In this study, perovskite films with the composition $FA_{0.9}Cs_{0.1}PbI_{3-x}Cl_x$ is fabricated using the four-source, co-evaporation of formamidinium iodide (FAI), CsI, $PbI_2$ and $PbCl_2$ under high vacuum. the initial co-evaporation process is monitored by introducing one additional shuttered quartz crystal microbalance (QCM) in close proximity to the substrate position. Having a shuttered QCM allows us to

record substrate rates at different points throughout the process. Therefore, by simultaneously opening the QCM and substrate shutters, the rates are recorded only after starting deposition on the substrate. The findings show that it takes some time for the rate to stabilise on a bare shuttered QCM during the initial stages of the evaporation. This stabilisation time increases when the shuttered QCMs are pre-coated with CTLs (Figures 5.1a and 5.1b). This finding confirms that depending on the type of substrate used, a number of different initial crystal growth processes can affect the incorporation of subsequent precursors and the continuity of crystal growth. This then inevitably influences how effective charge transport through the perovskite film is, and finally has a significant impact on device performance.[155] One concern arising from this observation is the difficulty in individually assessing the quality of the bottom interface since the bulk perovskite is also unavoidably changed when different substrates are employed.

A potential solution to this problem is to utilise a templating layer which can regulate the crystallisation and growth of perovskite films, such that the influence of the underlying substrate is obviated. Alkylammonium halides readily adsorb onto the surface of metal halides to form perovskites,[63] while evaporating metal halides onto various substrates is reproducible owing to excellent adhesion. For the sequential, two-step deposition technique, the inorganic layer ($PbI_2$) is deposited onto the substrate followed by either the solution or vapour-based deposition of the organic layer, after which the film is annealed.[159] Although this process may suffer from issues arising from the diffusion of the organic layer,[148] it presents an interesting approach in terms of using $PbI_2$ as a templating layer. To examine this, $PbI_2$ is pre-coated onto the shuttered QCM and indeed find that this effectively reduces the time taken for the readings on the QCM to stabilise (Figure 5.1c).

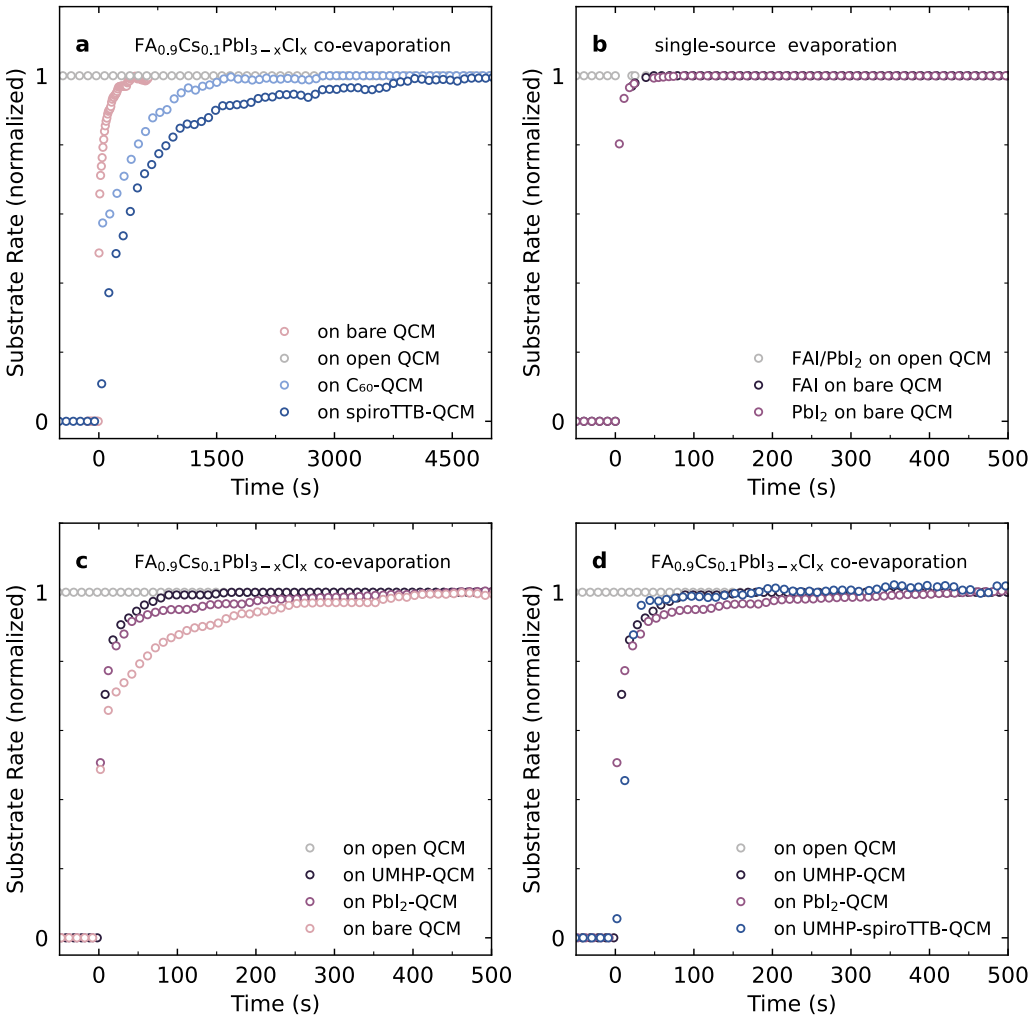


**Figure 5.1:** The substrate rate of initial co-evaporation process recorded by the QCMs. QCM shutter and substrate shutter are opened simultaneously at Time = 0s. (a) The initial process of $FA_{0.9}Cs_{0.1}PbI_{3-x}Cl_x$ co-evaporated on the open QCM, bare QCM (shuttered QCM without pre-coating), C60 pre-coated shuttered QCM and spiroTTB pre-coated shuttered QCM. (b) The initial process of FAI and $PbI_2$ single source deposited on the open QCM and bare shuttered QCM. (c) The initial process of $FA_{0.9}Cs_{0.1}PbI_{3-x}Cl_x$ co-evaporated on the open QCM, ultra-thin MHP pre-coated shuttered QCM, $PbI_2$ pre-coated shuttered QCM and bare shuttered QCM. (d) The initial process of $FA_{0.9}Cs_{0.1}PbI_{3-x}Cl_x$, ultra-thin MHP pre-coated shuttered QCM, $PbI_2$ pre-coated shuttered QCM and ultra-thin MHP-spiroTTB pre-coated shuttered QCM.

However, the presence of $PbI_2$ still might introduce non-stoichiometric perovskite near the bottom interface.

To overcome these issues, I develop a novel approach of depositing a templating layer consisting of a stoichiometric ultra-thin (estimated 15 nm) MHP via a vapour-based, two-step sequential deposition approach. Specifically, using thermal vapour deposition, I co-evaporate the inorganic precursors ($PbI_2$, CsI, and $PbCl_2$) to a total thickness of 9 nm, and then deposit a 9-nm film of FAI on top. Then this film is annealed at 135°C for 2 minutes in pure $N_2$ gas at atmospheric pressure to form the ultrathin-MHP templating layer. This templating layer then acts as a seed for the growth of fully co-evapoated MHP layers.

Figure 5.1d shows that pre-coating the shuttered QCM with this templating layer results in the shortest stabilisation time of the rate. To verify that the use of this templating is able to totally circumvent the compositional variations found during the initial phases of growth on un-templated substrates, it is also deposited on a 2,2',7,7'-tetra(N,N-di-p-tolyl)amino-9,9-spirobifluorene (spiroTTB) pre-coated shuttered QCM. Here, the rate stabilises almost immediately, pointing towards a significantly reduced likelihood of compositional variation at the CTL/perovskite interface. As such, I proceed to investigate the effect of this templating layer on the properties of co-evaporated perovskite films.

### 5.3.2 Morphology Characterisation

To probe the universality of our templating approach, I select 5 different CTLs which are often used in high performance PSCs: spiroTTB, nickel oxide (NiOx), tin

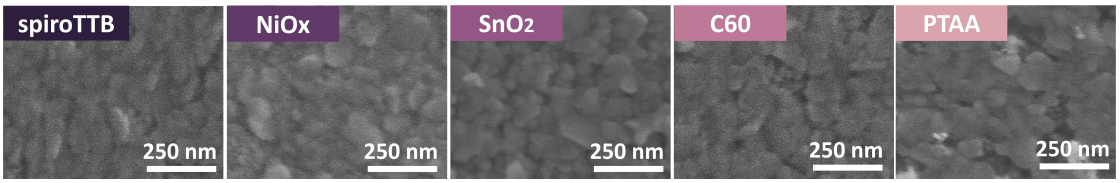


**Figure 5.2:** Top-view scanning electron microscopy images of the ultra-thin templating layers deposited on spiroTTB, NiOx, $SnO_2$, C60 and PTAA, respectively.

oxide ($SnO_2$), C60 and poly[bis(4-phenyl)(2,4,6-trimethylphenyl)amine] (PTAA). The perovskite films are then simultaneously co-evaporated onto all these substrates with or without a templating layer, named as "templated" or "control" films, respectively.

After the templating layers are deposited, the initial characterization results show that these templating layers have consistent morphology on different CTLs (Figure 5.2). Then, the influence of the templating layer on the morphology of perovskite films is investigated using scanning electron microscopy (SEM) and present the data in Figure 5.3. Top-view SEM images show that both control (Figures 5.3a-e) templated (Figures 5.3k-o) films form uniform, homogenous films. Figures 5.3a-e show that control films deposited on the various substrates have significant morphological changes. This is particularly evident on the inorganic substrates, in this case, $NiO_x$ and $SnO_2$. Conversely, the morphology of templated films (Figures 5.3k-o) is very similar in all cases, suggesting that the crystallisation dynamics are now independent of the substrate material. Cross-sectional SEM images, consistent with top-view SEM images, show significant differences in the vertical ordering of apparent grains (Figures 5.3f-j). Specifically, on spiroTTB and $SnO_2$, control films appear to have columnar growth, whereas on $NiO_x$ and PTAA, films appear to consist of small, randomly sized grains with noticeable gaps. On C60, control films are also comprised of smaller crystallites of random orientations.

**Figure 5.3:** Morphological characterisation of $FA_{0.9}Cs_{0.1}PbI_{3-x}Cl_x$ perovskite films deposited with and without an ultra-thin MHP layer, labelled UT and Ctrl respectively. Top-view scanning electron microscopy (SEM) images of Ctrl (a to e) and UT (k to o) films on spiroTTB, NiOx, $SnO_2$, C60 and PTAA, respectively. (See SI for lower magnification top-view SEM images). Cross-sectional SEM images of Ctrl (f to j) and UT (p to t) films on spiroTTB, $NiO_x$, $SnO_2$, C60 and PTAA. The cross-section profile of Ctrl (u and v) and UT (w and x) films on the textured Si. SEM measurements performed by Jay B. Patel and Siyu Yan.

Interestingly, when films are grown on the templating layer, in all cases the crystals appear to have formed more columnar structures with fewer voids and visible boundaries (Figures 5.3p-t). This suggests more continuous grain growth and thus, the formation of higher quality perovskite thin films, specifically with regards to improved charge transport through the absorber. As previously mentioned, MHPs have been used as top cells in perovskite/Si tandems, achievinging the highest performance of any double-junction monolithic tandem solar cell. It is worth noting that the most efficient perovskite/Si tandems are constructed using textured Si as the bottom cell. Depositing conformal perovskite layers on such substrates via spin-coating is non-trivial and as such, devices of this sort are often fabricated using one of three types of two-step deposition methods: either entirely vapour-based, hybrid vapour/solution-based, or entirely solution-based.[160,161] With this in mind, I consider the feasibility of using this templating approach to control the deposition of co-evaporated perovskite films on textured Si. Here, control and templated films are deposited on Si substrates with pyramid heights of over 10 $\mu$m (Figures 5.3u-x). The results show that co-evaporation can readily produce conformal, pinhole-free films on top of the pyramidal structures. However, as with the substrates previously investigated, the cross-sectional profile of control films grown on the textured Si shows multiple crystallites stacked on top of each other in the other in the vertical direction, while templated films again form vertically continuous, columnar structures. These initial results show the likelihood of successfully transferring our templating approach to a variety of substrates.

### 5.3.3 Structure and Composition Characterisation

However, merely having similar morphology is insufficient to confirm the utility of the templating layer. I now proceed to probe the structure and composition of control and templated films. First, Table 5.1 presents the bandgap values of these films, extracted from the absorption onsets fitted using the Elliott model.[74] The absorption coefficient of a particular material should be consistent as it is an intrinsic property. However, if the absorption coefficients of perovskite on different substrates are varied, this might suggest the presence of non-perovskite components in these films. Surprisingly, the bandgap values of control films grown on different substrates vary within the range of 1.57-1.60 eV. It is worth noting that these films are deposited during the same deposition run, and as such, their bandgaps should be identical, making a 30 meV difference in bandgap significantly larger than one would expect. This lends credence to the hypothesis that variations in the composition of the first few nm of perovskite can indeed affect the stoichiometry of the bulk material.[154] Encouragingly however, with the inclusion of a templating layer the absorption coefficient and bandgap of the deposited films (1.59 eV) are consistent, regardless of the nature of the underlying substrate. This suggests that the templating layer can reproducibly control the crystallisation and composition of the perovskite.

Next, I explore the degree of crystallinity of these films, using X-ray diffraction (XRD). Figures 5.4a and 5.4b show the XRD patterns of control and templated films. Apart from the $PbI_2$ peaks and ITO peaks, all other peaks in control and templated films can be assigned to the cubic perovskite phase (Pm3m).[149] The intensities of the perovskite (200) peaks in templated films are 2 to 10 times

| | $E_g$ (eV) | | $E_B$ (meV) | | $\gamma$ (meV) | | Amp (a.u.) | |
|---|---|---|---|---|---|---|---|---|
| | Ctrl | UT | Ctrl | UT | Ctrl | UT | Ctrl | UT |
| On spiroTTB | 1.59 | 1.59 | 6.3 | 6.2 | 19.8 | 18.5 | 78.0 | 78.9 |
| On $NiO_x$ | 1.58 | 1.59 | 7.0 | 7.6 | 20.5 | 22.0 | 78.7 | 71.5 |
| On $SnO_2$ | 1.60 | 1.59 | 7.5 | 7.5 | 22.9 | 23.1 | 71.4 | 72.6 |
| On C60 | 1.57 | 1.59 | 7.1 | 7.8 | 21.4 | 21.7 | 78.8 | 70.5 |
| On PTAA | 1.57 | 1.59 | 5.2 | 8.2 | 19.5 | 23.3 | 76.6 | 70.4 |

**Table 5.1:** Parameters extracted from Elliott fits to the absorption onsets of Ctrl and UT films on different substrates. $E_g$ representing the optical bandgap, $E_B$ representing the exciton binding energy, $\gamma$ representing the electron-phonon coupling, and Amp representing the amplitude of the spectrum. Elliott fits performed by Jae Eun Lee.

higher than those in the control films (Table 5.2). The significantly higher peak intensity, as well as smaller full width half maximum (FWHM) in templated films suggests that perovskite films grown on this templating layer have a higher degree of crystallinity and are more highly oriented. To probe the crystal orientation, grazing incidence wide-angle X-ray scattering (GIWAXS) measurements are further conducted. Figure 5.4c shows diffuse rings, representing many weak reflections across the entire arc, indicative of a polycrystalline film with many randomly oriented crystallites. Conversely, Figure 5.4d clearly shows discrete spots in the diffraction pattern of templated films, indicating a higher level of orientation. This change in orientation is depicted schematically in Figures 5.4e and 5.4f, respectively. While these measurements are carried out on quartz substrates, the trend holds on relevant CTLs such as spiroTTB (Figure 5.5).

### 5.3.4 Optoelectronic Property Characterisation

Having established that when deposited on CTLs, the morphological and structural properties of control films are highly dependent on the nature of substrates, and

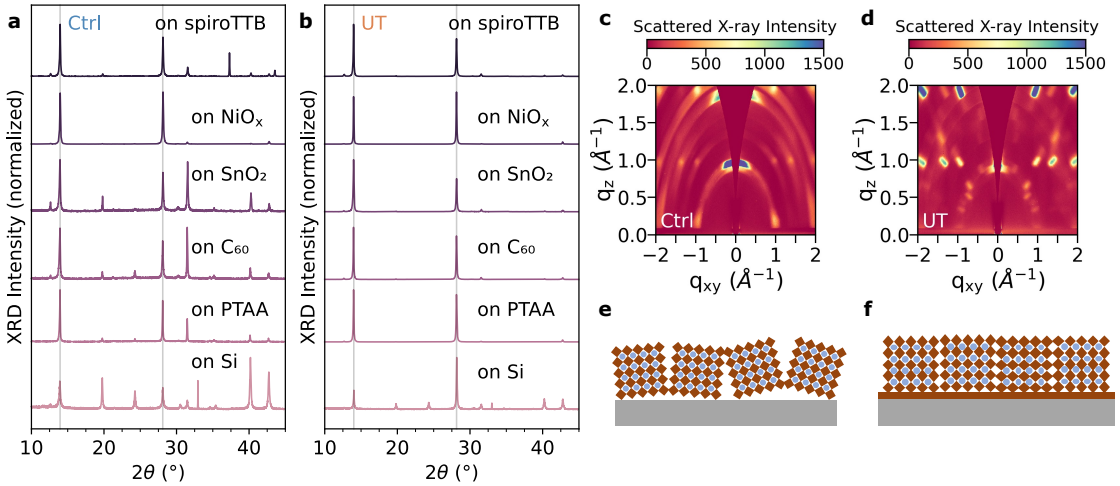


**Figure 5.4:** Structural characterisation of $FA_{0.9}Cs_{0.1}PbI_{3-x}Cl_x$ perovskite films deposited with and without an ultra-thin MHP layer, labelled UT and Ctrl respectively. X-ray diffraction (XRD) patterns of Ctrl (a) and UT (b) films on spiroTTB, $NiO_x$, $SnO_2$, C60, PTAA and textured Si. Grazing incidence wide-angle X-ray scattering (GIWAXS) results of Ctrl (c) and UT (d) films deposited on z-cut quartz. Simplified schematic representations of randomly oriented Ctrl films (e) and highly oriented UT films (f). GIWAXS measurements performed by Karim A. Elmestekawy.

| | Scattering X-ray intensity (arb. units) | | FWHM of (200) $2\theta$ peak (degree) | |
|---|---|---|---|---|
| | Ctrl | UT | Ctrl | UT |
| On spiroTTB | 4220.51 | 11987.63 | 0.1331 | 0.1227 |
| On $NiO_x$ | 17094.67 | 105002.70 | 0.1403 | 0.1061 |
| On $SnO_2$ | 879.00 | 8844.78 | 0.1397 | 0.1299 |
| On C60 | 922.35 | 18436.99 | 0.1409 | 0.1105 |
| On PTAA | 2524.18 | 48903.79 | 0.0954 | 0.1195 |
| On textured Si | 292.57 | 1491.93 | 0.2029 | 0.1345 |

**Table 5.2:** Intensity and full width half maximum (FWHM) of (200) peak of Ctrl and UT films on various substrates.

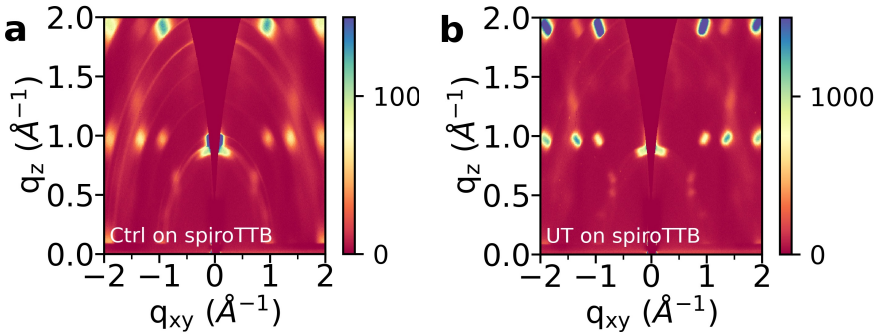


**Figure 5.5:** GIWAXS results of Ctrl and UT films spiroTTB (a and b), respectively. GIWAXS measurements performed by Karim A. Elmestekawy.

| | THz mobility ($cm^2$ $V^{-1}$ $s^{-1}$) | $k_2$ [$10^{-10}$] ($cm^3$ $s^{-1}$) |
|---|---|---|
| Ctrl | 46.56±2.15 | 1.41±0.01 |
| UT | 43.62±1.53 | 1.37±0.01 |

**Table 5.3:** Charge carrier mobility and second order recombination rate of Ctrl and UT films obtained from the OPTP measurement. Data analysis performed by Jae Eun Lee.

that the insertion of a templating layer circumvents these issues, I proceed to investigate the impact of this layer on the optoelectronic properties of the perovskite films. Figure 5.6a shows, in the absence of CTLs, a slightly increased absorption coefficient for templated films, while control and templated films have very similar absorption onsets at approximately 1.59 eV and have overlapping photoluminescence (PL) emission. Time-resolved terahertz photoconductivity spectroscopy is performed to assess the effect of the inclusion of a templating layer on the charge-carrier dynamics. Control and templated films are probed using the optical-pump tetraherz-probe (OPTP) technique (Figure 5.6b).[162,163] The bimolecular recombination constant $k_2$ was extracted from the fluence-dependence transient photoconductivity decays. Similar $k_2$ values indicate the almost unchanged electron-hole recombination in these two films. The corresponding charge-carrier mobilities (listed in Table 5.3) further show that the short-range mobilities are unaffected by the insertation of the templating layer. Then I probe control and templated films via time-resolved PL (Figure 5.6c and Table 5.4) to extract the trap-assisted recombination (monomolecular recombination) $k_1$,[80] and observe no significant difference between control ( 2.3 x$10^6$ $s^{-1}$) and templated ( 1.8 x$10^6$ $s^{-1}$) films.

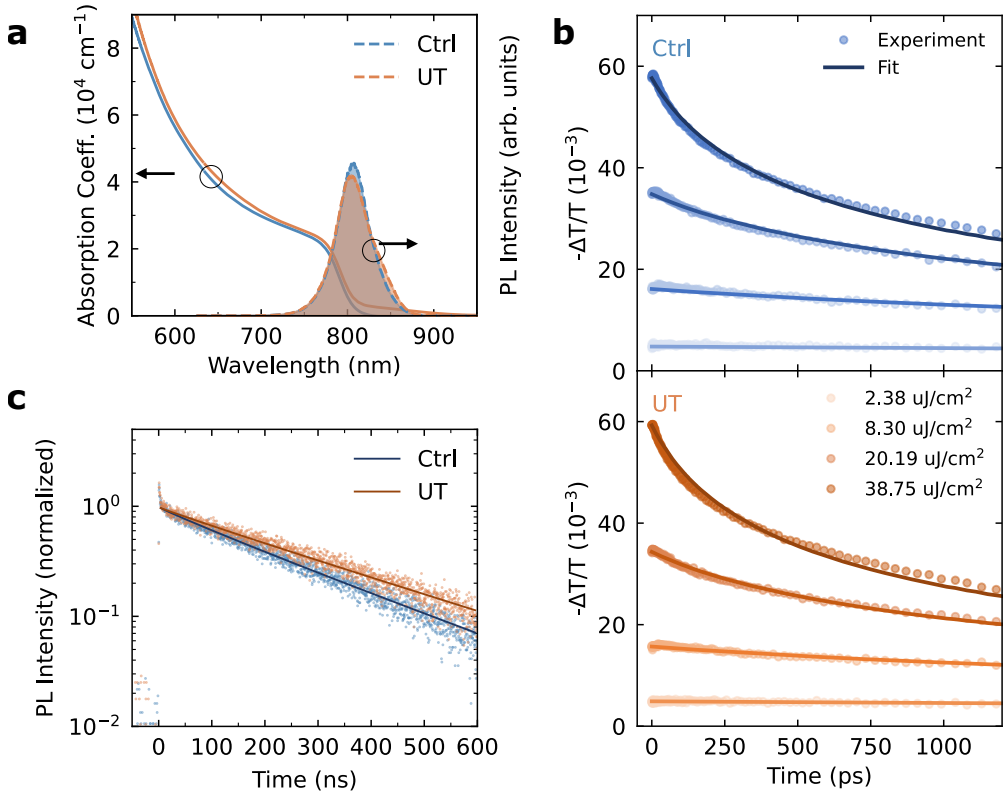


**Figure 5.6:** The optoelectronic properties of perovskite films. (a) Absorption coefficient and the unnormalized PL spectra (excited by the 470 nm laser) of Ctrl and UT films. (b) OPTP photoconductivity transients of Ctrl and UT films on quartz at various photoexcitation fluences. (c) PL dynamics of Ctrl and UT films on quartz (805 nm emission), at fluence 60 nJ/cm$^2$, fitted by stretched exponential without diffusion. The data is normalized to the value at 3 ns following the laser pulse allow for better visualisation. OPTP measurements performed by Jae Eun Lee.

| | $\tau_c$ (ns) | $\beta$ | $\tau_{avg}$ (ns) | $k_1$ [$10^6$] ($s^{-1}$) |
|---|---|---|---|---|
| Ctrl | 214.35 | 0.94 | 220.50 | $\approx 2.27$ |
| UT | 268.56 | 0.96 | 273.48 | $\approx 1.83$ |

**Table 5.4:** First-order non-radiative trap-mediated recombination parameters of Ctrl and UT films.

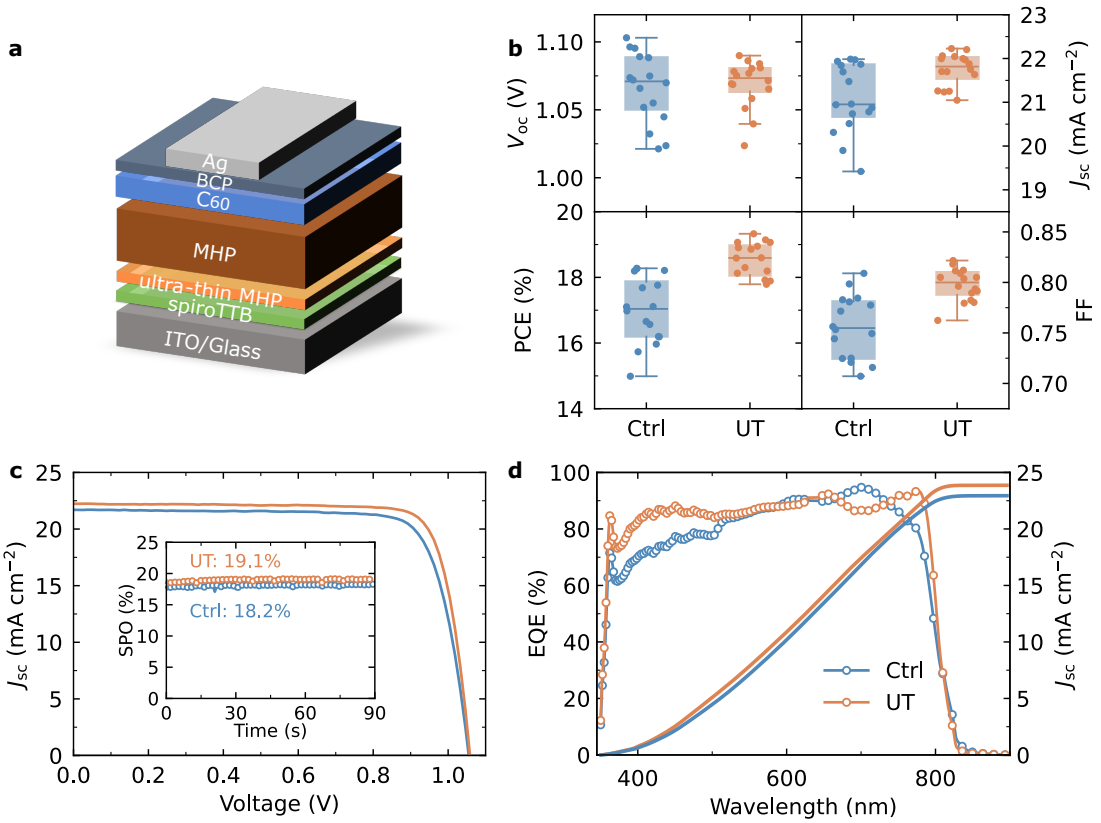


**Figure 5.7:** The improvement of device performance. The absorber layers are $FA_{0.9}Cs_{0.1}PbI_{3-x}Cl_x$ perovskite films with and without an ultra-thin MHP layer, labelled UT and Ctrl respectively. (a) Statistical results of Ctrl and UT device parameters. (b) *J-V* characteristics and corresponding SPO (inset) for the champion cell using the Ctrl and UT films. (c) EQE, and integrated $J_{sc}$ for the devices. The integrated $J_{sc}$ values for the Ctrl and UT devices are 22.2 and 23.9 mA cm$^{-2}$, respectively.

### 5.3.5 Device Performance

Our results thus far show that the templating layer gives us better control over the crystallisation and composition of vapour-deposited MHP films, while preserving their optoelectronic properties. To investigate the efficacy of this approach in solar cells, these films are incorporated into an all-vacuum-deposited, p-i-n device with the structure ITO/spiroTTB/control or templated MHP films/C60/Bathocuproine (BCP)/Ag (as shown in Figure 5.7a). After optimising the thickness of the perovskite layer to 630 nm (Figure 5.8), I show the best performing devices using

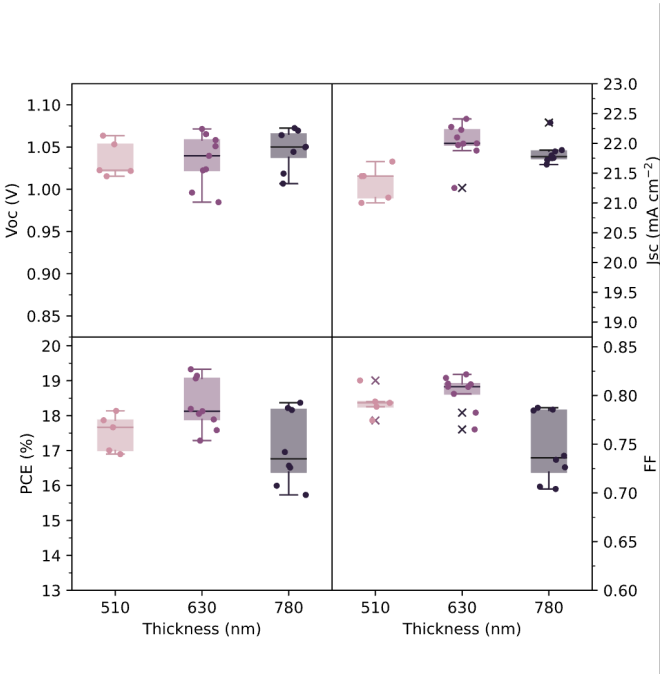


**Figure 5.8:** Statistical results of UT devices with the perovskite thickness of 510 nm, 630 nm, and 780 nm, respectively.

control and templated films devices in Figure 5.7b and 5.7c, and list the performance parameters in Table 5.5. The statistical results shown in Figure 5.7a are taken from a total 16 devices across 3 different batches, and show that devices made with the templating layer have a narrower distribution in performance than control devices, indicating better reproducibility. Interestingly, the insertion of the templating layer results in improved device performance, boosting the PCE from 18.3% (18.2% stabilized power output (SPO)) to 19.3% (19.1% SPO), as shown in Figure 5.7c. This improvement is a result of an increase in $J_{sc}$ and $FF$ in templated devices. The integrated $J_{sc}$ values obtained from the corresponding external quantum efficiency (EQE) (Figure 5.7d) are 22.2 mA cm$^{-2}$ and 23.9 mA cm$^{-2}$ for control and templated devices respectively, which are in close agreement with the measured values. Additionally, Table 5.5 illustrates the discrepency of average SPO between templated (18.3±0.1%) and control (16.9±0.3%) devices, confirming the efficiency enhancement in templated devices.

| Device | $J_{sc}$ (mA cm$^{-2}$) | $V_{oc}$ (V) | PCE (%) | FF | SPO (%) | Rsh (kΩ) | Rs (Ω) |
|---|---|---|---|---|---|---|---|
| Ctrl (champion) | 21.7 | 1.06 | 18.3 | 0.80 | 18.2 | 17.6 | 10.3 |
| Ctrl (average) | 21.1±0.2 | 1.07±0.02 | 17.0±0.3 | 0.76 ±0.04 | 16.9±0.3 | 9.1 ±3.1 | 11.2±1.3 |
| UT (champion) | 22.2 | 1.06 | 19.3 | 0.82 | 19.1 | 15.0 | 8.4 |
| UT (average) | 21.8±0.1 | 1.07±0.02 | 18.5 ±0.1 | 0.80±0.02 | 18.3±0.1 | 14.0±0.7 | 8.4±0.1 |

**Table 5.5:** Champion and average device performance parameters for solar cells fabricated from $FA_{0.9}Cs_{0.1}PbI_{3-x}Cl_x$ perovskite films with and without an ultra-thin MHP layer, labelled UT and Ctrl respectively. The values given in this table represent scans from open-circuit to short-circuit conditions.

The Urbach energy ($E_u$), which is a measure of the degree of electronic disorder in semiconductor films, can be obtained by fitting the tail of the EQE spectrum.[164,165] The results (Figure 5.9) show that the $E_u$ values are nominally the same (14.0±0.1 and 13.9±0.1 meV for control and templated films, respectively), implying similar electronic disorder in both films, in line with both the OPTP results and $V_{oc}$ values of control and templated devices. Given that the performance improvement is clearly not obtained through altering intrinsic materials properties, I re-examine the *J-V* curves to gather more information about the device stacks. Table 5.5 shows the average shunt resistance ($R_{sh}$) and series resistance ($R_s$). Compared with control devices, in templated devices, the average $R_s$ is reduced from 11.2±1.3 Ω to 8.4±0.1 Ω, and the average $R_{sh}$ increases from 9.1±3.1 kΩ to 14.0±0.8 kΩ. The reduced average $R_s$ for the templated devices may be ascribed to the absence of a $PbI_2$-rich layer at the bottom interface.[152] This would also explain the increase in $J_{sc}$ as the reduced resistance at the interface would allow for more efficient extraction of charges. In addition, as low $R_{sh}$ values are usually linked with pinholes and uneven perovskite films,[166,167] the improved $R_{sh}$ in templated devices may be attributed to the formation of higher-quality films comprised of columnar crystallites which have fewer boundaries in the direction of charge transport, and a more uniform distribution of the perovskite at the bottom interface.

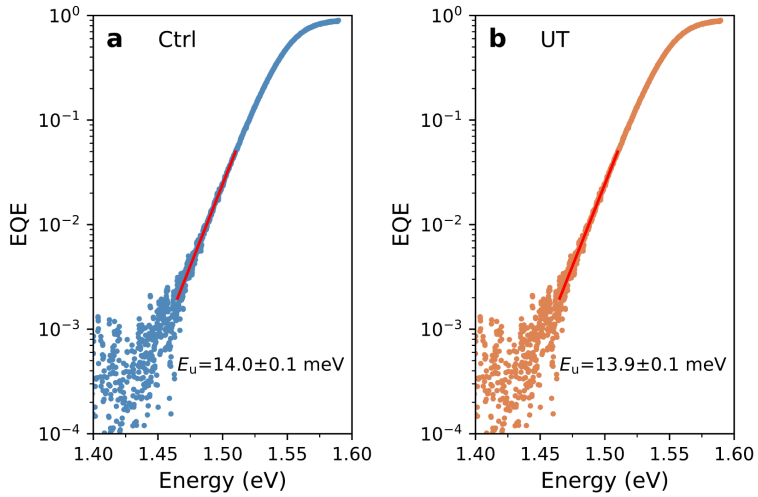


**Figure 5.9:** The Urbach energy extracted from the tail of EQE spectra of (a) Ctrl and (b) UT devices. Urbach energy measurements performed by Jay B. Patel.

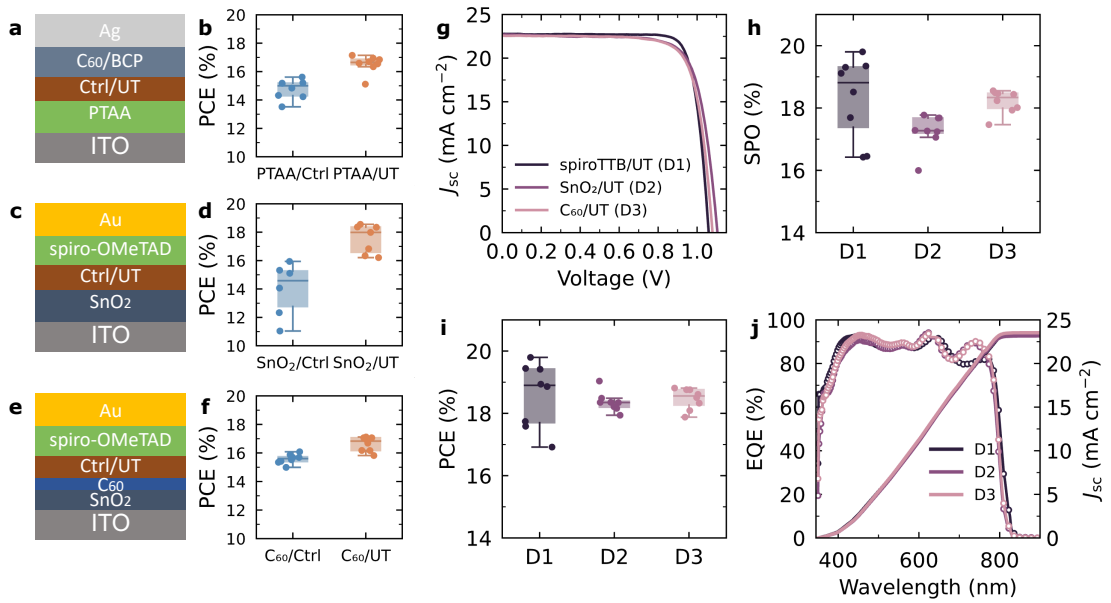


**Figure 5.10:** The impact of the ultra-thin MHP layer on different charge transport layers. The absorber layers are $FA_{0.9}Cs_{0.1}PbI_{3-x}Cl_x$ perovskite films with and without an ultra-thin MHP layer, labelled UT and Ctrl respectively. Schematics for the p-i-n device architecture (a) and n-i-p device architectures with $SnO_2$ (c) and C60 (e) n-type layers, with the corresponding statistical PCE results of Ctrl and UT devices (b, d, f). *J-V* characteristics (g), statistical SPO (h), statistical PCE (i), EQE, and integrated $J_{sc}$ (j) for the champion p-i-n and n-i-p UT devices made in the same batch.

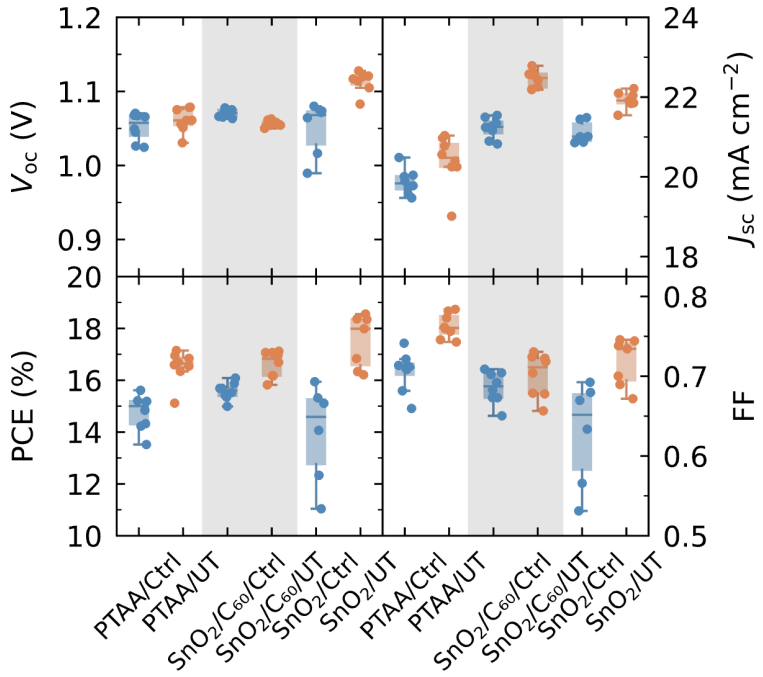


**Figure 5.11:** Statistical results of both p-i-n and n-i-p devices made by depositing Ctrl and UT films on organic (PTAA and C60) and inorganic ($SnO_2$) substrates.

Finally, I show that this templated growth approach is relevant for a wide range of solar-cell device architectures, not just p-i-n devices utilising spiroTTB. Control and templated films are deposited on organic (PTAA and C60) and inorganic ($SnO_2$) substrates to fabricate both p-i-n and n-i-p devices, as shown in Figures 5.10a-f. In all cases, device performance is markedly improved when the templating layer is inserted, due to the increased $J_{sc}$ and $FF$ in these devices (Figure 5.11). Furthermore, by growing the templated films on spiroTTB, $SnO_2$, and C60 substrates, p-i-n and n-i-p devices can be fabricated in one deposition run. This process was previously non-trivial as deposition conditions needed to be optimised for specific substrates. The $J$-$V$ characteristics of champion spiroTTB/templated-MHP, $SnO_2$/templated-MHP and C60/templated-MHP devices shown in Figure 5.10g illustrate that the $J_{sc}$ values in these three-types of devices are comparable. The small difference in $V_{oc}$ can be explained by the

| Device | $J_{sc}$ (mA cm$^{-2}$) | $V_{oc}$ (V) | PCE (%) | FF | SPO (%) |
|---|---|---|---|---|---|
| spiroTTB/UT | 22.8 | 1.06 | 19.8 | 0.82 | 19.8 |
| $SnO_2$/UT | 22.7 | 1.10 | 19.0 | 0.76 | 17.8 |
| C60/UT | 22.6 | 1.08 | 18.8 | 0.77 | 18.6 |

**Table 5.6:** Champion p-i-n and n-i-p device performance parameters for solar cells fabricated from UT films measured under 1 sun simulated AM1.5G solar illumination. The values given in this table represent scans from open-circuit to short-circuit conditions.

slightly different energetic alignment between perovskite and various CTLs. Figures 5.10h-5.10i show the statistical SPO and PCE results. For the best-performing spiroTTB/templated-MHP, $SnO_2$/templated-MHP and C60/templated-MHP devices, the PCEs are 19.8% (19.8% SPO), 19.0% (17.8% SPO) and 18.8% (18.6% SPO), respectively (Table 5.6). The integrated $J_{sc}$ values obtained from the EQE data in Figure 5.10j are consistent with the *J-V* measurements. This finding confirms that the use of perovskite templating layers allows for the fabrication of high performance p-i-n and n-i-p devices in the same batch, as a result of providing an effective and reproducible route of improving the quality of the CTL/perovskite interface and exerting fine control over the composition and crystallisation dynamics of vapour-deposited perovskite films.

## 5.4 Summary and Outlook

In conclusion, this chapter has successfully established a method of controlling the buried interface in vapour-deposited perovskite films, and have decoupled the nucleation and growth of these films from the influence of substrate materials. By inserting a templating layer between the perovskite film and the substrate, highly oriented co-evaporated perovskite films can be formed with identical morphology,

structure, and optoelectronic properties on a variety of different materials. The inclusion of this templating layer results in improved solar-cell device performance, as a result of reduced interfacial resistance (increased $J_{sc}$ and $FF$). This improvement can be attributed to our ability to exert fine control of the composition of the initial perovskite deposited onto the substrate. These results provide an effective and reproducible method for controlling the buried charge transport layer/perovskite interface in vapour-deposited perovskite solar cells, further increasing the competitiveness of this deposition technique, moving the field closer to large-scale fabrication of a wide-range of efficient perovskite optoelectronic devices.

# 6

# The Surface Passivation of Co-evaporated Perovskite Thin Films for High-Performance Solar Cells

## Contents



Siyu Yan fabricated the samples, designed and conducted the experiments, and analysed the data.

## 6.1 Broad Context

Metal halide perovskites have emerged as highly promising photovoltaic materials due to their excellent optoelectronic properties, simple fabrication processes, and compatibility with low-cost, scalable manufacturing. However, their long-term performance is often limited by interfacial defects, which can promote non-radiative recombination and ion migration. The passivation of these defects is essential for improving both the efficiency and stability of vapour-deposited perovskite solar cells and enabling commercialisation of perovskite optotelectronic devices. The most widely used passivation agents are ammonium-based salts which can form a thin layer on the surface of the perovskite film, or transform the surface structure of 3D perovskite to a low-dimensional structure, hence passivating the perovskite surface. The resulting passivation layers, which are highly dependent on fabrication conditions, can exhibit different effects and, consequently, influence both energetic alignment and overall device stability in distinct ways. Meanwhile, recent advances in applying passivation approaches to vapour-deposited perovskite films and the ability to modulate the orientation of vapour-deposited passivation layers by controlling the deposition parameters offer new opportunities for efficiency and stability improvements of vapour-deposited perovskite solar cells.

In this work, various arylammonium halide molecules are explored as vapour-deposited passivation agents for co-evaporated perovskite films; with a specific focus on how measurement atmospheres, annealing treatments and fabrication parameters affect the film structure, passivation, and device performance. These findings provide valuable insights towards the development of advanced passivation strategies for next-generation perovskite devices.

## 6.2 Introduction

Metal halide perovskites (MHPs) have made significant strides in photovoltaic applications due to their excellent optoelectronic properties and rapid progresses in fabrication techniques.[14,54,99] Combined with their manufacturing advantages–such as low-cost source materials, simple fabrication processes and compatibility with roll-to-roll printing–perovskite solar cells (PSCs) have emerged as one of the most promising photovoltaic technologies.[168,169] However, before commercial deployment, a major challenge is to achieve and maintain high solar cell performance in the long term.[170] For perovskites, the rapid crystallisation process results in the formation of polycrystalline films, which inherently contain a non-negligible level of defects. While the most thermodynamically favoured defect species in perovskites are shallow defects which do not strongly localise charge carriers; structural defects at surfaces, interfaces and grain boundaries often act as non-radiative recombination centres and trap charge carriers. Additionally, the presence of shallow defects can cause ion migration and accumulation at the interface, resulting in photocurrent hysteresis, unfavourable band bending and even phase segregation.[59,134,171] As such, the passivation of these defects is crucial for achieving a concomitant increase in efficiency and long-term stability of PSCs. To date, tremendous efforts have been devoted to the development of passivation strategies, which have been proven to be the most effective approaches to improve the efficiency and durability of PSCs.[107,143,172,173]

In the context of PSCs, the most established passivation strategy is chemical passivation, which reduces charged defects by forming chemical bonds with

undercoordinated cations or anions.[174–176] Given that most defects inducing non-radiative recombination are located at surfaces, interfaces or grain boundaries, a vast number of defect passivation studies concentrate on surface passivation, or interface engineering.[177–180] Among the various passivation materials, ammonium salts–comprising alkylammonium, cycloammonium and arylammonium cations with halide anions–are the most widely used agents to passivate the perovskite film surface.[181–185] Ammonium cations can bind to the surface through A-site vacancies or hydrogen bonding, forming a thin molecular layer at the surface of the perovskite film which then passivates the interface. However, these ammonium cations can also transform the surface structure of 3D perovskite and form the low-dimensional perovskite structures under certain conditions. Teale et al. have demonstrated that the resulting passivation layer–whether an organic layer, a 2D perovskite or a mixed 2D/organic layer–would have different influences on the passivation mechanism, energetic alignment and overall device stability.[186] Notably, the type of passivation layer formed is highly dependent on fabrication conditions, including precursor concentration, temperature, solvent polarity, 3D perovskite composition, steric hindrance and the reactivity between 2D and 3D cations.[57,187–191]

While the formation energy and the structure of defects in perovskites can vary substantially based on growth conditions, recent studies have successfully adopted passivation approaches which were initially developed for solution-processed perovskite films and devices, to their vapour-deposited counterparts.[172,192–198] This advancement presents a promising opportunity to boost the efficiency and improve the stability of vapour-deposited PSCs. Meanwhile, Choi et al. have reported that a highly ordered butylammonium-based Ruddlesden-Popper (RP) phase perovskite layer in the out-of-plane direction can be obtained via vapour deposition.[197] By

controlling the deposition rate of the RP phase perovskite, they were able to directly modulate the orientation of the resulting RP perovskite layer. This suggests that one can modulate the structure of vapour-deposited passivation layers through precise control of fabrication parameters. Therefore, a systematic investigation into the effects of vapour-deposited passivation agents on vapour-deposited 3D perovskites is of great interest. Such a study could examine the underlying passivation mechanisms and explore how fabrication conditions–such as solvent use and annealing treatments applied to the passivation layer–might influence the formation and transformation of surface structures.

This work highlights that measurement atmosphere can significantly affect the observed optoelectronic properties, and that post-deposition annealing can drive surface structural transformations, thereby altering the passivation mechanisms. Comparisons between vapour-deposited and spin-coated passivation layers further reveal that the same organic molecule can exhibit different structural and functional properties depending on the deposition methods. These results offer valuable insights for the development future passivation approaches.

## 6.3 Results and Discussion

### 6.3.1 Evaluation of the Sublimation Behaviour of Candidate Passivation Agents

Here, 4 different arylammonium halides (Figure 6.1a), including 4-fluoro-phenylammonium iodide (FPAI), 4-fluorobenzyl-ammonium iodide (FBZAI), 4(trifluoromethyl)benzyl-ammonium iodide (TFMBAI), and 4-fluorophenethyl-ammonium

iodide (FPEAI) are selected to passivate the surface of the co-evaporated 3D perovskite for a variety of reasons; firstly, arylammonium salts are among the first spacers investigated for multilayer 2D perovskites as well as passivation molecules and have been extensively studied in solution processing, offering a myriad of valuable references for this study.[199–201] Secondly, the aromatic rings may be beneficial for charge transport by delocalising electrons through the conjugated system.[202] Additionally, it has been reported that fluorinated substituents on these aromatic rings can result in stronger bonding between the ligand and the perovskite, resulting in enhanced defect passivation and more durable perovskite solar cells.[189,203,204] Furthermore, the properties of the passivation surface can be modulated by tuning organic spacers with different bond lengths and bond angles,[205,206] for example, the corresponding 2D perovskite structure with different distances between two inorganic sheets, various stacking interactions of aromatic rings if they form 2D/3D heterostructures, or change the work function of the surface if they play the role as passivation molecules (Figure 6.1b).

Previous studies have shown that despite the apparent simplicity of thermal evaporation, the details of the precursor evaporation and film formation are rather complex.[211] In particular, the deposition of organic molecules proves difficult to control and reproduce. The main challenge is that the non-directional evaporation of organic precursors results in the diffusion of materials into the entirety of the evaporation chamber; significantly different from inorganic precursors which have long mean free paths due to their directional evaporation process under high vacuum.[63] Additionally, the substrate-dependent adsorption behaviour of organic molecules further complicates the process. As a result, their evaporation may lead

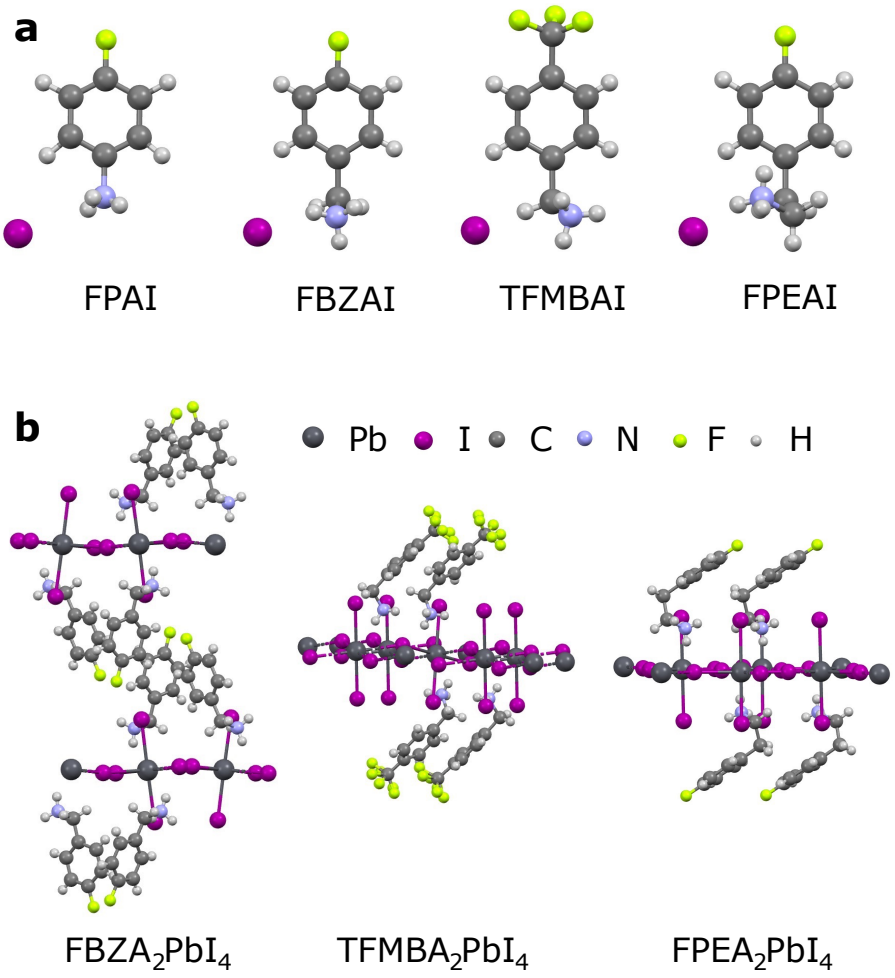


**Figure 6.1:** Schematic diagram of passivation molecules (a) and potential two-dimensional perovskite structures (b), sourced from the Cambridge Crystallographic Data Centre (CCDC) (FPAI CCDC number 1143977[207], $FBZA_2PbI_4$ CCDC number 1819854[208], $TFMBA_2PbI_4$ CCDC number 2041929[209], $FPEA_2PbI_4$ CCDC number 2013268[210]).

to unstable rate readings, poor control over deposition, and potential contamination of the chamber since heating up other sources may cause resublimation of residual organic molecules deposited within the chamber. More importantly, if the organic molecules are too volatile, they can increase the background pressure of the vacuum system by 2 to 3 orders of magnitude during deposition. This will shorten the mean free path of precursor vapors and increase the possibility of molecules reacting in the vapour phase before being adsorbed onto the substrate.

To address these challenges, two main criteria are adopted to select suitable organic molecules for thermal evaporation.

1. The rise of background pressure is less than one order of magnitude (i.e., from $3\times10^{-6}$ mbar to $3\times10^{-5}$ mbar).

2. The thin film has the same molecular structure as the organic molecule.

Based on criterion 1, the change of the chamber pressure is monitored when heating all four molecules with a target substrate rate of 0.10 Å/s. For FBZAI, TFMBAI and FPEAI, the increase of chamber pressure is less than one order of magnitude when both the source temperature and substrate rate are stable. However, for FPAI, the chamber pressure rapidly increases from $5\times10^{-6}$ mbar to $5\times10^{-4}$ mbar at a source temperature lower than 80 °C without an obvious substrate rate reading (Figure 6.2). This indicates that FPAI is too volatile to allow for controllable thermal evaporation. Therefore, FBZAI, TFMBAI and FPEAI are selected for the following study.

To test whether the vapour-deposited film has the same molecular structure as the organic precursor, X-ray diffraction patterns (XRD) and attenuated total reflectance-Fourier transform infrared spectroscopy (ATR-FTIR, experimental details in Chapter 3.5) are performed on both precursor powders and vapour-deposited films. Figure 6.3a shows that for vapour-deposited FBZAI and TFMBAI films, their XRD patterns display feature diffraction peaks consistent with those of powders, which indicates that the vapour-deposited films preserve the same crystal structure as their precursor powders. However, for FPEAI, the vapour-deposited film does not show the diffraction peaks at 5.6° and 11.2° compared with

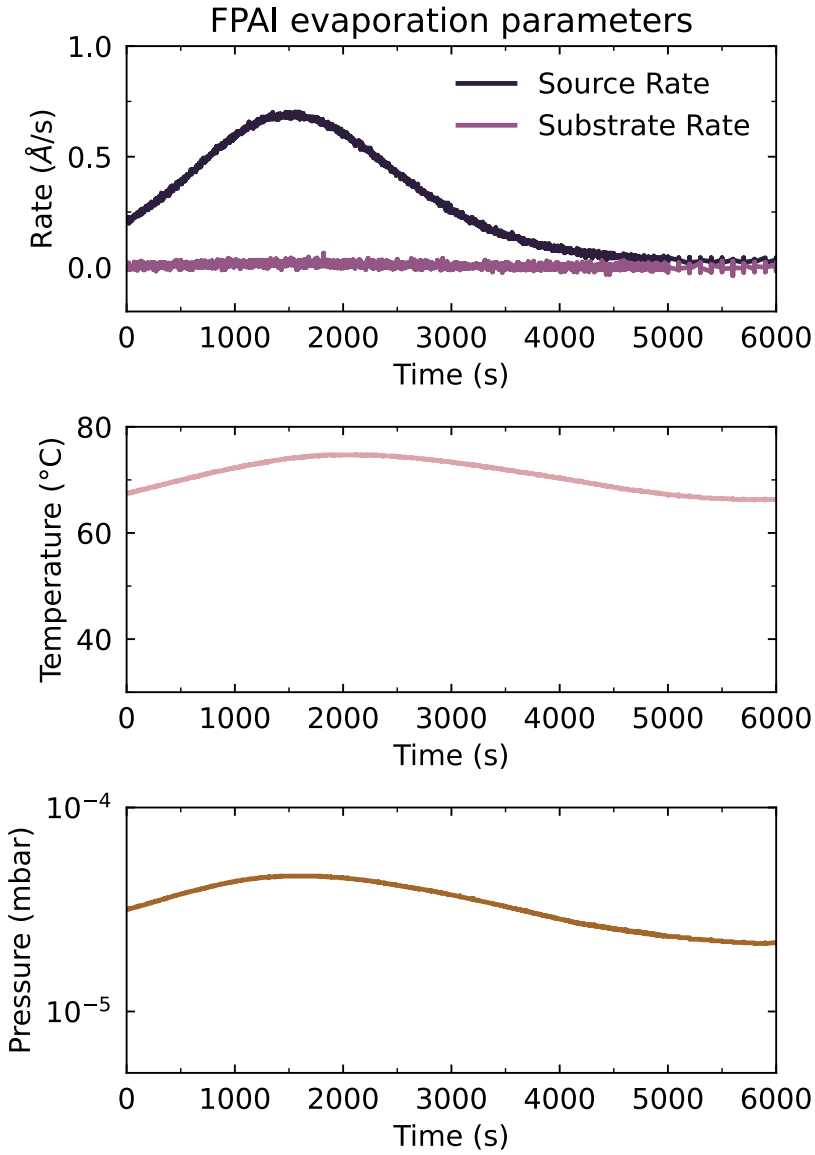


**Figure 6.2:** Evaporation parameters of FPAI, including source rate, substrate rate, source temperature and chamber pressure during the evaporation.

its precursor powder. Instead, new diffraction peaks emerge at 9.0° and 18.0°, which may occur as a result of different orientations in the vapour-deposited FPEAI film. To distinguish whether the weak XRD signals observed here are due to the low crystallinity, or decomposition of FPEAI during thermal evaporation, ATR-FTIR measurements are further conducted (Figure 6.3b). The vapour-deposited FPEAI film and FPEAI powder exhibit similar ATR-FTIR spectra, indicating that they

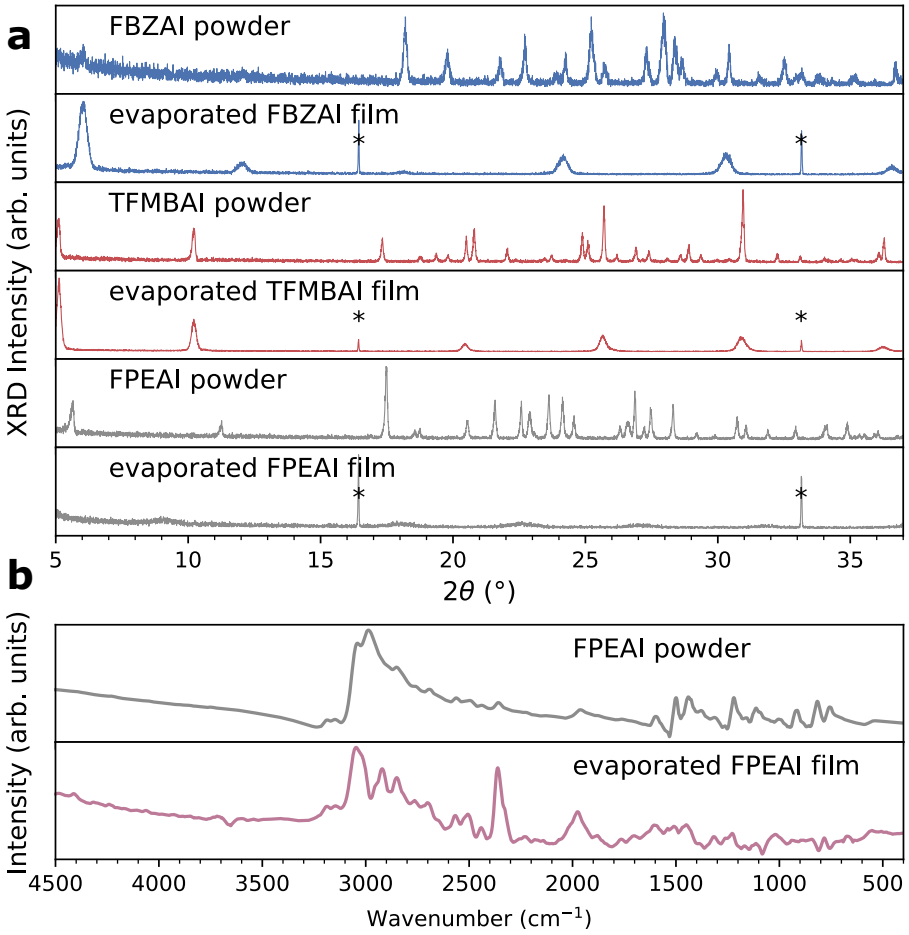


**Figure 6.3:** (a)XRD patterns of FBZAI, TFMBAI and FPEAI precursor powders and vapour-deposited films. (b) ATR-FTIR spectra FPEAI precursor powder and vapour-deposited film.

have the same chemical composition. Therefore, the low XRD signals and new XRD peaks likely suggest that the vapour-deposited FPEAI film lacks long-range order (lower degree of crystallinity) and adopts a different orientation.

Hence, these results have determined that the molecular structures of the three organic molecules–FBZAI, TFMBAI and FPEAI–remain the same after forming the vapour-deposited films. This confirms that all three organic molecules do not decompose after evaporation. However, FBZAI and TFMBAI form crystallised structures in the as-deposited films, while FPEAI film exhibits a lower degree of

crystallinity and different orientations compared with its precursor powder.

### 6.3.2 The Impact of Measurement Atmosphere on Neat and Passivated Films

To understand how these passivation molecules influence the optoelectronic properties of 3D perovskites, I deposit these passivation molecules on the top surface of co-evaporated $FA_{0.9}Cs_{0.1}PbI_{3-x}Cl_x$ perovskite films and conduct steady-state photoluminescence (PL) and time-resolved PL (time-correlated single photon counting, TCSPC) measurements.

Note that previous studies have reported the 'photo-brightening' and 'photo-darkening' phenomena of metal halide perovskite, referring to the evolution of PL intensity during exposure to light, which was strongly dependent on the atmosphere.[212–216] Godding et al. have demonstrated that under illumination, the superoxide species created from oxygen in the ambient environment can form Pb-O bonds at the perovskite surface. This oxidation process can reduce the number of shallow surface trap states, leading to the 'photo-brightening' . However, degradation of the perovskite occurred spontaneously due to the loss of MA and formation of $PbI_2$, which highly depended on the humidity level and light intensity. Therefore, when the degradation overtook the passivation effect of Pb-O bonds, 'photo-darkening' started until the perovskite fully degraded.[217] Since the PL intensity evolution likely suggests the change of the trap density or the degradation of the perovskite, it is necessary to find a stable measurement atmosphere without the presence of gases and molecules that may account for the illumination-induced

variations. Therefore, this work first compares the photophysical behaviours of the control and passivated films in air, vacuum and nitrogen atmospheres (Figure 6.4).

Figures 6.4a and 6.4b show the PL evolution of the control film when exposed to air under continuous ultraviolet light illumination. After 398nm pulsed laser illumination with the fluence of 36.5 nJ/$cm^2$ for 1800 s, the PL intensity increases fivefold, and the lifetime increases from 60.9 ns to 137.9 ns. The steady-state and time-resolved PL measurements both indicate that illuminating under ambient conditions can greatly inhibit non-radiative recombination and significantly reduce the number of defects. Since the PL intensity remains unchanged after storing the sample in the dark and nitrogen for over 12h, the passivation of control films under illumination in air is an irreversible process. The difference in surface hydrophobicity observed between the control and passivated films (Figure 6.5) suggests a change in surface following the bonding of passivation molecules to the perovskite surface. As a result, the control and passivated films have different numbers of available surface sites that can be passivated by oxygen during illumination in air. This introduces an additional variable that affects the optoelectronic properties of the perovskite films. Therefore, evaluating the effectiveness of passivation agents by comparing the optoelectronic properties of the control and passivated films measured in air is not a valid comparison.

Meanwhile, Figures 6.4c, 6.4d and 6.6 unveil that measuring in vacuum slightly alters the charge carrier dynamics of passivated perovskite films with different thicknesses of FPEAI. Compared with conducting the measurement in air, PL spectra of the control films are more stable under vacuum (Figure 6.4c). However, the PL intensity of FPEAI passivated film decreases significantly over the same

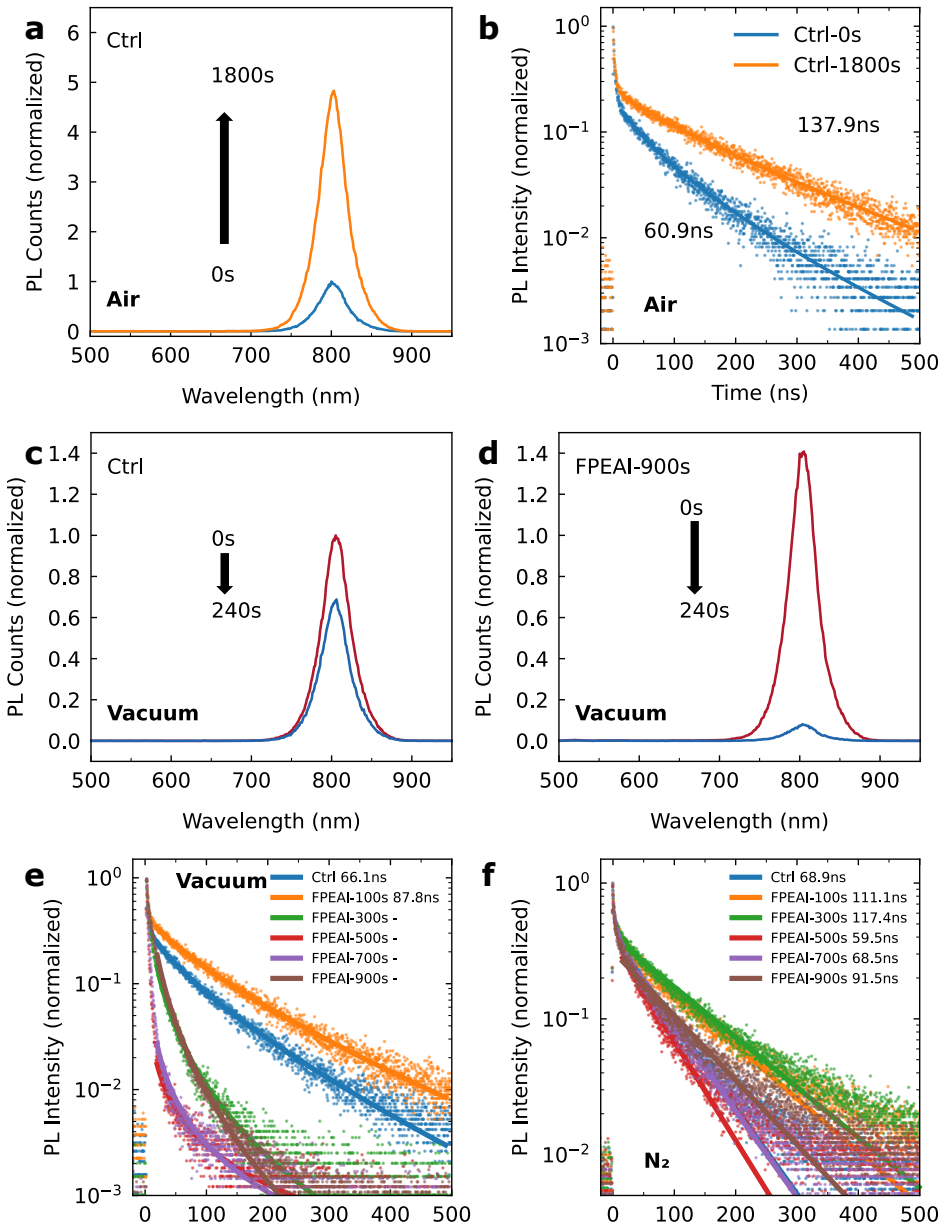


**Figure 6.4:** Optoelectronic characterisation of the 550 nm thick control (labelled as ctrl in the figure) and passivated $FA_{0.9}Cs_{0.1}PbI_{3-x}Cl_x$ perovskite films on z-cut quartz substrates in air, vacuum and nitrogen atmospheres. (a) Steady-state PL (398 nm excitation) spectra of the fresh control film and 1800s-illuminated control film after storing in the dark glovebox for 12h in air. (b) Time-resolved PL measurements of the fresh control film and 1800s-illuminated control film after storing in the glovebox for 12h in air, excited by the 398 nm pulsed laser with the 1MHz repetition rate and the fluence of 36.5 $nJ/cm^2$. (c) Steady-state PL (398 nm excitation) spectra of the fresh control film and 240s-illuminated control film in vacuum. (d) Steady-state PL (398 nm excitation) spectra of the fresh passivated film with FPEAI-900s and 240s-illuminated Passivated film with FPEAI-900s in vacuum. Time-resolved measurements of the control film and passivated films with different thickness values of FPEAI in vacuum (e) and in nitrogen (f), excited by the 398 nm pulsed laser with the 1MHz repetition rate and the fluence of 36.5 $nJ/cm^2$ (all samples illuminated from the film side).

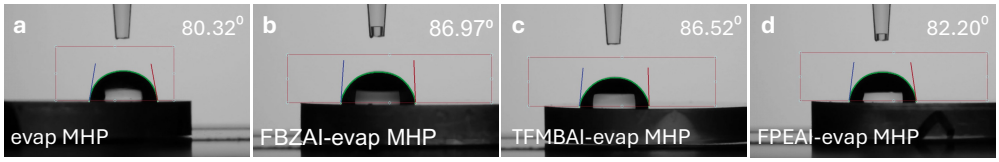


**Figure 6.5:** Contact angle measurements for control (a) and passivated (b-d) $FA_{0.9}Cs_{0.1}PbI_{3-x}Cl_x$ perovskite films (water used here as the solvent).

time interval (Figure 6.4d). One possible explanation for this is that the organic molecules may be loosely bonded to the surface of the perovskite, and hence can be easily removed under high vacuum.[218]

Henceforth, the steady-state and time-resolved PL measured in nitrogen exclude the impact of adsorbed gases and molecules, and ensure stability of the passivated surface. In this case, for both control and passivated films, time-resolved PL decays follow the monoexponential decay, suggesting similar charge carrier dynamic processes in both cases (Figure 6.4f). Moreover, no significant PL evolution or irreversible changes in photophysical properties occur across all samples.

### 6.3.3 Optoelectronic and Structural Properties of Passivated Perovskite Films

To verify whether the as-deposited passivation layers would directly form low-dimensional phases $FA_{n-1}A'_2Pb_nI_{3n+1}$ (A′ refers to FBZAI/TFMBAI/FPEAI in this study), different thicknesses of FBZAI, TFMBAI and FPEAI are deposited on top of co-evaporated 3D perovskite films. The steady-state PL measurements show that FBZAI and FPEAI (Figures 6.7a and 6.7c) exhibit intensified low-dimensional perovskite signals with increased thickness of the passivation layer. Specifically, for FBZAI, PL intensity from n = 2 (around 575 nm) is higher than those from n = 1 (around 525 nm) and n = 3 (around 625 nm). In the case of FPEAI, most of the

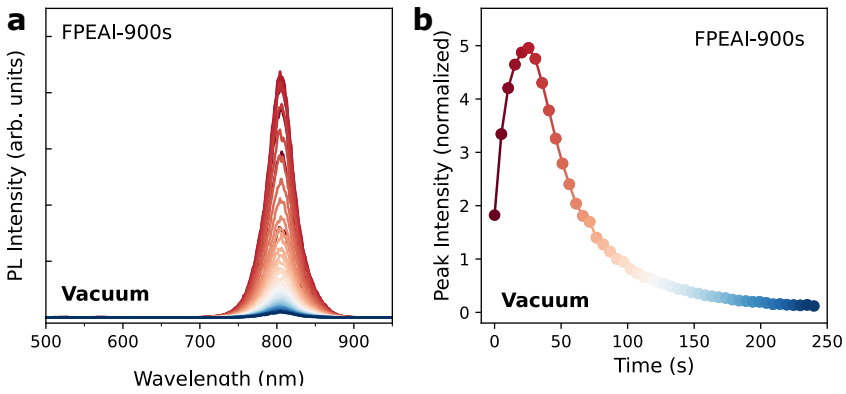


**Figure 6.6:** (a) Steady-state PL spectra of the 550 nm thick control (labelled as ctrl in the figure) and passivated $FA_{0.9}Cs_{0.1}PbI_{3-x}Cl_x$ perovskite films with FPEAI-900s on z-cut quartz substrates under the illumination of 398nm from 0s to 240s. (b) PL intensity extracted from (a) as a function of illumination time (all samples illuminated from the film side).

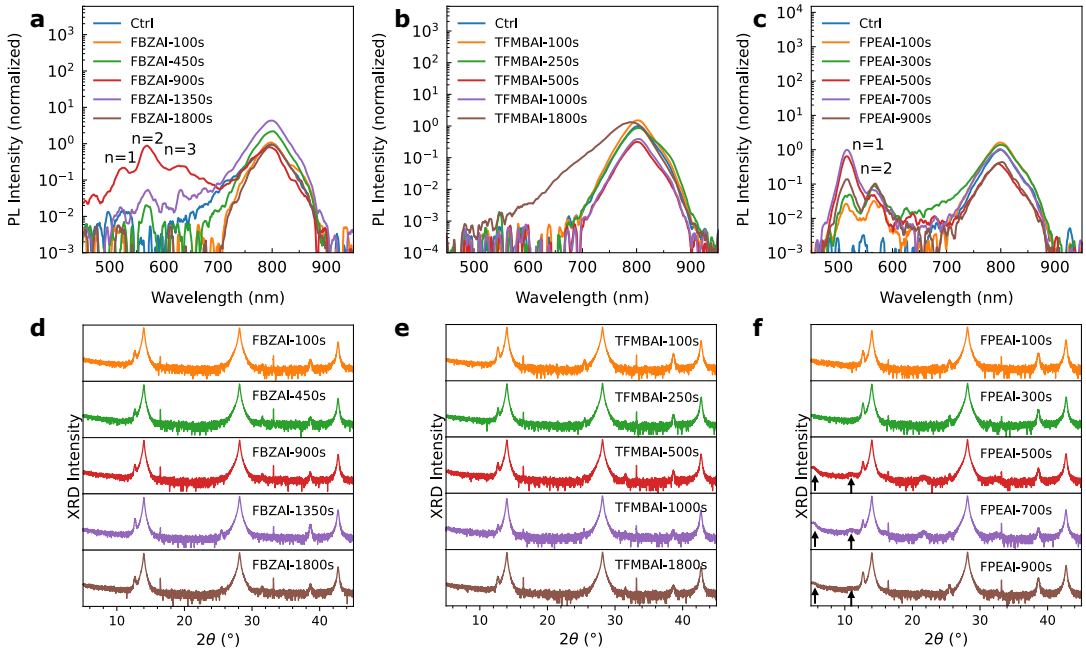


**Figure 6.7:** Optoelectronic and structural properties of passivated $FA_{0.9}Cs_{0.1}PbI_{3-x}Cl_x$ perovskite films. Steady-state PL (398 nm excitation) spectra of the 550 nm thick control (labelled as ctrl in the figure) and passivated films with different thicknesses of vapour-deposited FBZAI (a), TFMBAI (b) and FPEAI (c) on z-cut quartz substrates (all samples illuminated from the film side). XRD patterns of the passivated films with different thicknesses of vapour-deposited FBZAI (d), TFMBAI (e) and FPEAI (f).

low-dimensional PL signals originate from the n = 1 (around 515 nm) RP phases with a weaker PL peak from n = 2 (around 565 nm). For TFMBAI (Figure 6.7b), increasing the passivation layer thickness does not enhance low-dimensional PL features. Instead, the passivated films only exhibit a slight peak shift from 802 nm (1.55 eV) to 790 nm (1.57 eV), which may be related to the formation of mixed 3D/quasi-2D structures with high n values (n > 7).[219] These results suggest that while FBZAI, TFMBAI, and FPEAI can all directly form low-dimensional phases upon deposition on co-evaporated 3D perovskite, the preferentially formed n-values vary, which may stem from differences in their formation energies. In addition, XRD measurements on these samples (Figures 6.7d-f) reveal reflections from lower dimensional structures only in the FPEAI-passivated films. For the other samples, despite clear PL signals from lower dimensional structures, the XRD patterns do not show characteristic reflections from lower dimensional phases. This discrepancy is likely due to the lower sensitivity of XRD compared to PL for detecting small amount of low-dimensional phases.[220]

To evaluate the effects of passivation agents, their impacts on the optoelectronic properties of photogenerated carriers are investigated by characterising the steady-state and time-resolved PL with a 640 nm excitation source. This ensures the excitation of the 3D perovskite as opposed to the low-dimensional phases (Figure 6.8). The results show that after individually optimising the deposition time for each passivation layer, co-evaporated 3D perovskite films passivated with FBZAI, TFMBAI and FPEAI all exhibit stronger PL intensities with longer charge-carrier lifetimes compared to the control films.

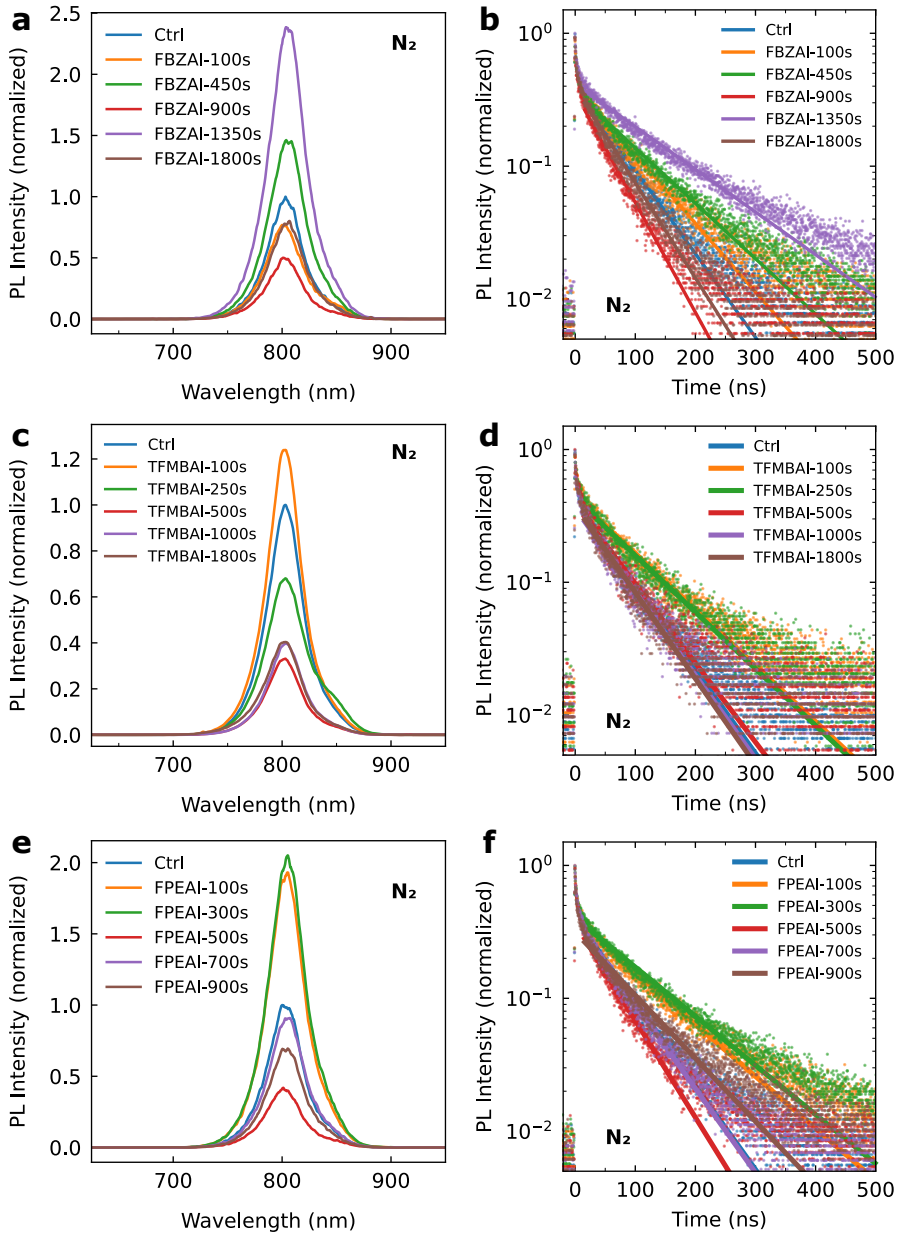


**Figure 6.8:** Steady-state PL (640 nm excitation) spectra of the passivated $FA_{0.9}Cs_{0.1}PbI_{3-x}Cl_x$ perovskite films with different thicknesses of vapour-deposited FBZAI (a), TFMBAI (c) and FPEAI (e), using the relative PL intensity compared with the 550 nm thick control films (labelled as ctrl in the figure) on z-cut quartz substrates. Time-resolved PL measurements of the passivated films with different thicknesses of vapour-deposited FBZAI (b), TFMBAI (d) and FPEAI (f), excited by the 640 nm pulsed laser with the 500 KHz repetition rate and the fluence of 113.6 nJ/$cm^2$ (all samples illuminated from the film side).

### 6.3.4 The Effect of Passivation Molecules on the MHP/CTL Interface under Different Treatment Conditions

Previous studies have illustrated the significant changes in the chemical composition and structure of the surface-passivated perovskite films with and without annealing the passivation layer.[186] These changes can influence the charge-carrier dynamics, device operation and even long-term stability.[221] Considering that the annealing of the passivation layer (100°C for 5 min, Figure 6.9a) might also have an effect on the 3D perovskite itself, Figures 6.9b and 6.9c compare the steady-state and time-resolved PL of the control films with and without the extra 5 min annealing at 100°C. After annealing, the PL intensity of the control film is slightly enhanced with lifetime increasing from 97.6 ns to 119.4 ns. Although the change is not substantial, it is noteworthy that the minor variations in steady-state and time-resolved PL observed for the passivated films after annealing may result from the improvement of 3D film rather than the influence of the passivation layers.

To study the effect of the passivation agents with and without annealing, 640 nm excitation is employed to selectively excite the 3D perovskite. Figure 6.10 shows that the annealing of the passivation layer significantly alters the optoelectronic properties of the passivated films. For all three passivation agents, the initial enhancement in PL intensity when depositing the passivation layer without extra annealing diminishes upon annealing, resulting in lower PL intensities and shorter charge-carrier lifetimes. The influence of annealing on the passivated films is opposite to its influence on the control films, suggesting a possible alteration of the passivation effect after extra annealing.

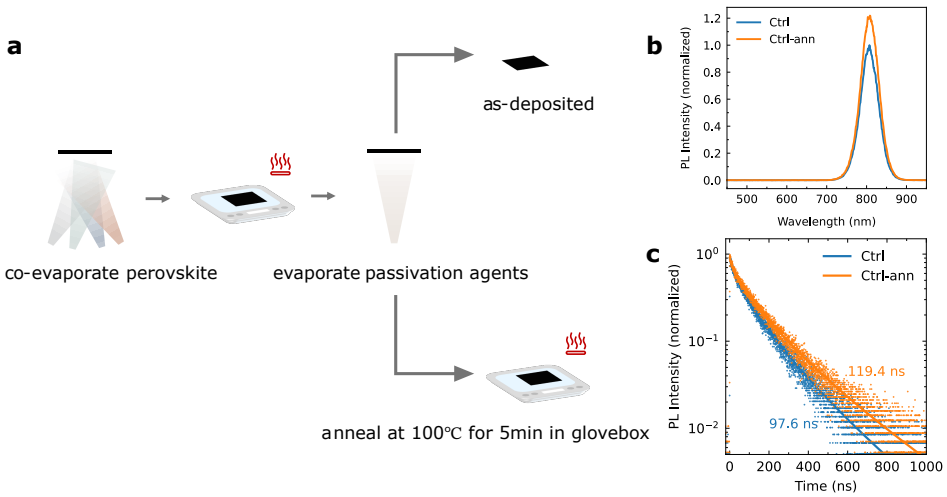


**Figure 6.9:** The influence of annealing on the 550 nm thick control (labelled as ctrl in the figure) $FA_{0.9}Cs_{0.1}PbI_{3-x}Cl_x$ perovskite films on z-cut quartz substrates. (a) Schematic diagram of the extra post-treatment. (b) Steady-state PL (640 nm excitation) spectra of the control films without (ctrl) and with (ctrl-ann) extra annealing at 100°C for 5 min. (c) Time-resolved PL measurements of the control films with and without extra annealing at 100°C for 5 min, excited by the 640 nm pulsed laser with the 500 KHz repetition rate and the fluence of 113.6 nJ/$cm^2$ (all samples illuminated from the film side).

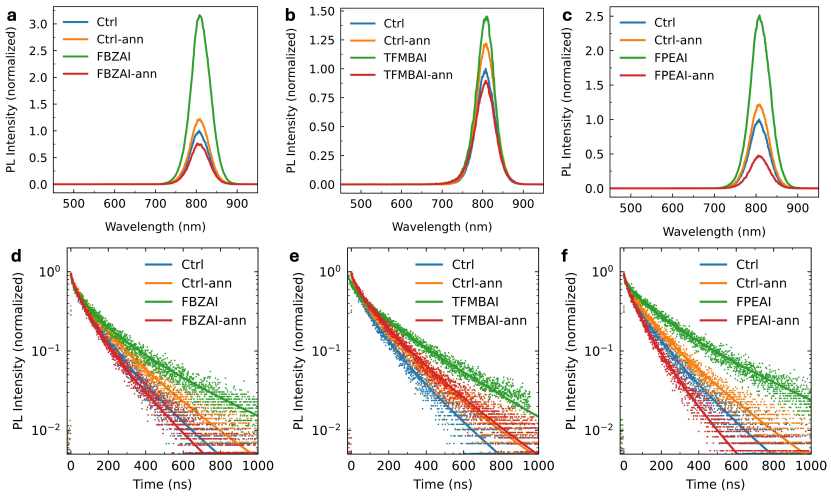


**Figure 6.10:** Steady-state PL (640 nm excitation) spectra of the 550 nm thick control (labelled as ctrl in the figure) and FBZAI- (a), TFMBAI- (b) and FPEAI- (c) passivated $FA_{0.9}Cs_{0.1}PbI_{3-x}Cl_x$ perovskite films with and without extra annealing at 100°C for 5 min on z-cut quartz substrates, using the relative PL intensity compared with the control films without extra annealing. Time-resolved PL measurements of the control films and FBZAI- (d), TFMBAI- (e) and FPEAI- (f) passivated films with and without extra annealing at 100°C for 5 min, excited by the 640 nm pulsed laser with the 500 KHz repetition rate and the fluence of 113.6 nJ/$cm^2$ (all samples illuminated from the film side).

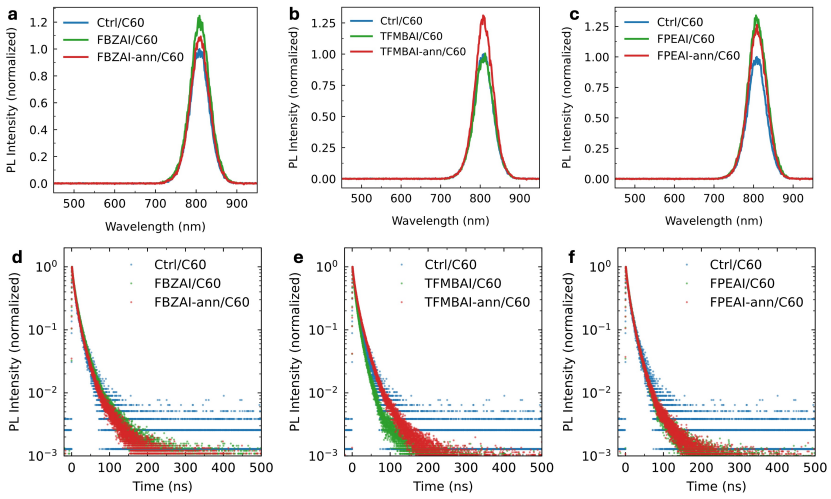


**Figure 6.11:** Steady-state PL (640 nm excitation) spectra of the 550 nm thick control (labelled as ctrl in the figure)/C60 and FBZAI- (a), TFMBAI- (b) and FPEAI- (c) passivated $FA_{0.9}Cs_{0.1}PbI_{3-x}Cl_x$ perovskite/C60 films with and without extra 5 min annealing at 100°C on z-cut quartz substrates, using the relative PL intensity compared with the control/C60 films without extra annealing. Time-resolved measurements of the control/C60 films and FBZAI- da), TFMBAI- (e) and FPEAI- (f) passivated/C60 films with and without extra 5 min annealing at 100°C, excited by the 640 nm pulsed laser with the 500 KHz repetition rate and the fluence of 113.6 nJ/$cm^2$ (all samples illuminated from the film side).

When the passivation layers are deposited between the 3D perovskite and the electron transport layer (ETL), C60 (Figure 6.11), neither the PL intensity nor the charge-carrier lifetime shows significant changes. However, when the passivation layers are deposited between 3D perovskite and hole transport layer (HTL), spiro-OMeTAD (Figures 6.12), the PL intensities increase twofold for TFMBAI and tenfold for FPEAI when annealing the passivation layers, accompanied with significant enhancement of lifetimes, indicating more effective interface passivation and suppressed non-radiative recombination. In contrast, the differences between the control/spiro-OMeTAD films and those using the passivation layers without extra annealing are negligible.

The results thus far show that the passivation layers without extra annealing can enhance the optoelectronic properties of the perovskite films but exhibit minimal

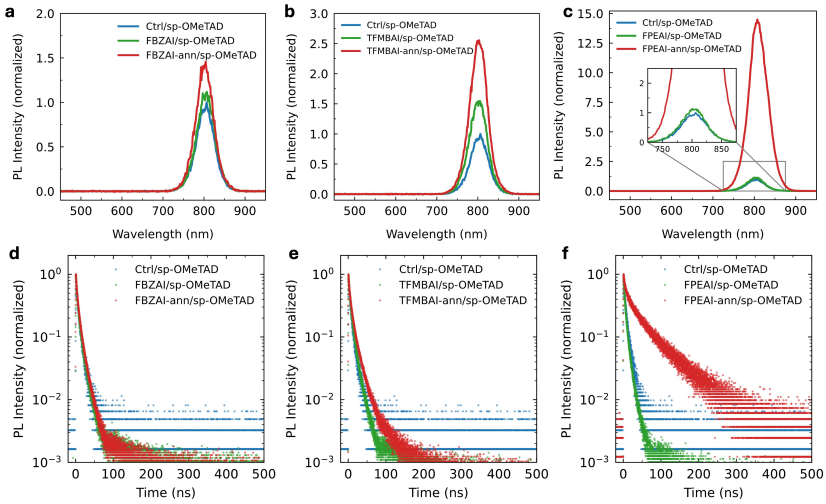


**Figure 6.12:** Steady-state PL (640 nm excitation) spectra of the 550 nm thick control (labelled as ctrl in the figure)/spiro-OMeTAD and FBZAI- (a), TFMBAI- (b) and FPEAI- (c) passivated $FA_{0.9}Cs_{0.1}PbI_{3-x}Cl_x$ perovskite/spiro-OMeTAD films with and without extra 5 min annealing at 100°C on z-cut quartz substrates, using the relative PL intensity compared with the control/spiro-OMeTAD films without extra annealing. Time-resolved PL measurements of the control/spiro-OMeTAD films and FBZAI- (d), TFMBAI- (e) and FPEAI- (f) passivated/spiro-OMeTAD films with and without extra 5 min annealing at 100°C, excited by the 640 nm pulsed laser with the 500 KHz repetition rate and the fluence of 113.6 nJ/$cm^2$ (all samples illuminated from the film side).

improvement at the perovskite/C60 and perovskite/spiro-OMeTAD interfaces. As for the passivation layers after extra annealing, they exhibit minimal or even detrimental effects on the optoelectronic properties of the perovskite films, with negligible impact on the perovskite/C60 interfaces. However, they significantly enhance the optoelectronic properties of the perovskite/spiro-OMeTAD samples, particularly when using the FPEAI with extra annealing. Since the improvement does not arise from the passivation of the defects at the 3D perovskite surface, it is likely to occur as a result of the reduction of trap states at the perovskite/spiro-OMeTAD interface.

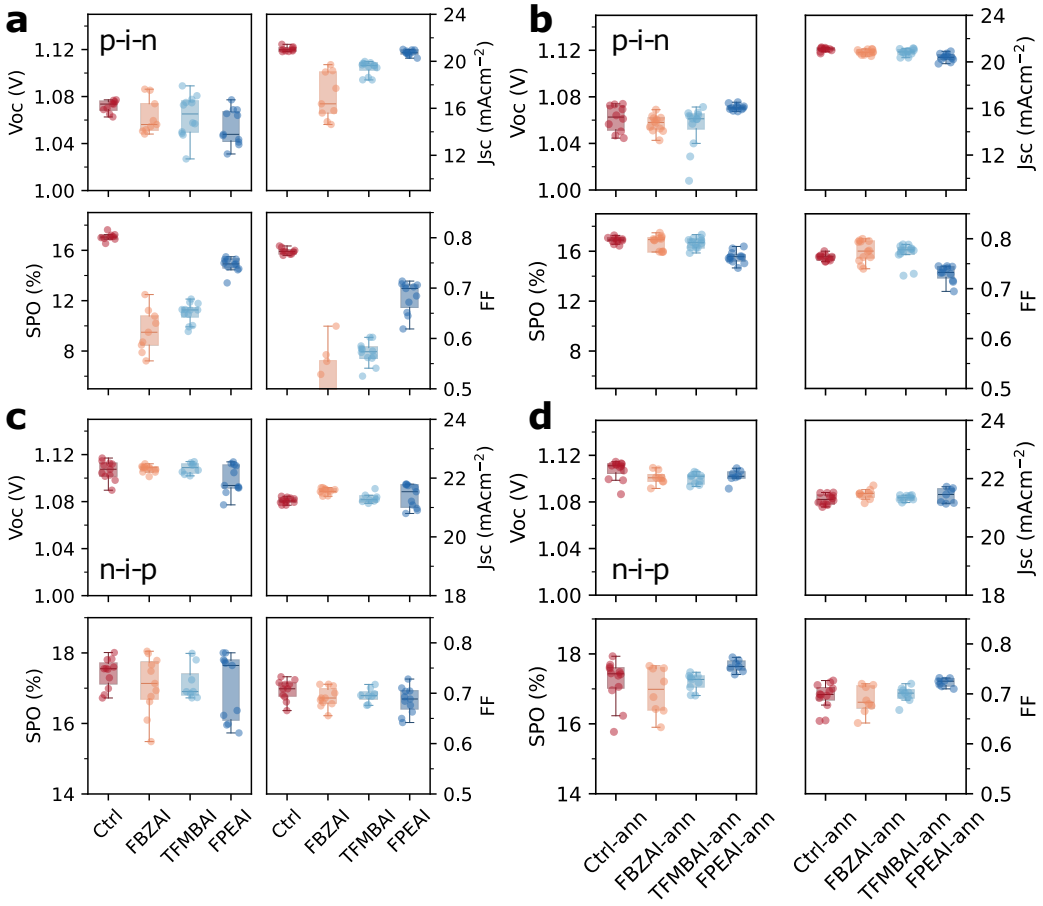


**Figure 6.13:** Performance parameters of p-i-n device by using the control (labelled as ctrl in the figure) and passivated (FBZAI, TFMBAI, FPEAI) $FA_{0.9}Cs_{0.1}PbI_{3-x}Cl_x$ perovskite films without (a) and with (b) extra annealing as the active layers. Performance parameters of n-i-p device by using the control films and passivated films without (c) and with (d) extra annealing as the active layers. In the box plots, the central line inside each box represents the median value of the dataset. The box edges (lower and upper sides) indicate the first quartile (Q1) and third quartile (Q3), corresponding to the $25^{th}$ and $75^{th}$ percentiles, respectively. The whisker extends from the box to the smallest and largest data points within 1.5 times the interquartile range (IQR) from Q1 and Q3. Data points lying outside of this range are plotted individually as outliers.

### 6.3.5 The Effect of Passivation on P-I-N and N-I-P Device Performance

Next, it is interesting to study whether the above-mentioned difference between the control and passivated films could be reflected on the device performance in both p-i-n and n-i-p architectures (Figure 6.13, Tables 6.1 and 6.2). The performance

| | | avg $J_{sc}$ (mA cm$^{-2}$) | avg $V_{oc}$ (V) | avg SPO (%) | avg FF |
|---|---|---|---|---|---|
| p-i-n | Ctrl | 21.03 ± 0.21 | 1.07 ± 0.01 | 17.07 ± 0.29 | 0.77 ± 0.01 |
| p-i-n | FBZAI | 17.00 ± 1.97 | 1.06 ± 0.02 | 9.61 ± 1.71 | 0.51 ± 0.07 |
| p-i-n | TFMBAI | 19.41 ± 0.58 | 1.06 ± 0.02 | 11.02 ± 0.81 | 0.57 ± 0.02 |
| p-i-n | FPEAI | 20.73 ± 0.23 | 1.05 ± 0.02 | 14.84 ± 0.58 | 0.68 ± 0.03 |
| p-i-n | Ctrl-ann | 21.07 ± 0.16 | 1.06 ± 0.01 | 16.88 ± 0.24 | 0.76 ± 0.01 |
| p-i-n | FBZAI-ann | 20.84 ± 0.20 | 1.06 ± 0.01 | 16.70 ± 0.57 | 0.77 ± 0.02 |
| p-i-n | TFMBAI-ann | 20.83 ± 0.27 | 1.05 ± 0.02 | 16.65 ± 0.42 | 0.77 ± 0.02 |
| p-i-n | FPEAI-ann | 20.39 ± 0.32 | 1.07 ± 0.01 | 15.53 ± 0.50 | 0.73 ± 0.02 |

**Table 6.1:** Average performance parameters for p-i-n devices by using the control (labelled as ctrl in the table)and passivated $FA_{0.9}Cs_{0.1}PbI_{3-x}Cl_x$ perovskite films with and without extra annealing as the active layers. The values given in this table represent scans from open-circuit to short-circuit conditions (reverse scan).

parameters are taken from 10-12 devices for each group. The control and passivated perovskite films are applied as active layers in p-i-n solar cells with the structure ITO/spiro-TTB/3D perovskite/passivation layer/C60/Bathocuproine (BCP)/Ag. When applying the passivation layers without extra annealing (Figure 6.13a), the average steady power outputs (SPOs) decrease compared to control devices, accompanied by lower short-circuit current density ($J_{sc}$) and fill factor ($FF$). When using the passivation layers with extra annealing (Figure 6.13b), the average SPOs of passivated devices enhance with improved $J_{sc}$ and $FF$ compared with their as-deposited counterparts. Furthermore, for devices treated with FBZAI and TFMBAI, annealing leads to narrower distributions across all measured device parameters.

When it comes to the n-i-p devices, one would expect to observe more significant changes in open-circuit voltage ($V_{oc}$) for passivated devices after annealing based on the film characterisation results. Here, the control and passivated perovskite films are applied as active layers in solar cells with the structure ITO/$SnO_2$/3D

| | | avg $J_{sc}$ (mA cm$^{-2}$) | avg $V_{oc}$ (V) | avg SPO (%) | avg FF |
|---|---|---|---|---|---|
| n-i-p | Ctrl | 21.23 ± 0.10 | 1.11 ± 0.01 | 17.43 ± 0.42 | 0.71 ± 0.02 |
| n-i-p | FBZAI | 21.56 ± 0.10 | 1.11 ± 0.01 | 17.09 ± 0.81 | 0.69 ± 0.02 |
| n-i-p | TFMBAI | 21.31 ± 0.16 | 1.11 ± 0.01 | 17.14 ± 0.49 | 0.70 ± 0.01 |
| n-i-p | FPEAI | 21.39 ± 0.40 | 1.10 ± 0.01 | 17.02 ± 0.94 | 0.69 ± 0.03 |
| n-i-p | Ctrl-ann | 21.29 ± 0.18 | 1.11 ± 0.01 | 17.22 ± 0.63 | 0.69 ± 0.03 |
| n-i-p | FBZAI-ann | 21.47 ± 0.19 | 1.10 ± 0.01 | 16.94 ± 0.67 | 0.69 ± 0.03 |
| n-i-p | TFMBAI-ann | 21.34 ± 0.09 | 1.10 ± 0.01 | 17.19 ± 0.24 | 0.70 ± 0.02 |
| n-i-p | FPEAI-ann | 21.42 ± 0.25 | 1.10 ± 0.01 | 17.66 ± 0.17 | 0.72 ± 0.01 |

**Table 6.2:** Average performance parameters for n-i-p devices by using the control (labelled as ctrl in the table) and passivated $FA_{0.9}Cs_{0.1}PbI_{3-x}Cl_x$ perovskite films with and without extra annealing as the active layers. The values given in this table represent scans from open-circuit to short-circuit conditions (reverse scan).

perovskite/passivation layer/spiro-OMeTAD/Au (Figures 6.13c and 6.13d). However, only when using the FPEAI with extra annealing, devices exhibit slightly higher SPOs with narrower distribution and improved FF compared with control devices; there are no significant difference in either $V_{oc}$ or SPO for the other cases. The inconsistency between the optoelectronic characterisation for perovskite/spiro-OMeTAD films and the device measurements for the full-device structure suggests that the passivation effect at the perovskite/spiro-OMeTAD interface is not the only or dominant parameter governing device performance. To identify the possible dominant factors, I carry out additional studies in the following sections.

### 6.3.6 Factors Influencing Final Device Performance

In previous sections, the 'photo-brightening' phenomenon observed upon illuminating the control samples in air is likely due to the surface passivation by oxygen at the perovskite surface. Brenes et al. have demonstrated that the 'photo-brightening' enhancement was not as evident when the interaction of the

atmospheric molecules with the perovskite surface was limited.[215] Hence, while all device measurements are conducted in air without encapsulation, 'photo-brightening' of the control films is expected to be significantly suppressed after depositing CTLs. Therefore, it is less likely that 'photo-brightening' of the control films is the primary factor leading to the minimal performance difference observed between control and passivated devices.

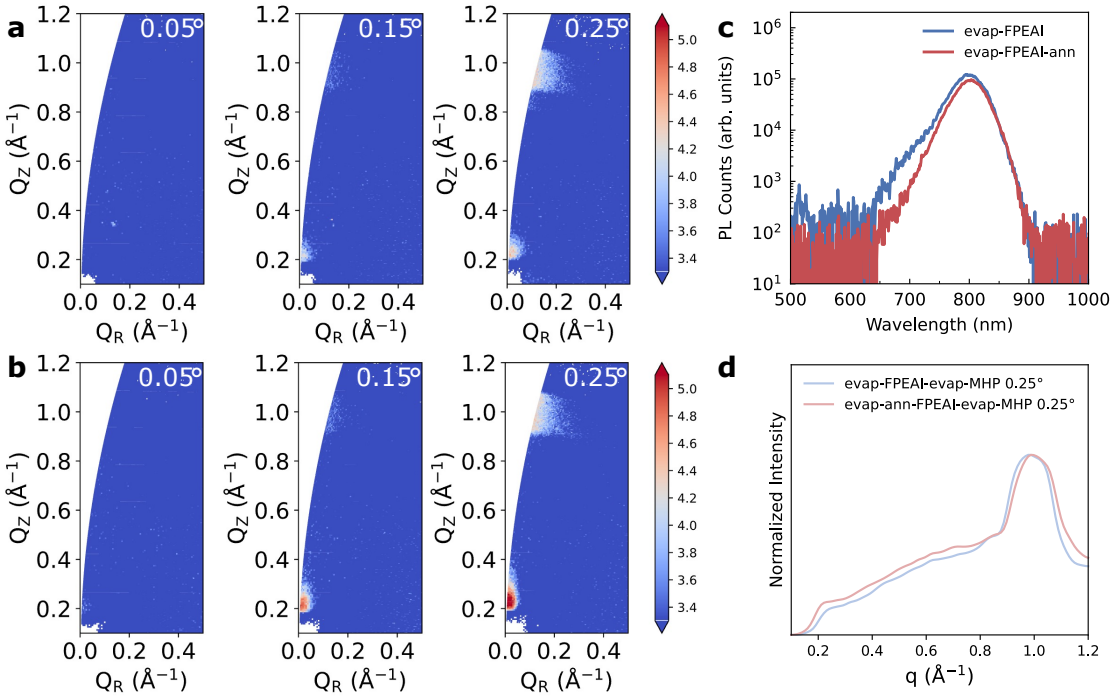


**Figure 6.14:** Grazing-incidence angle X-ray scattering patterns (a) and integrated XRD profiles (b) of vapour-deposited FPEAI-passivated co-evaporated $FA_{0.9}Cs_{0.1}PbI_{3-x}Cl_x$ perovskite films without extra annealing by using incident angles of 0.05°, 0.15° and 0.25°. (c) Steady-state PL (398nm excitation) spectra of FPEAI-passivated films with and without extra annealing. (d) Integrated XRD profile from GIWAXS results with the incident angle of 0.25°.

Considering that the absence of low-dimensional perovskite signals in the XRD pattern might arise from the limitation of XRD sensitivity, to study the crystallinity and orientation of co-evaporated 3D perovskite passivated by the vapour-deposited FPEAI, Figure 6.14 implements grazing incidence wide-angle X-ray scattering (GI-

WAXS) characterisation with different penetration depths. For vapour-deposited FPEAI-passivated films with and without annealing (Figures 6.14a and 6.14b), a scattering peak located at q = 0.21 $^{-1}$ appears. Since vapour-deposited FPEAI-passivated films with annealing do not have PL signals from low-dimensional perovskites (Figure 6.14c), the scattering signal at q = 0.21 $^{-1}$ is likely from vapour-deposited FPEAI molecule instead of low-dimensional perovskites. This also suggests that the low-dimensional phases observed in the PL spectra of vapour-deposited FPEAI-passivated films without annealing have low crystallinity. Additionally, annealing the vapour-deposited FPEAI causes an enhancement of its crystallinity and removes the low-dimensional structures with low crystallinity (Figure 6.14d).

Additionally, previous studies have observed the XRD signals from 2D phases when passivating the 3D perovskite with spin-coated FPEAI.[222,223] Therefore, it is reasonable to raise the question whether the formation of low-dimensional perovskite phases is influenced by the fabrication methods. Out of this consideration, spin-coated FPEAI-passivated perovskite films are fabricated to conduct GIWAXS measurements for comparison. Figure 6.15 shows the corresponding radial intensity profiles averaged the whole images. Interestingly, for spin-coated FPEAI-passivated films without annealing (Figures 6.15a, 6.15b), when the angle of incidence is 0.15°, the scattering peak is located at q = 0.32 $^{-1}$, arising from the FPEAI. For an incident angle of 0.25°, the scattering peak shifts to q = 0.36 $^{-1}$, corresponding to the 2D phase n = 1 ($FPEA_2PbI_4$). This illustrates that without annealing, more FPEAI molecules are at the surface of the film. As the penetration depth increases, they gradually transform into 2D phases. In contrast, for spin-coated FPEAI-passivated films after annealing (Figures 6.15c, 6.15d), the scattering peak remains at q = 0.36 $^{-1}$ when the incident angle increases from

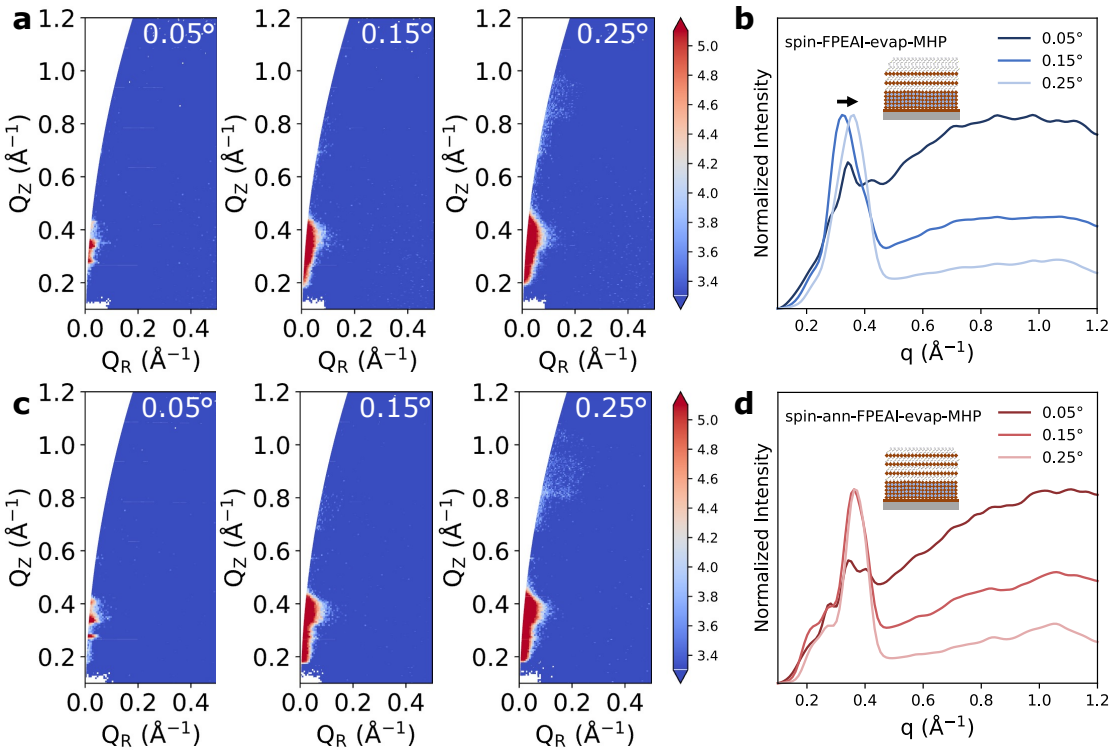


**Figure 6.15:** Grazing-incidence angle X-ray scattering patterns (a) and integrated XRD profiles (b) of spin-coated FPEAI-passivated co-evaporated $FA_{0.9}Cs_{0.1}PbI_{3-x}Cl_x$ perovskite films without extra annealing by using incident angles of 0.05°, 0.15° and 0.25°. Grazing-incidence angle X-ray scattering patterns (c) and integrated XRD profiles (d) of spin-coated FPEAI-passivated films with extra annealing by using incident angles of 0.05°, 0.15° and 0.25°.

0.15° to 0.25°, suggesting more uniform formation of 2D phases across different depths at the surface of 3D perovskite.

GIWAXS results suggest that the main differences between vapour-deposited and spin-coated FPEAI-passivated films lie in the crystallinity of the passivation layers and the effect of annealing on the surface structure. For vapour-deposited FPEAI-passivated films, annealing contributes to enhancing the crystallinity of vapour-deposited FPEAI. For spin-coated FPEAI-passivated films, annealing leads to the further conversion from a substrate/3D/2D/FPEAI to a substrate/3D/2D structure.

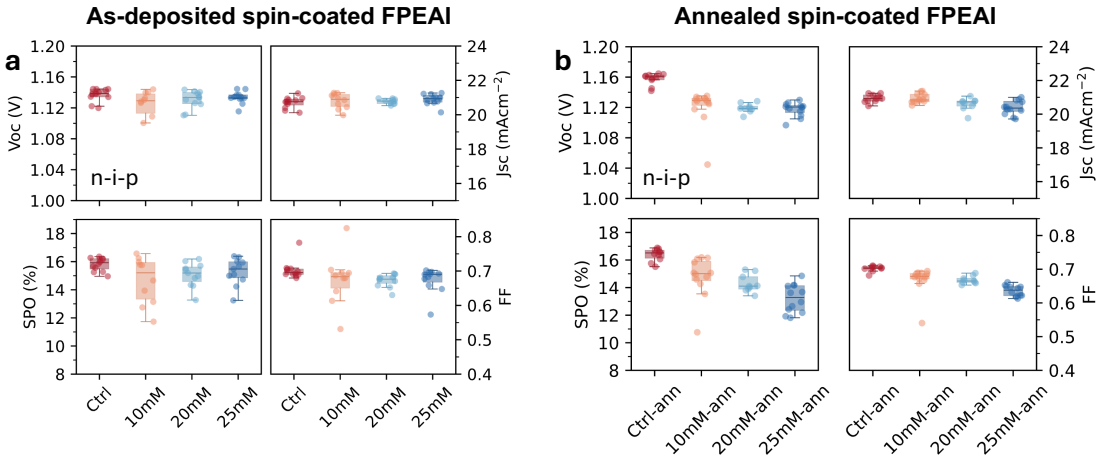


**Figure 6.16:** Performance parameters of n-i-p device by using the 550nm thick control (labelled as ctrl in the figure) and passivated co-evaporated $FA_{0.9}Cs_{0.1}PbI_{3-x}Cl_x$ perovskite films with different concentrations of FPEAI without (a) and with (b) extra annealing as the active layers.

To better understand how the conversion from a substrate/3D/2D/FPEAI to a substrate/3D/2D structure influences the device performance, spin-coated FPEAI-passivated films are incorporated as active layers in n-i-p devices with the architecture ITO/$SnO_2$/co-evaporated 3D perovskite/spin-coated FPEAI with or without annealing/spiro-OMeTAD/Au. Figure 6.16a and Table 6.3 show that for devices passivated by spin-coated FPEAI without annealing, the average SPOs decrease compared with control devices, accompanied by slightly lower $V_{oc}$ and wider distribution of device performance. For devices passivated by annealed spin-coated FPEAI (Figure 6.16b and Table 6.3), the average SPOs decrease more significantly with increasing FPEAI concentration, accompanied by reductions across all photovoltaic parameters, particularly $V_{oc}$. Jiang et al. demonstrated that the passivation with 2D perovskites was less effective as that of the organic molecule at the surface of $FA_{1-x}MA_xPbI_3$ perovskite, leading to diminished performance in the n-i-p devices.[57] The similar trend observed here suggests that the performance reduction upon annealing the spin-coated FPEAI is likely due to the formation

| | avg $J_{sc}$ (mA cm$^{-2}$) | avg $V_{oc}$ (V) | avg SPO (%) | avg FF |
|---|---|---|---|---|
| Ctrl | 20.71 ± 0.32 | 1.14 ± 0.01 | 15.81 ± 0.47 | 0.70 ± 0.03 |
| FPEAI-10mM | 20.80 ± 0.45 | 1.09 ± 0.12 | 14.66 ± 1.68 | 0.67 ± 0.07 |
| FPEAI-20mM | 20.77 ± 0.14 | 1.13 ± 0.01 | 15.07 ± 0.86 | 0.67 ± 0.02 |
| FPEAI-30mM | 20.89 ± 0.32 | 1.13 ± 0.01 | 15.28 ± 0.95 | 0.67 ± 0.04 |
| Ctrl-ann | 20.94 ± 0.24 | 1.16 ± 0.01 | 16.38 ± 0.46 | 0.70 ± 0.01 |
| FPEAI-10mM-ann | 20.93 ± 0.27 | 1.12 ± 0.03 | 14.78 ± 1.50 | 0.67 ± 0.04 |
| FPEAI-20mM-ann | 20.60 ± 0.37 | 1.12 ± 0.01 | 14.30 ± 0.66 | 0.67 ± 0.01 |
| FPEAI-30mM-ann | 20.38 ± 0.42 | 1.12 ± 0.01 | 13.21 ± 1.02 | 0.64 ± 0.02 |

**Table 6.3:** Average performance parameters for n-i-p devices by using the control (labelled as ctrl in the figure) and spin-coated FPEAI-passivated co-evaporated $FA_{0.9}Cs_{0.1}PbI_{3-x}Cl_x$ perovskite films with and without extra annealing as the active layers. The values given in this table represent scans from open-circuit to short-circuit conditions (reverse scan).

of 2D $FPEA_2PbI_4$ at the perovskite/spiro-OMeTAD interface. Furthermore, the narrower distributions of $V_{oc}$, $FF$ and SPOs in devices passivated by annealed spin-coated FPEAI indicate a more uniform distribution of composition after annealing, which is consistent with the GIWAXS results.

Based on spin-coated FPEAI-passivated device data, it appears that the formation of 2D perovskite at the perovskite/spiro-OMeTAD interface is not beneficial for the device performance. Therefore, the slightly higher SPOs with narrower distribution and improved FF achieved when using annealed vapour-deposited FPEAI are likely due to the removal of amorphous 2D phase and more uniform distribution of composition. However, the main reason that no significant performance difference is observed between control and annealed vapour-deposited FPEAI passivated devices remains unclear. By further deepening the understanding of the mechanism and optimising the fabrication parameters for co-evaporated 3D perovskite, this issue may be solved, allowing for a more stable system on which to conduct further passivation studies.

## 6.4 Summary and Outlook

The study in this chapter selects three arylammonium halides, 4-fluorobenzylammonium iodide (FBZAI), 4(trifluoromethyl)benzylammonium iodide (TFMBAI), and 4-fluorophenethylammonium iodide (FPEAI), which can remain the same molecular structures after forming the vapour-deposited films, to passivate the top surface of the co-evaporated $FA_{0.9}Cs_{0.1}PbI_{3-x}Cl_x$ perovskite. The optoelectronic characterisation results show that it is important to perform measurements in nitrogen instead of in air/vacuum. This can help avoid introducing additional variables which may also affect the optoelectronic properties of the films. The as-deposited FBZAI, TFMBAI and FPEAI passivation layers can all directly form low-dimensional phases on co-evaporated $FA_{0.9}Cs_{0.1}PbI_{3-x}Cl_x$ perovskite, with various preferential n values.

While these vapour-deposited passivation agents, without extra annealing, can effectively passivate surface defects and suppress the non-radiative recombination in co-evaporated perovskite films, their passivation effects diminish after extra annealing or when applied at the perovskite/C60 interfaces. In contrast, annealed passivation layers–particularly FPEAI–can significantly enhance the optoelectronic properties of perovskite/spiro-OMeTAD samples. However, the improvement of optoelectronic properties at the perovskite/spiro-OMeTAD interface when applying vapour-deposited FPEAI with extra annealing, does not directly translate into enhanced open-circuit voltage and overall performance in n-i-p devices.

To understand whether changes in optoelectronic properties and device performance are related to the structural alterations of passivation layers, more studies

are conducted to explore possible factors. GIWAXS results show that for vapour-deposited FPEAI-passivated films, annealing can remove the low-dimensional phases and improve the crystallinity of FPEAI. For comparison, FPEAI is spin-coated onto the co-evaporated perovskite films with and without extra annealing. For spin-coated FPEAI-passivated films, annealing converts the structure from a 3D/2D/FPEAI structure to a 3D/2D structure. The formation of 2D $FPEA_2PbI_4$ phase at the perovskite/spiro-OMeTAD interface impairs device performance, especially open-circuit voltage. Therefore, slightly higher steady power outputs with narrower distribution and improved fill factors when using annealed vapour-deposited FPEAI at the perovskite/spiro-OMeTAD interface are likely due to the removal of amorphous 2D phase and more uniform distribution of composition. While the main reason that no significant performance difference is observed between control and annealed vapour-deposited FPEAI passivated devices remains unclear, these findings show how the surface structure transformation influences the passivation effect and device performance.

In summary, the studies in this chapter highlight the impact of measurement atmospheres on the optoelectronic properties of perovskite films, the influence of surface structural transformation induced by annealing passivation layers on the passivation mechanisms, as well as the effect of deposition methods (vapour deposition vs. spin-coating) on the crystallinity of the same organic molecule. These results offer valuable insights into the vapour-phase passivation of co-evaporated halide perovskites.

# 7

# Conclusions and Outlook

This thesis has predominantly explored the factors limiting the power conversion efficiency of vapour-deposited perovskite solar cells and proposed potential strategies to address these challenges. The first research work detailed in Chapter 4.4 revealed the influence of impurities in FAI on solution- and vapour-processed perovskite solar cells. Through a simple recrystallisation procedure, the as-received FAI could be purified with the goal of removing the impurities identified via nuclear magnetic resonance measurements. The presence of these impurities impacted the optoelectronic properties of both solution- and vapour-processed perovskite films, hence affecting device performance. While ethyl acetate, as one of the impurities, can be beneficial for the quality of solution-processed perovskite films by modulating crystallisation dynamics and passivating defects, for vapour-processing, the impurities lead to decomposition of the precursor and off-stoichiometry in the final film. Off-stoichiometry resulted in the formation of non-photoactive phases, which negatively affected the optoelectronic properties of perovskite thin films. This impaired both film stability and solar cell performance. The study has demonstrated that purification and removal of impurities in FAI via recrystallisation is

an effective mitigation strategy to achieve high-quality, reproducible and stable perovskite films and devices.

While thermal vapour deposition is particularly promising, allowing for high-throughput fabrication and large-scale production, the ability to control the nucleation and growth of these materials, particularly at the CTL/perovskite interface, is critical to unlocking the full potential of vapour-deposited perovskite photovoltaics. Therefore, Chapter 5.4 described a promising strategy to decouple the nucleation and growth of co-evaporated perovskite films from the influence of substrate materials. By employing a templating layer, co-evaporated perovskite films displayed identical morphology, structure, and optoelectronic properties, irrespective of the substrate choices. The precise control of the interface facilitated fine-tuning the stoichiometry of the initial perovskite deposited onto the substrate, thus enhancing photovoltaic performance. These results provided an effective and reproducible method for controlling the buried charge transport layer/perovskite interface in vapour-deposited perovskite solar cells, further increasing the competitiveness of this deposition technique, moving the field closer to large-scale fabrication of a wide-range of efficient perovskite optoelectronic devices.

The final experimental chapter of this thesis, Chapter 6.4 explored the use of aromatic ammonium halide molecules as vapour-deposited passivation agents for co-evaporated perovskite films, examining how measurement atmospheres, annealing treatments and fabrication conditions influenced their passivation behaviours and the resulting device performance. The findings highlighted that measurement atmosphere can significantly affect the observed optoelectronic properties, and that post-deposition annealing can drive surface structural transformations, thereby

altering the passivation mechanisms. Comparisons between vapour-deposited and spin-coated passivation layers further revealed that the same organic molecule can exhibit different structural and functional properties depending on the deposition methods. These results may offer valuable insights for the development of perovskite passivation engineering in the future.

Overall, this thesis presented a study of vapour-deposited perovskite solar cells, with a focus on various methods to reduce bulk and interface defect densities in metal halide perovskite thin films. Future research should systematically investigate how various chemical additives or reactants influence the sublimation and decomposition behaviours of precursors during vapour deposition processes. By selecting a chemical which can modulate the crystallisation kinetics and avoid the degradation pathway, it is a promising approach to further improve the quality and stability of perovskite films. The templating strategy explored in this thesis offers a controlled pathway for directing the nucleation and growth of perovskite films. Future studies should aim to elucidate the mechanism of this approach, such as how the orientation and surface energy of the templating layer influence the crystal growth of the following three-dimensional perovskites. Meanwhile, the templating strategy can be extended to other deposition techniques and different templating layers. Recent studies suggest the potential of this approach in strain management, the optimisation of wide bandgap absorption layers and its integration with pulsed layer deposition techniques.[224–226] The findings from the molecular passivation study further demonstrate that the structural and functional properties of organic passivating species can be tuned through the choice of deposition methodology. This highlights the importance of interface engineering not only at the materials level but also within the broader context of process design. Furthermore, a

thorough investigation into the irreversible photo-brightening effect on optimising the co-evaporated perovskite film quality should be conducted to uncover the mechanism behind defect suppression. This effect may represent a highly promising route to significantly improve the quality of co-evaporated perovskite films and boost device performance.

# References


[1] Olhoff, A.; Christensen, J.; Lamb, W. F.; Pathak, M.; Kuramochi, T.; Fransen, T.; Rogelj, J.; Elzen, M. den; Portugal-Pereira, J.; Grant, N., *et al.* "Emissions Gap Report 2024: No more hot air⋯please! With a massive gap between rhetoric and reality, countries draft new climate commitments". 2024.

[2] IRENA, I. "Renewable power generation costs in 2023". *Report, International Renewable Energy Agency, Abu Dhabi*, 2024.

[3] IEA PVPS Task 1; Masson, G.; Rechem, A. V.; l' Epine, M. de, and Jäger-Waldau, A. *Snapshot of Global PV Markets 2025*. Tech. rep. IEA PVPS Report. Paris, France, 2025.

[4] Wei, Q.; Zheng, D.; Liu, L.; Liu, J.; Du, M.; Peng, L.; Wang, K., and Liu, S. "Fusing Science with Industry: Perovskite Photovoltaics Moving Rapidly into Industrialization". *Advanced Materials*, 2024, **36**, 2406295.

[5] Correa-Baena, J.-P.; Saliba, M.; Buonassisi, T.; Grätzel, M.; Abate, A.; Tress, W., and Hagfeldt, A. "Promises and challenges of perovskite solar cells". *Science*, 2017, **358**, 739–744.

[6] Correa-Baena, J.-P.; Abate, A.; Saliba, M.; Tress, W.; Jacobsson, T. J.; Grätzel, M., and Hagfeldt, A. "The rapid evolution of highly efficient perovskite solar cells". *Energy & Environmental Science*, 2017, **10**, 710–727.

[7] Kutsarov, D. I.; Rezaee, E.; Lambert, J.; Stroud, W. T.; Panagiotopoulos, A., and Silva, S. R. P. "Progress in Flexible Perovskite Solar Cells: Paving the Way for Scalable Manufacturing". *Advanced materials technologies*, 2025, 2401834.

[8] Wang, W.; Tade, M. O., and Shao, Z. "Research progress of perovskite materials in photocatalysis-and photovoltaics-related energy conversion and environmental treatment". *Chemical Society Reviews*, 2015, **44**, 5371–5408.

[9] Kojima, A.; Teshima, K.; Shirai, Y., and Miyasaka, T. "Organometal halide perovskites as visible-light sensitizers for photovoltaic cells". *Journal of the american chemical society*, 2009, **131**, 6050–6051.

[10] NREL. *Best Research-Cell Efficiencies*. `https://www.nrel.gov/pv/cell-efficiency`. Accessed: April 21, 2025.

[11] He, C. and Liu, X. "The rise of halide perovskite semiconductors". *Light: Science & Applications*, 2023, **12**, 15.

[12] Adinolfi, V.; Peng, W.; Walters, G.; Bakr, O. M., and Sargent, E. H. "The electrical and optical properties of organometal halide perovskites relevant to optoelectronic performance". *Advanced Materials*, 2018, **30**, 1700764.

[13] Manser, J. S.; Christians, J. A., and Kamat, P. V. "Intriguing optoelectronic properties of metal halide perovskites". *Chemical reviews*, 2016, **116**, 12956–13008.

[14] Noel, N. K.; Habisreutinger, S. N.; Wenger, B.; Klug, M. T.; Hörantner, M. T.; Johnston, M. B.; Nicholas, R. J.; Moore, D. T., and Snaith, H. J. "A low viscosity, low boiling point, clean solvent system for the rapid crystallisation of highly specular perovskite films". *Energy & Environmental Science*, 2017, **10**, 145–152.

[15] McMeekin, D. P.; Wang, Z.; Rehman, W.; Pulvirenti, F.; Patel, J. B.; Noel, N. K.; Johnston, M. B.; Marder, S. R.; Herz, L. M., and Snaith, H. J. "Crystallization kinetics and morphology control of formamidinium–cesium mixed-cation lead mixed-halide perovskite via tunability of the colloidal precursor solution". *Advanced Materials*, 2017, **29**, 1607039.

[16] Al-Ashouri, A.; Köhnen, E.; Li, B.; Magomedov, A.; Hempel, H.; Caprioglio, P.; Márquez, J. A.; Morales Vilches, A. B.; Kasparavicius, E.; Smith, J. A., *et al.* "Monolithic perovskite/silicon tandem solar cell with> 29% efficiency by enhanced hole extraction". *Science*, 2020, **370**, 1300–1309.

[17] Bush, K. A.; Palmstrom, A. F.; Yu, Z. J.; Boccard, M.; Cheacharoen, R.; Mailoa, J. P.; McMeekin, D. P.; Hoye, R. L.; Bailie, C. D.; Leijtens, T., *et al.* "23.6%-efficient monolithic perovskite/silicon tandem solar cells with improved stability". *Nature Energy*, 2017, **2**, 1–7.

[18] Shi, Y.; Berry, J. J., and Zhang, F. "Perovskite/silicon tandem solar cells: insights and outlooks". *ACS Energy Letters*, 2024, **9**, 1305–1330.

[19] Blakesley, J. C.; Bonilla, R. S.; Freitag, M.; Ganose, A. M.; Gasparini, N.; Kaienburg, P.; Koutsourakis, G.; Major, J. D.; Nelson, J.; Noel, N. K., *et al.* "Roadmap on established and emerging photovoltaics for sustainable energy conversion". *Journal of Physics: Energy*, 2024, **6**, 041501.

[20] Abzieher, T.; Moore, D. T.; Roß, M.; Albrecht, S.; Silvia, J.; Tan, H.; Jeangros, Q.; Ballif, C.; Hoerantner, M. T.; Kim, B.-S., *et al.* "Vapor phase deposition of perovskite photovoltaics: short track to commercialization?" *Energy & Environmental Science*, 2024, **17**, 1645–1663.

[21] Ashcroft, N. W. and Mermin, N. D. *Solid State Physics*. Holt-Saunders, 1976.

[22] Peter, Y. and Cardona, M. *Fundamentals of semiconductors: physics and materials properties*. Springer Science & Business Media, 2010.

[23] Kittel, C. *Introduction to Solid State Physics*. Wiley, 2004.

[24] Zannoni, A. "On the quantization of the monoatomic ideal gas". *arXiv preprint cond-mat/9912229*, 1999.

[25] Dirac, P. A. M. "On the theory of quantum mechanics". *Proceedings of the Royal Society of London. Series A, Containing Papers of a Mathematical and Physical Character*, 1926, **112**, 661–677.

[26] Nelson, J. A. *The physics of solar cells*. World Scientific Publishing Company, 2003.

[27] Goldsman, N. and Darmody, C. "Semiconductor and device physics: a concise introduction". 2018.

[28] Gueymard, C. A. "Parameterized transmittance model for direct beam and circumsolar spectral irradiance". *Solar Energy*, 2001, **71**, 325–346.

[29] Gueymard, C. A.; Myers, D, and Emery, K. "Proposed reference irradiance spectra for solar energy systems testing". *Solar energy*, 2002, **73**, 443–467.

[30] Shockley, W. and Queisser, H. "Detailed balance limit of efficiency of p–n junction solar cells". *Renewable energy*. Routledge, 2018, Vol2_35–Vol2_54.

[31] Polman, A.; Knight, M.; Garnett, E. C.; Ehrler, B., and Sinke, W. C. "Photovoltaic materials: Present efficiencies and future challenges". *Science*, 2016, **352**, aad4424.

[32] Urbach, F. "The long-wavelength edge of photographic sensitivity and of the electronic absorption of solids". *Physical review*, 1953, **92**, 1324.

[33] Rambadey, O. V.; Kumar, A.; Sati, A., and Sagdeo, P. R. "Exploring the interrelation between Urbach energy and dielectric constant in Hf-substituted $BaTiO_3$". *ACS omega*, 2021, **6**, 32231–32238.

[34] Kaiser, C.; Sandberg, O. J.; Zarrabi, N.; Li, W.; Meredith, P., and Armin, A. "A universal Urbach rule for disordered organic semiconductors". *Nature Communications*, 2021, **12**, 3988.

[35] Sun, Y.-Y.; Agiorgousis, M. L.; Zhang, P., and Zhang, S. "Chalcogenide perovskites for photovoltaics". *Nano letters*, 2015, **15**, 581–585.

[36] Ramesh, R. and Schlom, D. G. "Creating emergent phenomena in oxide superlattices". *Nature Reviews Materials*, 2019, **4**, 257–268.

[37] D' innocenzo, V.; Grancini, G.; Alcocer, M. J.; Kandada, A. R. S.; Stranks, S. D.; Lee, M. M.; Lanzani, G.; Snaith, H. J., and Petrozza, A. "Excitons versus free charges in organo-lead tri-halide perovskites". *Nature communications*, 2014, **5**, 3586.

[38] Yu, Z. and Sun, L. "Recent progress on hole-transporting materials for emerging organometal halide perovskite solar cells". *Advanced Energy Materials*, 2015, **5**, 1500213.

[39] Liu, M.; Johnston, M. B., and Snaith, H. J. "Efficient planar heterojunction perovskite solar cells by vapour deposition". *Nature*, 2013, **501**, 395–398.

[40] Rong, Y.; Hu, Y.; Mei, A.; Tan, H.; Saidaminov, M. I.; Seok, S. I.; McGehee, M. D.; Sargent, E. H., and Han, H. "Challenges for commercializing perovskite solar cells". *Science*, 2018, **361**, eaat8235.

[41] Park, N.-G. *Perovskite solar cell: research direction for next 10 years*. 2019.

[42] Chowdhury, T. A.; Zafar, M. A. B.; Islam, M. S.-U.; Shahinuzzaman, M; Islam, M. A., and Khandaker, M. U. "Stability of perovskite solar cells: issues and prospects". *RSC advances*, 2023, **13**, 1787–1810.

[43] Byranvand, M. M. and Saliba, M. "Defect passivation of perovskite films for highly efficient and stable solar cells". *Solar Rrl*, 2021, **5**, 2100295.

[44] Li, C.; Lu, X.; Ding, W.; Feng, L.; Gao, Y., and Guo, Z. "Formability of $ABX_3$ (X=F, Cl, Br, I) halide perovskites". *Structural Science*, 2008, **64**, 702–707.

[45] Pellet, N.; Gao, P.; Gregori, G.; Yang, T.-Y.; Nazeeruddin, M. K.; Maier, J., and Grätzel, M. "Mixed-organic-cation Perovskite photovoltaics for enhanced solar-light harvesting". *Angewandte Chemie International Edition*, 2014, **53**, 3151–3157.

[46] Yi, C.; Luo, J.; Meloni, S.; Boziki, A.; Ashari-Astani, N.; Grätzel, C.; Zakeeruddin, S. M.; Röthlisberger, U., and Grätzel, M. "Entropic stabilization of mixed A-cation ABX 3 metal halide perovskites for high performance perovskite solar cells". *Energy & Environmental Science*, 2016, **9**, 656–662.

[47] Ono, L. K.; Juarez-Perez, E. J., and Qi, Y. "Progress on perovskite materials and solar cells with mixed cations and halide anions". *ACS applied materials & interfaces*, 2017, **9**, 30197–30246.

[48] Saidaminov, M. I.; Mohammed, O. F., and Bakr, O. M. "Low-dimensional-networked metal halide perovskites: the next big thing". *ACS Energy Letters*, 2017, **2**, 889–896.

[49] Stranks, S. D.; Eperon, G. E.; Grancini, G.; Menelaou, C.; Alcocer, M. J.; Leijtens, T.; Herz, L. M.; Petrozza, A., and Snaith, H. J. "Electron-hole diffusion lengths exceeding 1 micrometer in an organometal trihalide perovskite absorber". *Science*, 2013, **342**, 341–344.

[50] Brivio, F.; Butler, K. T.; Walsh, A., and Van Schilfgaarde, M. "Relativistic quasiparticle self-consistent electronic structure of hybrid halide perovskite photovoltaic absorbers". *Physical Review B*, 2014, **89**, 155204.

[51] Unger, E.; Kegelmann, L.; Suchan, K; Sörell, D; Korte, L., and Albrecht, S. "Roadmap and roadblocks for the band gap tunability of metal halide perovskites". *Journal of Materials Chemistry A*, 2017, **5**, 11401–11409.

[52] Kim, G.-W. and Petrozza, A. "Defect tolerance and intolerance in metal-halide perovskites". *Advanced Energy Materials*, 2020, **10**, 2001959.

[53] Turren-Cruz, S.-H.; Saliba, M.; Mayer, M. T.; Juárez-Santiesteban, H.; Mathew, X.; Nienhaus, L.; Tress, W.; Erodici, M. P.; Sher, M.-J.; Bawendi, M. G., *et al.* "Enhanced charge carrier mobility and lifetime suppress hysteresis and improve efficiency in planar perovskite solar cells". *Energy & Environmental Science*, 2018, **11**, 78–86.

[54] Lim, J.; Kober-Czerny, M.; Lin, Y.-H.; Ball, J. M.; Sakai, N.; Duijnstee, E. A.; Hong, M. J.; Labram, J. G.; Wenger, B., and Snaith, H. J. "Long-range charge carrier mobility in metal halide perovskite thin-films and single crystals via transient photo-conductivity". *Nature Communications*, 2022, **13**, 4201.

[55] Fu, L.; Li, H.; Wang, L.; Yin, R.; Li, B., and Yin, L. "Defect passivation strategies in perovskites for an enhanced photovoltaic performance". *Energy & Environmental Science*, 2020, **13**, 4017–4056.

[56] Tress, W.; Marinova, N.; Inganäs, O.; Nazeeruddin, M. K.; Zakeeruddin, S. M., and Graetzel, M. "Predicting the open-circuit voltage of $CH_3NH_3PbI_3$ perovskite solar cells using electroluminescence and photovoltaic quantum efficiency spectra: the role of radiative and non-radiative recombination". *Advanced Energy Materials*, 2015, **5**, 1400812.

[57] Jiang, Q.; Zhao, Y.; Zhang, X.; Yang, X.; Chen, Y.; Chu, Z.; Ye, Q.; Li, X.; Yin, Z., and You, J. "Surface passivation of perovskite film for efficient solar cells". *Nature Photonics*, 2019, **13**, 460–466.

[58] Liu, P.; Wang, W.; Liu, S.; Yang, H., and Shao, Z. "Fundamental understanding of photocurrent hysteresis in perovskite solar cells". *Advanced Energy Materials*, 2019, **9**, 1803017.

[59] Ball, J. M. and Petrozza, A. "Defects in perovskite-halides and their effects in solar cells". *Nature Energy*, 2016, **1**, 1–13.

[60] Liu, N. and Yam, C. "First-principles study of intrinsic defects in formamidinium lead triiodide perovskite solar cell absorbers". *Physical chemistry chemical physics*, 2018, **20**, 6800–6804.

[61] Lin, D.; Zhan, Z.; Huang, X.; Liu, P., and Xie, W. "Advances in components engineering in vapor deposited perovskite thin film for photovoltaic application". *Materials Today Advances*, 2022, **16**, 100277.

[62] Hsiao, S.-Y.; Lin, H.-L.; Lee, W.-H.; Tsai, W.-L.; Chiang, K.-M.; Liao, W.-Y.; Ren-Wu, C.-Z.; Chen, C.-Y., and Lin, H.-W. "Efficient all-vacuum deposited perovskite solar cells by controlling reagent partial pressure in high vacuum." *Advanced Materials (Deerfield Beach, Fla.)*, 2016, **28**, 7013–7019.

[63] Lohmann, K. B.; Patel, J. B.; Rothmann, M. U.; Xia, C. Q.; Oliver, R. D.; Herz, L. M.; Snaith, H. J., and Johnston, M. B. "Control over crystal size in vapor deposited metal-halide perovskite films". *ACS energy letters*, 2020, **5**, 710–717.

[64] Guesnay, Q.; Sahli, F.; Ballif, C., and Jeangros, Q. "Vapor deposition of metal halide perovskite thin films: Process control strategies to shape layer properties". *Apl Materials*, 2021, **9**.

[65] Du, P.; Wang, L.; Li, J.; Luo, J.; Ma, Y.; Tang, J., and Zhai, T. "Thermal evaporation for halide perovskite optoelectronics: fundamentals, progress, and outlook". *Advanced Optical Materials*, 2022, **10**, 2101770.

[66] Liu, J.; Shi, B.; Xu, Q.; Li, Y.; Chen, B.; Wang, Q.; Wang, P.; Zhao, Y., and Zhang, X. "Crystalline quality control in sequential vapor deposited perovskite film toward high efficiency and large scale solar cells". *Solar Energy Materials and Solar Cells*, 2021, **233**, 111382.

[67] Kasap, S. and Capper, P. *Springer handbook of electronic and photonic materials*. Springer, 2017.

[68] Parrott, E. S.; Patel, J. B.; Haghighirad, A.-A.; Snaith, H. J.; Johnston, M. B., and Herz, L. M. "Growth modes and quantum confinement in ultrathin vapour-deposited $MAPbI_3$ films". *Nanoscale*, 2019, **11**, 14276–14284.

[69] Held, V.; Mrkyvkova, N.; Halahovets, Y.; Nádaždy, P.; Vegso, K.; Vlk, A.; Ledinský, M.; Jergel, M.; Bernstorff, S.; Keckes, J., *et al.* "Evolution of defects, morphology, and strain during $FAMAPbI_3$ perovskite vacuum deposition: Insights from in situ photoluminescence and X-ray scattering". *ACS Applied Materials & Interfaces*, 2024, **16**, 35723–35731.

[70] Chen, H. "Two-step sequential deposition of organometal halide perovskite for photovoltaic application". *Advanced Functional Materials*, 2017, **27**, 1605654.

[71] Liu, C.; Cheng, Y.-B., and Ge, Z. "Understanding of perovskite crystal growth and film formation in scalable deposition processes". *Chemical Society Reviews*, 2020, **49**, 1653–1687.

[72] Nambiar, R. A.; McMeekin, D. P.; Czenry, M. K.; Smith, J. A.; Taddei, M.; Caprioglio, P.; Kumar, A.; Putland, B. W.; Wang, J.; Elmestekawy, K. A., *et al.* "Interdiffusion control in sequentially evaporated organic–inorganic perovskite solar cells". *EES Solar*, 2025, **1**, 129–138.

[73] Davies, C. L.; Filip, M. R.; Patel, J. B.; Crothers, T. W.; Verdi, C.; Wright, A. D.; Milot, R. L.; Giustino, F.; Johnston, M. B., and Herz, L. M. "Bimolecular recombination in methylammonium lead triiodide perovskite is an inverse absorption process". *Nature communications*, 2018, **9**, 293.

[74] Elmestekawy, K. A.; Wright, A. D.; Lohmann, K. B.; Borchert, J.; Johnston, M. B., and Herz, L. M. "Controlling intrinsic quantum confinement in formamidinium lead triiodide perovskite through Cs substitution". *ACS nano*, 2022, **16**, 9640–9650.

[75] Tanaka, K.; Takahashi, T.; Ban, T.; Kondo, T.; Uchida, K., and Miura, N. "Comparative study on the excitons in lead-halide-based perovskite-type crystals $CH_3NH_3PbBr_3$ $CH_3NH_3PbI_3$". *Solid state communications*, 2003, **127**, 619–623.

[76] Wright, A. D.; Verdi, C.; Milot, R. L.; Eperon, G. E.; Pérez-Osorio, M. A.; Snaith, H. J.; Giustino, F.; Johnston, M. B., and Herz, L. M. "Electron–phonon coupling in hybrid lead halide perovskites". *Nature communications*, 2016, **7**, 11755.

[77] Verma, G. *Nanostructures: Properties, Processing, and Applications*. Elsevier, 2023.

[78] Kazarian, S. G. and Chan, K. A. "ATR-FTIR spectroscopic imaging: recent advances and applications to biological systems". *Analyst*, 2013, **138**, 1940–1951.

[79] Grdadolnik, J. "ATR-FTIR spectroscopy: Its advantage and limitations". *Acta Chimica Slovenica*, 2002, **49**, 631–642.

[80] Quilettes, D. W. de; Vorpahl, S. M.; Stranks, S. D.; Nagaoka, H.; Eperon, G. E.; Ziffer, M. E.; Snaith, H. J., and Ginger, D. S. "Impact of microstructure on local carrier lifetime in perovskite solar cells". *Science*, 2015, **348**, 683–686.

[81] Richter, J. M.; Abdi-Jalebi, M.; Sadhanala, A.; Tabachnyk, M.; Rivett, J. P.; Pazos-Outón, L. M.; Gödel, K. C.; Price, M.; Deschler, F., and Friend, R. H. "Enhancing photoluminescence yields in lead halide perovskites by photon recycling and light out-coupling". *Nature communications*, 2016, **7**, 13941.

[82] Bragg, W. H. and Bragg, W. L. "The reflection of X-rays by crystals". *Proceedings of the Royal Society of London. Series A, Containing Papers of a Mathematical and Physical Character*, 1913, **88**, 428–438.

[83] Yan, S.; Patel, J. B.; Lee, J. E.; Elmestekawy, K. A.; Ratnasingham, S. R.; Yuan, Q.; Herz, L. M.; Noel, N. K., and Johnston, M. B. "A templating approach to controlling the growth of coevaporated halide perovskites". *ACS Energy Letters*, 2023, **8**, 4008–4015.

[84] Steele, J. A.; Solano, E.; Hardy, D.; Dayton, D.; Ladd, D.; White, K.; Chen, P.; Hou, J.; Huang, H.; Saha, R. A., *et al.* "How to GIWAXS: grazing incidence wide angle X-ray scattering applied to metal halide perovskite thin films". *Advanced Energy Materials*, 2023, **13**, 2300760.

[85] Baker, J. L.; Jimison, L. H.; Mannsfeld, S.; Volkman, S.; Yin, S.; Subramanian, V.; Salleo, A.; Alivisatos, A. P., and Toney, M. F. "Quantification of thin film crystallographic orientation using X-ray diffraction with an area detector". *Langmuir*, 2010, **26**, 9146–9151.

[86] Rivnay, J.; Mannsfeld, S. C.; Miller, C. E.; Salleo, A., and Toney, M. F. "Quantitative determination of organic semiconductor microstructure from the molecular to device scale". *Chemical reviews*, 2012, **112**, 5488–5519.

[87] Parratt, L. G. "Surface studies of solids by total reflection of X-rays". *Physical review*, 1954, **95**, 359.

[88] Genzel, C. "X-ray residual stress analysis in thin films under grazing incidence–basic aspects and applications". *Materials science and technology*, 2005, **21**, 10–18.

[89] Wehrenfennig, C.; Liu, M.; Snaith, H. J.; Johnston, M. B., and Herz, L. M. "Charge-carrier dynamics in vapour-deposited films of the organolead halide perovskite $CH_3NH_3PbI_{3-x}Cl_x$". *Energy & Environmental Science*, 2014, **7**, 2269–2275.

[90] Lohmann, K. B.; Motti, S. G.; Oliver, R. D.; Ramadan, A. J.; Sansom, H. C.; Yuan, Q.; Elmestekawy, K. A.; Patel, J. B.; Ball, J. M.; Herz, L. M., *et al.* "Solvent-free method for defect reduction and improved performance of pin vapor-deposited perovskite solar cells". *ACS energy letters*, 2022, **7**, 1903–1911.

[91] Rehman, W.; McMeekin, D. P.; Patel, J. B.; Milot, R. L.; Johnston, M. B.; Snaith, H. J., and Herz, L. M. "Photovoltaic mixed-cation lead mixed-halide perovskites: links between crystallinity, photo-stability and electronic properties". *Energy & Environmental Science*, 2017, **10**, 361–369.

[92] Zhou, W.; Apkarian, R.; Wang, Z. L., and Joy, D. "Fundamentals of scanning electron microscopy (SEM)". *Scanning microscopy for nanotechnology: techniques and applications*, 2007, 1–40.

[93] Vernon-Parry, K. D. "Scanning electron microscopy: an introduction". *III-Vs review*, 2000, **13**, 40–44.

[94] Hore, P. J. *Nuclear magnetic resonance*. Oxford University Press, 2015.

[95] McLafferty, F. W. "Mass spectrometric analysis. Molecular rearrangements". *Analytical chemistry*, 1959, **31**, 82–87.

[96] Snaith, H. J. "Present status and future prospects of perovskite photovoltaics". *Nature materials*, 2018, **17**, 372–376.

[97] Jeon, N. J.; Noh, J. H.; Yang, W. S.; Kim, Y. C.; Ryu, S.; Seo, J., and Seok, S. I. "Compositional engineering of perovskite materials for high-performance solar cells". *Nature*, 2015, **517**, 476–480.

[98] Zhang, J.; Wu, J.; Barabash, A.; Du, T.; Qiu, S.; Le Corre, V. M.; Zhao, Y.; Zhang, K.; Schmitt, F.; Peng, Z., *et al.* "Precise control of process parameters for$>23\%$ efficiency perovskite solar cells in ambient air using an automated device acceleration platform". *Energy & Environmental Science*, 2024, **17**, 5490–5499.

[99] Zheng, D.; Raffin, F.; Volovitch, P., and Pauporté, T. "Control of perovskite film crystallization and growth direction to target homogeneous monolithic structures". *Nature Communications*, 2022, **13**, 6655.

[100] Zhu, H.; Teale, S.; Lintangpradipto, M. N.; Mahesh, S.; Chen, B.; McGehee, M. D.; Sargent, E. H., and Bakr, O. M. "Long-term operating stability in perovskite photovoltaics". *Nature Reviews Materials*, 2023, **8**, 569–586.

[101] Shen, Z.; Han, Q.; Luo, X.; Shen, Y.; Wang, Y.; Yuan, Y.; Zhang, Y.; Yang, Y., and Han, L. "Efficient and stable perovskite solar cells with regulated depletion region". *Nature Photonics*, 2024, **18**, 450–457.

[102] Chen, L.; Liu, T.; Yu, H.; Zhang, Z.; Qin, C.; Zhang, N.; Yu, L.; Yang, F.; Song, G., and Liu, Z. "Modulated crystallization and enhanced stable of high efficient perovskite solar cells with $Pb(Ac)_2$". *Journal of alloys and compounds*, 2023, **942**, 168924.

[103] Cai, S.; Li, Z.; Zhang, Y.; Liu, T.; Wang, P.; Ju, M.-G.; Pang, S.; Lau, S. P.; Zeng, X. C., and Zhou, Y. "Intragrain impurity annihilation for highly efficient and stable perovskite solar cells". *Nature communications*, 2024, **15**, 2329.

[104] Zhu, P.; Wang, D.; Zhang, Y.; Liang, Z.; Li, J.; Zeng, J.; Zhang, J.; Xu, Y.; Wu, S.; Liu, Z., *et al.* "Aqueous synthesis of perovskite precursors for highly efficient perovskite solar cells". *Science*, 2024, **383**, 524–531.

[105] Zhang, C. and Park, N.-G. "Materials and methods for cost-effective fabrication of perovskite photovoltaic devices". *Communications Materials*, 2024, **5**, 194.

[106] Senevirathna, D. C.; Yu, J. C.; Nirmal Peiris, T.; Li, B.; Michalska, M.; Li, H., and Jasieniak, J. J. "Impact of anion impurities in commercial PbI2 on lead halide perovskite films and solar cells". *ACS Materials Letters*, 2021, **3**, 351–355.

[107] Abdi-Jalebi, M.; Andaji-Garmaroudi, Z.; Cacovich, S.; Stavrakas, C.; Philippe, B.; Richter, J. M.; Alsari, M.; Booker, E. P.; Hutter, E. M.; Pearson, A. J., *et al.* "Maximizing and stabilizing luminescence from halide perovskites with potassium passivation". *Nature*, 2018, **555**, 497–501.

[108] Kerner, R. A.; Christensen, E. D.; Harvey, S. P.; Messinger, J.; Habisreutinger, S. N.; Zhang, F.; Eperon, G. E.; Schelhas, L. T.; Zhu, K.; Berry, J. J., *et al.* "Analytical evaluation of lead iodide precursor impurities affecting halide perovskite device performance". *ACS Applied Energy Materials*, 2022, **6**, 295–301.

[109] Borchert, J.; Levchuk, I.; Snoek, L. C.; Rothmann, M. U.; Haver, R.; Snaith, H. J.; Brabec, C. J.; Herz, L. M., and Johnston, M. B. "Impurity tracking enables enhanced control and reproducibility of hybrid perovskite vapor deposition". *ACS applied materials & interfaces*, 2019, **11**, 28851–28857.

[110] Yang, Z.; Dou, J.; Kou, S.; Dang, J.; Ji, Y.; Yang, G.; Wu, W.-Q.; Kuang, D.-B., and Wang, M. "Multifunctional phosphorus-containing Lewis acid and base passivation enabling efficient and moisture-stable perovskite solar cells". *Advanced Functional Materials*, 2020, **30**, 1910710.

[111] Wen, H.; Zhang, Z.; Guo, Y.; Luo, W.; Si, S.; Yin, T.; Wu, H., and Huang, S. "Synergistic full-scale defect passivation enables high-efficiency and stable perovskite solar cells". *Advanced Energy Materials*, 2023, **13**, 2301813.

[112] Gao, X.-X.; Luo, W.; Zhang, Y.; Hu, R.; Zhang, B.; Züttel, A.; Feng, Y., and Nazeeruddin, M. K. "Stable and high-efficiency methylammonium-free perovskite solar cells". *Advanced Materials*, 2020, **32**, 1905502.

[113] Turren-Cruz, S.-H.; Hagfeldt, A., and Saliba, M. "Methylammonium-free, high-performance, and stable perovskite solar cells on a planar architecture". *Science*, 2018, **362**, 449–453.

[114] Eperon, G. E.; Stranks, S. D.; Menelaou, C.; Johnston, M. B.; Herz, L. M., and Snaith, H. J. "Formamidinium lead trihalide: a broadly tunable perovskite for efficient planar heterojunction solar cells". *Energy & environmental science*, 2014, **7**, 982–988.

[115] Dolan, C. J.; Yakel, E. R.; Liu, S.; Kerner, R. A.; Palmer, J. R.; Vences, K. X.; Vossler, H. M.; Han, C.; Dunfield, S. P., and Fenning, D. P. "Single crystal purification reduces trace impurities in halide perovskite precursors, alters perovskite thin film performance, and improves phase stability". *Journal of Materials Chemistry C*, 2025, **13**, 9584–9592.

[116] Borchert, J.; Milot, R. L.; Patel, J. B.; Davies, C. L.; Wright, A. D.; Martínez Maestro, L.; Snaith, H. J.; Herz, L. M., and Johnston, M. B. "Large-area, highly uniform evaporated formamidinium lead triiodide thin films for solar cells". *ACS Energy Letters*, 2017, **2**, 2799–2804.

[117] Kroll, M.; Öz, S. D.; Zhang, Z.; Ji, R.; Schramm, T.; Antrack, T.; Vaynzof, Y.; Olthof, S., and Leo, K. "Insights into the evaporation behaviour of FAI: material degradation and consequences for perovskite solar cells". *Sustainable Energy & Fuels*, 2022, **6**, 3230–3239.

[118] Zhang, W.; Li, Y.; Liu, X.; Tang, D.; Li, X., and Yuan, X. "Ethyl acetate green antisolvent process for high-performance planar low-temperature $SnO_2$-based perovskite solar cells made in ambient air". *Chemical Engineering Journal*, 2020, **379**, 122298.

[119] Zhang, P.; Gu, N.; Song, L.; Chen, X.; Du, P.; Zha, L.; Chen, W.-H., and Xiong, J. "The disappearing additive: introducing volatile ethyl acetate into a perovskite precursor for fabricating high efficiency stable devices in open air". *Nanoscale*, 2022, **14**, 5204–5213.

[120] Wright, A. D.; Volonakis, G.; Borchert, J.; Davies, C. L.; Giustino, F.; Johnston, M. B., and Herz, L. M. "Intrinsic quantum confinement in formamidinium lead triiodide perovskite". *Nature Materials*, 2020, **19**, 1201–1206.

[121] Elmestekawy, K. A.; Gallant, B. M.; Wright, A. D.; Holzhey, P.; Noel, N. K.; Johnston, M. B.; Snaith, H. J., and Herz, L. M. "Photovoltaic performance of $FAPbI_3$ perovskite is hampered by intrinsic quantum confinement". *ACS Energy Letters*, 2023, **8**, 2543–2551.

[122] Guo, D.; Selby, T. A.; Kahmann, S.; Gorgon, S.; Dai, L.; Dubajic, M.; Yang, T. C.-J.; Fairclough, S. M.; Marsh, T.; Jacobs, I. E., *et al.* "Visualizing nanodomain superlattices in halide perovskites giving picosecond quantum transients". *arXiv preprint arXiv:2502.13609*, 2025.

[123] Liu, H.; Zheng, B.; Wang, X.; Ning, W.; Wan, L.; Wang, Y., and Liu, T. "Mitigating face-sharing octahedral impurity phases for efficient FA-based perovskite photovoltaics". *Advanced Functional Materials*, 2025, 2425620.

[124] Li, S.; Xia, J.; Wen, Z.; Gu, H.; Guo, J.; Liang, C.; Pan, H.; Wang, X., and Chen, S. "The formation mechanism of (001) facet dominated $\alpha$-$FAPbI_3$ film by pseudohalide ions for high-performance perovskite solar cells". *Advanced Science*, 2023, **10**, 2300056.

[125] Juarez-Perez, E. J.; Ono, L. K., and Qi, Y. "Thermal degradation of formamidinium based lead halide perovskites into sym-triazine and hydrogen cyanide observed by coupled thermogravimetry-mass spectrometry analysis". *Journal of Materials Chemistry A*, 2019, **7**, 16912–16919.

[126] National Institute of Advanced Industrial Science and Technology (AIST). *Spectral Database for Organic Compounds (SDBS)*. AIST: Tsukuba, Japan. 2025. `https://sdbs.db.aist.go.jp/`.

[127] Grundmann, C. and Ratz, R. "Triazines. XVI. A new synthesis for 1, 2, 4-triazoles". *The Journal of Organic Chemistry*, 1956, **21**, 1037–1038.

[128] Linstrom, P. J. and Mallard, W. G., eds. *NIST Chemistry WebBook*. Retrieved August 11, 2025. National Institute of Standards and Technology, 2025.

[129] Stranks, S. D.; Eperon, G. E.; Grancini, G.; Menelaou, C.; Alcocer, M. J. P.; Leijtens, T.; Herz, L. M.; Petrozza, A., and Snaith, H. J. "Electron-hole diffusion lengths exceeding 1 micrometer in an organometal trihalide perovskite absorber". *Science*, 2013, **342**, 341–344.

[130] Park, N.-G. "Perovskite solar cells: an emerging photovoltaic technology". *Materials today*, 2015, **18**, 65–72.

[131] Herz, L. M. "Charge-carrier mobilities in metal halide perovskites: fundamental mechanisms and limits". *ACS Energy Letters*, 2017, **2**, 1539–1548.

[132] Huang, Y.; Lei, X.; He, T.; Jiang, Y., and Yuan, M. "Recent progress on formamidinium-dominated perovskite photovoltaics". *Advanced Energy Materials*, 2022, **12**, 2100690.

[133] Zhang, Y.; Liu, Y., and Liu, S. "Composition engineering of perovskite single crystals for high-performance optoelectronics". *Advanced Functional Materials*, 2023, **33**, 2210335.

[134] Ni, Z.; Bao, C.; Liu, Y.; Jiang, Q.; Wu, W.-Q.; Chen, S.; Dai, X.; Chen, B.; Hartweg, B.; Yu, Z., *et al.* "Resolving spatial and energetic distributions of trap states in metal halide perovskite solar cells". *Science*, 2020, **367**, 1352–1358.

[135] Wang, R.; Xue, J.; Wang, K.-L.; Wang, Z.-K.; Luo, Y.; Fenning, D.; Xu, G.; Nuryyeva, S.; Huang, T.; Zhao, Y., *et al.* "Constructive molecular configurations for surface-defect passivation of perovskite photovoltaics". *Science*, 2019, **366**, 1509–1513.

[136] Wang, F.; Bai, S.; Tress, W.; Hagfeldt, A., and Gao, F. "Defects engineering for high-performance perovskite solar cells". *npj Flexible Electronics*, 2018, **2**, 22.

[137] Sherkar, T. S.; Momblona, C.; Gil-Escrig, L.; Avila, J.; Sessolo, M.; Bolink, H. J., and Koster, L. J. A. "Recombination in perovskite solar cells: significance of grain boundaries, interface traps, and defect ions". *ACS energy letters*, 2017, **2**, 1214–1222.

[138] Tan, H.; Jain, A.; Voznyy, O.; Lan, X.; Arquer, F. P. García de; Fan, J. Z.; Quintero-Bermudez, R.; Yuan, M.; Zhang, B.; Zhao, Y., *et al.* "Efficient and stable solution-processed planar perovskite solar cells via contact passivation". *Science*, 2017, **355**, 722–726.

[139] Wang, Z.; McMeekin, D. P.; Sakai, N.; Reenen, S. van; Wojciechowski, K.; Patel, J. B.; Johnston, M. B., and Snaith, H. J. "Efficient and air-stable mixed-cation lead mixed-halide perovskite solar cells with n-doped organic electron extraction layers". *Advanced Materials*, 2017, **29**, 1604186.

[140] Yoo, J. J.; Wieghold, S.; Sponseller, M. C.; Chua, M. R.; Bertram, S. N.; Hartono, N. T. P.; Tresback, J. S.; Hansen, E. C.; Correa-Baena, J.-P.; Bulović, V., *et al.* "An interface stabilized perovskite solar cell with high stabilized efficiency and low voltage loss". *Energy & Environmental Science*, 2019, **12**, 2192–2199.

[141] Noel, N. K.; Habisreutinger, S. N.; Pellaroque, A.; Pulvirenti, F.; Wenger, B.; Zhang, F.; Lin, Y.-H.; Reid, O. G.; Leisen, J.; Zhang, Y., *et al.* "Interfacial charge-transfer doping of metal halide perovskites for high performance photovoltaics". *Energy & environmental science*, 2019, **12**, 3063–3073.

[142] Yang, G.; Wang, C.; Lei, H.; Zheng, X.; Qin, P.; Xiong, L.; Zhao, X.; Yan, Y., and Fang, G. "Interface engineering in planar perovskite solar cells: energy level alignment, perovskite morphology control and high performance achievement". *Journal of Materials Chemistry A*, 2017, **5**, 1658–1666.

[143] Li, H.; Zhou, J.; Tan, L.; Li, M.; Jiang, C.; Wang, S.; Zhao, X.; Liu, Y.; Zhang, Y.; Ye, Y., *et al.* "Sequential vacuum-evaporated perovskite solar cells with more than 24% efficiency". *Science advances*, 2022, **8**, eabo7422.

[144] Gil-Escrig, L.; Dreessen, C.; Palazon, F.; Hawash, Z.; Moons, E.; Albrecht, S.; Sessolo, M., and Bolink, H. J. "Efficient wide-bandgap mixed-cation and mixed-halide perovskite solar cells by vacuum deposition". *ACS energy letters*, 2021, **6**, 827–836.

[145] Lin, D.; Gao, Y.; Zhang, T.; Zhan, Z.; Pang, N.; Wu, Z.; Chen, K.; Shi, T.; Pan, Z.; Liu, P., *et al.* "Vapor deposited pure $\alpha$-$FAPbI_3$ perovskite solar cell via moisture-induced phase transition strategy". *Advanced Functional Materials*, 2022, **32**, 2208392.

[146] Chiang, Y.-H.; Anaya, M., and Stranks, S. D. "Multisource vacuum deposition of methylammonium-free perovskite solar cells". *ACS Energy Letters*, 2020, **5**, 2498–2504.

[147] Zhou, J.; Tan, L.; Liu, Y.; Li, H.; Liu, X.; Li, M.; Wang, S.; Zhang, Y.; Jiang, C.; Hua, R., *et al.* "Highly efficient and stable perovskite solar cells via a multifunctional hole transporting material". *Joule*, 2024, **8**, 1691–1706.

[148] Feng, J.; Jiao, Y.; Wang, H.; Zhu, X.; Sun, Y.; Du, M.; Cao, Y.; Yang, D., and Liu, S. F. "High-throughput large-area vacuum deposition for high-performance formamidine-based perovskite solar cells". *Energy & Environmental Science*, 2021, **14**, 3035–3043.

[149] Patel, J. B.; Wright, A. D.; Lohmann, K. B.; Peng, K.; Xia, C. Q.; Ball, J. M.; Noel, N. K.; Crothers, T. W.; Wong-Leung, J.; Snaith, H. J., *et al.* "Light absorption and recycling in hybrid metal halide perovskite photovoltaic devices". *Advanced Energy Materials*, 2020, **10**, 1903653.

[150] Gil-Escrig, L.; Momblona, C.; La-Placa, M.-G.; Boix, P. P.; Sessolo, M., and Bolink, H. J. "Vacuum deposited triple-cation mixed-halide perovskite solar cells". *Advanced Energy Materials*, 2018, **8**, 1703506.

[151] Ono, L. K.; Leyden, M. R.; Wang, S., and Qi, Y. "Organometal halide perovskite thin films and solar cells by vapor deposition". *Journal of Materials Chemistry A*, 2016, **4**, 6693–6713.

[152] Xu, H.; Wu, Y.; Cui, J.; Ni, C.; Xu, F.; Cai, J.; Hong, F.; Fang, Z.; Wang, W.; Zhu, J., *et al.* "Formation and evolution of the unexpected $PbI_2$ phase at the interface during the growth of evaporated perovskite films". *Physical Chemistry Chemical Physics*, 2016, **18**, 18607–18613.

[153] Patel, J; Wong-Leung, J.; Van Reenen, S.; Sakai, N.; Wang, J; Parrott, E; Liu, M.; Snaith, H; Herz, L, and Johnston, M. "Influence of interface morphology on hysteresis in vapor-deposited perovskite solar cells". *Advanced Electronic Materials*, 2016, **3**.

[154] Olthof, S. and Meerholz, K. "Substrate-dependent electronic structure and film formation of $MAPbI_3$ perovskites". *Scientific reports*, 2017, **7**, 40267.

[155] Abzieher, T.; Feeney, T.; Schackmar, F.; Donie, Y. J.; Hossain, I. M.; Schwenzer, J. A.; Hellmann, T.; Mayer, T.; Powalla, M., and Paetzold, U. W. "From groundwork to efficient solar cells: On the importance of the substrate material in co-evaporated perovskite solar cells". *Advanced Functional Materials*, 2021, **31**, 2104482.

[156] Roß, M.; Severin, S.; Stutz, M. B.; Wagner, P.; Köbler, H.; Favin-Lévêque, M.; Al-Ashouri, A.; Korb, P.; Tockhorn, P.; Abate, A., *et al.* "Co-evaporated formamidinium lead iodide based perovskites with 1000 h constant stability for fully textured monolithic perovskite/silicon tandem solar cells". *Advanced Energy Materials*, 2021, **11**, 2101460.

[157] Yuan, Q.; Lohmann, K. B.; Oliver, R. D.; Ramadan, A. J.; Yan, S.; Ball, J. M.; Christoforo, M. G.; Noel, N. K.; Snaith, H. J.; Herz, L. M., *et al.* "Thermally stable perovskite solar cells by all-vacuum deposition". *ACS Applied Materials & Interfaces*, 2022, **15**, 772–781.

[158] Ritzer, D. B.; Abzieher, T.; Basibüyük, A.; Feeney, T.; Laufer, F.; Ternes, S.; Richards, B. S.; Bergfeld, S., and Paetzold, U. W. "Upscaling of perovskite solar modules: The synergy of fully evaporated layer fabrication and all-laser-scribed interconnections". *Progress in Photovoltaics: Research and Applications*, 2022, **30**, 360–373.

[159] Lee, J.-W. and Park, N.-G. "Two-step deposition method for high-efficiency perovskite solar cells". *MRS Bulletin*, 2015, **40**, 654–659.

[160] Sahli, F.; Werner, J.; Kamino, B. A.; Bräuninger, M.; Monnard, R.; Paviet-Salomon, B.; Barraud, L.; Ding, L.; Diaz Leon, J. J.; Sacchetto, D., *et al.* "Fully textured monolithic perovskite/silicon tandem solar cells with 25.2% power conversion efficiency". *Nature materials*, 2018, **17**, 820–826.

[161] Ioakeimidis, A.; Christodoulou, C.; Lux-Steiner, M., and Fostiropoulos, K. "Effect of $PbI_2$ deposition rate on two-step PVD/CVD all-vacuum prepared perovskite". *Journal of Solid State Chemistry*, 2016, **244**, 20–24.

[162] Johnston, M. B. and Herz, L. M. "Hybrid perovskites for photovoltaics: charge-carrier recombination, diffusion, and radiative efficiencies". *Accounts of chemical research*, 2016, **49**, 146–154.

[163] Herz, L. M. "Charge-carrier dynamics in organic-inorganic metal halide perovskites". *Annual review of physical chemistry*, 2016, **67**, 65–89.

[164] Kranjčec, M.; Studenyak, I., and Kurik, M. "On the Urbach rule in non-crystalline solids". *Journal of Non-Crystalline Solids*, 2009, **355**, 54–57.

[165] Cody, G. "Urbach edge of crystalline and amorphous silicon: a personal review". *Journal of non-crystalline solids*, 1992, **141**, 3–15.

[166] Glowienka, D. and Galagan, Y. "Light intensity analysis of photovoltaic parameters for perovskite solar cells". *Advanced Materials*, 2022, **34**, 2105920.

[167] Qiu, W.; Merckx, T.; Jaysankar, M.; De La Huerta, C. M.; Rakocevic, L.; Zhang, W.; Paetzold, U. W.; Gehlhaar, R.; Froyen, L.; Poortmans, J., *et al.* "Pinhole-free perovskite films for efficient solar modules". *Energy & Environmental Science*, 2016, **9**, 484–489.

[168] Mohd Yusoff, A. R. bin; Vasilopoulou, M.; Georgiadou, D. G.; Palilis, L. C.; Abate, A., and Nazeeruddin, M. K. "Passivation and process engineering approaches of halide perovskite films for high efficiency and stability perovskite solar cells". *Energy & Environmental Science*, 2021, **14**, 2906–2953.

[169] Yang, C.; Hu, W.; Liu, J.; Han, C.; Gao, Q.; Mei, A.; Zhou, Y.; Guo, F., and Han, H. "Achievements, challenges, and future prospects for industrialization of perovskite solar cells". *Light: Science & Applications*, 2024, **13**, 227.

[170] Zhang, Z.; Qiao, L.; Meng, K.; Long, R.; Chen, G., and Gao, P. "Rationalization of passivation strategies toward high-performance perovskite solar cells". *Chemical Society Reviews*, 2023, **52**, 163–195.

[171] Thiesbrummel, J.; Shah, S.; Gutierrez-Partida, E.; Zu, F.; Peña-Camargo, F.; Zeiske, S.; Diekmann, J.; Ye, F.; Peters, K. P.; Brinkmann, K. O., *et al.* "Ion-induced field screening as a dominant factor in perovskite solar cell operational stability". *Nature Energy*, 2024, **9**, 664–676.

[172] Chiang, Y.-H.; Frohna, K.; Salway, H.; Abfalterer, A.; Pan, L.; Roose, B.; Anaya, M., and Stranks, S. D. "Vacuum-deposited wide-bandgap perovskite for all-perovskite tandem solar cells". *ACS energy letters*, 2023, **8**, 2728–2737.

[173] Liu, J.; He, Y.; Ding, L.; Zhang, H.; Li, Q.; Jia, L.; Yu, J.; Lau, T. W.; Li, M.; Qin, Y., *et al.* "Perovskite/silicon tandem solar cells with bilayer interface passivation". *Nature*, 2024, **635**, 596–603.

[174] Aydin, E.; De Bastiani, M., and De Wolf, S. "Defect and contact passivation for perovskite solar cells". *Advanced Materials*, 2019, **31**, 1900428.

[175] Zhang, H.; Wu, Y.; Shen, C.; Li, E.; Yan, C.; Zhang, W.; Tian, H.; Han, L., and Zhu, W.-H. "Efficient and stable chemical passivation on perovskite surface via bidentate anchoring". *Advanced Energy Materials*, 2019, **9**, 1803573.

[176] Yang, Y.; Chen, H.; Liu, C.; Xu, J.; Huang, C.; Malliakas, C. D.; Wan, H.; Bati, A. S.; Wang, Z.; Reynolds, R. P., *et al.* "Amidination of ligands for chemical and field-effect passivation stabilizes perovskite solar cells". *Science*, 2024, **386**, 898–902.

[177] Wu, G.; Liang, R.; Ge, M.; Sun, G.; Zhang, Y., and Xing, G. "Surface passivation using 2D perovskites toward efficient and stable perovskite solar cells". *Advanced Materials*, 2022, **34**, 2105635.

[178] Lan, Z.-R.; Wang, Y.-D.; Shao, J.-Y.; Ma, D.-X.; Liu, Z.; Li, D.; Hou, Y.; Yao, J., and Zhong, Y.-W. "Surface passivation with diaminopropane dihydroiodide for p-i-n perovskite solar cells with over 25% efficiency". *Advanced Functional Materials*, 2024, **34**, 2312426.

[179] Zhou, H.; Chen, Q.; Li, G.; Luo, S.; Song, T.-b.; Duan, H.-S.; Hong, Z.; You, J.; Liu, Y., and Yang, Y. "Interface engineering of highly efficient perovskite solar cells". *Science*, 2014, **345**, 542–546.

[180] Chen, J. and Park, N.-G. "Materials and methods for interface engineering toward stable and efficient perovskite solar cells". *ACS Energy Letters*, 2020, **5**, 2742–2786.

[181] Zhang, H.; Nazeeruddin, M. K., and Choy, W. C. "Perovskite photovoltaics: the significant role of ligands in film formation, passivation, and stability". *Advanced materials*, 2019, **31**, 1805702.

[182] Lee, D. S.; Yun, J. S.; Kim, J.; Soufiani, A. M.; Chen, S.; Cho, Y.; Deng, X.; Seidel, J.; Lim, S.; Huang, S., *et al.* "Passivation of grain boundaries by phenethylammonium in formamidinium-methylammonium lead halide perovskite solar cells". *ACS Energy Letters*, 2018, **3**, 647–654.

[183] Liu, Y.; Duan, J.; Zhang, J.; Huang, S.; Ou-Yang, W.; Bao, Q.; Sun, Z., and Chen, X. "High efficiency and stability of inverted perovskite solar cells using phenethyl ammonium iodide-modified interface of NiOx and perovskite layers". *ACS applied materials & interfaces*, 2019, **12**, 771–779.

[184] Jiang, X.; Chen, S.; Li, Y.; Zhang, L.; Shen, N.; Zhang, G.; Du, J.; Fu, N., and Xu, B. "Direct surface passivation of perovskite film by 4-fluorophenethylammonium iodide toward stable and efficient perovskite solar cells". *ACS Applied Materials & Interfaces*, 2021, **13**, 2558–2565.

[185] Isikgor, F. H.; Furlan, F.; Liu, J.; Ugur, E.; Eswaran, M. K.; Subbiah, A. S.; Yengel, E.; De Bastiani, M.; Harrison, G. T.; Zhumagali, S., *et al.* "Concurrent cationic and anionic perovskite defect passivation enables 27.4% perovskite/silicon tandems with suppression of halide segregation". *Joule*, 2021, **5**, 1566–1586.

[186] Teale, S.; Degani, M.; Chen, B.; Sargent, E. H., and Grancini, G. "Molecular cation and low-dimensional perovskite surface passivation in perovskite solar cells". *Nature Energy*, 2024, **9**, 779–792.

[187] Lai, H.; Luo, J.; Zwirner, Y.; Olthof, S.; Wieczorek, A.; Ye, F.; Jeangros, Q.; Yin, X.; Akhundova, F.; Ma, T., *et al.* "High-performance flexible all-perovskite tandem solar cells with reduced $V_{oc}$-deficit in wide-bandgap subcell". *Advanced Energy Materials*, 2022, **12**, 2202438.

[188] Suo, J.; Yang, B.; Jeong, J.; Zhang, T.; Olthof, S.; Gao, F.; Grätzel, M.; Boschloo, G., and Hagfeldt, A. "Interfacial engineering from material to solvent: a mechanistic understanding on stabilizing $\alpha$-formamidinium lead triiodide perovskite photovoltaics". *Nano Energy*, 2022, **94**, 106924.

[189] Li, T.; Xu, J.; Lin, R.; Teale, S.; Li, H.; Liu, Z.; Duan, C.; Zhao, Q.; Xiao, K.; Wu, P., *et al.* "Inorganic wide-bandgap perovskite subcells with dipole bridge for all-perovskite tandems". *Nature Energy*, 2023, **8**, 610–620.

[190] Tan, S.; Huang, T.; Yavuz, I.; Wang, R.; Yoon, T. W.; Xu, M.; Xing, Q.; Park, K.; Lee, D.-K.; Chen, C.-H., *et al.* "Stability-limiting heterointerfaces of perovskite photovoltaics". *Nature*, 2022, **605**, 268–273.

[191] Jiang, Q.; Tong, J.; Xian, Y.; Kerner, R. A.; Dunfield, S. P.; Xiao, C.; Scheidt, R. A.; Kuciauskas, D.; Wang, X.; Hautzinger, M. P., *et al.* "Surface reaction for efficient and stable inverted perovskite solar cells". *Nature*, 2022, **611**, 278–283.

[192] Tan, L.; Zhou, J.; Zhao, X.; Wang, S.; Li, M.; Jiang, C.; Li, H.; Zhang, Y.; Ye, Y.; Tress, W., *et al.* "Combined vacuum evaporation and solution process for high-efficiency large-area perovskite solar cells with exceptional reproducibility". *Advanced Materials*, 2023, **35**, 2205027.

[193] Gu, W.-M.; Zhang, Y.; Jiang, K.-J.; Yu, G.; Xu, Y.; Huang, J.-H.; Zhang, Y.; Wang, F.; Li, Y.; Lin, Y., *et al.* "Surface fluoride management for enhanced stability and efficiency of halide perovskite solar cells via a thermal evaporation method". *Journal of Materials Chemistry A*, 2022, **10**, 12882–12889.

[194] Hu, S.; Pascual, J.; Liu, W.; Funasaki, T.; Truong, M. A.; Hira, S.; Hashimoto, R.; Morishita, T.; Nakano, K.; Tajima, K., *et al.* "A universal surface treatment for p–i–n perovskite solar cells". *ACS Applied Materials & Interfaces*, 2022, **14**, 56290–56297.

[195] Datta, K.; Kim, S.; Li, R.; LaFollette, D. K.; Yang, J.; Perini, C. A., and Correa-Baena, J.-P. "Nanometer control of Ruddlesden-Popper interlayers by thermal evaporation for efficient perovskite photovoltaics". *Advanced Materials*, 2024, **36**, 2404795.

[196] La-Placa, M.-G.; Gil-Escrig, L.; Guo, D.; Palazon, F.; Savenije, T. J.; Sessolo, M., and Bolink, H. J. "Vacuum-deposited 2D/3D perovskite heterojunctions". *ACS Energy Letters*, 2019, **4**, 2893–2901.

[197] Choi, Y.; Koo, D.; Jeong, G.; Kim, U.; Kim, H.; Huang, F., and Park, H. "A vertically oriented two-dimensional Ruddlesden–Popper phase perovskite passivation layer for efficient and stable inverted perovskite solar cells". *Energy & Environmental Science*, 2022, **15**, 3369–3378.

[198] Lin, D.; Zhang, T.; Wang, J.; Long, M.; Xie, F.; Chen, J.; Wu, B.; Shi, T.; Yan, K.; Xie, W., *et al.* "Stable and scalable 3D-2D planar heterojunction perovskite solar cells via vapor deposition". *Nano Energy*, 2019, **59**, 619–625.

[199] Calabrese, J; Jones, N.; Harlow, R.; Herron, N; Thorn, D., and Wang, Y. "Preparation and characterization of layered lead halide compounds". *Journal of the American Chemical Society*, 1991, **113**, 2328–2330.

[200] Alharbi, E. A.; Alyamani, A. Y.; Kubicki, D. J.; Uhl, A. R.; Walder, B. J.; Alanazi, A. Q.; Luo, J.; Burgos-Caminal, A.; Albadri, A.; Albrithen, H., *et al.* "Atomic-level passivation mechanism of ammonium salts enabling highly efficient perovskite solar cells". *Nature communications*, 2019, **10**, 3008.

[201] Zhang, H.; Pfeifer, L.; Zakeeruddin, S. M.; Chu, J., and Grätzel, M. "Tailoring passivators for highly efficient and stable perovskite solar cells". *Nature Reviews Chemistry*, 2023, **7**, 632–652.

[202] Jiang, X.; Zhu, L.; Zhang, B.; Yang, G.; Zheng, L.; Dong, K.; Yin, Y.; Wang, M.; Liu, S.; Pang, S., *et al.* "Insights into the role of $\pi$-electrons of aromatic aldehydes in passivating perovskite defects". *Angewandte Chemie International Edition*, 2025, **64**, e202420369.

[203] Zhang, H.; Xiang, W.; Zuo, X.; Gu, X.; Zhang, S.; Du, Y.; Wang, Z.; Liu, Y.; Wu, H.; Wang, P., *et al.* "Fluorine-containing passivation layer via surface chelation for inorganic perovskite solar cells". *Angewandte Chemie*, 2023, **135**, e202216634.

[204] Zhu, H.; Ren, Y.; Pan, L.; Ouellette, O.; Eickemeyer, F. T.; Wu, Y.; Li, X.; Wang, S.; Liu, H.; Dong, X., *et al.* "Synergistic effect of fluorinated passivator and hole transport dopant enables stable perovskite solar cells with an efficiency near 24%". *Journal of the American Chemical Society*, 2021, **143**, 3231–3237.

[205] García-Benito, I.; Quarti, C.; Queloz, V. I.; Orlandi, S.; Zimmermann, I.; Cavazzini, M.; Lesch, A.; Marras, S.; Beljonne, D.; Pozzi, G., *et al.* "Fashioning fluorous organic spacers for tunable and stable layered hybrid perovskites". *Chemistry of Materials*, 2018, **30**, 8211–8220.

[206] Sirbu, D.; Balogun, F. H.; Milot, R. L., and Docampo, P. "Layered perovskites in solar cells: structure, optoelectronic properties, and device design". *Advanced Energy Materials*, 2021, **11**, 2003877.

[207] *CCDC 1143977: Experimental Crystal Structure Determination.* `https://doi.org/10.5517/ccdc.csd.cc1n7xd8`. Cambridge Crystallographic Data Centre. 2025.

[208] Hao, Y.; Qiu, Z.; Zhang, X.; Wei, Z.; Yao, J., and Cai, H. *CCDC 1819854: Experimental Crystal Structure Determination.* `https://doi.org/10.5517/ccdc.csd.cc1z2pzq`. Cambridge Crystallographic Data Centre. 2018.

[209] Wang, P.-X.; Najarian, A. M.; Hao, Z.; Johnston, A.; Voznyy, O.; Hoogland, S., and Sargent, E. H. *CCDC 2041929: Experimental Crystal Structure Determination.* `https://doi.org/10.5517/ccdc.csd.cc26jsp7`. Cambridge Crystallographic Data Centre. 2021.

[210] Polimeno, L.; Lerario, G.; Giorgi, M. D.; Marco, L. D.; Dominici, L.; Todisco, F.; Coriolano, A.; Ardizzone, V.; Pugliese, M.; Prontera, C. T.; Maiorano, V.; Moliterni, A.; Giannini, C.; Olieric, V.; Gigli, G.; Ballarini, D.; Xiong, Q.; Fieramosca, A.; Solnyshkov, D. D.; Malpuech, G., and Sanvitto, D. *CCDC 2013268: Experimental Crystal Structure Determination.* `https://doi.org/10.5517/ccdc.csd.cc25kz4w`. Cambridge Crystallographic Data Centre. 2021.

[211] Kosasih, F. U.; Erdenebileg, E.; Mathews, N.; Mhaisalkar, S. G., and Bruno, A. "Thermal evaporation and hybrid deposition of perovskite solar cells and mini-modules". *Joule*, 2022, **6**, 2692–2734.

[212] Galisteo-López, J. F.; Anaya, M; Calvo, M., and Míguez, H. "Environmental effects on the photophysics of organic–inorganic halide perovskites". *The Journal of Physical Chemistry Letters*, 2015, **6**, 2200–2205.

[213] Brenes, R.; Eames, C.; Bulović, V.; Islam, M. S., and Stranks, S. D. "The impact of atmosphere on the local luminescence properties of metal halide perovskite grains". *Advanced materials*, 2018, **30**, 1706208.

[214] Hu, Z.; Liu, Z.; Ono, L. K.; Jiang, M.; He, S.; Son, D.-Y., and Qi, Y. "The impact of atmosphere on energetics of lead halide perovskites". *Advanced Energy Materials*, 2020, **10**, 2000908.

[215] Brenes, R.; Guo, D.; Osherov, A.; Noel, N. K.; Eames, C.; Hutter, E. M.; Pathak, S. K.; Niroui, F.; Friend, R. H.; Islam, M. S., *et al.* "Metal halide perovskite polycrystalline films exhibiting properties of single crystals". *Joule*, 2017, **1**, 155–167.

[216] Fang, H.-H.; Wang, F.; Adjokatse, S.; Zhao, N., and Loi, M. A. "Photoluminescence enhancement in formamidinium lead iodide thin films". *Advanced Functional Materials*, 2016, **26**, 4653–4659.

[217] Godding, J. S.; Ramadan, A. J.; Lin, Y.-H.; Schutt, K.; Snaith, H. J., and Wenger, B. "Oxidative passivation of metal halide perovskites". *Joule*, 2019, **3**, 2716–2731.

[218] Hofstetter, Y. J.; García-Benito, I.; Paulus, F.; Orlandi, S.; Grancini, G., and Vaynzof, Y. "Vacuum-induced degradation of 2D perovskites". *Frontiers in chemistry*, 2020, **8**, 66.

[219] Soe, C. M. M.; Nagabhushana, G.; Shivaramaiah, R.; Tsai, H.; Nie, W.; Blancon, J.-C.; Melkonyan, F.; Cao, D. H.; Traoré, B.; Pedesseau, L., *et al.* "Structural and thermodynamic limits of layer thickness in 2D halide perovskites". *Proceedings of the National Academy of Sciences*, 2019, **116**, 58–66.

[220] Quan, L. N.; Yuan, M.; Comin, R.; Voznyy, O.; Beauregard, E. M.; Hoogland, S.; Buin, A.; Kirmani, A. R.; Zhao, K.; Amassian, A., *et al.* "Ligand-stabilized reduced-dimensionality perovskites". *Journal of the American Chemical Society*, 2016, **138**, 2649–2655.

[221] Perini, C. A. R.; Rojas-Gatjens, E.; Ravello, M.; Castro-Mendez, A.-F.; Hidalgo, J.; An, Y.; Kim, S.; Lai, B.; Li, R.; Silva-Acuña, C., *et al.* "Interface reconstruction from Ruddlesden–Popper structures impacts stability in lead halide perovskite solar cells". *Advanced Materials*, 2022, **34**, 2204726.

[222] Gozukara Karabag, Z.; Karabag, A.; Gunes, U.; Gao, X.-X.; Syzgantseva, O. A.; Syzgantseva, M. A.; Varlioglu Yaylali, F.; Shibayama, N.; Kanda, H.; Rafieh, A. I., *et al.* "Tuning 2D perovskite passivation: Impact of electronic and steric effects on the performance of 3D/2D perovskite solar cells". *Advanced Energy Materials*, 2023, **13**, 2302038.

[223] Xu, X.; Zhang, Z.; Liu, T.; Zhu, P.; Zhang, Z., and Xing, G. "Suppressing the penetration of 2D perovskites for enhanced stability of perovskite solar cells". *Journal of Materials Chemistry A*, 2025, **13**, 12097–12103.

[224] Škorjanc, V.; Miaskiewicz, A.; Roß, M.; Maniyarasu, S.; Severin, S.; Leyden, M. R.; Holzhey, P.; Ruske, F.; Korte, L., and Albrecht, S. "Seed layers for wide-band gap coevaporated perovskite solar cells: CsCl regulates band gap and reduces process variability". *ACS Energy Letters*, 2024, **9**, 5639–5646.

[225] Diercks, A.; Petry, J.; Feeney, T.; Singh, R.; Zhao, T.; Hu, H.; Li, Y.; Paetzold, U. W., and Fassl, P. "Sequential Evaporation of Inverted $FAPbI_3$ Perovskite Solar Cells–Impact of Substrate on Crystallization and Film Formation". *ACS Energy Letters*, 2025, **10**, 1165–1173.

[226] Kralj, S.; Artuk, K.; Wieczorek, A.; Orlov, N.; Eftekhari, Z.; Saive, R.; Garnett, E.; Siol, S.; Wolff, C. M., and Morales-Masis, M. "Template-assisted growth of $Cs_xFA_{1-x}PbI_3$ with pulsed laser deposition for single junction perovskite solar cells". *Advanced Energy Materials*, 2025, 2406033.